

MECHANICAL BEHAVIOR AND DEFORMATION MECHANISM IN LIGHT
METALS AT DIFFERENT STRAIN RATES

by

Jianghua Shen

A dissertation submitted to the faculty of
The University of North Carolina at Charlotte
in partial fulfillment of the requirements
for the degree of Doctor of Philosophy in
Mechanical Engineering

Charlotte

2015

Approved by:

Dr. Qiuming Wei

Dr. Laszlo Kecskes

Dr. Harish Cherukuri

Dr. Don Chen

Dr. Jing Zhou

©2015
Jianghua Shen
ALL RIGHTS RESERVED

ABSTRACT

JIANGHUA SHEN. Mechanical behavior and deformation mechanism in light metals at different strain rates. (Under the direction of Dr. QIUMING WEI)

Developing light metals that have desirable mechanical properties is always the object of the endeavor of materials scientists. Magnesium (Mg), one of the lightest metals, had been used widely in military and other applications. Yet, its relatively poor formability, as well as its relatively low absolute strength, in comparison with other metals such as aluminum and steels, caused the use of Mg to be discontinued after World War II. Owing to the subsequent energy crisis of the seventies, recently, interest in Mg development has been rekindled in the materials community. The main focus of research has been quite straight-forward: increasing the strength and formability such that Mg and its alloys may replace aluminum alloys and steels to become yet another choice for structural materials. This dissertation work is mainly focused on fundamental issues related to Mg and its alloys. More specifically, it investigates the mechanical behavior of different Mg-based materials and the corresponding underlying deformation mechanisms. In this context, we examine the factors that affect the microstructure and mechanical properties of pure Mg, binary Mg-alloy (with addition of yttrium), more complex Mg-based alloys with and without the addition of lanthanum, and finally Mg-based metal matrix composites (MMCs) reinforced with ex-situ ceramic particles. More specifically, the effects of the following factors on the mechanical properties of Mg-based materials will be investigated: addition of rare earths (yttrium and lanthanum), in-situ/ex-situ formed particles, particle size or volume fraction and materials processing, effect of

thermal-mechanical treatment (severe plastic deformation and warm extrusion), and so on and so forth.

A few interesting results have been found from this dissertation work: (i) although rare earths may improve the room temperature ductility of well-annealed Mg, the addition of yttrium results in ultrafine and un-recrystallized grains in the Mg-Y alloy subjected to equal channel angular pressing (ECAP); (ii) the reverse volume fraction effect arises as the volume fraction of nano-sized ex-situ formed reinforcements is beyond 10%; (iii) nano-particles are more effective in strengthening Mg than micro-particles when the volume fraction is below 10%; (iv) complete dynamic recovery and/or recrystallization is required to accomplish the moderate ductility in Mg, together with a strong matrix-particle bonding if it is a Mg-based composite; and (v) localized shear failure is observed in all Mg samples, recrystallized completely, which is attributed to the reduced strain hardening rate as a result of the exhaustion of twinning and/or dislocation multiplication.

ACKNOWLEDGEMENTS

I sincerely appreciate Dr. Qiuming Wei and Dr. Yulong Li being my advisors during my tenure at Northwestern Polytechnical University (NPU) and UNC Charlotte. Without their support, I would not be able to accomplish the dissertation.

I would like to express my sincere gratitude to Dr. Laszlo J. Kecskes for advising me on my research and being one of my committee members. I would also like to give my special thanks to Dr. Harish P. Cherukuri, Dr. Don Chen and Dr. Jing Zhou for being my committee members and giving valuable suggestions on my research.

My thanks also go to Dr. Baobao Cao, Dr. Zhiliang Pan, Dr. Weihua Yin, Dr. Thomas Koch and Mr. Franklin Greene for their assistance with my experiments, as well as Dr. K. Kondoh, Mr. T. L. Jones, Dr. Linan An, Dr. Jinling Liu, Dr. Aleš Jäger for providing the specimens for my research. I also want to thank all my academic brothers and sisters for the useful discussion about my research, as well as my other friends for their support and encouragement. I would also like to express my thanks to the following organizations for their financial support during my tenure at UNC Charlotte: China Scholarship Council (CSC), U.S. Army Research Laboratory (ARL) and Graduate Assistant Scholarship (GAS).

Finally, I would like to express my greatest gratitude to my parents, Genwang Shen and Liqin Li, for their unconditional dedication to my life, and my wife, Hongju Yin, for supporting me with endless love and bringing me a lovely son.

TABLE OF CONTENTS

LIST OF TABLES	x
LIST OF FIGURES	xi
LIST OF ABBREVIATIONS	xx
CHAPTER 1: INTRODUCTION	1
1.1 History	1
1.2 Development of Mg Alloys	2
1.2.1 Deformation Mechanisms in Mg	3
1.2.2 The Effect of Second-phase on Mg Properties	6
1.2.2.1 Metallic Elements	7
1.2.2.2 Ex-situ Second-phase Hard Particles	10
1.2.3 The Effect of Heat Treatment on Mg Properties	14
1.2.4 Approaches of Fabricating Metal Matrix Composites	15
1.3 Adiabatic Shear Banding	19
1.4 Scope and Objectives of the Dissertation	30
1.5 Organization of the Dissertation	32
CHAPTER 2: EXPERIMENTAL METHODS	34
2.1 Materials Processing	34
2.1.1 Pure Mg and Mg-0.6 wt.% Y	35
2.1.2 Mg Alloys AZXE7111 and AMX602	36
2.1.3 Mg-based Metal Matrix Composites	39
2.2 Mechanical Testing	40
2.2.1 Polishing	40

2.2.2 Mechanical Tests	41
2.2.3 Fundamental Principles of SHPB	43
2.2.3.1 Stress Wave Generation and Propagation	43
2.2.3.2 Magnitude of the Stress-wave	46
2.2.3.3 Interaction between Stress-waves	47
2.2.3.4 Stress-wave Propagation through an Interface	50
2.2.3.5 Recording and Analyzing	53
2.3 Microstructural Characterization	55
CHAPTER 3: PURE MAGNESIUM AND MG-0.6% YTTRIUM	57
3.1 Materials Characterization	59
3.2 Mechanical Properties	63
3.2.1 Compressive Behavior	63
3.2.2 Activation Volume and Strain Rate Sensitivity	65
3.2.3 Post-loading Examination	69
3.3 Discussion	72
3.4 Summary	76
CHAPTER 4: MAGNESIUM ALLOYS WITH IN-SITU FORMED PARTICLES	78
4.1 AMX602	79
4.1.1 Microstructure of Extruded AMX602	79
4.1.2 Mechanical Properties of AMX602	82
4.1.3 Post-loading Examination of AMX602	84
4.1.4 Discussion of Results of AZX602	88
4.1.4.1 Strengthening Mechanism in AMX602	88

4.1.4.2 The anisotropy of strain hardening	90
4.1.4.3 Strain Rate Sensitivity	91
4.1.5 Summary	93
4.2 AZXE7111	93
4.2.1 Texture and Microstructure of AZXE7111	94
4.2.2 Mechanical Properties of AZXE7111	100
4.2.3 Post-mortem Examination of AZXE7111	104
4.2.4 Discussion and Conclusion of AZXE7111	108
4.2.4.1 Precipitation strengthening	110
4.2.4.2 Hall-Petch strengthening	113
4.2.4.3 Strain-rate hardening, adiabatic heating and strain hardening	114
4.2.5 Summary	116
4.3 Adiabatic Shear Banding	117
4.3.1 Temperature Rise and Heat Diffusion in Shear Bands	117
4.3.1.1 The Estimation of Temperature Rise	118
4.3.1.2 Thermal Diffusion during Strain Localization	120
4.3.2 Strain Localization in Mg Alloys	123
4.3.3 Discussion of the Failure Mechanism in the Alloys	124
4.3.4 Hypotheses on the Formation of ASB	127
4.4 Discussion and Conclusions	129
CHAPTER 5: MG-BASED METAL-MATRIX COMPOSITES	133
5.1 Materials Characterization	135
5.2 Mechanical Properties	141

5.3 Post-loading Examination	146
5.4 Discussion	150
5.4.1 Microstructure Features	150
5.4.2 Strengthening Effects	152
5.5 Summary	161
CHAPTER 6: SUMMARY AND CONCLUDING REMARKS	163
CHAPTER 7: FUTURE WORK	167
REFERENCES	169
APPENDIX A: HEAT DIFFUSION	194
APPENDIX B: CODE FOR MATLAB	199
LIST OF PUBLICATIONS	210
VITA	211

LIST OF TABLES

TABLE 2.1: The chemical composition of Mg-0.6 wt% Y.	37
TABLE 4.1: List of the offset yield and ultimate strengths of AMX602 under compressive loading.	83
TABLE 4.2: Yield and maximum compressive strengths of the AZXE7111 alloy, under quasi-static and dynamic compressive loading conditions.	103
TABLE 4.3: Yield and maximum compressive strengths of two conventional alloys, under quasi-static and dynamic compressive loading conditions.	129
TABLE 5.1: Strengthening effect estimations.	159

LIST OF FIGURES

FIGURE 1.1: Deformation modes in Mg: (a ~ d) slip systems; (e ~ h) twinning systems.	3
FIGURE 1.2: Grain size as a function of SiC particle size in AZ91-based MMCs.	11
FIGURE 1.3: The (a) Vickers hardness and (b) tensile and compressive yield stresses of Y ₂ O ₃ -reinforced Mg-MMCs as a function of the volume fraction of Y ₂ O ₃ .	13
FIGURE 1.4: (a) volume of clusters and mode I fracture toughness and (b) tensile strength of SiC-reinforced Al-MMCs as a function of the volume fraction of SiC.	14
FIGURE 1.5: Two different material processing methods for MMCs: (a) melt matrix poured into fabricated reinforcing mesh and following with compression; (b) mixing melt matrix with solid particles and following with casting.	17
FIGURE 1.6: (a) Scanning electron microscope (SEM) image of an ASB in tungsten heavy alloy after uniaxial dynamic compression; (b) a fractured shear band with equiaxed voids in a U-2Mo alloy.	20
FIGURE 1.7: A successive showing of the evolution of shear localization as the strain increases from (a) to (d).	27
FIGURE 1.8: Micrographs showing the highly deformed shear band and white etching band in an Al-Li alloy.	28
FIGURE 2.1: A schematic illustration of the equal-channel angular pressing (ECAP) process and the direction identifications.	37
FIGURE 2.2: Photos of the ECAPed (a) pure Mg and (b) Mg-0.6 wt.%Y following the route Bc with a back pressure of 200 ~ 400 MPa up to four passes.	37
FIGURE 2.3: (a) A schematic illustration of spinning water atomization (SWA) facility, which combines a vacuum furnace, water cooled spinning chamber and a collection pot; (b) the morphology of the collected powders from SWA processing.	38

- FIGURE 2.4: Schematic graph of desk-top compression Split-Hopkinson pressure bar system (SHPB or called desk-top Kolsky bar system). 42
- FIGURE 2.5: A schematic illustration of stress propagation in an elastic bar. A small part of the bar that is affected by the impact load at the very moment is pulled out for analysis. 44
- FIGURE 2.6: A schematic illustration of stress-wave generation during impacting. When the impact happens, a physical compatibility shall be satisfied at the interface, i.e. 1 and 2, where 1 is the face of the striker and 2 is the face of the input bar. 47
- FIGURE 2.7: A schematic illustration of the interaction between two stress-waves. When the stress-waves meet, a physical compatibility shall be satisfied at region L and region R, where L is the wave-front of left stress-wave while R is the wave-front of right stress-wave. 48
- FIGURE 2.8: A schematic illustration of the interaction between a stress-wave and a boundary. The right dashed part is an imaginary bar with an imaginary stress-wave travelling towards the real one. 49
- FIGURE 2.9: A schematic illustration of the stress-wave propagation through an interface with same or different cross-sectional areas. The in-put stress-wave separates into reflected and transmitted parts propagating in separate directions. 51
- FIGURE 3.1: (a) An inverse pole figure (IPF) map of as-ECAPed p-Mg taken from the centre of the ID-ED plane. The EBSD image displays a well-annealed and uniformly distributed grain structure with grain size of $\sim 5\text{-}\mu\text{m}$; (b) XRD result for p-Mg subjected to 4-pass ECAP via route Bc. The narrow profile of diffraction peaks and well-distinguished $K\alpha_1$ and $K\alpha_2$ lines indicate a very low accumulated strain in the sample. 60
- FIGURE 3.2: The (0002) and direct pole figures taken from the ID-ED plane of as-ECAPed p-Mg are shown, accompanied with the direction indicators and the maximum intensities. Those figures display a tendency for the grains to align the basal planes parallel with the theoretical shear plane of the ECAP die. 60
- FIGURE 3.3: A bright-field TEM image of Mg-Y alloy after 4-pass ECAP via route Bc. The highly deformed microstructure can be 62

- identified through either distorted grains with an estimated size of ~ 400 -nm or unrecrystallized regions with strong deformation contrast.
- FIGURE 3.4: XRD spectrums for Mg-Y alloy subjected to (a) 4-pass ECAP via route Bc and (b) 4-pass ECAP via route Bc + 2-hour annealing at 573K. It is obviously that the profile of diffraction peaks became much narrower as the as-ECAPed Mg-Y was annealed, and the $K\alpha_1$ and $K\alpha_2$ lines at high 2θ angle became well-distinguished while they were unidentified in the as-ECAPed Mg-Y alloy. Those confirm the accumulation of internal strain in the as-ECAPed Mg-Y alloy. 62
- FIGURE 3.5: Compressive true stress-strain curves of as-ECAPed (a) p-Mg and (b) Mg-Y alloy at the plastic deformation region are presented. The results from extrusion direction (ED), transverse direction (TD) and insert direction (ID), as well as at quasi-static and dynamic loading rates are included. 64
- FIGURE 3.6: The representative profiles of multi-relaxation for as-ECAPed (a) p-Mg and (b) Mg-Y alloy. 66
- FIGURE 3.7: The linear dependence of $\ln(-)$ as the function of $\Delta\tau$ for (a) p-Mg and (b) Mg-Y alloy at two successive relaxations. Straight lines are obtained for each plot, the slopes of which were measured and presented according to each plot. As can be seen, two relaxation of one sample provide almost the same value of V_r/kT . 66
- FIGURE 3.8: A representative nano-hardness vs. strain rate plots of p-Mg and Mg-Y in a logarithmic scale. 68
- FIGURE 3.9: The SEM images of (a) quasi-statically and (b) dynamically compressed Mg-Y specimens along ED direction. The arrows indicate the direction of the compression load. One major crack with near 45° to the loading direction can be viewed from both samples. Enlarged images (not shown here) also show small cracks in the similar direction, which are very noticeable in figure (b). 69
- FIGURE 3.10: (a) An enlarged view of the black square in Figure 11(a), a view of the fracture surface. Three locations of the fracture surface were magnified, shown in (b), (c) and (d). Besides the rest burrs from dimples, numerous micro-voids are also visible in figure (b). Figure (c) displays a great amount of dimples and ridges that were left during ductile fracture. The 70

- dimple size is measured to be approximately 2- μm . Figure (d) shows a smooth feature that was probably left after the ductile fracture by one part slips on the other.
- FIGURE 3.11: A small area of the fracture surface in Mg-Y showing multiple shallow dimples. The sample was compressed dynamically along ED direction. 71
- FIGURE 4.1: (a) Bright field image of AMX602 extruded at 250°C; (b) The corresponding selected area diffraction pattern of the sample; (c) EDX results of the selected square area in (a). 80
- FIGURE 4.2: Scanning electron microscope observation of AMX602 extruded at various temperatures: a. 250 °C; b. 300 °C; c. 350 °C with two magnifications. Apparently, the size of matrix grains, as well as the white particles, is larger for samples from a higher extrusion temperature. Clustering of the particles up to ~ 5- μm can be viewed. 81
- FIGURE 4.3: Compressive true stress-strain curves of AMX602 in the flow direction (a) and in the transverse direction (b) under both quasi-static and dynamic loading with various extrusion temperatures. 83
- FIGURE 4.4: The nano-hardness vs. strain rate of AMX602 with different extrusion temperatures. 85
- FIGURE 4.5: The representative fractured specimens of AMX602 partially restored from fragments after (a) quasi-static and (b) dynamic testing. 86
- FIGURE 4.6: (a) Low-magnification of the incomplete adiabatic shear band of AMX602 under dynamic testing; (b) ~ (d) high-magnification of the corresponding areas that marked by black squares in (a). 86
- FIGURE 4.7: The representative SEM images of the fracture surface of AMX602 after (a) dynamic and (b) quasi-static loading. 87
- FIGURE 4.8: The strain hardening rate θ vs. the strain ϵ of AMX602 with different loading rates: (a) along flow direction; (b) along transverse direction. 90
- FIGURE 4.9: XRD texture measurement results of AZXE7111 (extruded at 250 °C). The results are very similar to those reported by El-Sayed and co-authors on a similar alloy processed under similar conditions. The pole-figures shown here indicate that 95

the La-doped Mg-alloy AZXE7111 still exhibits some texture upon extrusion, but the texture is not as strong as conventional Mg-alloys without addition of mischmetal.

- FIGURE 4.10: Optical micrographs of AZXE7111 extruded at 250 °C (a) and 200 °C, respectively, and the grain size distributions of the two samples based on measurement of the optical micrographs. We can see that the average grain size of both samples is around 1.0 μm. The extrusion temperature does not have a very strong effect on the grain size of this Mg-alloy. 96
- FIGURE 4.11: Bright- (a) and dark-field (b) TEM images of an AZXE7111 specimen, extruded at 350 °C, with an inset of the corresponding selected area diffraction pattern (SADP) in (a). Particles of size <100 nm can be observed. Note, particles are present both at the grain boundaries and inside the matrix grains. 97
- FIGURE 4.12: (a) A bright-field TEM image of an AZXE7111 specimen (extruded at 250 °C) with an inset of the corresponding SADP; (b) EDX analysis of the selected area of (a) (see boxed region); and, (c) Bright-field TEM image of an AZXE7111 specimen (extruded at 200 °C) with the SADP of the circled area shown as the inset. 97
- FIGURE 4.13: The particle size distribution of the AZXE7111 alloy, extrusion at temperatures of (a) 350 °C, and (b) 200 °C. The average particle size after extrusion at 350 °C is ~88 nm, while that after 200 °C extrusion is ~85 nm. Note, a lower temperature extrusion results in a relatively narrow particle size distribution. For each condition, the total number of particles measured is ~100. 99
- FIGURE 4.14: A representative SEM image of AZXE7111 sample (along transverse direction), extruded at 200 °C. The grain size revealed here is roughly the same as provided in Figure 4-10. 99
- FIGURE 4.15: Compressive true stress vs. true strain curves of the AZXE7111 alloy; (a) in the flow direction and (b) in the transverse direction under at both quasi-static (a1 and b1) and dynamic (a2 and b2) loading conditions. The extrusion temperatures are also indicated in the captions. Note the strong strain hardening under both quasi-static and dynamic loading, and the relatively isotropic behavior of this Mg-alloy. 101

- FIGURE 4.16: SEM images (low magnification) taken from the post-loaded AZXE7111 alloy (extruded at 200°C) under (a) quasi-static and (b) dynamic compression along transverse direction. 104
- FIGURE 4.17: High magnification side view of an incomplete crack in an unfailed dynamic AZXE7111 specimen (extruded at 200°C) along transverse direction. The inset shows a macroscale side view of the entire specimen. The primary crack runs from the top right corner to the lower left corner of the specimen at an angle of $\sim 45^\circ$ with respect to the loading direction, i.e., in the maximum shear stress plane. Secondary cracks can also be identified in this image. 106
- FIGURE 4.18: SEM images of the fracture surfaces of AZXE7111 (extruded at 350 °C): (a) after quasi-static loading; (b) after dynamic loading along transverse direction. Note that both images are taken at the same magnification level. In (a) for the quasi-static specimen more ductile features are present which are also smaller than those observed in the dynamic specimen (b). 107
- FIGURE 4.19: Inter-particle distance distribution of the intermetallic compound phases for AZXE7111 extruded at 250 °C. The vast majority of the particles have an inter-particle distance on the order of ~ 100 nm. 112
- FIGURE 4.20: The strain rate sensitivity of AMXE7111 extruded at 350 °C and 200 °C as measured by instrumented nanoindentation. The material extruded at 200 °C exhibits higher SRS, presumably because of its finer microstructure. 114
- FIGURE 4.21: The strain hardening rates of AZXE7111 vs. strain in the (a) flow and (b) transverse directions. The solid lines are the smoothed results of the dash lines. 115
- FIGURE 4.22: A simplified two dimensional illustration of the heated shear banding region (yellow) and unheated remaining region (blue). 120
- FIGURE 4.23: The temperature evolution around an adiabatic shear band: (a) $t = 25 \mu\text{s}$; (b) $t = 100 \mu\text{s}$; (c) $t = 0.5 \text{ ms}$; (d) $t = 1 \text{ ms}$; (e) $t = 5 \text{ ms}$ and (f) $t = 25 \text{ ms}$. 121
- FIGURE 4.24: SEM image of an incomplete ASB in AZXE7111 (extruded at 250 °C) after high strain rate compression along transverse 123

direction. The image shows evidence of shear flow on both sides of the shear band. That is, the shear band exhibits a “canonical structure” in the sense of Wright [115], where the flow lines curve into the ASB while they curve away from it the other side of the band.

- FIGURE 5.1: (a) Bright field TEM image of 5 vol. % SiC MMNC. The nano-particles appear to be uniformly distributed within the matrix. Some large agglomerates of the Mg-matrix are present. (b) Dark field TEM image corresponding to (a). The dark bright particles are the nano-particles of the β -SiC phase. (c) Selected area diffraction pattern of the sample. This pattern can be indexed according to the cubic β -SiC phase and the hcp Mg matrix. 134
- FIGURE 5.2: (a) Particle size distribution in the Mg-5 vol% SiC MMNC. Most of the particles have been refined during the comilling process as the start SiC powder has an average particle size of ~ 20 nm. (b) The distribution of the interparticle distance in the Mg-5 vol% SiC MMNC. It shows that the interparticle distance is mostly below 60 nm. 136
- FIGURE 5.3: (a) Bright-field TEM image of the Mg-10 vol% SiC MMNC. Again the nanoparticles of the β -SiC phase appear to be uniformly distributed. However, large particle are seen in this material, with some of the large particles marked by black arrows. (b) Dark-field TEM image corresponding to (a). The bright particles in the dark-field TEM image is the β -SiC phase. 136
- FIGURE 5.4: (a) Bright-field TEM image of the Mg-15 vol% MMNC sample. Again large particles with size around ~ 100 nm are seen. Some of these large particles are marked by arrows. (b) Dark-field TEM image of (a), the bright particles being the b-SiC phase. (c) An enlarged view of one of the large particles in this material. It is faceted, with stacking faults or twinning in the particle. (d) SADP from the faceted particle of (c), which is from the [011] zone of the b-SiC cubic phase. This SAD pattern can be indexed to be from two twinned crystals. (e) Energy-dispersive spectroscopic result from the particle of (c). It shows clearly that the particle is the b-SiC cubic phase. 138
- FIGURE 5.5: Scanning electron micrographs (back scattered images) of consolidated pure Mg (a), Mg-5 vol% SiC MMNC (b), Mg-10 vol% SiC MMNC (c) and Mg-15 vol% SiC MMNC, 140

respectively. In (b–d), the lighter particles are the SiC particles due to charging effect (SiC is an insulator). Thus we can see that the as-processed MMNC samples have some large reinforcement particles. Notice the scale bar of (d) is different from other images.

- FIGURE 5.6: Quasistatic true stress-strain curves of the micro- and nanoparticle-reinforced Mg-based composites. The curves with solid symbols are for the conventional MMCs, whereas those with hollow symbols are for the nanoparticle-reinforced MMNCs. PD means the loading is in the hot pressing direction. 141
- FIGURE 5.7: High-strain-rate true stress-strain curves of the Mg-based composites. The solid symbols are for the conventional MMCs reinforced with microsized SiC particles (M in the legend), and the hollow symbols are for the nanoparticle-reinforced MMNCs (N). As the materials are very brittle, all samples pulverized upon high-strain rate loading. In these samples, only the peak stresses are used to indicate the dynamic strength of the samples. 143
- FIGURE 5.8: (a) Yield strength (YS) and Compressive ultimate stress (CUS) of the conventional Mg-based MMC reinforced with microsized particles samples; and (b) those Mg-based MMNC samples reinforced with nanoparticles of SiC. Mg means pure, as received Mg. 20 h means pure Mg milled for 20 h followed by warm consolidation. DY means dynamic loading. All samples were loaded in the hot-pressing direction (PD). 5, 10 and 15% are the volume fraction of the reinforcement phase. 144
- FIGURE 5.9: Comparison of the strength of the conventional Mg-based MMC samples (a) and the nano-particle reinforced Mg-MMNC samples (b) between the pressing direction and radial direction. In either case, the PD samples are consistently stronger than their RD counterparts, indicating some anisotropy in the mechanical properties of the hot pressed materials. 144
- FIGURE 5.10: (a) Low-magnification SEM micrograph of the fractured specimen of Mg-5 vol% SiC MMNC partially recovered after quasi-static loading. The sample was broken into several pieces. Loading was roughly in the vertical direction. This low-magnification SEM image reveals off-axis cracks, presumable initiated from the specimen corners. 147

(b) Medium-magnification SEM micrograph of the same sample, showing microcracks on the fracture surface. (c) High-magnification SEM micrograph of multiple microcracks. All images show minor evidence for ductile fracture.

- FIGURE 5.11: (a) Low-magnification SEM of a fractured sample of Mg-10 vol% SiC MMNC partially recovered after quasi-static loading. Loading is roughly in the vertical direction. (b) An enlarged view of fracture surface to show the macrocrack. Loading was in the horizontal direction in (b). No strong evidence for ductile fracture can be found in this sample. 147
- FIGURE 5.12: (a) Low-magnification SEM image of specimen of Mg-15 vol% SiC MMNC partially recovered after quasi-static loading. Loading is roughly vertical. The sample was broken into a few pieces upon quasi-static compression. The fracture surface is quite flat, and typical of brittle fracture. (b) An enlarged view of the fracture surface, showing cracks on the surface. (c) Cracks and crack branching in this sample. (d) A high magnification SEM micrograph. The arrow points to a particle of size close to 1.0 μm . The light (bright) contrast of this particle comes from charging of the insulating SiC phase. EDS analysis (not shown here) also indicates that the particle is SiC. 149
- FIGURE 7.1: A schematic illustration of shear localization formation, where point A is a random location. w is the distance between the shear plane and point A; while τ is the shear component of applied compressive loading stress parallel to the shear plane, σ_n on the normal component. 168

LIST OF ABBREVIATIONS

HCP	hexagonal close-packed
FCC	face centered cubic
BCC	body centered cubic
CRSS	critical-resolved shear stress
ECAP/ECAE	equal channel angular pressing/extrusion
SHPB	split Hopkinson pressure bar
SPD	severe plastic deformation
MMC/MMNC	metal matrix (nano-) composite
SWA	spinning water atomization
EDM	electrical discharge machining
XRD	X-ray diffraction
SEM	scanning electron microscopy
OM	optical microscopy
TEM	transmission electron microscopy
EDS	energy dispersive spectroscopy
EBSD	electron back-scattered diffraction
ASB	adiabatic shear banding
SRS	strain rate sensitivity
BMG	bulk metallic glass
DRX	dynamic recrystallization

CHAPTER 1: INTRODUCTION

High performance materials having lightweight character are desirable for industrial applications, particularly in the automotive, aerospace and sports industries. To this end, the materials research community has been sparing no effort to develop stronger and lighter materials. Magnesium is the lightest structural metal having a mass density of 1.74 g/cm^3 , which is only two thirds the density of aluminum. Besides, magnesium is the sixth richest elements in the earth's crust and third richest dissolved mineral in seawater [1]. Thus, magnesium is an ideal candidate as a widely used lightweight structural material.

1.1 History

Magnesium (Mg) was first recognized by N. Grew as magnesium sulfate in 1695, whereas, Sir Humphrey Davy was the first person who isolated the element in the year 1808 [2]. However, it was a German chemist, named Robert W. Bunsen, who firstly made commercial production of Mg possible by electrolysis in 1852, while there is another important name in magnesium history, Lloyd M. Pidgeon, who developed safely commercial production of magnesium and largely promoted its commercial development [3]. In the early twentieth century, magnesium attracted a great deal of attention in the materials research community, and was widely used in military applications such as aircrafts. However, magnesium was restricted from use in engine components as the melting temperature of Mg is very low [3]. After the World War II, the usage of magnesium as a structural material was gradually reduced due to increasing performance

requirements. Instead, aluminum alloys and steels replaced magnesium and have become the primary choice of structural materials in key load-bearing structures. Magnesium alloys were then mostly used in non-critical roles for the purpose of weight reduction, such as steering wheels, seat support and rear transfer case in automobiles or golf club heads, in-line skates, tennis racquets and bicycles in sports equipment [1]. Yet, owing to the increasing world energy consumption and the fact that the most frequently used energy sources are unrecoverable and will soon be exhausted, groups of scientists are eager to find ways to slow down the pace of energy consumption while others are exploring alternative energy sources. One effective way to save energy is to reduce the weight in transportation conveyances, such as airplanes and automotive vehicles. In light of this, a new renaissance in magnesium research has been triggered, because it is the lightest metal and the weight of vehicles can be largely reduced by replacing heavy structural materials (e.g., aluminum alloys and steels) with magnesium-based materials.

1.2 Development of Mg Alloys

The name of the scientist who was the first to study and introduce Mg as a structural material is probably unknown; so is the one who discovered the hexagonal close packed (HCP) structure of Mg. Yet, their work greatly promotes the research of Mg and helps us to extensively understand the deformation mechanisms and mechanical properties of Mg. In addition to its structure, the alloying elements and materials processing are also important to the overall performance of Mg materials. Since the middle of the twentieth century, much scientific effort has been put into research of the effect of different elements, as well as heat treatment and fabrication processes on the mechanical properties of Mg materials. Many important and useful findings have been accomplished

and archived in published literature. In the following sub-sections, some of the research findings will be reviewed with respect to the influence of alloy elements, heat treatment and fabrication methods on the mechanical properties of Mg-based materials.

1.2.1 Deformation Mechanisms in Mg

Figure 1.1 shows all commonly observed deformation modes in Mg, which include prismatic, pyramidal I and II slips, as well as tension and compression twinning systems. Those deformation systems have long been observed in both Mg single and poly-crystals [5-9]. However, as a member of the family of HCP metals, only four independent slip systems are expected to be easily activated and contribute to the deformation of Mg at room or lower temperatures, i.e., two from basal slip and two from prismatic slip [10].

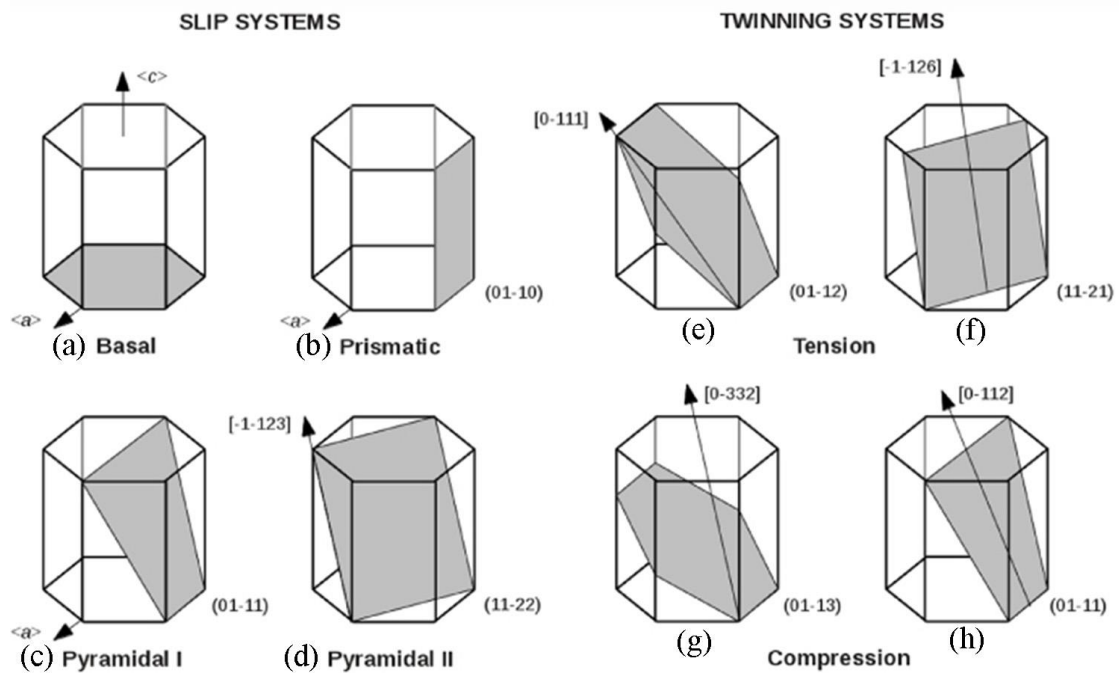


Figure 1.1: Deformation modes in Mg: (a ~ d) slip systems; (e ~ h) twinning systems [4].

Further, the basal slip is dominant. Both statistical analysis and experimental results indicate that the distribution of the basal plane largely controls the mechanical behavior of Mg and its alloys [11-13]. This is, because of a much lower critical resolved shear stress (CRSS) is required for basal slip than that for the other systems. At room temperature, the CRSS for basal slip has been reported to be around or less than 1.0 MPa by many investigators [14-18]. This value is far smaller than that for prismatic and pyramidal slips, both of which were reported to be around 50 MPa [6, 19-21]. The CRSS for twinning mode is around 90 MPa [16], which is even larger than non-basal slips. Due to the large difference of CRSS values among the basal, non-basal slips and twinning, non-basal slips and twinning are rarely activated in polycrystalline pure Mg and its alloys unless some special conditions are satisfied. It is noteworthy that Byer et al. [21] and Lilleodden [20] independently performed micro-compression tests on Mg single crystals with *c*-axis orientation, and both obtained much higher yield strengths of the samples than that in Ref.[18]. It was found that pyramidal slip, but no other mechanisms, dominated the plastic deformation. In that case, the Schmid factor for basal slip must be much smaller than that for other modes, which for polycrystalline Mg means a strongly textured microstructure. Agnew et al. [12] applied a load to polycrystalline Mg at room temperature in the direction where the majority of grains were oriented favorably for basal slip and obtained tremendous ductility and low yield strength, while a low ductility and high yield strength were obtained when a load was applied perpendicular, so that basal slip was not preferred. The same conclusion was reached by Lin et al. [22] independently while studying the relationship between texture and low temperature super-plasticity of magnesium alloy AZ31 after equal channel angular pressing (ECAP)

processing. There are more experimental evidences in the literature revealing the texture dependence of mechanical behavior and deformation mechanisms of Mg alloys [23-33]. Additionally, Agnew et al. [12] and Kim et al. [34] studied the texture effect on the mechanical behavior of Mg alloys, (AZ31 and AZ61), by means of ECAP, where the true stress-strain curves for both alloys exhibited strong texture- and direction-linked behavior. Consequently, results of these studies suggest a crystallographic effect on the deformation of single and poly-crystalline Mg. Given this, one may conclude that the mechanical behavior and deformation mechanisms of polycrystalline Mg and its alloys could strongly depend on the texture.

As a consequence of the dominant role of basal slip, Mg and its alloys exhibit very low ductility at room temperature. This is because, according to the Von Mises rule, at least five independent deformation modes are required to accommodate homogeneous plastic deformation of polycrystals [35, 36]. Though, non-basal slip systems, including prismatic and pyramidal slips as well as twinning, are possible to contribute to the plastic deformation of Mg, they were mostly found in highly textured Mg alloys [5-7, 37-41]. In addition, those unfavorable mechanisms were found to contribute at the late stage of the plastic deformation. Experiments have revealed an increased strain hardening rate of Mg and its alloys present in the plastic deformation, which is attributed to the activation of non-basal slip systems and twinning [18, 42, 43]. This has been confirmed by evidence of the activation of non-basal slip systems, as well as twinning, in the late stage of plastic deformation. Bhattacharya and Niewczas [18] studied the work-hardening behavior of Mg single crystals with basal slip oriented by means of tensile tests, from which they noticed two stages of work-hardening characteristics: a long easy-glide stage starting

from the beginning of plastic deformation and a stage of rapid hardening leading up to specimen failure. Since inhomogeneous distribution of tensile twins and complex dislocation networks were observed within the deformed crystal by transmission electron microscopy (TEM) and X-ray diffraction (XRD), the activation of twinning and non-basal slip systems were identified as the cause of the increased work-hardening rate. To further understand the mechanical behavior and deformation mechanisms of Mg and its alloys, numerical modelling of the effect of deformation modes and/or texture on yielding, hardening and microstructure evolution of those materials has also been performed [10, 44-47]. It was shown that a best simulated result, in agreement with experiments, can be obtained only when deformation modes including basal, prismatic, pyramidal $\langle \mathbf{a} + \mathbf{c} \rangle$ slips and tensile twinning are all considered. Both experimental and simulated results suggested that non-basal slips and twinning have a significant effect on the macro-mechanical behavior of Mg polycrystals, even though they are very hard and rare to occur due to their high CRSS values.

In summary, the plastic deformation mechanisms of Mg are more than complicated and are still open to discussion.

1.2.2 The Effect of Second-phase on Mg Properties

In general, metal matrix composites (MMCs) are considered to be the materials that consist of a ductile metal matrix and rigid particles, resulting in advanced mechanical properties, such as high strength and modulus. However, impurity atoms, intermetallic compounds and hard ceramic particles can all be considered as second-phases in metals and alloys. A less restrictive definition of MMCs would allow all types of such hybrid materials, in which one component serves as the matrix and the other(s) serve as

impurities/reinforcements [48], to be considered as MMCs. Thus, in this work, three types of hybrid materials reinforced with different reinforcements are studied. The reinforcements include alloying elements, in-situ particles synthesized by chemical reactions between elements or between elements and other compounds during processing and ex-situ particles prepared and blended into the matrix prior to the fabrication of composites. Sometimes, the impurity atoms present at interstitial sites in the matrix serve as soft reinforcements or form aggregates [49], while sometimes they react with matrix atoms to form compounds [50], depending on the alloy element and its content and the materials production conditions. Many intermetallic compounds have been found in Mg alloys, including Al-Mg, Mg-Y and Mg-Zn particles [50-53]. The addition of different alloy elements yields various effects on the mechanical properties of Mg. On the other hand, general MMCs reinforced by ex-situ rigid particles yield quite a different property.

1.2.2.1 Metallic Elements

To seek various end-use purposes of Mg alloys, different alloy elements have been added into Mg or its alloys to obtain desired mechanical properties. Scientific investigations have established the roles of different elements on the mechanical properties of Mg. There are many alloying elements having been used in Mg for different application purposes. Gupta and Sharon [54] have made a comprehensive collection and a detailed discussion of the effect of each metallic element on magnesium. Here, only the commonly used ones and the ones which are part of our research will be discussed, including aluminum, calcium, manganese, zinc, yttrium and some rare earth elements.

- i. Aluminum (Al). Aluminum is one of the most beneficial alloying elements to Mg alloys. It has been suggested in the literature that intermetallic particles such as $\text{Mg}_{17}\text{Al}_{12}$

and Al_2Ca that form during the hot processing may act as dislocation barriers against plastic deformation. It has been found that the strength, hardness and creep resistance of Mg alloys increase with increasing the content of Al [55, 56]. In addition, increase of Al content may also result in increased castability of Mg alloys due to improved fluidity [57]. Thus, Al has been widely used in Mg alloys such as AZ- and AM- series for strength enhancement.

ii. Calcium (Ca). It is well-reported in the literatures [58-60] that Ca plays a significant role in grain refinement, corrosion resistance and thermal and mechanical properties of Mg alloys. Addition of Ca may also influence the microstructure of Mg alloys [51, 61]. For example, with increasing content of Ca above 1%, intermetallic phase particles of Al_2Ca form in AZ91 Mg alloy, accompanying $\text{Mg}_{17}\text{Al}_{12}$, while another new phase Mg_2Ca forms replacing $\text{Mg}_{17}\text{Al}_{12}$ as the Ca content increases up to 4% [51]. Calcium's presence in casting alloys can reduce oxidation during melt and heat treatment process [62, 63] as well.

iii. Manganese (Mn). The addition of Mn into Mg alloys is intended to increase the seawater corrosion resistance [64]. In addition, research studies have also shown that addition of a small amount of Mn may also improve the strength and creep resistance of Mg alloys, owing to the formation of Mn-containing intermetallic phase particles [65, 66], as well as grain refinement [67, 68]. The presence of Mn has also been proved to promote the formability of AZ31 [69].

iv. Zinc (Zn). Zinc is one of the primary alloying elements in commercial Mg alloys. On one hand, the aim of Zn addition is to improve the room temperature strength [70]. On the other hand, research works have shown that a slight increase of Zn can also

improve creep resistance of Mg alloys [71, 72].

v. Yttrium (Y) and rare earth (RE) elements. Yttrium and rare earth elements such as lanthanum (La) and cerium (Ce) have been widely proved helpful to Mg alloys. It has been reported that a small amount doping of Y/RE can significantly refine the microstructure of Mg alloys [50, 73]. The most well-known effect of Y/RE on the optimization of Mg alloys is their improvement of formability. A great deal of efforts in the literature have revealed the phenomenon that addition of Y/RE elements increases the ductility of Mg alloys greatly [51, 58, 74, 75], primarily due to the weakening of texture.

As can be seen from the literature [16, 17, 75-77], most of the metallic elements, despite of their effect, can chemically react with Mg or other alloying elements during heat-treating or other hot processing, forming hard particles in Mg alloys, while some of them are still present as solute atoms that may be viewed as soft particles. Through which way or how the alloying element exerts its effects on the microstructure and mechanical properties of Mg alloys still needs of more scientific effort. For example, Y/REs have been observed in both forms in the Mg alloy, and it seems that regardless the ductility of the Mg alloy was improved [75, 77]. Nevertheless, second-phase hard particles have been recognized as nucleation sites for dynamic recrystallization while they also act as grain boundary pinning centers, thus assisting in the microstructure refinement [78]. In light of the Hall-Patch relation [79-85], grain refinement is one of the most effective methods to improve the strength of metallic materials, as shown in Eq.(1.1).

$$\sigma_y = \sigma_0 + k \cdot d^{-1/2} \quad (1.1)$$

where σ_y is the yield strength, k is Hall-Patch slope, d is the grain size and σ_0 is a value relating to the intrinsic stress that resists dislocation motion (lattice friction). Thus, ex-

situ hard particles have been intentionally mixed into Mg alloys for the purpose of strength enhancement.

1.2.2.2 Ex-situ Second-phase Hard Particles

First of all, the microstructure of MMCs will be different from the baseline matrix material due to the addition of reinforcing particles. As a consequence, the mechanical properties of MMCs are strongly dependent on several factors, such as the type, size, volume fraction and geometrical shape of the particles. For example, the ex-situ particles usually have weaker interfacial bonding with the matrix than above-mentioned in-situ formed particles because of contamination at the particle surface [86]. The influence of size and volume fraction of the particles on the microstructural characteristics and mechanical properties of MMCs has been studied for decades from theoretical and experimental perspectives. The inter-particle spacing (λ), one of the important characteristic parameters of MMCs, that determines the average distance among pinning sites via the Zener-pinning effect, has been estimated theoretically as follows, relating the average particle size (d) and the volume fraction of particles (f_v) [87].

$$\lambda = d \cdot \left(\frac{1}{f_v^{1/3}} - 1 \right). \quad (1.2)$$

In addition, different equations to estimate the grain size (D) of MMCs, which is an alternative approximation to the inter-particle spacing, were also developed based on different geometric models. For instance, one of them is given by Hellman and Hillert [88, 89], for high volume fractions ($f_v > 0.1$) of particles, as follows:

$$D = 1.8 \times \frac{d}{f_v^{1/3}}. \quad (1.3)$$

Later, Han et al. [90] derived a similar equation with a coefficient of 1.12 instead of

1.8 to estimate the grain size. Nevertheless, another approximation model based on particulate-stimulated nucleation that each particle nucleates one grain was proposed by Humphery et al. [91] in the form of Eq. (1.4):

$$D = d \cdot \left(\frac{1 - f_v}{f_v} \right)^{1/3} \quad (1.4)$$

Experimental studies, at the same time, confirmed that the matrix grain size decreases as the volume fraction of particles increased [92], while it increases with the increase of particle size for a fixed particle volume fraction, as shown in Figure 1.2 [93].

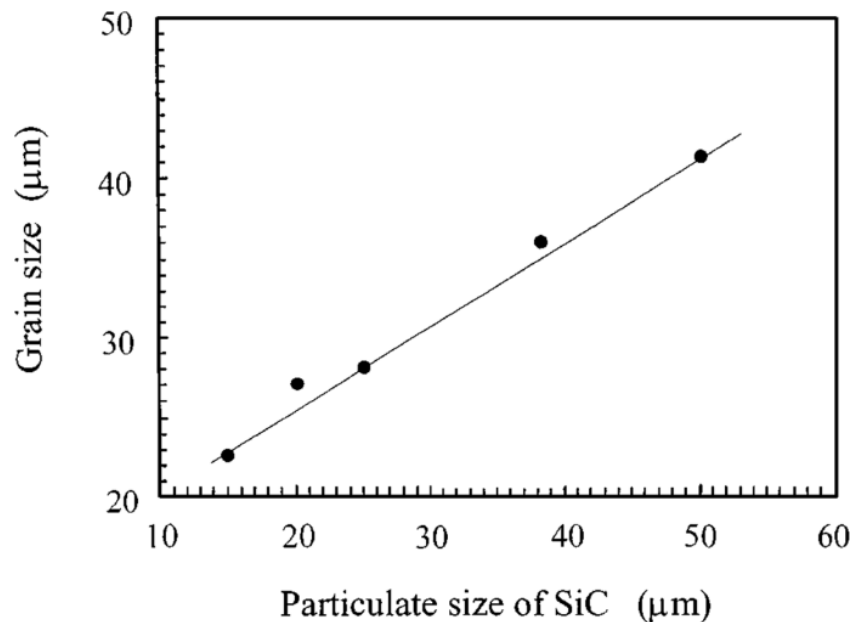


Figure 1.2: Grain size as a function of SiC particle size in AZ91-based MMCs [93].

The inter-particle spacing is a direct contributor to the higher flow stress of MMCs due to the array of particles hindering the motion of dislocations. Their contribution can be estimated by Eq. (1.5). It is also known as the Orowan stress.

$$\Delta\sigma_{or} = \alpha \cdot \frac{\mu_m \cdot b}{\lambda}, \quad (1.5)$$

where α is a constant close to 1; μ_m and b are the elastic shear modulus and Burgers vector of the matrix material, respectively. Other contributions, from the isotropic and kinematic strain gradient, as well as thermal expansion mismatch between the matrix and particles, are approximated by the following equations [94]:

$$\Delta\sigma_{iso} = \beta \cdot \mu_m \cdot \sqrt{\frac{f_v \cdot \varepsilon_p \cdot b}{d}}, \quad (1.6)$$

$$\Delta\sigma_{kin} = \gamma \cdot \mu_m \cdot f_v \cdot \sqrt{\frac{\varepsilon_p \cdot b}{d}}, \quad (1.7)$$

and

$$\Delta\sigma_{te} = \eta \cdot \mu_m \cdot b \cdot \sqrt{\rho}. \quad (1.8)$$

where β , γ and η are constants on the order of unity; ε_p is the plastic strain in the matrix and ρ is the dislocation density generated by thermal expansion mismatch, which can be estimated as follows [94]:

$$\rho = \frac{6\Delta T \cdot \Delta\varepsilon \cdot f_v}{b \cdot d \cdot (1 - f_v)}. \quad (1.9)$$

where ΔT and $\Delta\varepsilon$ are the temperature change from heat treatment to room temperature and the relaxed thermal expansion. Those theoretical equations all connect the strength of MMCs with the particle size and volume fraction. As predicted, the strength of MMCs has an inverse relation to increased particle size, and a direct relation to increased volume fraction.

On the other hand, experimental studies of the effect of the scale and volume fraction of particles have shown that, even though the strength of MMCs increases with the volume fraction of particles, the strength increase plateaus. When a volume fraction between 15% and 20% is reached, and when the particle sizes are less than one micro-

meter, no further increase in strength is observed as shown in Figure 1.3(a) [95].

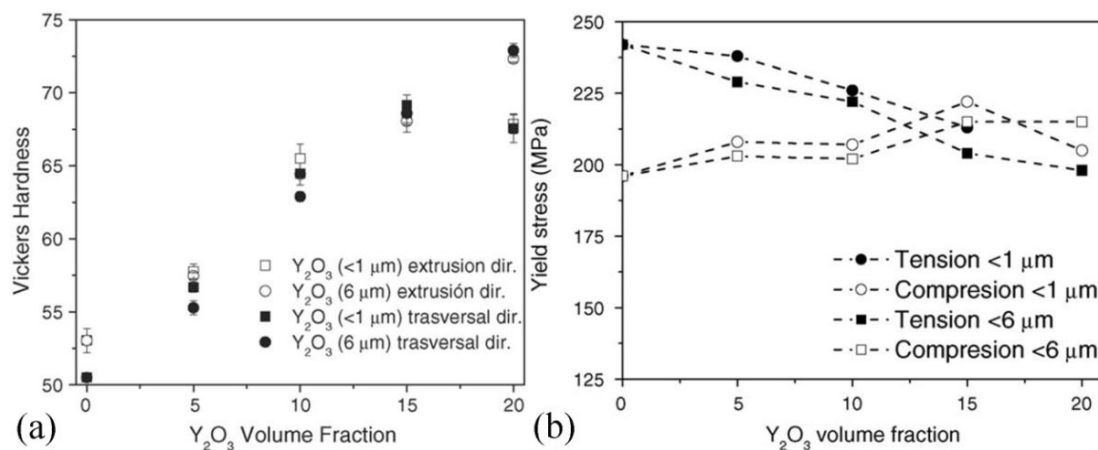


Figure 1.3: The (a) Vickers hardness and (b) tensile and compressive yield stresses of Y_2O_3 -reinforced Mg-MMCs as a function of the volume fraction of Y_2O_3 [95].

Furthermore, while the compressive yield strength of the Mg-MMC increases with the particle volume fraction, the yield strength under tension decreases regardless of the particle size, shown in Figure 1.3(b). This was attributed to the softening of $\{10\bar{1}0\}$ fiber texture for the reason that the addition of particles oriented more grains favorably for basal slip [95]. On the other hand, with increasing the volume fraction of particles, the matrix-particle interface area increases at which contamination and stress concentration is inevitable to cause failure of the composite under tension. Particle clustering also accounts for the degradation of the mechanical properties of MMCs as well. As shown in Figure 1.4, Hong et al. [96] studied the influence of clustering on the mechanical properties of SiC reinforced Al-MMCs. The experimental results obviously show that the volume fraction of clusters increases at higher volume fractions of SiC and, as a

consequence, the MMCs exhibits decreased toughness and a saturation of the tensile strength.

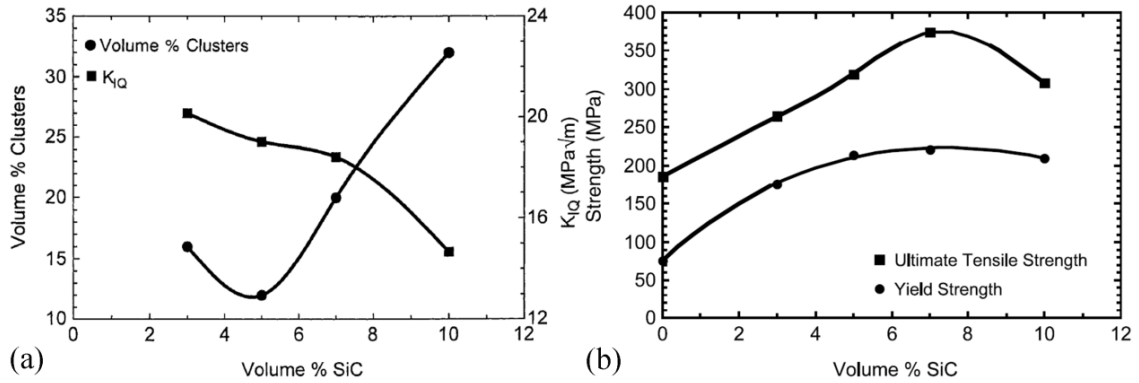


Figure 1.4: (a) volume of clusters and mode I fracture toughness and (b) tensile strength of SiC-reinforced Al-MMCs as a function of the volume fraction of SiC [96].

1.2.3 The Effect of Heat Treatment on Mg Properties

The relatively low melting temperature of Mg, which is about 923 K, renders the homologous temperature of Mg at room temperature to be approximately 0.32. This value suggests that dynamic recovery may well occur in Mg alloys even at room temperature, which was confirmed in Koike et al.'s work [97]. Thus, heat treatment at elevated temperatures must have a substantial impact on the microstructure evolution and, in turn, the performance of Mg materials. As defined in Valiev and Langdon's review paper on ECAP [98], two stages are required to produce ultrafine-grained materials from coarse-grained bulk solids: imposing a high strain to increase the dislocation density and rearranging the dislocations to form an array of grain boundaries. It is thus very important for the heat treatment process to be executed right after severe plastic deformation of metallic alloys to give rise to the dislocation rearrangement, subgrain formation and

sometimes recrystallization. In other words, such practice helps to ensure the internal stress elimination and thus the improved mechanical properties thereafter. For high melting temperature metals, the later stage usually requires post-heat treatment process, so-called annealing. Nevertheless, post-annealing is not really necessary for Mg alloys [13, 34, 99, 100]. This is because of the low melting temperature and the relatively high temperature applied during the severe plastic deformation (SPD) process to avoid crack generation before a prescribed high strain is imposed to the bulk Mg sample. In this case, dynamic recrystallization can readily take place in the Mg sample during the SPD process. An example is given in Ref.[101] where complete dynamic recrystallization occurred in pure Mg during the room temperature ECAP process, which can be attributed to the increased temperature during ECAP [102]. This is why there is a limitation of the capability of refining grains for Mg alloys [30].

Besides controlling the grain structure, heat treatment is also an important technique to manipulate the formation of in-situ particles in Mg alloys. An original scientific research on the Mg alloy (Mg-3Nd-0.2Zn-0.4Zr, wt.%) [103] revealed that, within as-cast and different heat treated alloys, the component and appearance of eutectic precipitates are very different. Xu et al. [104] also found that the mechanical properties and fracture characteristics of ZK60-Y are related to the variation of the rod-like MgZn precipitate that is formed under different heat treatment conditions. In particular, post-treatment with heating is required for producing high performance MMCs.

1.2.4 Approaches of Fabricating Metal Matrix Composites

Approaches of fabricating MMCs can be categorized into three types: in-situ process, liquid-solid process and solid-solid process [105-107]. The type of processing depends on

the way the reinforcement forms and the state of the metal matrix.

The in-situ process suggests that the reinforcements are intermetallic compounds which are generated during the cooling or later annealing process by a eutectic reaction. There are two routes to complete the process: start with molten alloys followed by cooling and solidification, or start with alloy powders followed by cold/hot pressing with/without subsequent extrusion. The benefit of the in-situ process is not having to worry about the wettability of particulates and it often results in strong bonding between the particulates and matrix. Nevertheless, the former route requires melting all component metals, which raises safety problems and expense, particularly, when processing metals like Mg that is highly flammable and explosive at high temperatures. In this context, the powder-to-bulk product route seems to be a much better option, but it is still difficult to control the geometry and volume fraction of the reinforcement.

The liquid-solid process, also known as semi-solid metal processing, has two different routes. One is much like building foundations where liquid concrete is poured into a pre-fabricated reinforcing mesh, as shown in Figure 1.5(a); while the other requires mixing and blending the molten matrix and particle powders before casting, as shown in Figure 1.5(b). It is obvious that this method allows adding pre-produced hard particles into the matrix melt and still promising a good contact between the matrix and particles. However, it requires a careful selection of the reinforcement in terms of the chemical reaction and thermal coefficient mismatch between the molten matrix and reinforcement. Coating the surface of the reinforcements is found to be an effective way to improve the wettability of the reinforcement and the bonding force at the matrix-reinforcement interface [108-110]. Nevertheless, this method is still dangerous for processing Mg-based

composites.

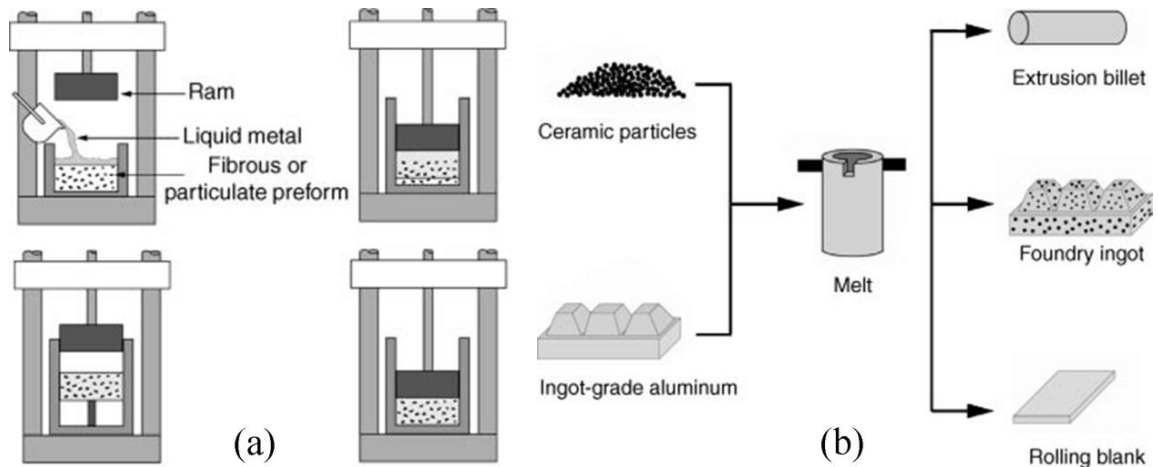


Figure 1.5: Two different material processing methods for MMCs [110]: (a) melt matrix poured into fabricated reinforcing mesh and following with compression; (b) mixing melt matrix with solid particles and following with casting.

The solid-solid process is analogous to the above-mentioned second route for the in-situ process. Both of them can be called powder metallurgy, which has been widely used for alloys. In general, it includes two or maybe three simple steps: mixing the powder of the matrix and reinforcement, sintering the mixture with pressure at desired temperatures and further extrusion may or may not be performed thereafter. The advantage of this method is the ability to process a wide variety of reinforcements in combination with different matrix materials and easily control the parameters of the reinforcement, such as the size, orientation and volume fraction [107]. For this method, some pre- and post-steps can be performed to improve the final mechanical properties of the composites. For instance, mechanical refinement of the powders such as ball milling and mechanical attrition can effectively reduce the size of the particles and matrix powder, which may

result in completely different matrix microstructure, reinforcement size and its distribution, and thus yield excellent mechanical properties [111, 112]. In addition, SPD processes such as ECAE may also be applied to sintered products for the purpose of further densification and/or microstructure modification, therefore, improving the properties [92, 113, 114]. Due to the highly flammable and explosive property at high temperatures, Mg-based materials are preferably processed using the solid-solid approach. The fact is that most of Mg-based composites reported in the literatures to date have been fabricated through the solid process or, at least, the key steps were completed in the solid condition.

Mg-based composites are of great interest in the aerospace and automotive industries, as well as individual and sports applications, due to their significantly decreased weight and high specific strength [115]. However, the relatively low absolute strength and rapid loss of strength at elevated temperatures along with low creep resistance renders limited applicability of Mg as a structural material at temperatures above 120 °C. A few studies have proven that adding rigid secondary phases into a Mg matrix can effectively improve the creep resistance and strength at elevated temperatures [116-118]. However, there are still many unknowns about Mg-based MMCs. For example, the role of particles, microstructural characteristics and materials properties under different service conditions are far from well understood. Thus, an in-depth and comprehensive study is required prior to the wide application of these materials. Yet, owing to the time limitation and the length of the dissertation, the emphasis will be put on microstructural characterization, as well as the influence of volume fraction, particle size and formation of reinforcements on the mechanical performance of Mg-based MMCs. Thus, in this work, Mg composites

reinforced with either in-situ particles formed during hot extrusion process or ex-situ particles blended into Mg matrix prior to sintering process are studied. As a part of the dissertation, ECAPed pure Mg and Mg-0.6%Y are also investigated to study the effect of Y on the microstructure and deformation mechanisms of Mg.

1.3 Adiabatic Shear Banding

Another interesting and noteworthy area of study regarding structural materials is their dynamic mechanical performance, especially the failure pattern under high speed impact, because they may serve in vehicles, which are required to meet certain impact standards. One type of important failure pattern under impact loading is referred to as adiabatic shear banding (ASB), and has been widely observed in many circumstances involving high speed deformation. It is generally characterized as fracture through the formation of a localized shear band, within which much more severe plastic deformation occurs compared to the rest of the material; this is shown in Figure 1.6(a). This phenomenon was systematically discussed by Zener and Hollomon in the middle of the twentieth century when they first named it as an adiabatic shear band [119]. Accompanying the more severe plastic deformation, a highly elevated temperature is usually observed within the narrow band that, in a few special cases, might cause melting in the narrow region. One instance is shown in Figure 1.6(b) where it can be seen that along the shear band, many equiaxed voids are formed, resulting from plastic flow at elevated temperatures.

The ASB has been observed in various technical areas with high speed machining or loading processes. For example, Burns and Davies [122-124], Recht and Rogers [125, 126] and Molinari et al. [127] have been working on high speed machining processes. A

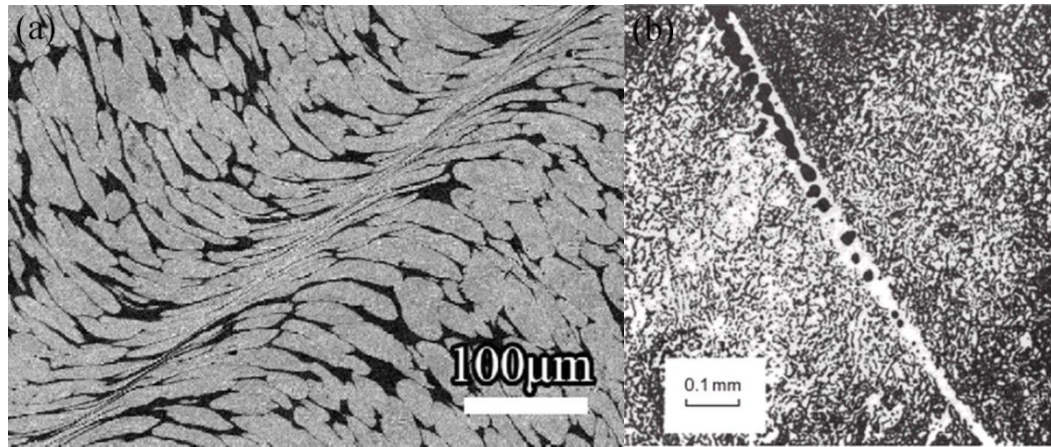


Figure 1.6: (a) Scanning electron microscope (SEM) image of an ASB in tungsten heavy alloy after uniaxial dynamic compression [120]; (b) a fractured shear band with equiaxed voids in a U-2Mo alloy [121].

group of articles by these authors have discussed the formation of chip segmentation during high speed machining due to ASB formation, from both theoretical and experimental perspectives. Meanwhile, Zurek and other scientists have produced ASB by various methods within the same material, as well as different materials [128-134]. Laboratory methods, such as high-speed punch, explosion, compression and torsion, are the most frequently used methods to produce ASB. A great number of metallic materials, including steel, titanium, aluminum, magnesium, their corresponding alloys and bulk metallic glasses (BMGs), have been observed to fail and fracture in ASB mode at high or low strain rates [131-136]. Owing to their unpredictable incidence and rapid completion time, ASBs may lead to unexpected and sudden failure of structures. This can be a disaster to any structural material and needs to be avoided for many commercial applications. However, the main concern as Wright concludes [137], of the occurrence of adiabatic shear failure is usually not during the service lifetime of a device in which plastic deformation is to be avoided, but during the material processing or manufacturing

process in which high speed forming (forging, impacting, machining etc.) may apply. As is well-known now, adiabatic shear banding can lead to quenching effects in the localized regions, and sometimes leave micro-cracks or voids behind. Yet, for a structure that will experience cyclic loading in application, any presence of residual micro-cracks or voids can be problematic or even disastrous. Therefore, better design processes are required to avoid the introduction of deleterious sites. A better understanding of ASBs is not only necessary in order to avoid them, but to assess their positive contributions as well. Magness [138] recently observed that kinetic energy (KE) penetrators that can develop ASBs could penetrate more efficiently than those that develop ‘mushroom’ shaped heads. ‘The earlier discard of the material reduces the build-up of the mushroomed head on the penetrator, allowing these materials to penetrate more efficiently’, he concluded. In other words, introducing ASB into penetrators can be beneficial to their penetration capability. Either way, a better understanding of the physics and mechanism of ASB is essential. To this end, the significance of different factors on the propensity for ASB needs to be studied.

Preceding this research, a series of experimental techniques have been developed to trigger ASB for research purposes. Common methods include the torsion test, compression and shear test, cylinder expansion test, uniaxial compression test by using the split Hopkinson pressure bar (SHPB, also known as the Kolsky bar), and so on and so forth. Since the experimental techniques are not the emphasis of the dissertation and the details of each method have been specifically reviewed by Meyer and Pursche [139], they will not be repeated in detail here. Any information about specific methods for triggering ASB can be referred to in the comprehensive review book, ‘Adiabatic Shear Localization:

Frontiers and Advances (second edition), edited by Dodd and Bai [140]. Nevertheless, a specific explanation of the experimental methods used for the present work will be given in a later section. In this section, literature published in the past few decades that focus on the observation of ASB within different metallic materials from the perspectives of material scientists and mechanicians will be reviewed briefly. It is interesting to note that, mechanicians have primarily focused on developing characteristic parameters by using constitutive equations in order to predict the propensity for ASB formation, while material scientists have mainly been interested in the influence of the microstructural evolution and deformation mechanisms of different materials on plastic instability. Therefore, mechanicians generally use the parameters, such as work hardening rate, thermal softening rate and strain rate sensitivity (SRS), to establish constitutive equations that can predict the propensity for ASB macroscopically, based on analytical or numerical solutions to the governing equations. On the other hand, material scientists usually examine the microstructure of postmortem samples, especially in the ASB region, to accomplish the understanding of ASB formation. The state of the art instrumental methods used include: optical microscopy (OM), scanning electron microscopy (SEM) and attached electron back-scattered diffraction (EBSD) and transmission electron microscopy (TEM) used to examine the microstructure. Mechanical properties such as micro-/nano-hardness within or away from the ASB are also measured by hardness testers [141-143]. Due to the different views from materials scientists and mechanicians, the literature will be reviewed in two-fold: mechanicians' work and material scientists' work.

As commonly accepted in the community of dynamic mechanics of solids, it is the

competition between the stabilizing factors such as work hardening, strain rate hardening and the destabilizing factors such as thermal softening that determines the propensity for ASB. One of the popular criteria, initially proposed by Zener and Hollomon [119], for predicting ASB generation was based on the effects of work hardening and thermal softening on the material. Later, Recht [125] incorporated an additional effect, heat conduction, in the interpretation of shear band formation during high speed machining. Other factors such as the strain-rate sensitivity (SRS) and strength were also incorporated later on as subsequent criteria for ASB propensity. Molinari and Clifton [144], by using a nonlinear perturbation analysis to a plate with pre-existing defects, derived different criteria for ASB propensity in various materials that behave with/without strain hardening as well as with strain softening. According to their conclusion, there are three factors, work hardening (n), thermal softening (ν) and SRS (m), which taken together in the form of a set of inequality equations, determine the propensity for ASB. At the same time, expressions for both the critical strain and critical energy were also developed to determine the critical moment when adiabatic shear instability occurs. For instance, Staker proposed an expression for critical strain shown in Eq. (1.10) [145].

$$\gamma_c = -Cn \left/ \frac{\partial \tau}{\partial T} \right)_{\gamma, \dot{\gamma}} . \quad (1.10)$$

This was obtained through the condition of a vanishing slope of the true stress-strain curves in parabolic hardening materials. Clifton and coauthors [146], by using the same condition and several governing equations, also developed a characteristic strain for ASB using the method of linear perturbation analysis. Bai [147], on the other hand, not only derived a critical strain for shear instability during the first mode induced by thermal softening, but also suggested that there could be another type of possible shear instability

induced by work-softening. The most interesting treatment of ASB formation might be credited to Grady [148, 149], who treated ASB formation as a growing crack that has a tip process zone. Due to this, he developed a shear-band toughness to determine the ASB propensity with the help of both momentum and energy balance. The shear-band toughness is very similar to the concept of fracture toughness, and has a similar expression as well, shown in Eq.(1.11) [149]. In addition, equation (1.12) shows an expression for the shear band dissipation energy Γ_s .

$$K_s = \sqrt{2G\Gamma_s}. \quad (1.11)$$

$$\Gamma_s = \frac{\rho C}{\alpha_\theta} \left(\frac{9\rho^3 C^2 \chi^3}{\tau_y^3 \alpha_\theta^2 \dot{\gamma}} \right)^{1/4}. \quad (1.12)$$

In Eq.(1.10) ~ (1.12), C is the bulk specific heat, γ and $\dot{\gamma}$ are the shear strain and strain rate, G is the corresponding shear modulus, χ is the thermal diffusivity coefficient and α_θ is the coefficient for linear thermal softening effect. According to this criterion, the internal effects from material properties such as the mass density, shear modulus, heat capacity and the thermal diffusivity were comprehensively incorporated with the external effects from the temperature, strain rate and current stress value. Grady also calculated the values of shear band dissipation Γ_s and toughness K_s for a broad range of materials, and provided them in Ref. [149]. It seems that the larger the value of the shear band toughness, the less the tendency for a shear band to form. Nevertheless, experimental results are still inadequate to test the concept.

In addition to explicit expressions to describe critical variables for ASB propensity, other researchers have been dedicated to developing implicit methods for ASB formation, using finite element analysis and numerical simulation. In these methods, the values of

different parameters that represent different influences were varied to examine the stability of simulation models or evaluate the width of ASB. In this way, the main factors governing the shear instability or the width of ASB could be determined. For example, Burns and Davies [122] developed a new lumped-parameter model for the orthogonal cutting of metals, which precisely predicted the supercritical Hopf bifurcation of chip formation in hardened steels. In addition, Burns [150] also analyzed the linear stability of the perturbation of a simple shear by using a finite time interval, and derived a criterion for the minimum strain rate where the perturbation changes from oscillatory to exponential with time. On the other hand, Merzer [151] modified Litonski's model to predict the width of ASBs. According to his conclusion, it is the dependence of thermal conductivity and strain rate, rather than the properties of the initial imperfection, on the width of ASBs. Wright [152-154] however used two methods, asymptotic analysis and numerical solutions, to predict the patterns of shear instability, and provided scaling laws for the critical conditions of shear band formation. Thereafter, he proposed a critical temperature rather than critical strain or time for the occurrence of shear localization, and provided a figure of merit for comparing the susceptibilities of different materials to shear instability [155]. Based on four equations: balance of linear momentum, kinematic compatibility, energy balance and thermal visco-plastic response of the material, Cherukuri and Shawki [156-158] used a numerical technique to discuss the occurrence of shear localization. They concluded that it was the dissipation number, a ratio of the thermal energy produced over the energy required to raise the temperature, that plays a significant role in the shear instability of materials.

All of the works reviewed above are mostly in respect to a theoretical prediction of

the occurrence of ASB. Nevertheless, there have been excellent works done by experimental mechanicians and some materials scientists who have been trying to track the course of strain localization. For example, Hartley et al. [159] measured the temperature evolution during shear localization in steels up to 450 °C. Later, Cho et al. [128] performed tests on tracking the shear localization process of an HY-100 steel subjected to torsion at a strain rate of $\sim 10^3 \text{ s}^{-1}$. Through the use of a high speed camera and infrared technique, three consecutive stages of shear deformation were captured: a) homogeneous shear strain; b) inhomogeneous and continuously concentrated strain and c) completely localized strain. Accompanying the localized strain, a sharp increase of temperature up to $\sim 600 \text{ °C}$ or even higher was measured within the localized region. Recently, Wei and coauthors [160] also published their efforts on capturing the formation process of ASBs in commercial purity tungsten rolled at low temperatures. A mechanistic model was used to semi-quantitatively explain the ASBs within cold-rolled tungsten, and so was geometric softening due to the microstructural change during cold rolling. Instead of taking successive snapshots of the deformation process during one test, Bai, Xu and coworkers [136, 161, 162] performed a series of interrupted high-strain-rate torsion tests to observe what happens to the specimen at different strain levels. Figure 1.7(a) ~ (d) correspond to the increased strains showing successive progress of the localized shear deformation [136]. Furthermore, Xu et al. [136] observed a white shear band generated beyond the appearance of a highly deformed shear band as the strain increases from 0.14 to 0.17. Figure 1.8(a) and (b) are the micrographs displaying the distinct appearance of shear bands in the Al-Li alloy corresponding to the above strains. Due to the different metallographic appearance of shear bands, many scientists first thought that phase

transformation might have taken place within the white band. Actually, a couple of years before Hartley et al.'s work, Marchand and Duffy [163] had conducted similar work where they left the reasoning of phase transformation within the band in question. This is one of the issues in that materials scientists are more likely to contribute than mechanicians.

White colored shear bands have often been referred to as transformed bands because of their distinct color and high hardness compared to the matrix. There are indeed some instances of phase transformation in steels and titanium alloys under dynamic loading,

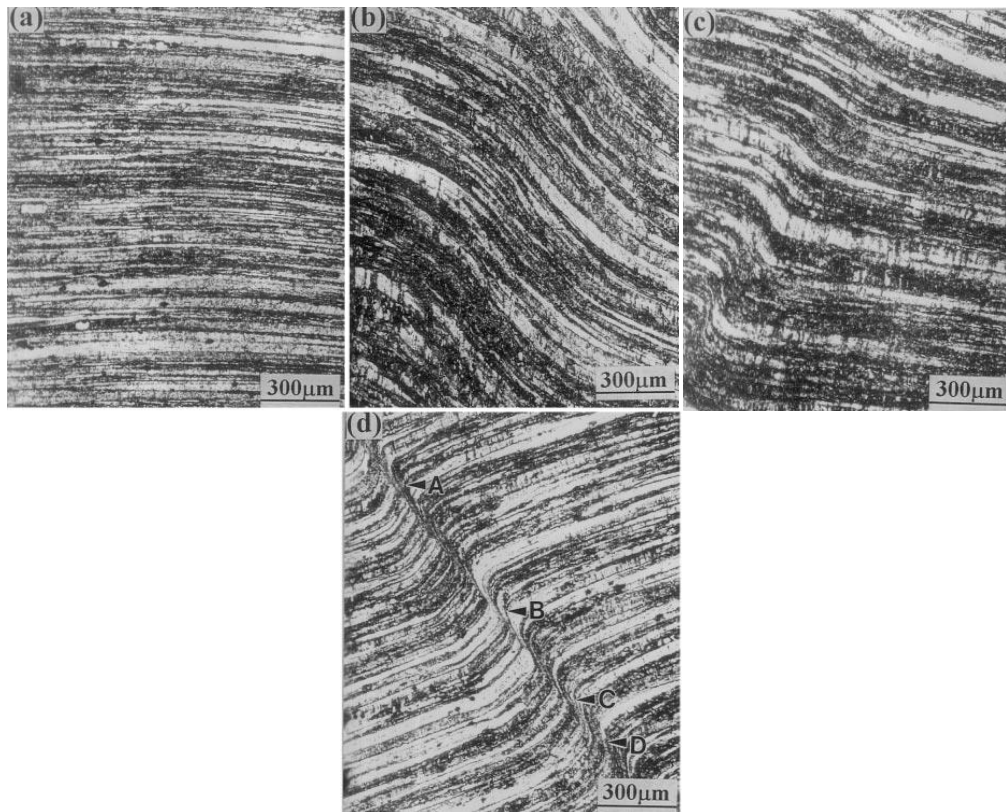


Figure 1.7: A successive showing of the evolution of shear localization as the strain increases from (a) to (d) [136].

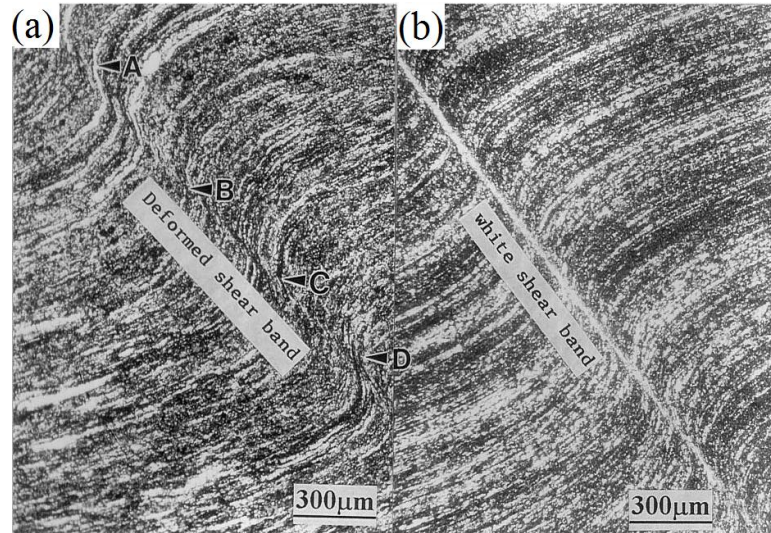


Figure 1.8: Micrographs showing the highly deformed shear band and white etching band in an Al-Li alloy [136].

explained as being driven by intense deformation or highly elevated temperatures. For example, Kestenbach and Meyers [164] identified ϵ and α martensite transformation by X-ray diffraction in 304-type stainless steel under shock-loading, and they explained it as strain-induced phase transformation. Many years later, Meyers et al. [165] performed dynamic compression tests on a hat-shaped AISI 304L stainless steel sample in a SHPB. Occasional martensitic phase transformation was noticed at either twin-band interactions or locations of severe plastic deformation, as well as amorphization in highly concentrated plastic regions. Wang and Yang [166] carried out a similar experiment on a fine-grained titanium alloy where α -phase and α'' -phase were observed coexisting in the white shear band. They explained that a maximum temperature of 1069K within the ASB was estimated even though no direct monitoring of the temperature was made. Therefore, a dynamic recrystallization process was attributed to the production of equiaxed β -phase grains at high temperatures, which quickly transformed to α'' -phase grains. Syn et al.

[143] also reasoned that adiabatic heating during shear localization causes an austenite phase transformation with a further ferrite transformation in a pearlitic ultrahigh carbon steel. Nevertheless, there are also many experimental results as well, summarized by Xu et al. [167], showing that white etching bands located in the shear region did not necessarily result from phase transformation, but from an ultrafine grained structure that might be due to dynamic recrystallization or dynamic recovery or other mechanisms. Routinely, during the localization process, grains are elongated within the shear band at the early stage of localization; fragmentation, dynamic recovery, recrystallization or sub-grain rotation take place as the strain concentration proceeds. For instance, Wei, Jia and coworkers [135, 168] reported an elongated grain structure inside the shear band compared to an originally equiaxed grain structure in an ultrafine grained iron sample. Meyers et al. [169] used hat-shaped specimens in a compressive Hopkinson bar to initiate ‘forced shear bands’ in alpha-titanium so as to study the microstructure evolution during the shear band formation. Likewise, they observed that elongated grains were gradually formed in the vicinity of the shear band and were gradually transformed into sub-grains when moving close to the interior of the shear band; small dislocation-free grains were discovered inside the shear band. These dislocation-free grains were attributed to the combined effects of break-up of sub-grains and dynamic recovery and recrystallization. However, the recrystallization was disproved in a similar experiment on tantalum and tantalum-10% tungsten alloy where the same grain pattern around the shear band was identified as that in the alpha-titanium specimen [170]. Instead, shear deformation plus dynamic recovery or sub-grain rotation were attributed to the microstructural evolution. Yet, this does not mean that recrystallization cannot happen in tantalum under dynamic

loading. Nesterenko and coworkers [171] indeed discovered both dynamic recrystallization and post-deformation recrystallization corresponding to an effective strain of 2 ~ 2.5 and larger than 2.5 in tantalum under explosive loading, where the corresponding temperatures were estimated to be 800K ~ 900K and even higher than 1000K, respectively. Therefore, although there is substantial evidence to support microstructural evolution such as grain elongation, fragmentation, rotation, dynamic recovery, and recrystallization as well as phase transformation within ASBs, only two factors are ascertained no matter what mechanism is occurring. One is the intense plastic deformation, while the other is the concentrated temperature rise in ASBs. The sole argument is whether the increase in temperature is high enough to cause recrystallization or phase transformation, which depends on the level of strain and strain rates and the properties of materials.

1.4 Scope and Objectives of the Dissertation

As pointed out in previous sections, due to their potential of becoming a key structural material, Mg-based materials will be studied in this dissertation. Three different types of Mg materials will be investigated under quasi-static (at a strain rate of $\sim 10^{-3} \text{ s}^{-1}$) and dynamic (at a strain rate of $\sim 10^3 \text{ s}^{-1}$) compressive loading. One group of the samples are pure Mg and pure Mg with 0.6-wt.% Y alloyed and processed by ECAE; another group of samples are Mg alloys, AZXE7111 and AMX602, fabricated by a powder metallurgy method; and, the last group of samples are Mg-based metal matrix composites reinforced with either nano- or micrometer-sized SiC particles. In this research, the following aspects will be elucidated: the role of Y in the microstructure evolution of pure Mg during ECAE, the microstructure and macroscopic features of each material, the role

of particles of different sizes and their volume fractions in the mechanical properties of composites, different effects of in-situ and ex-situ formed reinforcement on the mechanical properties of composites and different failure modes and the corresponding mechanisms. A wide survey of the literature shows that limited efforts have been focused on the shear band formation in Mg materials even though a failure mode with shear band formation has been discovered in both pure and alloyed Mg specimens in the preliminary work. Therefore, mechanisms leading to the formation of ASBs in Mg materials due to its intrinsic instability need to be investigated. Rittel et al. [172] have performed experiments on a Mg alloy, AM50, to study the critical condition for shear band formation. However, they spent little effort on the microstructure and deformation mechanisms of Mg and their role in shear localization. Another article regarding shear band formation in Mg alloy AM60B was published by Zhen et al. [173], in which a major discussion about the microstructural evolution in both deformed and transformed bands was made. However, as in many of the investigations into ASBs reviewed previously, those shear bands were also produced by geometrically non-uniform stress, which might expose the microstructural evolution but could hardly reveal the intrinsic plastic instability of the materials. Special testing techniques, such as using hat-shaped specimens in a Hopkinson compression bar, using torsion or shearing systems and using punching machines, are used to trigger localized deformation due to a non-uniform stress distribution [139]. This geometrically produced shear band can only reveal the microstructural evolution during localization but cannot expose the intrinsic instability of materials. Nonetheless, the intrinsic stability of materials due to their material properties and deformation mechanisms is significant to key load-bearing structures in resisting small and local stress

or strain fluctuations. This is why regular compression specimens with cuboid-shape have been and will be used under uniaxial compressive loading in the preliminary and future work. Before compression testing, microstructures of each material will be examined by using transmission electron microscopy (TEM). Every possible piece of sample residue from compression tests at both quasi-static and dynamic loading rates will be collected for the purpose of a further fractographic examination. The fractography will be conducted with using scanning electron microscopy (SEM). Different failure modes are expected for materials. Theories for different failure manners due to different deformation mechanisms between those materials will be discussed with the knowledge of microstructure and fractography from pre- and post-loading samples. The organization of this research work is specified in the following section.

1.5 Organization of the Dissertation

In the previous sections of this chapter, a brief review of the development and research on Mg materials and plastic deformation instability has been given. This section is then intended to give a lead of the entire organization of this dissertation. In Chapter 2, the experimental methods will be described, including the material preparation, mechanical testing as well as the fundamental principle of the SHPB. Then, in the following Chapters, i.e., 3, 4 and 5, the experimental results as well as the corresponding discussion of each type of Mg materials will be organized in the following order. Chapter 3, pure Mg and Mg-Y alloy; Chapter 4, two Mg alloys produced by powder metallurgy (AMX 602, and lanthanum doped AZXE7111); Chapter 5, Mg composites reinforced with nano- and micro-SiC particles. As we can see, each chapter belongs to one or two of the following Mg types: pure Mg, binary Mg alloys, ternary and multi-component Mg

alloys and Mg-based composites. Basically, these types of Mg materials include all commonly used Mg materials. However, due to the time and space limitation, we could not study every single one of Mg alloys or composites produced via different technologies. On the other hand, there is no such need, since many of them have already been extensively investigated by other scientists. In this case, only the particular examples of each kind that we are interested in were chosen for this work. An in-depth discussion on the compressive behavior of different Mg materials as well as the corresponding deformation mechanisms will be given in Chapter 6. The last chapter will include the conclusions of the dissertation, as well as an insight of the potential work that may be valuable to be performed in the future.

CHAPTER 2: EXPERIMENTAL METHODS

In this chapter, synthesis, microstructural characterization and mechanical testing of the specimens employed in my dissertation work will be addressed in detail. The materials studied in this work include pure magnesium and Mg-0.6 wt.%Y extruded through an ECAP die, Mg alloys AZXE7111 (lanthanum doped) and AMX602 fabricated by a powder metallurgy technique and Mg-based metal matrix composites reinforced with micro/nano-silicon carbide (SiC). Mechanical testing performed to investigate the materials included compressive quasi-static (strain rate $1.0 \times 10^{-3} \text{ s}^{-1}$) and dynamic (strain rate $\sim 10^3 \text{ s}^{-1}$) loading in addition to nanoindentation strain rate jump tests. The key tools used for microstructural characterization of the pre/post-loading samples were transmission electron microscopy (TEM) and scanning electron microscopy (SEM) and their analytical attachments.

2.1 Materials Processing

As mentioned in the previous chapter, three types of Mg materials have been investigated in my dissertation work, wherein different material processing techniques such as equal channel angular pressing or extrusion and powder metallurgy were used to modify the microstructure of the materials. First, it should be noted that all material processing work was completed outside of UNC Charlotte, by our collaborators from other institutions. The pure Mg and Mg-0.6 wt.%Y were prepared by Dr. Aleš Jäger's group in the Czech Republic; the Mg alloys of AZXE7111 and AMX602 were prepared

at the Joining and Welding Research Institute, Osaka University, Japan; the Mg-based MMCs were fabricated by Dr. Linan An's group at the Advanced Materials Processing and Analysis Center, University of Central Florida, USA. My contribution will be on mechanical testing and most of the microstructural examination, as well as the analysis and discussion of the experimental results. The detailed descriptions of material processing in the following paragraphs for each material category, then, do not mean the efforts of mine, but a necessary clarification of the history and background of the specimens.

2.1.1 Pure Mg and Mg-0.6 wt.% Y

The pure Mg and Mg-0.6 wt.% Y materials were produced by Dr. Aleš Jäger's group after obtaining commercially pure magnesium of claimed 99.99% purity and a Mg-30 wt.% Y master alloy purchased from Yurui Chemical Co. Ltd. (Shanghai, P.R. China). The compositions of these raw materials were double checked before re-melting and casting by Dr. Aleš Jäger's group, showing 99.9% for the pure magnesium and Mg-26 wt.% Y for the master alloy. The Mg-0.6 wt.% Y alloy was then melted and cast from those two raw starting materials. Specifically, the pure Mg and Mg-26 wt.% Y were melted in a graphite crucible and argon atmosphere, and subsequently cast into a steel mold with the dimensions of 12.0 mm × 12.0 mm × 120.0 mm to form an ingot. Then, this ingot was annealed at 500 °C for 20 hours followed by cooling in the furnace. In addition, further solution treatment at 580 °C for 2 hours and quenching into warm water were performed. The weight percentage of each component of Mg-0.6 wt.% Y was measured and the results are shown in Table 2.1. The pure Mg and Mg-0.6 wt.% Y billets with the dimensions of approximately 10.0 mm × 10.0 mm × 40.0 mm were machined

from the as-received and re-produced ingots, and subsequently subjected to equal channel angular pressing (ECAP) at a speed of 0.4 mm/s via 4 passes using Route Bc. A schematic illustration of the ECAP channel and the convention of sample directions are presented in Figure 2.1. The die used in the present research had an internal angle of 90° and no outer curvature at the channel intersection. Therefore, the imposed strain for each press was expected to be approximately 1.2 [98]. Graphite-based lubricant was applied to the surface of the billets before each pressing. Also, to maintain an average plunger load of ~ 1 GPa and to avoid cracking, a back pressure (BP) in the range of 200 \sim 400 MPa was applied. The extruded bars are shown in Figure 2.2, for pure and yttrium-alloyed Mg, respectively. Depending on the presence or absence of defects or cracks, portions are marked with YES and NO to indicate the usable and unusable regions of the bars. Both quasi-static and dynamic samples were machined from the usable section by wire electrical discharge machining (wire-EDM) along the insertion direction (ID), the extrusion direction (ED) and the transverse direction (TD) with the dimensions of 2.00 mm \times 2.00 mm \times 4.00 mm (quasi-static samples) and 2.00 mm \times 2.00 mm \times 1.60 mm (dy), respectively.

2.1.2 Mg Alloys AZXE7111 and AMX602

The Mg alloys of AZXE7111 and AMX602 were also produced, starting from a corresponding melt with the proper chemical constituents. But, the difference is that the spinning water atomization (SWA) technique was used immediately following melting to produce powders of the alloys with containing ultrafine grains. The corresponding powder producing facility is shown schematically in Figure 2.3(a) with three main parts: a vacuum furnace, a water-cooled spinning chamber and a powder collection pot. The

Table 2.1: The chemical composition of Mg-0.6 wt% Y.

	Mg	Fe	Ni	Zn	Y
Mg-Y	99.305 ±0.100	0.013 ±0.005	0.014 ±0.004	0.005 ±0.002	0.663 ±0.020

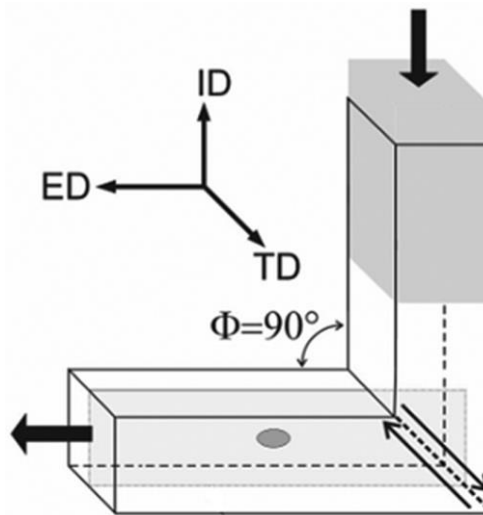


Figure 2.1: A schematic illustration of the equal-channel angular pressing (ECAP) process and the direction identifications.

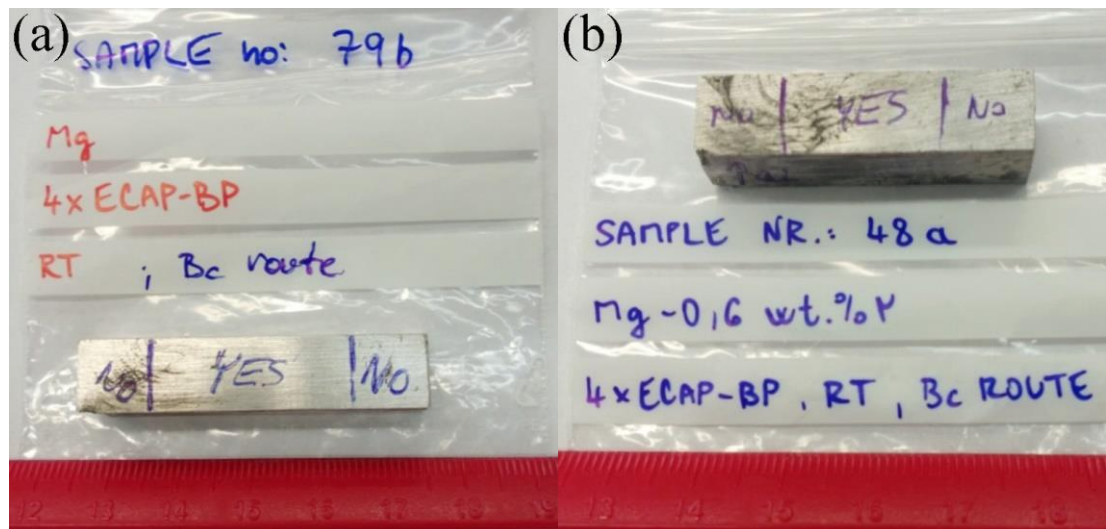


Figure 2.2: Photos of the ECAPed (a) pure Mg and (b) Mg-0.6 wt.% Y following the route Bc with a back pressure of 200 ~ 400 MPa up to four passes.

powder production includes the following procedures: first, the alloys were melted at 1053 K in a ceramic crucible; then, the melt was streamed inside the high speed spinning chamber cooled with running water; finally, alloy powder pieces with lengths of 1 ~ 4 mm were generated and collected. The morphology of the powders collected from the SWA process is shown in Figure 2.3(b). Thereafter, the powders were consolidated at room temperature with a force of 2000 kN to fabricate a green compact, which had a relative density of 85%. The green compact was then heated at a particular temperature for 180 seconds followed by immediate consolidation to full density by extrusion. An argon gas atmosphere was used during the heating process to protect the alloys from oxidation. Three extrusion temperatures were applied for both alloys, 250 °C, 300 °C, 350 °C for AMX602 and 200 °C, 250 °C, 350 °C for AZXE7111, respectively. In the end, the samples with dimensions of 2.50 mm × 2.50 mm × 5.00 mm and 2.50 mm × 2.50 mm × 2.00 mm were cut from the extruded bars for quasi-static and dynamic testing along the flow and transverse directions by wire-EDM.

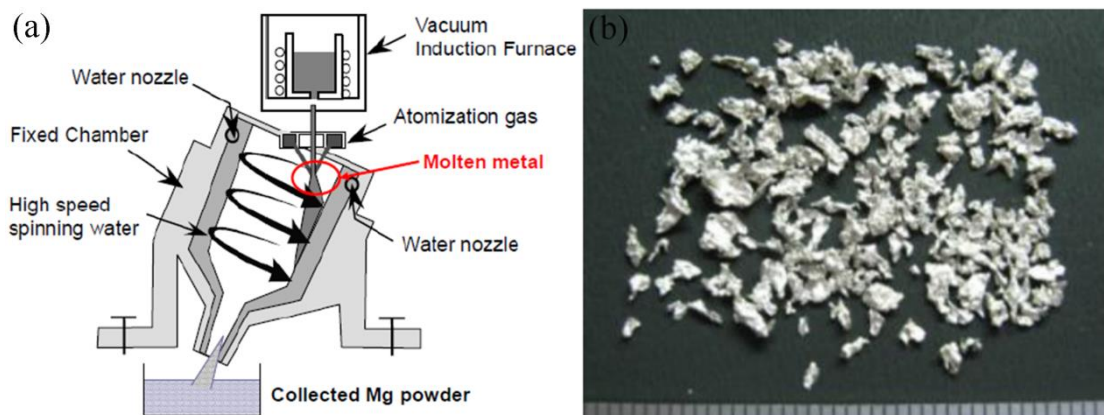


Figure 2.3: (a) A schematic illustration of spinning water atomization (SWA) facility, which combines a vacuum furnace, water cooled spinning chamber and a collection pot; (b) the morphology of the collected powders from SWA processing [76].

2.1.3 Mg-based Metal Matrix Composites

Mg-based metal matrix composites reinforced by micro/nano-silicon carbide (SiC) were fabricated by Dr. Linan An's group at the University of Central Florida. This section could be considered as an explanation of materials processing for a preliminary understanding of these composites. Details can be found in the dissertation of Dr. Jinling Liu [174]. Initially, two components, commercially available Mg powder of 99.8% purity serving as the matrix and β -SiC serving as the reinforcement, were mixed together in the desired volume fractions. One of two types of β -SiC particles, either from Alfa Aesar Corporation (Ward Hill, MA, USA) with a mesh size of -325 or from MTI Corporation (Richmond, CA, USA) with a nominal size of 20-nm, was incorporated into the mixture. The mixing was completed inside an argon filled glove box to minimize any contamination resulting from handling of the powders. Thereafter, the mixed powders were ball milled in a SPEX 8000M mill at room temperature, where a fan was used during the milling process in order to maintain a temperature rise below 50 K. The grinding chamber and balls were made of tungsten carbide and zirconia, and the diameter of the balls was 10 mm. The weight ratio of the balls to the total mixture was kept at approximately 10:1. During the milling process, up to 5 wt.% of 98% purity stearic acid from Alfa Aesar Corporation (Ward Hill, MA, USA) was added into the powder mixture to prevent any undesired and excessive cold welding among the powders, onto the internal surfaces of the chamber or onto the grinding medium. The pure Mg powder and the mixtures containing 5, 10 or 15 vol.% reinforcement particles were all milled 20 hours individually and then transferred into a graphite die for consolidation. The cylindrical die with 20 mm inner diameter was placed into a DR. SINTER (Model SPS-

1030, SPS Syntex Inc., Kanagawa, Japan). During consolidation, a compressive load of 50 MPa was applied and sintering with a heating rate of 100 °C/min was carried out in vacuum (10 Pa or lower) within this sintering system. The target sintering temperature of 575 °C was held for 5 minutes followed by a cooling process at a cooling rate of 60 °C/min without compressive load. Specimens were finally cut from the circular plate by wire-EDM with the dimensions of 2.50 mm × 2.50 mm × 5.00 mm for quasi-static loading and 2.50 mm × 2.50 mm × 2.00 mm for dynamic loading along the press direction.

2.2 Mechanical Testing

2.2.1 Polishing

Mechanical polishing down to 5 μm and 1 μm was performed on the two loading faces and two perpendicular side faces for the compressive loading specimens. Sandpapers purchased from LECO Corporation (St. Joseph, MI) with grit designations of 800/2400P and 1200/4000P were used for grinding the loading faces to smooth finish and for coarse grinding of the side faces. Diamond papers from Ted Pella, Inc. (Redding, CA) were used for fine grinding of the side faces down to a 1-μm finish. Electron backscatter diffraction (EBSD) samples were mechanically polished to 2400 grit using SiC paper and then polished with a solution of colloidal silica followed by ion milling. For nanoindentation samples, the mechanical polishing on diamond paper with 0.5-μm finish and on imperial polishing cloth with 0.05-μm alumina suspension was carried out until a mirror-finish was obtained. Both of the imperial polishing cloth and alumina suspension were purchased from LECO Corporation (St. Joseph, MI). The polishing sequences were all completed manually, and anhydrous alcohol was used as the water-free polishing

lubricant and rinsing liquid throughout the polishing process to prevent oxidation.

2.2.2 Mechanical Tests

The quasi-static compression tests (at a strain rate of $\sim 10^{-3} \text{ s}^{-1}$) were performed on the MTS 810 hydro-servo system (MTS Systems Corporation, Eden Prairie, MN) with a self-alignment feature. The principle of the quasi-static testing is quite straightforward, so it will be explained only briefly. The constant strain rate was achieved through controlling the velocity of the lower compression head by giving the desired moving distance and time while holding the upper compression head. The dimension of the quasi-static samples was $2.50 \text{ mm} \times 2.50 \text{ mm} \times 5.00 \text{ mm}$ ($2.00 \text{ mm} \times 2.00 \text{ mm} \times 4.00 \text{ mm}$ for pure Mg and Mg-0.6 wt.% Y) with a gauge length of 5.00 mm (4.00 mm for pure Mg and Mg-0.6 wt.% Y). Lubricant was applied at both loading faces for all specimens to mitigate friction. Raw data including the loading force, displacement and time were recorded by MTS TestSuite software. For each material, at least three samples with the same conditions were tested in order to ensure the reproducibility of the experimental results.

The dynamic compression tests (at a strain rates $\sim 10^3 \text{ s}^{-1}$) were performed on a desktop compression SHPB (or Kolsky bar) system. Figure 2.4 is a schematic illustration of the system, which essentially consists of a striking bullet, incident bar and transmitted bar that are usually made of the same high strength alloy steel and of the same diameter. The dimension for dynamic samples was $2.50 \text{ mm} \times 2.50 \text{ mm} \times 2.00 \text{ mm}$ ($2.00 \text{ mm} \times 2.00 \text{ mm} \times 1.60 \text{ mm}$ for pure Mg and Mg-0.6 wt.% Y) with a gauge length of 2.00 mm (1.60 mm for pure Mg and Mg-0.6 wt.% Y). The same lubricant as used in the quasi-static tests was applied at both loading faces to mitigate friction. The input, reflected and output signals from the strain gauges that were attached to the incident and transmitted bars were

recorded for every shot. As before, at least three samples with the same conditions were tested for each material to minimize the experimental error. The principle of loading for the system will be discussed in section 2.2.3 starting with one-dimensional wave theory. Since all of the work has been elaborated by other researchers [175-178], section 2.2.3 is only a recast for the purpose of integrity.

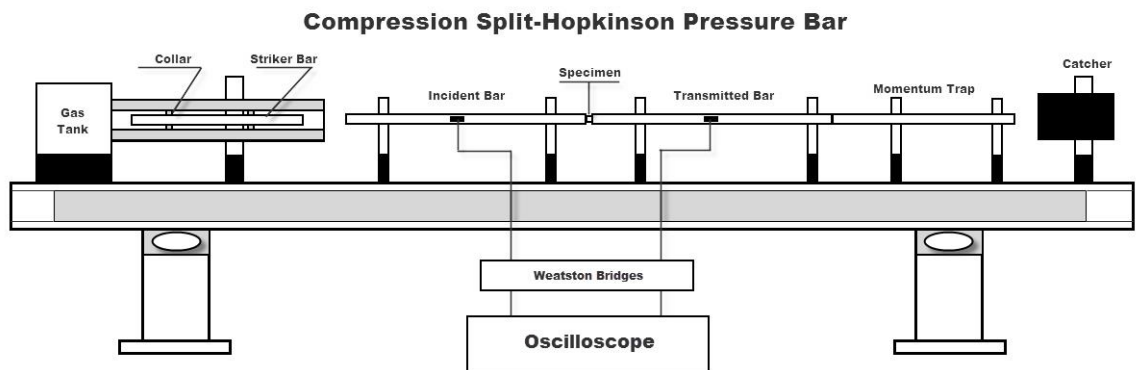


Figure 2.4: Schematic graph of desk-top compression Split-Hopkinson pressure bar system (SHPB or called desk-top Kolsky bar system).

The nanoindentation strain rate jump tests were performed on Agilent Nano Indenter G200 with four successive strain rates, starting from 0.001 /s to a maximum of 0.05 /s. At least ten locations, sometimes up to twenty due to poor polishing quality, were tested on each selected sample. For each test, the initial displacement was set to 800 nm, from which the indenter jumps to a high velocity every 150 nm until completing the designated test at the maximum strain rate. The second and third strain rates are automatically calculated by the software that controls the indenter. The nanohardness is also automatically evaluated corresponding to each strain rate.

2.2.3 Fundamental Principles of SHPB

2.2.3.1 Stress Wave Generation and Propagation

The loading process during impact usually completes within a few micro seconds, therefore, load transfer and specimen deformation are not as simple and straightforward as in the case of quasi-static loading. To understand the principle of specimen deformation under impact loading, the first concept that needs to be understood is how the load and deformation transferred from the input bar to the specimen during impact. Hence, a simplified schematic of an impact event in a Hopkinson bar is implemented to demonstrate the stress-wave generation, propagation and action upon the specimen, shown in Figure 2.5. Consider for the moment a time when you handled a spring, where after suddenly putting a force on one end of the spring, the other end did not react immediately, as the force had not yet traveled along the spring. The phenomenon occurs in every elastic bar including the one used in this work, because any elastic body can be regarded as a spring that only has a different spring constant. The impact load upon the end of the bar progressively propagates to the other end, but does not immediately take effect at the other end. This is completely different from our knowledge about the loading process during quasi-static loading, and we have to appeal to one-dimension stress-wave theory to understand the loading process involved in a Kolsky bar experiment. However, before any further explanation of one-dimensional stress-wave theory, there are a few assumptions we need to make: (1) the cross-section of the bars remains flat throughout the loading process; (2) the stress σ has a unique corresponding strain variable ε , i.e. $\sigma = \sigma(\varepsilon)$.

The first assumption makes equation (2.1) true within limited time, dt , which leads to

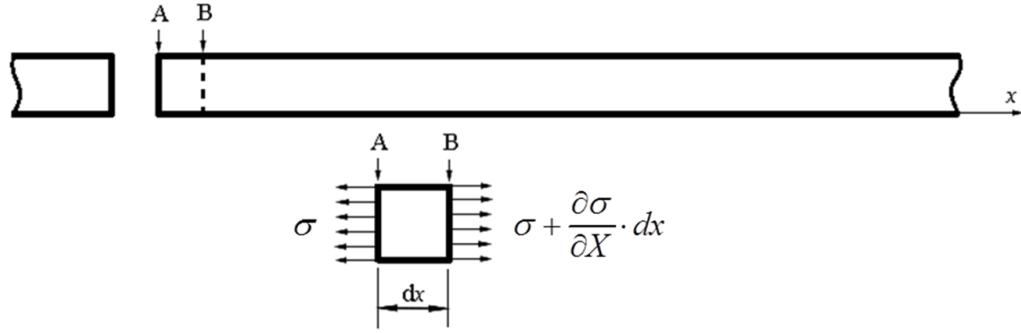


Figure 2.5: A schematic illustration of stress propagation in an elastic bar. A small part of the bar that is affected by the impact load at the very moment is pulled out for analysis.

equation (2.2).

$$\left(\sigma + \frac{\partial \sigma}{\partial X} \cdot dx - \sigma\right) \cdot A = \rho A dx \cdot \frac{\partial v}{\partial t}, \quad (2.1)$$

$$\frac{\partial \sigma}{\partial X} = \rho \cdot \frac{\partial v}{\partial t}; \quad (2.2)$$

where X denotes the material coordinates; A is the cross-section area of the bars; ρ is the mass density of the bar material, and $v = \partial u / \partial t$ is the velocity of the small piece. The above equation can be rewritten in the form of equation (2.3) or (2.4), where u is the displacement of particles.

$$\frac{\partial v}{\partial t} = \frac{1}{\rho} \cdot \frac{\partial \sigma}{\partial X} = \frac{1}{\rho} \cdot \frac{\partial \sigma}{\partial \varepsilon} \frac{\partial \varepsilon}{\partial X}, \quad (2.3)$$

$$\frac{\partial^2 u}{\partial t^2} = \left(\frac{1}{\rho} \cdot \frac{\partial \sigma}{\partial \varepsilon}\right) \frac{\partial^2 u}{\partial X^2}. \quad (2.4)$$

As long as the stress function, $\sigma = \sigma(\varepsilon)$, is differentiable and $d\sigma / d\varepsilon > 0$, we can have

$$C^2 = \frac{1}{\rho} \cdot \frac{d\sigma}{d\varepsilon} > 0, \quad (2.5)$$

or

$$\frac{\partial^2 u}{\partial t^2} = C^2 \frac{\partial^2 u}{\partial X^2}. \quad (2.6)$$

There are many ways to find the solutions of Eq. (2.6). Here is a simple example.

Rewriting Eq.(2.6) in the form of Eq.(2.7) leads to Eq.(2.8) or Eq.(2.9) [179]:

$$\left(\frac{\partial}{\partial t} + C \frac{\partial}{\partial X} \right) \left(\frac{\partial}{\partial t} - C \frac{\partial}{\partial X} \right) u = 0. \quad (2.7)$$

$$\frac{\partial W}{\partial t} + C \frac{\partial W}{\partial X} = 0, \text{ where } W = \frac{\partial u}{\partial t} - C \frac{\partial u}{\partial X} = v - C\varepsilon; \quad (2.8)$$

$$\frac{\partial V}{\partial t} - C \frac{\partial V}{\partial X} = 0, \text{ where } V = \frac{\partial u}{\partial t} + C \frac{\partial u}{\partial X} = v + C\varepsilon. \quad (2.9)$$

On the other hand, we have

$$\frac{dW(X(t), t)}{dt} = \frac{\partial W}{\partial t} + \frac{\partial W}{\partial X} \frac{dX}{dt}, \quad (2.10)$$

and

$$\frac{dV(X(t), t)}{dt} = \frac{\partial V}{\partial t} + \frac{\partial V}{\partial X} \frac{dX}{dt}. \quad (2.11)$$

It is apparent, from Eq.(2.8) and (2.10), that W is a constant when $C = dX/dt$. Similarly,

V is a constant when $C = -dX/dt$ from Eq.(2.9) and (2.11). These give two groups of solutions:

$$1^{\text{st}} \text{ solution: } dX = C \cdot dt \text{ with } v - C\varepsilon = R_1 \text{ (constant);}$$

$$2^{\text{nd}} \text{ solution: } dX = -C \cdot dt \text{ with } v + C\varepsilon = R_2 \text{ (constant).}$$

Actually, dX/dt is the velocity of the stress-wave front. It can also be represented by Eq.(2.5) as $C = \sqrt{E/\rho}$ for linearly-elastic materials, where E is the Young's modulus. It is necessary to point out that, the wave velocity is not fundamentally equal to the particle velocity. Now, if we define the right direction as positive while the left direction as negative, the first (second) solution shall imply that when the stress-wave front

propagates with a speed of C in the positive (negative) direction, the particle velocity and the strain within the wave-front fulfill the relation of $v - C\varepsilon = R_1$ ($v + C\varepsilon = R_2$). Then, Eq.(2.12) and (2.13) are reached by combining Eq.(2.5) with the solutions.

$$(\sigma_0 - \sigma) = (\rho C) \cdot (v - v_0) \quad (\text{Positive}); \quad (2.12)$$

$$(\sigma_0 - \sigma) = -(\rho C) \cdot (v - v_0) \quad (\text{Negative}). \quad (2.13)$$

where σ_0 is the stress at the wave-front B (or the initial stress in the bar); v and v_0 are the particle velocities at the current and initial states, respectively.

2.2.3.2 Magnitude of the Stress-wave

In the last section, the generation and propagation of two stress-waves (right and left) after impact loading have been demonstrated, and both compatible conditions affiliated to either of the wave-fronts have been obtained. Therefore, in this section, the magnitude of these stress-waves will be evaluated. To reach this goal, one thing needs to be agreed on which is that at the impact interface, both the stress and particle velocity in the striker and input bar will be equal. In other words, a physical compatibility is reached at the striker-bar interface, shown by 1 and 2 in Figure 2.6. Then, beginning with a general case as shown in Figure 2.6, a striker moving at a speed of v_1 hits against one end of a bar moving at v_2 ($v_1 > v_2$). The striker and the bar, with the same diameter, are for now assumed to be made of different materials. The initial stresses are shown in the schematic for both the striker and the input bar.

From (2.12) and (2.13), two equations are generated for region 1 and region 2, separately, corresponding to the ends of the striker and input bar.

$$(\sigma_1 - \sigma) = -(\rho C)_1 \cdot (v - v_1) \quad (\text{Region 1}), \quad (2.14)$$

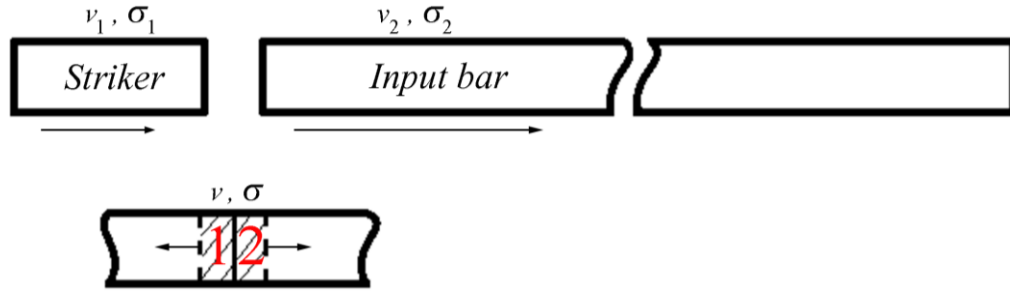


Figure 2.6: A schematic illustration of stress-wave generation during impacting. When the impact happens, a physical compatibility shall be satisfied at the interface, i.e. 1 and 2, where 1 is the face of the striker and 2 is the face of the input bar.

$$(\sigma_2 - \sigma) = (\rho C)_2 \cdot (v - v_2) \quad (\text{Region 2}). \quad (2.15)$$

where $(\rho C)_1$ represents the property values from region 1. By solving those equations,

$$\sigma = \frac{(\rho C)_1 \cdot \sigma_2 + (\rho C)_2 \cdot \sigma_1}{(\rho C)_1 + (\rho C)_2} + \frac{(\rho C)_1 (\rho C)_2 \cdot (v_2 - v_1)}{(\rho C)_1 + (\rho C)_2},$$

$$v = \frac{(\sigma_2 - \sigma_1)}{(\rho C)_1 + (\rho C)_2} + \frac{(\rho C)_1 \cdot v_1 + (\rho C)_2 \cdot v_2}{(\rho C)_1 + (\rho C)_2}. \quad (2.16)$$

Now consider a special case where, both the striker and the input bar are made of the same material and initially are stress-free, i.e. $(\rho C)_1 = (\rho C)_2 = \rho C$ and $\sigma_1 = \sigma_2 = 0$; and the input bar is initially in an idle state, i.e. $v_2 = 0$. The solution becomes:

$$\sigma = -\frac{1}{2}(\rho C) \cdot v_1, \quad v = \frac{1}{2}v_1. \quad (2.17)$$

This is exactly the case in the SHPB system. Two compressive stress-waves are produced, one travels right into the input bar while the other travels left into the striker.

2.2.3.3 Interaction between Stress-waves

The stress-wave changes its properties when it meets either another stress-wave or the boundary of the transmitting medium. Hence, in this part, the interaction between

stress-waves or between the stress-wave and the boundary will be discussed. Figure 2.7 shows a schematic of two stress-waves propagating from the ends of a bar consisting of unspecified material. The properties and travel directions of the stress-waves are indicated in the diagram. When those two stress-waves meet somewhere in the medium, a physical compatibility at the interface between the wave-fronts, shown by L and R, shall be fulfilled as well as that upon impact. Hence, the same solution as (2.16) shall be reached except that $(\rho C)_1 = (\rho C)_2 = \rho C$. Furthermore, we also have the following conditions by considering the two sides of the medium separately.

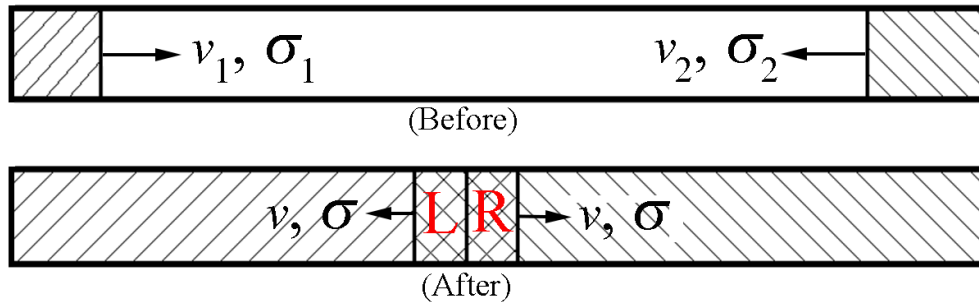


Figure 2.7: A schematic illustration of the interaction between two stress-waves. When the stress-waves meet, a physical compatibility shall be satisfied at region L and region R, where L is the wave-front of left stress-wave while R is the wave-front of right stress-wave.

$$\sigma_1 = -(\rho C) \cdot v_1 \text{ and } \sigma_2 = (\rho C) \cdot v_2. \quad (2.18)$$

Then, combine the conditions of (2.16), (2.18) and $(\rho C)_1 = (\rho C)_2 = \rho C$, we have

$$\sigma = \sigma_1 + \sigma_2, \quad v = v_1 + v_2. \quad (2.19)$$

This result implies that when two stress-waves travelling within one homogeneous medium meet together, the resultant stress-wave is only a superposition of the old ones.

Of additional interest is the following question: for the case of a stress-wave traveling in a bar, how will it respond when it meets the bar end? In this case, we may suppose there is another stress-wave that comes from the opposite direction in a virtual bar connecting to the previous one, shown in Figure 2.8. Then, this becomes the same problem as the above one but $(\rho C)_1 \neq (\rho C)_2$, where $(\rho C)_2$ is actually the property of air if we assign $(\rho C)_1$ for the bar material. Therefore, the solutions of the problem are exactly the same as that of (2.16).

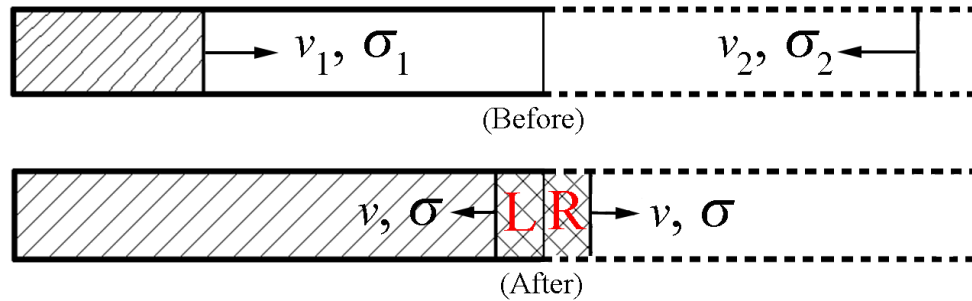


Figure 2.8: A schematic illustration of the interaction between a stress-wave and a boundary. The right dashed part is an imaginary bar with an imaginary stress-wave travelling towards the real one.

Nevertheless, the air is initially in a stress-free and idle state, and $(\rho C)_1 \gg (\rho C)_2$. The solutions can be simplified as follows:

$$\sigma = 0, \quad v = -\frac{1}{(\rho C)_1} \sigma_1 + v_1 = 2v_1. \quad (2.20)$$

Similarly, if $(\rho C)_1 \ll (\rho C)_2$, i.e. the end of the bar is fixed onto something extremely rigid, the solution is then simplified to (2.21):

$$\sigma = 2\sigma_1, \quad v = 0 \quad (2.21)$$

The above results convey two facts: when a stress-wave reflects at the free-end, the particle velocity is doubled and the stress is released; when it reflects at a fixed-end, the stress is doubled and the particle velocity becomes vanishing. Yet, in view of the principle of superposition, the first one is a result of the original stress-wave meeting with a ‘new’ stress-wave generated at the free end with $\sigma_{new} = -\sigma_1$ and $v = v_1$ propagating in the opposite direction; similarly, the second one is the superposition with a ‘new’ stress-wave generated at the fixed end with $\sigma_{new} = \sigma_1$ and $v = -v_1$ propagating in the opposite direction.

2.2.3.4 Stress-wave Propagation through an Interface

Heretofore, I have delineated the stress-wave generation, propagation and responses of interactions between themselves or with media boundaries. Yet, the most important question is what happens when the stress-wave passes through an interface between two media with the same or different cross-sectional areas. This question relates to how the dynamic load is transferred from the bar to the specimen. Therefore, in this section, we will illustrate the separation of the stress-wave into the reflected and transmitted parts at an interface, and give the conditions that need to be satisfied to guarantee valid stress-strain data from the specimen.

A schematic drawing is adopted, shown in Figure 2.9, to demonstrate the entire process of stress propagation at an interface with different cross-sectional areas, A_L and A_S ($A_L > A_S$, the subscripts L and S denote the ‘Large’ and ‘Small’ cross-sectional area in the graph). The right portion is assumed to be motionless and stress-free initially. An impact force is imposed on the left end of the large bar. An obvious conclusion can be drawn from the last section, that the resultant stress and particle velocity in the left media

(region L) is only a superposition of the input and reflected stress-waves. Since the forces must be balanced at the interface, and the particle velocity must be continuous, the following equations need to be fulfilled.

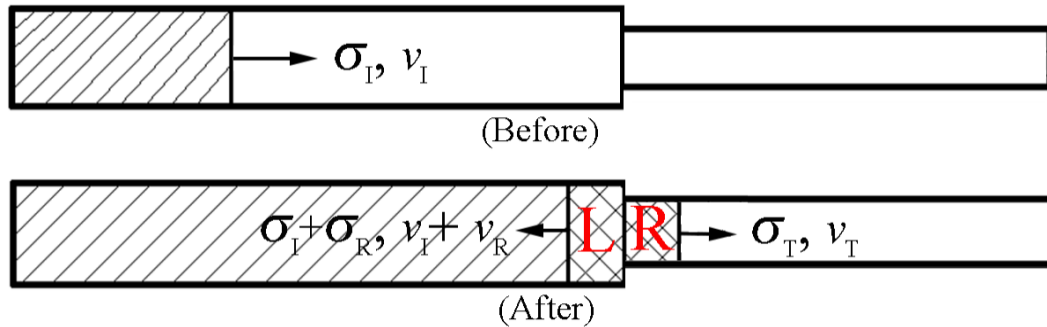


Figure 2.9: A schematic illustration of the stress-wave propagation through an interface with same or different cross-sectional areas. The in-put stress-wave separates into reflected and transmitted parts propagating in separate directions.

$$(\sigma_I + \sigma_R) \cdot A_L = \sigma_T \cdot A_S, \quad (2.22)$$

$$v_I + v_R = v_T, \quad (2.23)$$

where the subscripts I , R and T represent values from the input, reflected and transmitted portions, respectively. In addition, from (2.17), the stress and particle velocity also fulfill the following relations.

$$v_I = \frac{\sigma_I}{(\rho C)_L}, \quad v_R = -\frac{\sigma_R}{(\rho C)_L} \quad \text{and} \quad v_T = \frac{\sigma_T}{(\rho C)_S}. \quad (2.24)$$

Combining (2.22) ~ (2.24) and setting $n = (\rho CA)_L / (\rho CA)_S$, a solution of the reflected (transmitted) stress σ_R (σ_T) and particle velocity v_R (v_T) can be reached as a function of σ_I and v_I , respectively.

$$\sigma_R = \frac{1-n}{1+n} \cdot \sigma_I \text{ and } \sigma_T = \frac{2}{1+n} \frac{A_L}{A_S} \cdot \sigma_I, \quad (2.25)$$

$$v_R = \frac{n-1}{1+n} \cdot v_I \text{ and } v_T = \frac{2n}{1+n} \cdot v_I. \quad (2.26)$$

Although the schematic drawing shows a stress-wave propagating from a large cross-sectional area to a small cross-sectional area, the solution should also hold if the wave propagates from a small cross-sectional area to a large cross-sectional area. Hence, as of now, the separation of an input stress-wave at an interface and the resultant stress and particle velocity of each subpart are solved. It is also easy to see that the transmitted stress-wave will have a sub-separation when it arrives at the other end of the transmission bar, and so does the reflected one. From now on, the future propagation of the stress-waves can be anticipated based on the principles that have been discussed up till now. For example, if considering the stress-wave within the specimen only during a real SHPB testing, the first transmitted stress-wave (σ_{ST}, v_{ST}), generated from the separation of an input stress-wave, will separate into the reflected (σ_{RS1}, v_{RS1}) and transmitted parts at the specimen-output bar interface where the reflected part propagates back into the specimen. A similar outcome will occur to the sub-reflected stress-wave at the specimen-input bar interface, and then to new reflected stress-waves ($\sigma_{RS2}, v_{RS2}; \sigma_{RS3}, v_{RS3}; \dots$) generated at either one of the specimen ends by the last one. The values of every $\sigma_{RS(i+1)}$ and $v_{RS(i+1)}$ can be measured from the values of σ_{RSi} and v_{RSi} based on the separation principle, where $i = 0, 1, 2, \dots$ and $\sigma_{RS0} = \sigma_{ST}$ and $v_{RS0} = v_{ST}$. In addition, due to the superposition principle, as long as there is only one unique and endless input stress-wave, the stress and particle velocity in the specimen will be $\sigma_{ST} + \sigma_{RS1} + \sigma_{RS2} + \dots$ and $v_{ST} + v_{RS1} + v_{RS2} + \dots$

depending on time and location on the specimen. Zhou et al. and other researchers [180-182] have analyzed the stress uniformity in the specimen during impact loading. They concluded that, generally, the stress difference between the two ends of the specimen could be considered negligible ($< 5\%$) after six reflections of the stress-wave in the specimen depending on the value of n in equation (2.25) and (2.26).

2.2.3.5 Recording and Analyzing

The last problem about the SHPB system is how to obtain a stress-strain curve of the specimen from one loading. In fact, the stress values at the two ends of the specimen have already been evaluated in the last section. Only because of a technological limitation, they are not measured at the ends of the specimen directly. There is an alternative method that involves measuring the strain-wave signals (ε_I , ε_R , ε_T) from the middle of both the input and output bars by using strain gauges. This is viable because the input and reflected stress-waves are related to the stress at the left end of the specimen while the transmitted one is related to the stress at the right end of the specimen by the following equations.

$$(\sigma_I + \sigma_R) \cdot A_I = \sigma_{SLE} \cdot A_S \text{ (Input bar-specimen interface),} \quad (2.27)$$

$$\sigma_{SRE} \cdot A_S = \sigma_T \cdot A_T \text{ (Specimen-output bar interface).} \quad (2.28)$$

The subscripts SLE and SRE are to identify the left end of specimen and the right end of specimen, respectively. For a normal SHPB system, the input and output bars are made of the same material and of the same diameter. For example, in the present research work, both of the bars are made of maraging steel with a diameter of 7.86 mm for a regular SHPB system or ~5.0mm for the desk-top SHPB system. Recall, the requirement that both the input and output bars are kept in the linearly-elastic region during the experiment,

the stress within the specimen can then be represented by either one of the following equations after six reflections of the stress-wave in the specimen.

$$\sigma = \sigma_{SLE} = \frac{A}{A_S} \cdot (\sigma_I + \sigma_R) = \frac{EA}{A_S} \cdot (\varepsilon_I + \varepsilon_R), \quad (2.29)$$

$$\sigma = \sigma_{SRE} = \frac{A}{A_S} \cdot \sigma_T = \frac{EA}{A_S} \cdot \varepsilon_T, \quad (2.30)$$

where E and A are Young's modulus and the cross-sectional area of the bars. Apparently, it is also reasonable to use the average value of the above two.

On the other hand, as the strain is assumed to be uniform along the length of the specimen under a uniform stress distribution, the strain rate and strain can then be evaluated by the following equations.

$$\dot{\varepsilon} = \frac{v_{SRE} - v_{SLE}}{l_S}, \quad (2.31)$$

$$\varepsilon = \int_0^t \dot{\varepsilon} dt. \quad (2.32)$$

Moreover, from the relation in (2.23), the particle velocities at the ends of specimen must fulfill the following relations:

$$v_I + v_R = v_{SLE}, \quad v_{SRE} = v_T. \quad (2.33)$$

Recall the linear relation between the particle velocity and the strain in section 2.2.3.1, the strain rate and strain can be represented as a function of ε_I , ε_R , ε_T .

$$\dot{\varepsilon} = \frac{v_{SRE} - v_{SLE}}{l_S} = \frac{v_T - (v_I + v_R)}{l_S} = \frac{C_B}{l_S} (\varepsilon_T - \varepsilon_I + \varepsilon_R), \quad (2.34)$$

$$\varepsilon = \frac{C_B}{l_S} \int_0^t (\varepsilon_T - \varepsilon_I + \varepsilon_R) dt, \quad (2.35)$$

where, C_B is the acoustic velocity of the maraging steel.

So far, the stress, strain and strain rate of the specimen have all been represented by the strains of the bars. To obtain the strain signal is a matter of translating the electronic signal from the strain gauge into the strain of the bars; this description will be skipped here for the consideration of space. Certainly, the SHPB technique is far more complicated when this is applied to different materials or for different purposes. Two books [178, 183] are recommended for a more detailed discussion as well as some noteworthy problems in this experimental technique.

2.3 Microstructural Characterization

It is helpful for a fundamental understanding of the deformation mechanisms and failure modes of materials by gathering as much information as possible. In addition to examining the microstructure before testing, sometimes the microstructure, fractography and the crack pattern of the materials after testing are very useful. To this end, all types of specimens before and after testing are gathered and examined using optical or electron microscopy. However, for different samples, the extent of the examination may vary to a certain extent.

The microstructure of pure Mg and Mg-Y samples after 4 ECAP passes was characterized by EBSD and XRD along the ID-ED plane. EBSD measurements were performed using an FEI Quanta 3D FEG SEM fitted with a TSL/EDAX Hikari camera. To obtain reasonable statistics, 5 EBSD maps of similar size ($\sim 0.3 \text{ mm}^2$) were measured from each sample with a mapping step of 300 nm. The percentage of the material that could be indexed by EBSD was above 80%. Crystallographic texture measurements were conducted using a PANalytical X'Pert PRO diffractometer in Bragg-Brentano geometry with $\text{Co K}\alpha$ radiation ($\lambda = 1.789 \text{ \AA}$). Complete orientation distributions and recalculated

full pole figures were determined. As it is only possible for EBSD to observe systematic tilting of the lattice due to dislocations of the same sign rather than dislocations themselves [184], the confidence in the accuracy of EBSD results is not absolute. For this reason XRD was carried out in order to reveal the accumulated strain. XRD was also chosen because, unlike EBSD, the specimen surface does not need to be treated by ion polishing that can heat the surface, thus preventing any post-processing recovery and/or recrystallization. However, instead of EBSD, TEM was used to examine the microstructure of Mg-Y due to the sub-micrometer scale grain structure with excess of defects, which prevents us from obtaining useful EBSD signals. Samples for TEM were prepared from the as processed billet by gentle grinding to a thickness of 70 μm , finished by ion milling (Gatan PECS) and then observed with an FEI TECNAI G2 F20 X-TWIN and JEOL 1200EX. Additionally, post-loading samples from uniaxial quasi-static and dynamic compression tests were also examined using a JEOL JSM 6480 SEM operated at 15 kV.

In addition, the Mg alloys (AZXE7111 and AMX602) and composites are examined by a JEOL JEM 2100 TEM operated at 200 kV before mechanical loading. An energy-dispersive X-ray spectrometer (EDS) attached to either SEM or TEM could also be used to identify the chemical composition of the particles. The TEM samples were first cut from bulk samples with ~ 1 mm in thickness using a diamond saw, and followed by mechanical grinding to about 100 μm . Further steps including dimpling and final thinning to electron transparency were carried out on a dimple grinder (Model 656, Gatan) and a precision ion polishing system (PIPS, Gatan), respectively. Post-loading examinations of these samples are also performed on a JEOL JSM 6480 operated at 15 kV.

CHAPTER 3: PURE MAGNESIUM AND MG-0.6% YTTRIUM

Since it is intended to investigate the effect of different impurities or alloying elements on the mechanical properties of Mg, it seems appropriate to start with studying pure Mg. Thus, the research work on pure Mg and Mg-0.6%Y alloy is presented first. The materials characterization, mechanical behavior and the discussions of pure Mg and Mg-Y will be summarized in sequence. But, since the mechanical properties and deformation mechanisms of pure Mg have been widely investigated, the greatest interest of this project will be in the difference of mechanical properties and deformation mechanisms between pure magnesium and the Mg-Y alloy. Specifically, in this section, the mechanical properties and deformation mechanisms of pure Mg and Mg-Y alloy after equal channel angular pressing via route Bc will be studied. There are two reasons: (1) the role of the element yttrium has been confirmed as positive to the ductility improvement of magnesium after annealing [75]; yet, the role of yttrium on grain fragmentation, dynamic recovery and recrystallization during severe plastic deformation (SPD) is still unknown; (2) the mechanical properties and deformation mechanisms of as-ECAPed Mg-Y alloy have not been reported, yet are very important to the understanding of the actual role of yttrium on ductility improvement.

There are some publications emphasizing the role of rare earths on the property improvement of Mg. For example, Mishra et al. [28] improved the ductility of a Mg alloy by adding only 0.2% Ce; Elsayed et al. [29] improved the anisotropy of Mg alloys by the

addition of La. However, the underlying mechanism of rare earths on the microstructure evolution during either the synthesis or the large plasticity has not been well understood. For example, there is limited literature shedding light on how the rare earths operate to control the texture of samples. Elsayed et al. [77] reported that the element La formed ultrafine Al-La particles acting as nucleation sites and dislocation barriers in Mg alloys. In the early work by Sandlöbes et al. [75], a positive role of yttrium on enhancing the activity of $\langle a+c \rangle$ slip and twinning was determined by experiments, where twinning-induced shear bands were also inferred. The high frequency of shear banding as well as non-basal slips was then accounted for as a reason of the high ductility in this Mg-Y alloy. In their later works, Sandlöbes et al. [52, 185] computationally proved that alloying by either yttrium or lanthanide elements can reduce the intrinsic I_1 stacking fault energy (I_1 SFE) in pure Mg. The I_1 SFE was experimentally found as sources for $\langle a+c \rangle$ dislocations. Nevertheless, there are still quite a few remaining questions that need to be answered before we can widely use rare earths for property improvements in Mg. Being a structural material, plastic forming at large strains or serving at impact loading rates is inevitable. Therefore, the knowledge of the role of rare earths on the microstructure evolution and deformation mechanisms at extreme strain rates is essential to Mg as structural materials.

The aim of this chapter is to understand (i) the effect of yttrium on the microstructure evolution during SPD and (ii) the difference of mechanical properties and deformation mechanisms between pure Mg and Mg-Y alloy after SPD at different loading rates. To this end, the microstructure and mechanical properties of pure Mg and Mg-Y will be presented; the underlying mechanisms will be discussed in the following sections as well.

3.1 Materials Characterization

An inverse pole figure (IPF) map of pure Mg after 4 passes of ECAP is shown in Figure 3.1(a), taken from the center of the ID-ED plane. Similar results were obtained from other locations within the same plane. The average grain size, determined by EBSD on high angle grain boundaries ($> 10^\circ$) using the TSL software, was 4.5- μm , which is slightly smaller than that from Fan et al.'s [186] 6- μm after 4 passes via Route Bc at 250 $^\circ\text{C}$. It is also equivalent to that for AZ61 subjected to 8 passes ECAP via Route Bc at 275 $^\circ\text{C}$ [13]. The comparably fine grains obtained in the present study could be attributed to the lower processing temperature that suppresses the grain growth. Of course, the use of back pressure made it possible to carry out up to 4 passes of ECAP at such a low temperature without cracks. Yamashita et al. [187], on the other hand, observed cracks in pure Mg after more than two passes ECAP at 400 $^\circ\text{C}$ where no back pressure was applied. However, from the EBSD figure, it is apparent that recrystallization processes must have occurred during our ECAP-BP, as the microstructure is free of shear bands and contains a large number of reasonably equiaxed grains resembling those usually observed in annealed samples. These findings are further verified by low level of strains accumulated in many of the grain interiors as determined by EBSD analytical software based on point-to-point misorientation profiles or from kernel average misorientation maps (not shown here). In addition, the recrystallization process was also verified by XRD results. Figure 3.1(b) shows the XRD result for the ECAPed pure Mg, from which a low value of accumulated strain was confirmed by the narrow profile of diffraction peaks combined with the well-distinguished $K\alpha_1$ and $K\alpha_2$ lines. For the sake of completeness, the texture was also measured by XRD and is shown in Figure 3.2. The (0002) and $\{10\bar{1}0\}$ direct

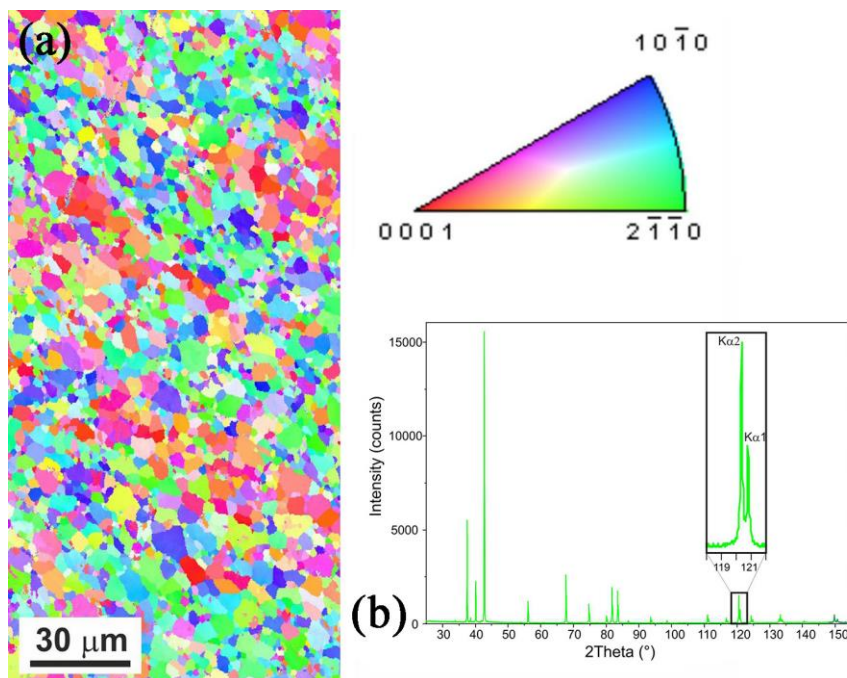


Figure 3.1: (a) An inverse pole figure (IPF) map of as-ECAPed p-Mg taken from the centre of the ID-ED plane. The EBSD image displays a well-annealed and uniformly distributed grain structure with grain size of $\sim 5\text{-}\mu\text{m}$; (b) XRD result for p-Mg subjected to 4-pass ECAP via route Bc. The narrow profile of diffraction peaks and well-distinguished $K\alpha 1$ and $K\alpha 2$ lines indicate a very low accumulated strain in the sample.

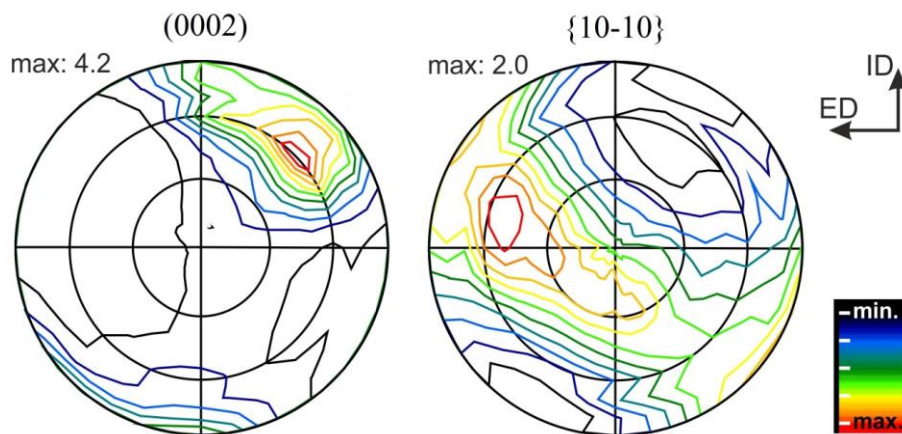


Figure 3.2: The (0002) and $\{10\bar{1}0\}$ direct pole figures taken from the ID-ED plane of as-ECAPed p-Mg are shown, accompanied with the direction indicators and the maximum intensities. Those figures display a tendency for the grains to align the basal planes parallel with the theoretical shear plane of the ECAP die.

pole figures display a tendency for the grains to align with the basal planes, i.e., parallel to the theoretical shear plane of the ECAP die.

As no useful information of the microstructure of Mg-Y was obtained by EBSD, a TEM image was provided for the alloy after ECAP processing instead, shown in Figure 3.3. It can be observed that the highly deformed microstructure contains either distorted grains with an estimated size of ~ 400 -nm or un-recrystallized regions with strong deformation contrast that hindered microstructure identification. The elongated spots or arcs in the selected area diffraction (SAD) pattern shown in the inset of Figure 3.3, however, indicate slightly textured polycrystalline microstructure. In contrast to the pure-Mg (p-Mg) processed under the same conditions, the Y-doped microstructure shows more than one order smaller grain size ($4.5\text{-}\mu\text{m}$ for p-Mg vs. $0.4\text{-}\mu\text{m}$ for Mg-Y). Meanwhile, the highly deformed microstructure in as-ECAPed Mg-Y was also confirmed by the XRD patterns. Figure 3.4(a) and (b) provide both XRD spectra of Mg-Y for the conditions of as-ECAPed and as-ECAPed + 2-hour annealing at 573K. A visible difference in peak broadening between these two samples is notable in Figure 3.4(c) at higher 2Θ angles. This difference can be attributed to the residual stresses (i.e., microstresses) in the as-ECAPed Mg-Y [188]. The residual stresses are caused by some source of local lattice distortion which in our case can be mainly generated either from large difference in the atomic radius between Y and Mg (atomic size misfits) or from defects generated by severe plastic deformation. The values of micro-strains for the as processed and annealed (at 573 K for 2 hours) samples are measured to be $0.105 \pm 0.003\%$ and $0.005 \pm 0.003\%$, respectively. This implies that peak broadening for the as-processed sample stems from accumulated deformation. For comparison, pure Mg subjected to the

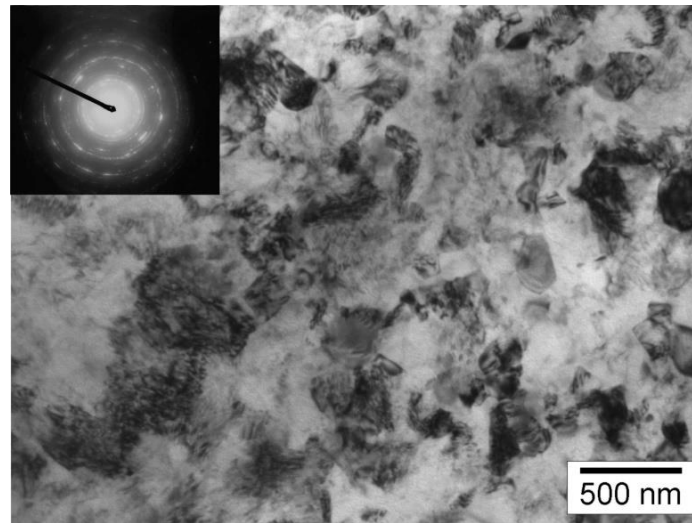


Figure 3.3: A bright-field TEM image of Mg-Y alloy after 4-pass ECAP via route Bc. The highly deformed microstructure can be identified through either distorted grains with an estimated size of ~ 400 -nm or unrecrystallized regions with strong deformation contrast that hindered microstructure identification.

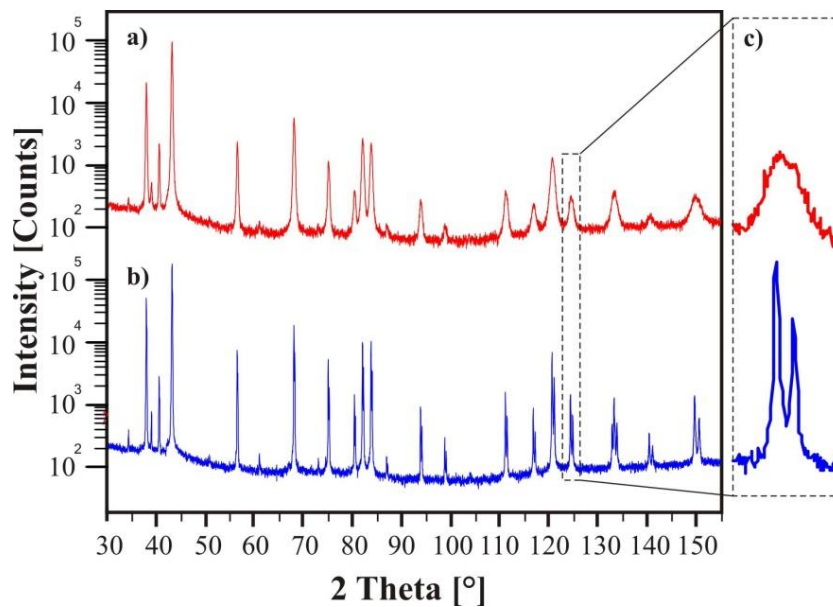


Figure 3.4: XRD spectrums for Mg-Y alloy subjected to (a) 4-pass ECAP via route Bc and (b) 4-pass ECAP via route Bc + 2-hour annealing at 573K. It is obviously that the profile of diffraction peaks became much narrower as the as-ECAPed Mg-Y was annealed, and the $K\alpha_1$ and $K\alpha_2$ lines at high 2Θ angle became well-distinguished while they were unidentified in the as-ECAPed Mg-Y alloy. Those confirm the accumulation of internal strain in the as-ECAPed Mg-Y alloy.

same procedure showed a recrystallized microstructure with very low accumulated micro-strains [189]. It is worth pointing out that, the XRD patterns showed distinct reflection signals characteristic of metallic Mg with HCP-structure; microstructural analysis via TEM and XRD did not reveal the presence of Y-based particles. Thus, it is reasonable to conclude that the element Y is mainly in solid solution of the Mg matrix. Despite the low concentration of Y, it serves as an effective retainer of accumulated defects during the ECAP processing at RT.

3.2 Mechanical Properties

3.2.1 Compressive Behavior

Figure 3.5 presents the representative true stress-strain curves of (a) p-Mg and (b) Mg-Y for the plastic deformation region for all three directions under both quasi-static (1.0×10^{-3} /s) and dynamic ($\sim 10^3$ /s) compressive loading. It can be observed that both p-Mg and Mg-Y exhibit a strain-rate strengthening effect, i.e., the strength increases with the strain rate. In addition, as the plastic strain increases, the p-Mg first exhibits a non-hardening (perfectly plastic) deformation within approximate 4% strain, after which the strain hardening rate increases rapidly to some point followed by a gradually decreasing strain hardening rate until an absolute loss in ability of the sample to sustain any load. A direct sense of the behavior is that the deformation mechanisms could be transformed from one to another during compression. It is apparent that the deformation mechanisms that contribute to strengthening are in a secondary position at the beginning; then one or more of them gradually strengthens and dominates the deformation until exhaustion. The slowing-down and even the negative strain hardening prior to failure can be a sign of the exhaustion of strengthening factors. On the other hand, it is quite obvious that the strain

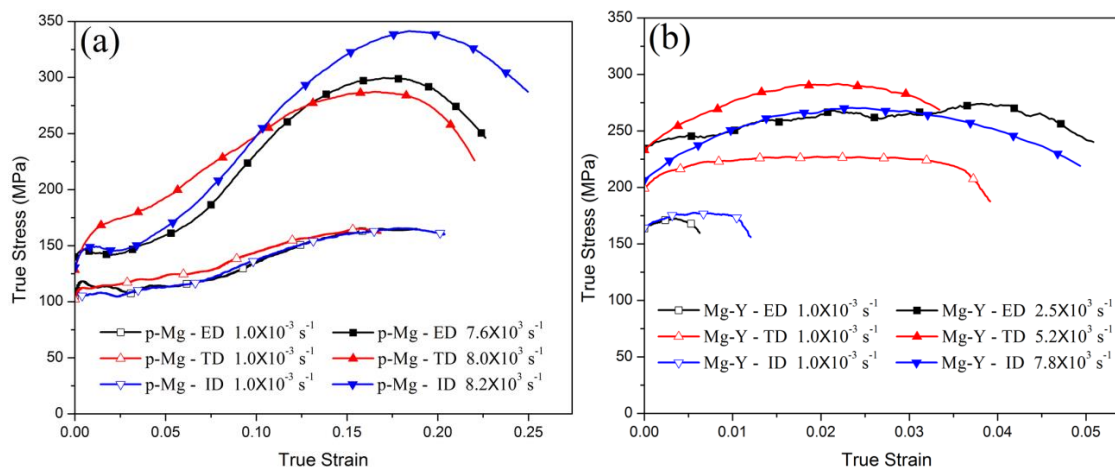


Figure 3.5: Compressive true stress-strain curves of as-ECAPed (a) p-Mg and (b) Mg-Y alloy at the plastic deformation region are presented. The results from extrusion direction (ED), transverse direction (TD) and insert direction (ID), as well as at quasi-static and dynamic loading rates are included.

hardening effect at dynamic loading rates is much stronger than that at quasi-static loading rates, which means the strengthening factor(s) are sensitive to strain-rates. In fact, similar behavior was observed in previous study of two other Mg alloys, AZXE7111 and AMX602, by the authors [190], as well as in some other Mg alloys by other investigators [39, 42, 43]. The activation of deformation twinning has constantly been reported to account for the increased strain hardening rate, although twins were hardly observed by direct viewing in ultrafine grained Mg samples after loading [39]. However, there are some positive observations of deformation twins in pure Mg and Mg alloys after compression, where the grains ranged from a few microns to hundreds of microns [42, 43, 82]. In contrast to p-Mg, the compressive true stress-strain curves of Mg-Y, shown in Figure 3.5(b), display a considerably low strain hardening rate, even if it has a slightly increased strain hardening rate under dynamic loading. It is also noted that the compressive plasticity of Mg-Y is significantly reduced in comparison with that of p-Mg

produced by the same route, even though the yield stress of Mg-Y is improved at those loading rates. The compressive strain-to-failure of Mg-Y is comparable to the compressive strain of p-Mg prior to the turning point that the strain hardening starts to take over the deformation. The reason for this will be further discussed in the future. Furthermore, owing to the low compressive plasticity and the little strain hardening capacity, the ultimate strength of Mg-Y is slightly lower than that of p-Mg.

3.2.2 Activation Volume and Strain Rate Sensitivity

Figure 3.6 show the representative multi-relaxation profiles of as-ECAPed (a) p-Mg and (b) Mg-Y alloy. The stress peak for each relaxation was pre-determined by referring to the compressive true stress-strain curves obtained at a quasi-static loading rate. The corresponding apparent activation volumes, V_r , can be calculated from each relaxation in terms of the following equation [191]:

$$V_r = kT \frac{\partial \ln(-\dot{\tau})}{\partial \tau}, \quad (3.1)$$

where k is the Boltzmann constant, T the absolute temperature, τ the shear stress and $\dot{\tau}$ the time derivative of the shear stress. A Taylor factor of 3.0 is used to convert the applied normal stress to the corresponding shear stress. Plots of $\ln(-\dot{\tau})$ as a function of $\Delta\tau$ are made for the first two relaxations of both samples. A fairly linear dependence of $\ln(-\dot{\tau})$ as the function of $\Delta\tau$ is found for each relaxation, shown in Figure 3.7. The slope for each plot, V_r/kT , was measured and presented in the figures accordingly. In agreement with the case referred in Ref. [191], the V_r/kT values are quite stable in two successive relaxations of one specimen. As a result, the first value of V_r/kT will be adopted for later calculation, i.e. 0.417 (MPa)^{-1} and 0.592 (MPa)^{-1} for p-Mg and Mg-Y alloy, respectively.

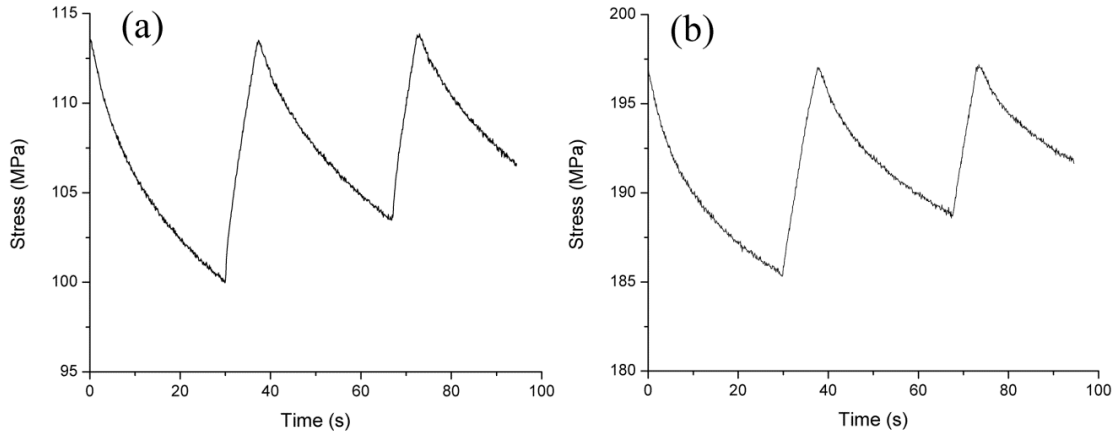


Figure 3.6: The representative profiles of multi-relaxation for as-ECAPed (a) p-Mg and (b) Mg-Y alloy.

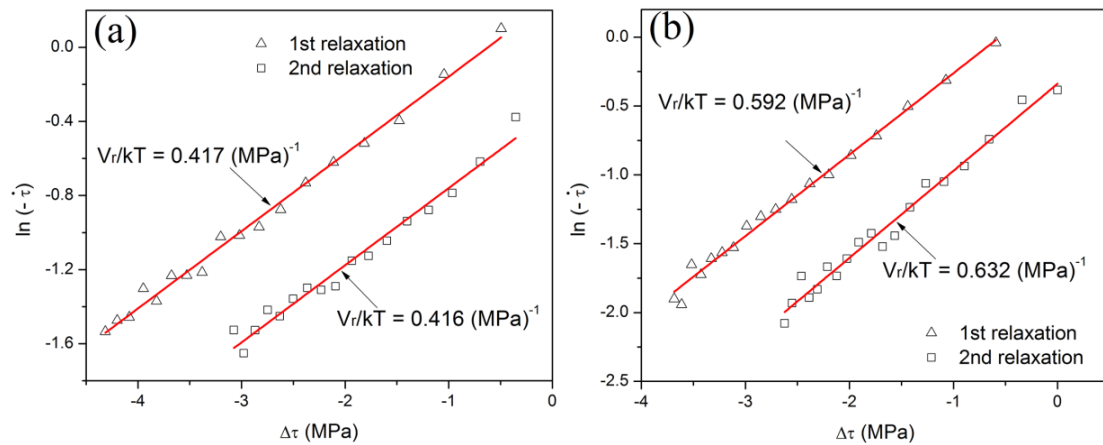


Figure 3.7: The linear dependence of $\ln(-\dot{\tau})$ as the function of $\Delta\tau$ for (a) p-Mg and (b) Mg-Y alloy at two successive relaxations. Straight lines are obtained for each plot, the slopes of which were measured and presented according to each plot. As can be seen, two relaxation of one sample provide almost the same value of V_r/kT .

With those values, the V_r can then be calculated for both samples as the Boltzmann constant and the temperature are known parameters.

The physical activation volume, V^* , is linearly proportional to the apparent activation volume by a factor of $1/\Omega_r$ [191]:

$$V^* = \frac{V_r}{\Omega_r}. \quad (3.2)$$

The factor Ω_r can be calculated by the following equation:

$$\Omega_r^{-1} = 1 - \left(\frac{kT}{V_r \sum_1^{n-1} \Delta\tau_j} \right) \ln \left(\frac{\exp\left(-\frac{V_r \Delta\tau_n}{kT}\right) - 1}{\exp\left(-\frac{V_r \Delta\tau_1}{kT}\right) - 1} \right). \quad (3.3)$$

In this equation, $\Delta\tau_j$ denotes a stress decrease after the j^{th} relaxation. The physical activation volumes V^* of the as-ECAPed p-Mg and Mg-Y alloy are estimated to be $33b^3$ and $48b^3$. It is very interesting to notice that the physical activation volumes of these two samples are nearly the same, in spite of the one order of magnitude difference of their grain sizes. On the other hand, as the normal yield stresses for p-Mg and Mg-Y are known to be ~ 110 MPa and ~ 200 MPa under quasi-static loading, we can estimate the value of SRS, m , for those samples using the Eq.(3.4) [192]. The estimated m values of p-Mg and Mg-Y are 0.058 and 0.023.

$$m = \frac{\sqrt{3}kT}{\sigma \cdot V^*} \quad (3.4)$$

Nano-indentation strain rate jump tests have also been performed to measure the SRS values of these samples. The representative nano-hardness vs. strain rate plots of p-Mg and Mg-Y are presented in a logarithmic scale, shown in Figure 3.8.

It is worth mentioning that nano-hardness vs. strain rate plots obtained from one sample are fairly close to each other. The SRS value, m , can also be expressed by the power-law rate dependence of the flow or yield stress [192], such as

$$m = \frac{\partial \ln H}{\partial \ln \dot{\epsilon}} = \frac{\Delta \ln H}{\Delta \ln \dot{\epsilon}} = \frac{\ln H_2 - \ln H_1}{\ln \dot{\epsilon}_2 - \ln \dot{\epsilon}_1}, \quad (3.5)$$

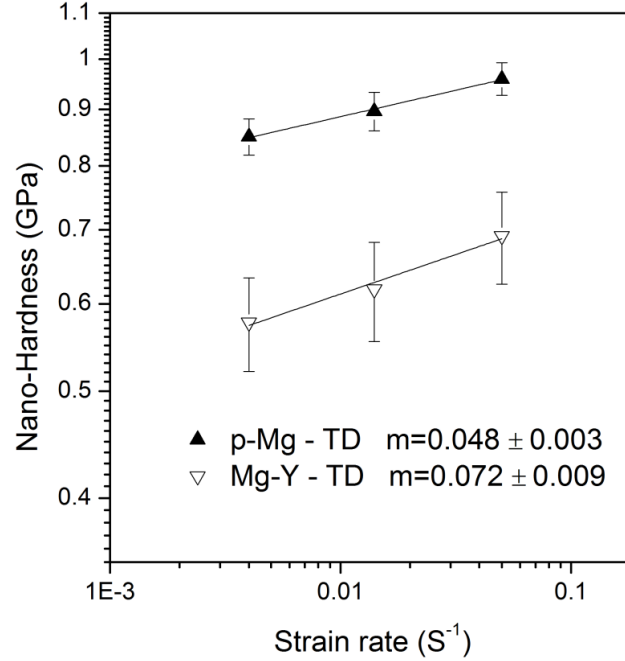


Figure 3.8: A representative nano-hardness vs. strain rate plots of p-Mg and Mg-Y in a logarithmic scale.

where H is the hardness, and $\dot{\epsilon}$ is the indentation strain rate. According to Guo et al. [193], the indentation strain rate can be expressed as

$$\dot{\epsilon} = \frac{\dot{h}}{h} = \frac{1}{2} \left(\frac{\dot{P}}{P} - \frac{\dot{H}}{H} \right), \quad (3.6)$$

where \dot{h} is the speed of the indenter tip, P the load and \dot{P} the loading rate, and \dot{H} is the rate of change of the hardness. Therefore, by measuring the slopes of the plots, the SRS values are approximately 0.048 and 0.072 for p-Mg and Mg-Y, respectively. Those values are reasonably close to those measured by the stress relaxation test. However, while the relationship of the nano-hardness to the yield stress of Mg-Y is consistent with the classical Tabor relation, the nano-hardness of p-Mg is much higher than that estimated by using the Tabor relation. In fact, the nano-hardness values of p-Mg are even higher than that of Mg-Y, which is contradictory to the uniaxial compression results.

More detailed discussions on the discrepancy will be provided in a later section, where the comparable physical activation volumes of p-Mg and Mg-Y will be elaborated as well.

3.2.3 Post-loading Examination

For the further investigation of the fracture process of the as-ECAPed Mg-Y alloy under compressive loading, the broken pieces of every loaded Mg-Y sample were collected. We have performed extensive SEM analysis of those partially recovered samples of three directions and of both loading rates. It was noticed that all of the samples were fractured along a main crack with many small branch cracks around it. Figure 3.9 shows a profile of the cracks growing in the fractured specimen after (a) quasi-static and (b) dynamic loading.

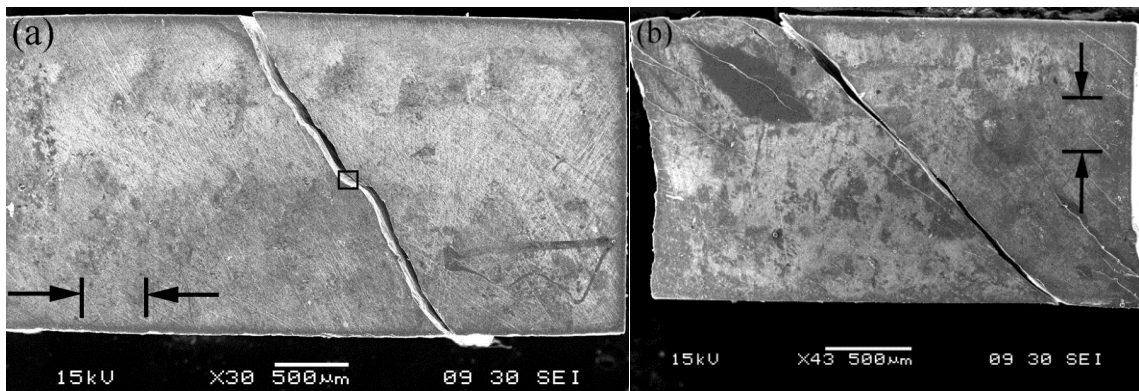


Figure 3.9: The SEM images of (a) quasi-statically and (b) dynamically compressed Mg-Y specimens along ED direction. The arrows indicate the direction of the compression load. One major crack with near 45° to the loading direction can be viewed from both samples. Enlarged images (not shown here) also show small cracks in the similar direction, which are very noticeable in figure (b).

It is noticeable that both of the specimens fractured following a main crack nearly at 45° to the loading direction. Yet, in addition to this crack, a number of small cracks in the

same direction are also observable by magnifying the side-face. A few branch cracks are even visible at low magnification, as shown in Figure 3.9(b). A magnified view of the black square marked in Figure 3.9(a) provides an appearance of the crack surface, which is shown in Figure 3.10(a) where two arrays of twisted micro-cracks are marked with arrows. This can indicate a localized deformation as well as void formation.

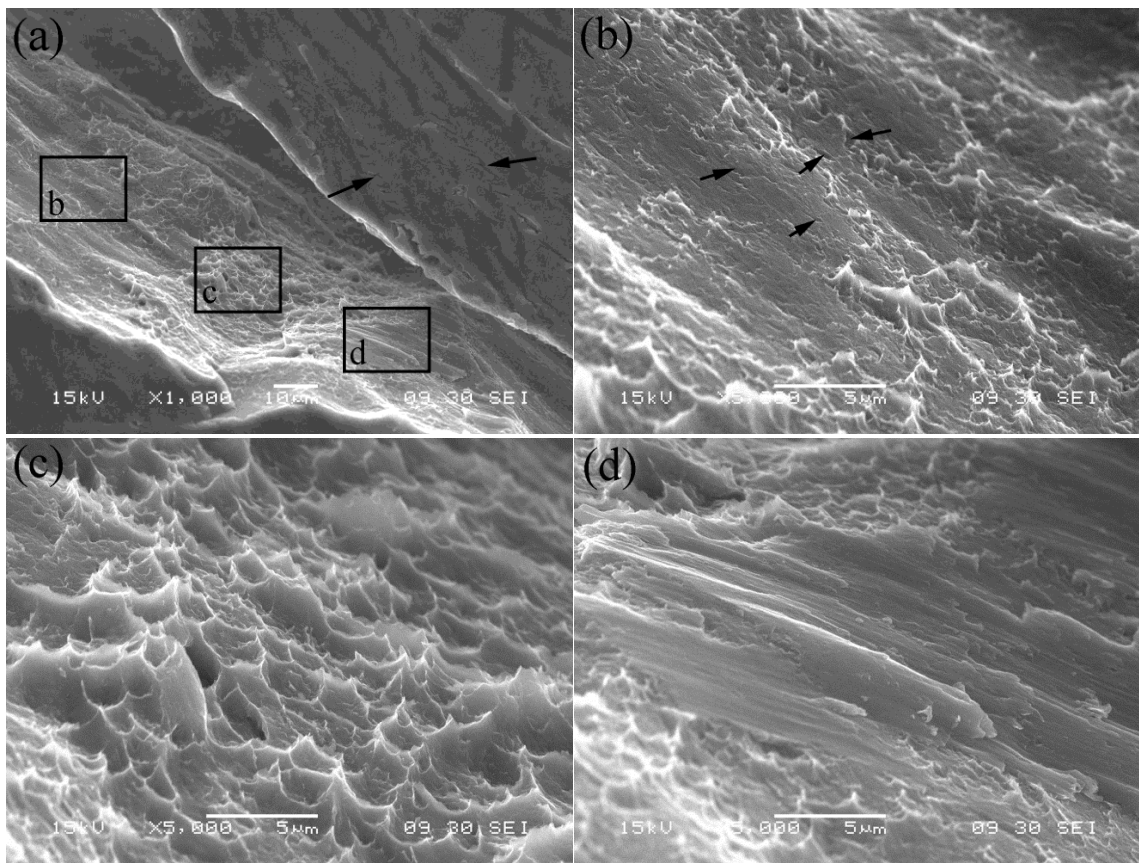


Figure 3.10: (a) An enlarged view of the black square in Figure 11(a), a view of the fracture surface. Three locations of the fracture surface were magnified, shown in (b), (c) and (d). Besides the rest burrs from dimples, numerous micro-voids are also visible in figure (b). Figure (c) displays a great amount of dimples and ridges that were left during ductile fracture. The dimple size is measured to be approximately 2- μm . Figure (d) shows a smooth feature that was probably left after the ductile fracture by one part slips on the other.

In addition, three different locations in the region, labeled as (b), (c) and (d), are scanned in an even higher magnification. A lot of micro-voids are observed in the figure (b), where several of them are marked by arrows. Figure (c) displays a typical ductile fracture surface that contains dimples and ridges, while figure (d) displays smooth and flow-line morphologies that can indicate a later scraping between the fracture faces. Moreover, the smooth face and small white residues left behind the scratch may imply a high temperature rise in the region. The dimension of the dimples is measured to be approximately 2- μm .

Figure 3.11(a) and (b) provide a low and high magnification of the fracture surface of Mg-Y alloy compressed at a high strain rate, where figure (b) is from the marked area in figure (a). The smooth surface and flow-lines are visible in both figures. The inset that shows a lot of dimples is pictured from the marked region in figure (b).

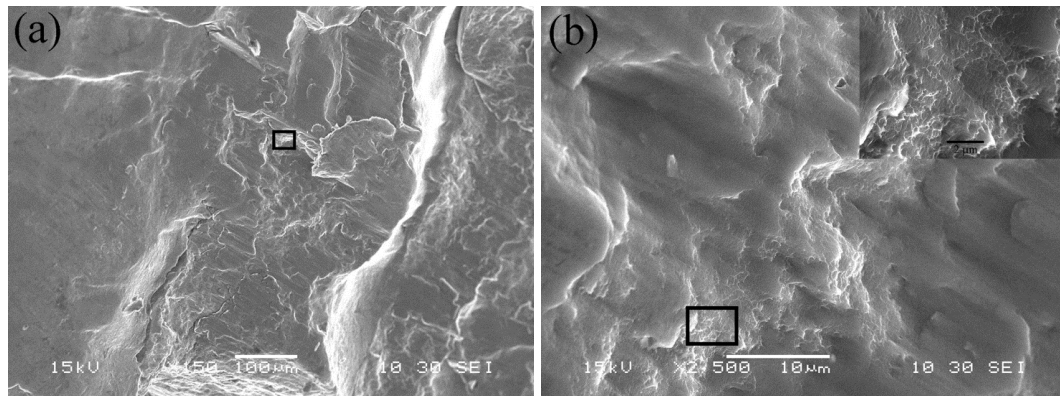


Figure 3.11: A small area of the fracture surface in Mg-Y showing multiple shallow dimples. The sample was compressed dynamically along ED direction.

It is noticed that the dimples in the dynamic specimen are much smaller than that in the quasi-static specimen. It has been well-known that dimples are a sign of the void

formation and ductile fracture. Therefore, a smaller size of the dimples in the dynamic specimen can mean a smaller size of the micro-voids than that in the quasi-static specimen.

3.3 Discussion

Rare earths such as cerium (Ce) and lanthanum (La) have been proved effective in improving the fluidity and ductility of Mg alloys by reorienting grains and softening textures [28, 53, 77]. In Sandlöbes et al.'s work [75], the alloying Y was held responsible for providing extra deformation modes such as non-basal slips and twinning in Mg-Y alloys. In contrast, the compressive true stress-strain curves of as-ECAPed Mg-Y shown in Figure 3.5 show a significantly decreased compressive strain-to-failure compared to as-ECAPed pure Mg. A general explanation for the low ductility may be derived from the von Mises criterion, which concludes that the inability to accommodate the strain incompatibility is due to a shortage of independent deformation mechanisms. In this case, there seems to be a contradiction in the reasoning for the low ductility in this study. On the one hand, a shortage of independent deformation modes may explain the reduced strain; on the other hand, the alloying element Y should be positive for ductility improvement in Mg alloys. Yet, this conclusion is not necessarily true. The XRD result for Mg-Y shows a large internal stress in the ECAPed Mg-Y. This residual stress could be a reason for the low ductility. At sites of severely distorted and of large accumulated strains, the nucleation and growth of voids can more easily occur than that at internal stress free sites. This is because the distorted grains and/or grain boundaries apparently have more difficulty in accommodating any further deformation.

The Mg-Y alloy has a Y concentration of ~0.6 wt.% (or 0.16 at.); based on an

rough estimate of the average distance L of two nearest Y atoms is around $15b$, where $b = 0.3196$ nm is the Burgers vector of a basal dislocation. In addition, since the Y-atom is much larger than the Mg-atom, it can be treated as a strong obstacle to dislocation motion in the Mg matrix. For an ideal condition, the shear stress required to overcome strong obstacles can be approximated as follows [194].

$$\tau_{\max} = \frac{Gb}{L}. \quad (3.7)$$

G is the shear modulus of the matrix. Besides, the interaction force per unit length between two dislocations can also be estimated [194].

$$F_x = \frac{Gb^2}{2\pi(1-\nu)} \frac{x(x^2 - y^2)}{(x^2 + y^2)^2}, \quad (3.8)$$

$$F_y = \frac{Gb^2}{2\pi(1-\nu)} \frac{y(3x^2 + y^2)}{(x^2 + y^2)^2}, \quad (3.9)$$

where x and y denote the distance between two dislocations along x - and y -directions and ν is the Poisson's ratio. By considering the dislocations gliding on the same plane, i.e., $y = 0$, the largest number of dislocations allowed to pile-up in front of the obstacles can be evaluated (using values of $G = 17$ GPa and $\nu = 0.29$) to be no more than three. Applying this number as well as the grain size of as-ECAPed Mg-Y, a dislocation density in the order of 10^{15} /m² is obtained. In fact, the real value of dislocation density could be higher if considering dislocations in three dimensions as well as that the dislocations may also serve as barriers. Though this estimation is not accurate due to the much more complex nature of a real situation, such as the dynamic recovery under thermal effects, it can still serve as a reference value. This density, according to Fleck et al. [195], is usually produced after more than 1% shear deformation of an annealed polycrystalline metal with

a similar grain size. Yet, owing to the presence of Y atoms, the high density of dislocations is expected to be preserved in the Mg-Y alloy when thermal effects are neglected. Besides, an alignment of three dislocations within the distance of $15b$ has already been pushing the interspace limit between dislocations. As a result, the room for further dislocation multiplication would be restricted. Thus, the strain hardening capability owing to dislocation multiplication could be very limited. Besides, the dislocation slip mechanism has been discovered to be dominant in Mg alloys that have a grain size less than $\sim 2\text{-}\mu\text{m}$ [82], which, therefore, rules out the possible hardening effect from twinning. Thus, the low strain hardening in the Mg-Y alloy is corresponding to the limited dislocation multiplication and lack of twinning. Yet, an increased strain hardening rate has been observed for both p-Mg and Mg-Y, due to an increasing loading rate. This mechanism, however, is much more effective for p-Mg. To this, the critical grain size for twinning-slip transition was calculated using Barnett et al.'s equation [82], which was estimated to be $\sim 2\text{-}\mu\text{m}$ and $\sim 240\text{-nm}$ under quasi-static and dynamic loading. Barnett et al. [42] also reported twins in the equiaxed recrystallized and $5\text{-}\mu\text{m}$ grain size p-Mg. Then, it is understandable that a higher strain hardening rate was observed in p-Mg than that in the Mg-Y alloy. Besides, twinning has also been experimentally proved sensitive to the loading rate, i.e., a higher volume fraction of twins tends to form at a higher loading rate [39], which agrees with the values of critical grain size for twinning-slip transition at different loading rates. Again, the reduced critical grain size at the high loading rate renders the possibility of twinning occurrence in Mg-Y. That probably is one of the contributions to the increase of the strain hardening rate of Mg-Y at high strain rates.

On the other hand, the activation volume is a representation of the average volume achieved by dislocation motion or atomic diffusion during plastic deformation. Generally, three regions of activation volumes are classified, which are less than $10b^3$, $10 \sim 50b^3$ and larger than $50b^3$. They are associated with (i) GB activities mediated by point defect migration, (ii) partial dislocations emission from one end of a GB and are absorbed at the opposite end and (iii) forest dislocation cutting through each other, respectively [196]. The activation volume of $48b^3$ and $33b^3$ measured in this work could then imply a mechanism of dislocation emission and annihilation occurring in the samples during the plasticity. However, one may think that, the high dislocation density in Mg-Y could result in forest dislocation cutting, which could provide a higher activation volume. Actually, a low activation volume is more reasonable to explain the thermal sensitivity of Mg-Y, due to the high accumulated strain and the low melting point of Mg. For p-Mg samples, as the grains are completely recrystallized during ECAP, a low dislocation density should be expected. As is well-known, dislocation slips are more likely to emit in paralleled (0002) planes for HCP Mg. Thus, it is reasonable to assume that only basal slip operates at the beginning of yielding for a single Mg crystal or grain. Bhattacharya et al. [18] used a single crystal specimen, having a size of $3.0 \times 3.0 \times 35 \text{ mm}^3$, to examine the deformation mechanism of pure Mg where multiple basal-slip lines were observed at the early stage of plasticity. Twins and kink boundaries were only observed when entering into the rapid hardening stage. As the dimension of the single crystal Mg was much larger than the grain size of our p-Mg sample, it is understandable that an activation volume one order larger than ours were measured by Bhattacharya et al. [18], bearing in mind the larger sweeping area of a dislocation could have in the single crystal Mg specimen. The size

effect was also found between macro-compression and nanoindentation tests, whereas an unusually large hardness value of p-Mg was measured by nanoindentation comparing with the one by uniaxial compression results. To elucidate this phenomenon, the procedure of nanoindentation test must be revisited. The effective nanoindentation data were obtained from an indentation depth of 800-nm up to a total of 2- μm . This should be enough to include the GB activities for Mg-Y as its grain size was only about 400 nm. Yet, the grain size of p-Mg is around 4.5 μm , which is more than twice large as the depth of indentation. It may then result in a scenario where the indenter was only penetrating a single grain, where the GB activities were trivial. In that case, the extra independent deformation systems such as twinning or non-basal slips must participate to accommodate the plasticity around the indenter as it proceeds to deform the grain.

Another interesting issue is the fracture behavior of the as-ECAPed Mg-Y alloy. The smaller dimension of dimples and the lower ridges indicate that a larger number of voids were produced in the dynamic Mg-Y sample than that in the quasi-static sample.

3.4 Summary

We have investigated the microstructure, mechanical properties and the fracture mode of pure Mg and Mg-Y alloy after 4-pass ECAP via route Bc. The role of the element Y on the performance of Mg was found to be not consistently positive, *esp.* for ductility. Despite the unidentified mechanism as to how the deformation modes are changing in Mg by adding rare earths to improve the ductility, our investigation revealed some useful facts:

- (i) Even though the answer to the question whether the element Y assisted in reorienting the grains was still unknown, the element indeed serves as an

effective dislocation barrier. As a result, the Mg-Y alloy exhibits unrecrystallized and distorted grain microstructure compared to p-Mg with a completely recrystallized microstructure after the ECAP process.

- (ii) Not like widely reported improved ductility in annealed Mg-Y alloys, the as-ECAPed Mg-Y alloy displays poor ductility due to the presence of residual microstress. The fracture surface of both quasi-static and dynamic Mg-Y samples shows multiple micro-sized dimples, indicating void formation and ductile fracture at least at local levels. Direct evidence based on tensile testing should be identified in this context.
- (iii) Regardless of the difference of grain structure, both p-Mg and Mg-Y have an activation volume indicating the dislocation emission and/or annihilation mechanism. The results were confirmed by both stress relaxation and nanoindentation tests.

CHAPTER 4: MAGNESIUM ALLOYS WITH IN-SITU FORMED PARTICLES

In this chapter, the research work on two Mg alloys with in-situ formed particles will be presented and discussed. In the loose definition, those alloys may also be recognized as composites since they are composed of a matrix phase and particulates of one or more phases. Those alloys were produced elsewhere, as stated in Chapter 2, for the purpose of armor applications, and were named AZXE7111 and AMX602 according to their chemical compositions. The research objective of this work focuses on two aspects: one is to study the role of in-situ formed particulates on the mechanical properties of the materials comparing to the role of ex-situ formed particles which constitutes the work in presented in Chapter 5; the other is to investigate the dynamic mechanical behavior and deformation mechanisms of those alloys as those alloys are intended for ballistic applications, which requires the knowledge of high-strain rate properties. The scientists who made the alloys have already deliberated and published the results of the constituents, microstructure and tensile properties of the alloys elsewhere [29, 76, 77]. As such, the only materials characterization that will be repeated here is for the purpose of the completeness of this dissertation. As the alloy AZXE7111 was designed and produced with the intent of, besides improving the mediocre ballistic performance of Mg alloys, studying the effect of rare earths on the property improvement of Mg alloys, an independent section will be assigned for the alloy. Thus, there will be four sections in this chapter. First, AMX602, which will closely focus on the effect of the materials

processing on its microstructure, mechanical properties and deformation mechanisms; second, AZXE7111, where the mechanical behavior of the La-doped Mg alloy at different strain rates will be demonstrated; third, a comprehensive discussion about the shear banding failure that appears in both alloys will be presented; then in the last section, there will be a summary of the work and the conclusions based on the experimental results and discussion.

4.1 AMX602

In this section, one strength-improved Mg alloy AMX602 with moderate ductility produced for the purpose of ballistic structural applications was investigated by uniaxial compressive quasi-static and dynamic loading and by nano-indentation strain rate jump test. The chemical composition of AMX602 is Mg-6%Al-0.5%Mn-2%Ca, all values in weight percents. The mechanical properties, deformation mechanisms and fracture modes were then presented. The microstructure of the pre-testing and post-mortem specimens has also been examined by scanning electron microscopy (SEM) and transmission electron microscopy (TEM) in order to explore the fundamental deformation mechanisms that took place at different strain rates in the alloy.

4.1.1 Microstructure of Extruded AMX602

Figure 4.1(a) and (b) show a bright field TEM image of AMX602 extruded at 250 °C and the corresponding selected area diffraction pattern (SADP). Indexing of the SADP reveals that the un-continuous diffraction rings are from Mg-based matrix, whereas the very first three inner diffraction rings correspond to $\{10\bar{1}0\}$, $\{0002\}$ and $\{10\bar{1}1\}$ planes, respectively. A quantitative measure of the particle marked with the dark square, by EDX analysis, revealed that it contains only Al and Ca with the atomic ratio of

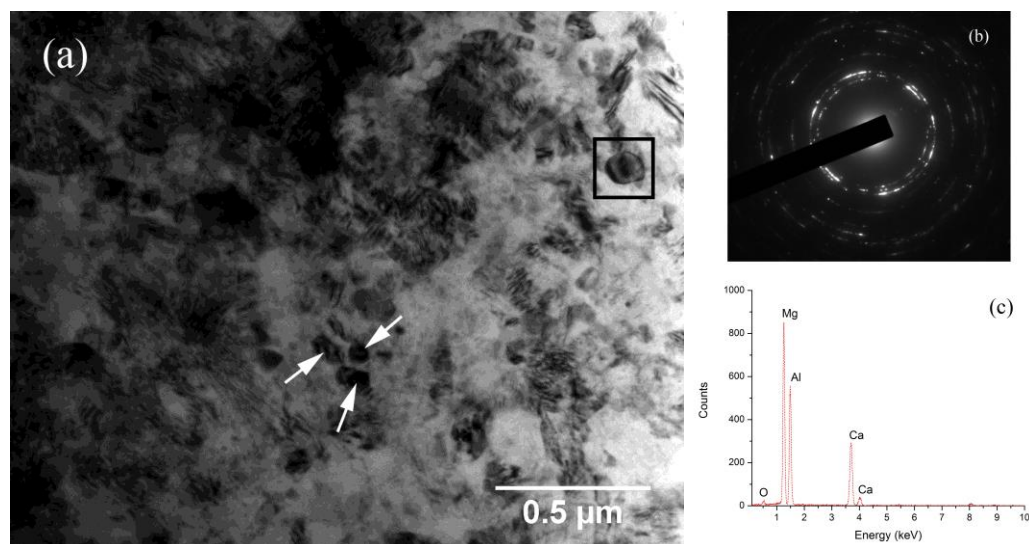


Figure 4.1: (a) Bright field image of AMX602 extruded at 250°C; (b) The corresponding selected area diffraction pattern of the sample; (c) EDX results of the selected square area in (a).

~2 (as shown in Figure 4.1(c)), besides the matrix element Mg. This result is consistent with that of the examination of white spots in Figure 4.2 by EDS attached to SEM and also follows the result found by Kondoh et al. [76] earlier by XRD in the same alloy, which concluded that these white spots were the intermetallic compound, Al_2Ca . The SEM images presented in Figure 4.2 clearly show that the scale of the compounds can range from less than 100-nm to ~1- μm , even though the TEM image only shows the compounds with the size of about 100-nm or less. It might be the small area of the sample involved in the TEM imaging. Such small particles could effectively impede the grain growth of the Mg-based matrix by Zener pinning effect, which was well proven here by the small grain size of no more than 1- μm and their uniform distribution throughout the specimen. Clustering of the compound was also found and the size of the agglomerates was measured up to 5- μm , as indicated by the arrows in Figure 4.2. Yet, the number of large agglomerates is relatively low. Larger agglomerates were more likely to form at

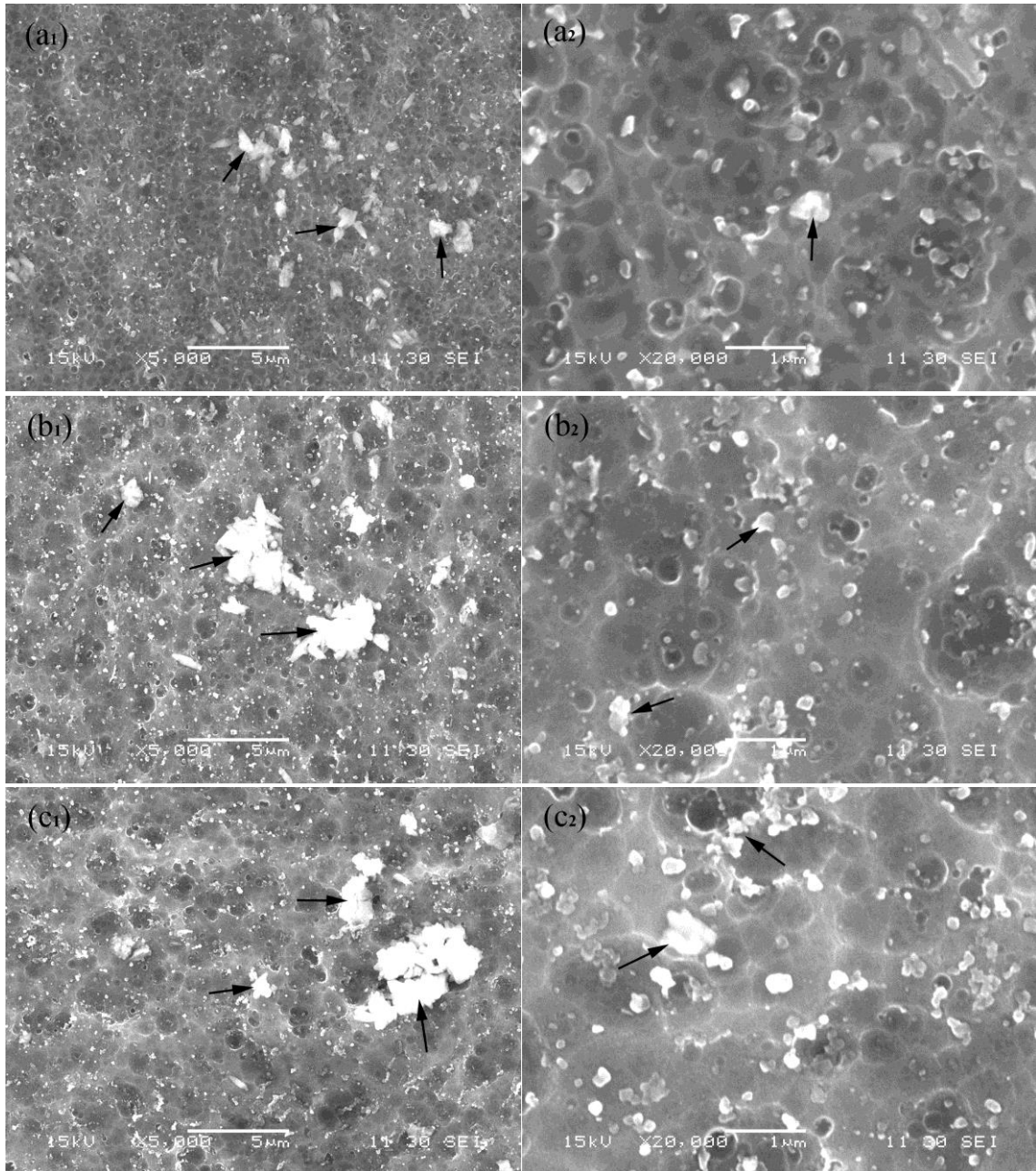


Figure 4.2: Scanning electron microscope observation of AMX602 extruded at various temperatures: a. 250 °C; b. 300 °C; c. 350 °C with two magnifications. Apparently, the size of matrix grains, as well as the white particles, is larger for samples from a higher extrusion temperature. Clustering of the particles up to $\sim 5\text{-}\mu\text{m}$ can be viewed.

higher temperatures during hot extrusion process. In addition, the intermetallic compound was found to be uniformly distributed throughout the whole specimen, and the particle size was found to increase with the extrusion temperature by a qualitative review of the

low and high magnification SEM images in Figure 4.2. This may serve as evidence that the compounds formed and grew during the hot extrusion process. On the other hand, the matrix grains grew faster as the extrusion temperature increases. Nevertheless, the matrix gains are no larger than 1- μm even at an extrusion temperature of 350 $^{\circ}\text{C}$.

4.1.2 Mechanical Properties of AMX602

Figure 4.3 shows the representative compressive true stress-strain curves of AMX602 for each condition. It is worth mentioning that the true stress-strain curves are from three independent tests of each sample under each condition and the results are highly reproducible. All the curves show three distinguishable stages of plastic deformation, irrespective of extrusion temperature and specimen orientation. The three stages include easy plastic flow after yielding, strong strain hardening and reduced hardening-rate prior to failure. Such behavior is reminiscent of that of single crystalline Mg oriented for basal slip, as studied by Bhattacharya et al. [18], where the easy-glide stage was attributed to the basal slip while the rapid hardening stage was attributed to the increased dislocation interactions between basal and non-basal dislocations and/or as a result of twinning.

Table 4.1 shows a list of offset yield and ultimate strengths of AMX602 for different extrusion temperatures and at different loading rates. The offset yield strength represents the true stress at a strain of 0.2% and 5% for quasi-static and dynamic loading, respectively. For short, both of them will be called offset strength thereafter, but they cannot be compared with each other because the offset strength was obtained at different strain levels for each loading rate. The value of the strengths showed in the table is an average of the results from three independent tests of each specimen with the same

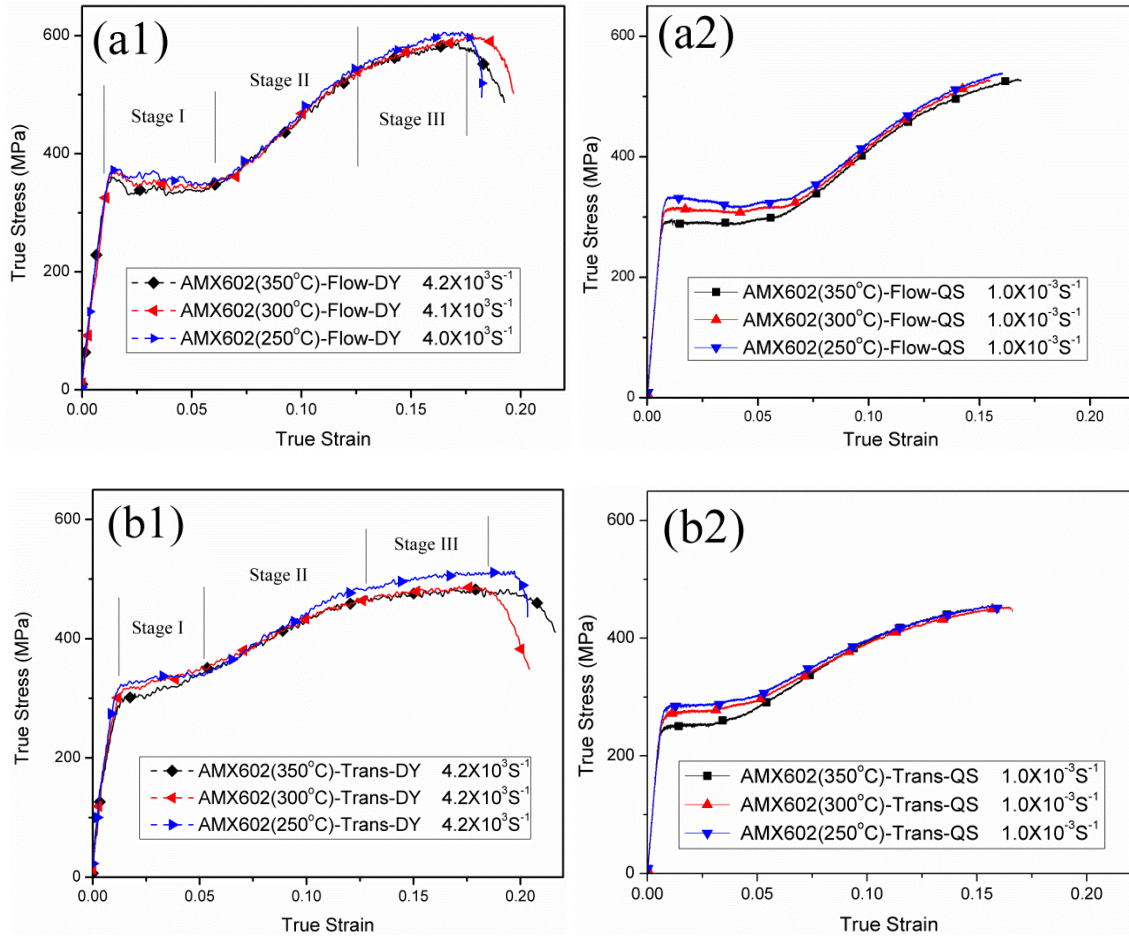


Figure 4.3: Compressive true stress-strain curves of AMX602 in the flow direction (a) and in the transverse direction (b) under both quasi-static and dynamic loading with various extrusion temperatures.

Table 4.1: List of the offset yield and ultimate strengths of AMX602 under compressive loading

Extrusion Temp.	Flow Direction				Transverse Direction			
	Yield Strength (MPa)		Ultimate Strength (MPa)		Yield Strength (MPa)		Ultimate Strength (MPa)	
	Quasi-static	Dynamic $\sigma_{5\%}$	Quasi-static	Dynamic	Quasi-static	Dynamic $\sigma_{5\%}$	Quasi-static	Dynamic
350 °C	283 ±18	348 ±2	510 ±20	585 ±5	242 ±7	361 ±20	441 ±7	489 ±12
300 °C	291 ±29	354 ±2	504 ±41	588 ±7	265 ±1	368 ±13	445 ±18	484 ±2
250 °C	318 ±10	355 ±0	517 ±22	604 ±5	275 ±0	362 ±3	453 ±21	513 ±21

condition. The errors are also given in the table following the average value. It seems that both the offset strength and ultimate strength decrease slightly with increased extrusion temperature. This agrees with our expectation by considering Hall-Petch effect that the matrix grains are larger for the alloy extruded at a higher temperature. The strength difference between the flow direction and transverse direction was measured quantitatively. It indicates that the strengths in the flow direction are $16.9 \pm 3.5\%$ greater than those in the transverse direction under all extrusion conditions independent of loading rates; except for the dynamic 5%-offset strengths, which is $\sim 4\%$ smaller in the flow direction than those in the transverse direction for all extrusion conditions. Moreover, the compressive failure strain of AMX602 is around 15% and 20% under quasi-static and dynamic loading, respectively, for the same condition.

In addition, the nano-indentation test shows an elastic modulus close to 48GPa for all AMX602 samples. The plots of the nano-hardness vs. strain rate of AMX602 extruded at different temperatures are illustrated in Figure 4.4. The strain rate sensitivity value, m , was estimated to be 0.015~0.018 for the various extrusion temperatures. It is noticed that the nano-hardness of AMX602 was consistent with the compression results in terms of that the classical Tabor relation. The nano-hardness of AMX602 also decreases with extrusion temperature.

4.1.3 Post-loading Examination of AMX602

The fragments of failed specimens were collected after each test for further investigation of the failure mode of the alloy. All of the specimens broke into two pieces under quasi-static loading, while the dynamic counterparts broke likely into more pieces with varied sizes. The typical partially recovered specimens from quasi-static and

dynamic loading are shown in Figure 4.5(a) and (b), respectively. It is worth mentioning that all of the quasi-statically loaded samples fragmented in the same pattern as that shown in Figure 4.5(a). All of the dynamically fractured samples show two nearly symmetric cracks similar to that shown in Figure 4.5(b) except one unique sample that successfully survived the loading without fragmentation as shown in Figure 4.6(a), which shows only one of the two symmetric cracks.

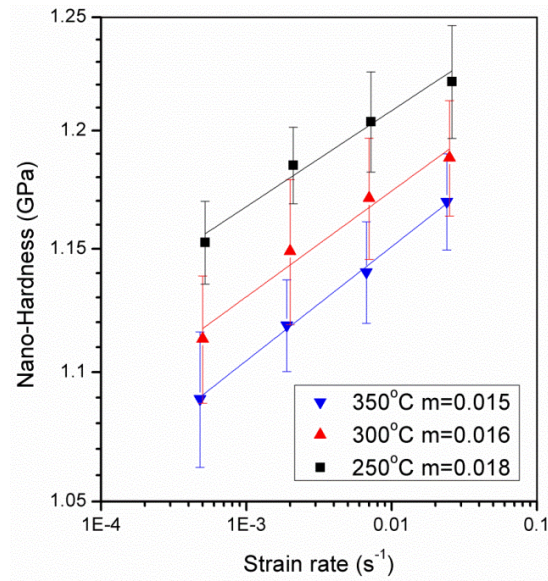


Figure 4.4: The nano-hardness vs. strain rate of AMX602 with different extrusion temperatures.

Through careful examination of the crack in Figure 4.6(a), one can observe that it is more like a result from adiabatic shear band (ASB), with a width of around 10 μm , rather than a brittle crack as shown in Figure 4.6(b). More discussion will be provided in the following section that upholds the suggestion of ASB. The high magnification SEM images of Figure 4.6(b) ~ (d) correspond to the labeled area b, c and d in Figure 4.6(a). It

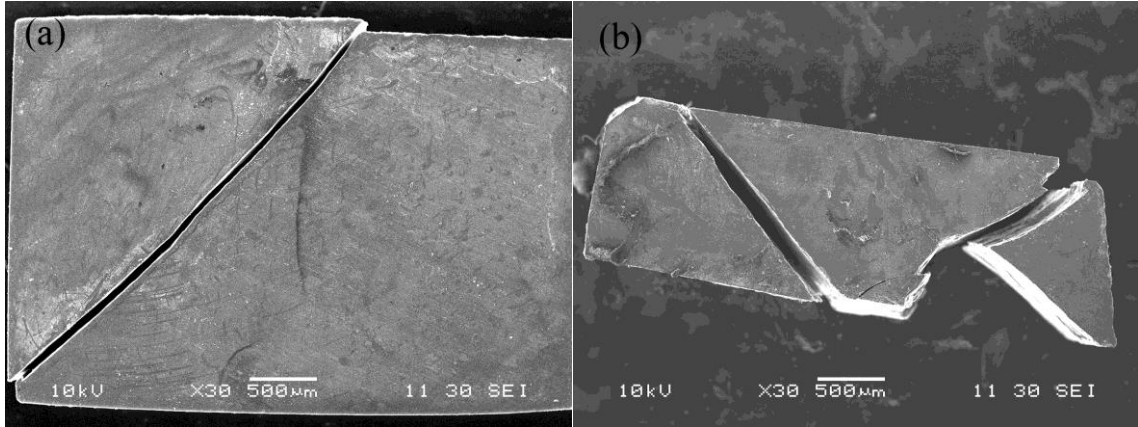


Figure 4.5: The representative fractured specimens of AMX602 partially restored from fragments after (a) quasi-static and (b) dynamic testing.

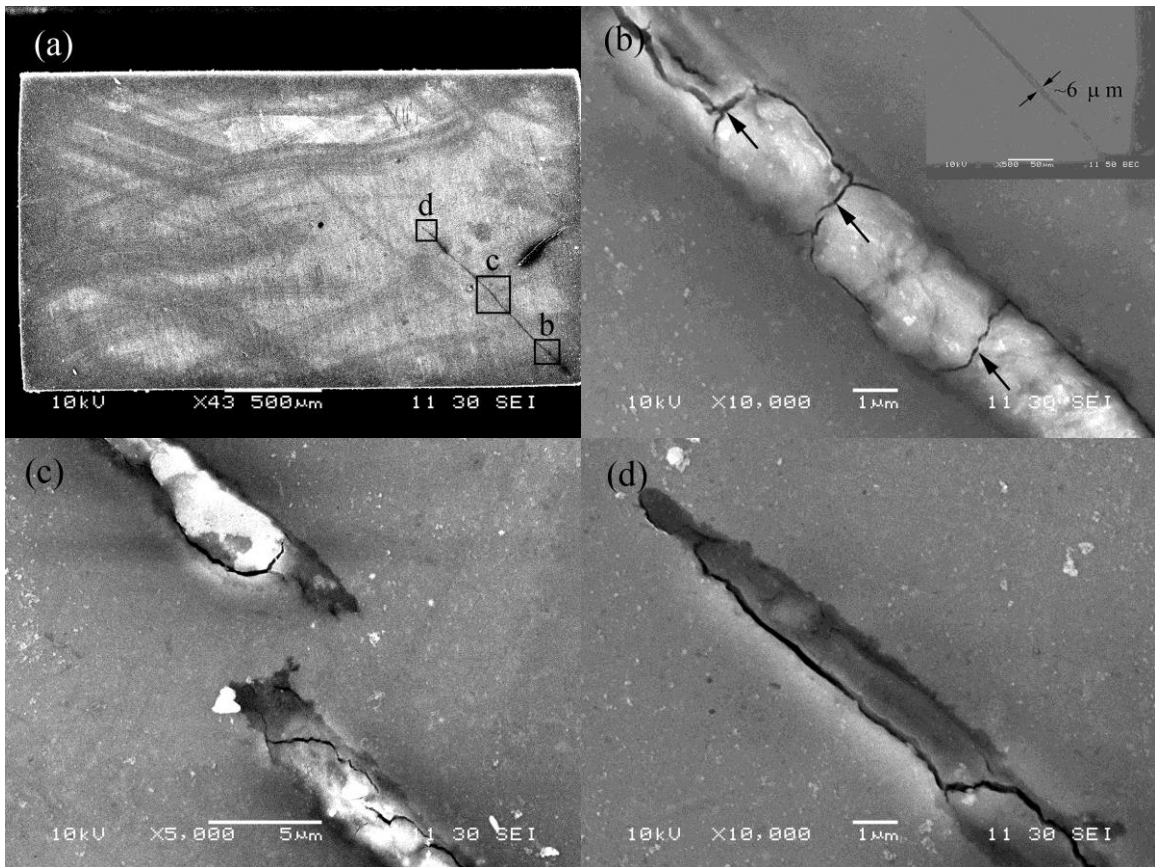


Figure 4.6: (a) Low-magnification of the incomplete adiabatic shear band of AMX602 under dynamic testing; (b) ~ (d) high-magnification of the corresponding areas that marked by black squares in (a).

shows that the ABS is narrower as it goes into the interior of the specimen. Arrest of the ASB can be observed as shown in Figure 4.6 (c). Micro-cracks can be found to be either continuous or dis-continuous in the ASB that are more favorable at the interfaces between the shear band and the matrix. Nevertheless, even smaller cracks can be observed from the fracture surface of specimens that have been fragmented, as indicated by black arrows in Figure 4.7(a).

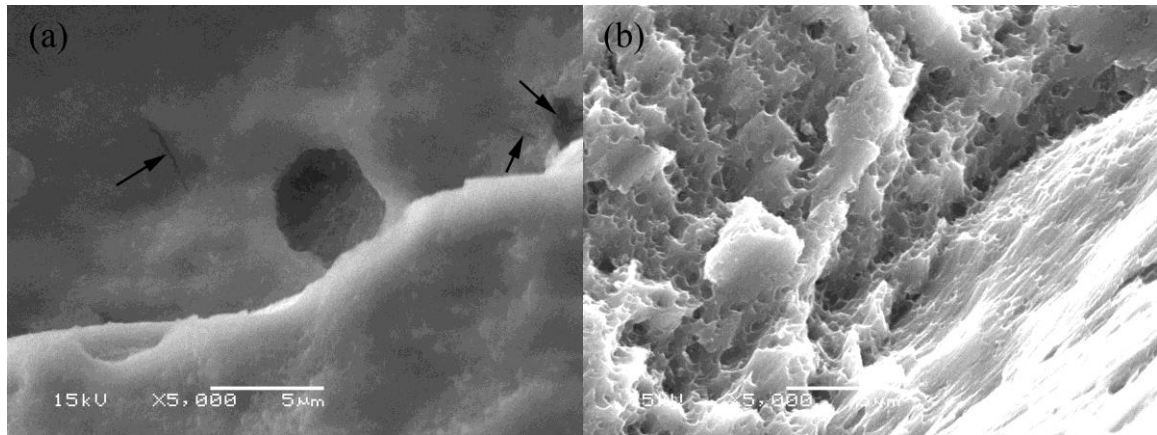


Figure 4.7: The representative SEM images of the fracture surface of AMX602 after (a) dynamic and (b) quasi-static loading.

The appearance of these micro-cracks will be further discussed in the discussion part and a conclusion will be provided. It is worth mentioning that the fracture surfaces of AMX602 obtained at the same loading rate have nearly the same features. Figure 4.7 shows a couple of representative fracture features from (a) dynamically and (b) quasi-statically loaded samples, respectively. The significant difference of the fracture surface in Figure 4.7 indicates distinct failure modes of AMX602 at various loading rates. The fractographic view of the dynamically fractured specimen suggests that a melting and

quenching process took place in the area, while the quasi-static specimens show typical ductile fracture surfaces with dimples. The dimples are found in all the quasi-static samples that have been examined, and also the smooth fracture surface was found in all of the dynamic samples. On the other hand, no micro-cracks of intermetallic compounds were found among all of the post-loading specimens by SEM observations, which is reasonable that the intermetallic compounds were on the sub-micro-meters length scale. This is in agreement with Ayman et al. [29] who believed that the sub-micro-compounds are responsible for the remarkable strength and ductility of AMX602.

4.1.4 Discussion of Results of AZX602

It is well known that the plastic deformation of structural materials strongly relies on the loading conditions, such as temperature, strain, and strain rate [197-200]. However, the dependence on the externally imposed loading conditions is a consequence of the internal nature of the material, *esp.* the microstructure. In the following, the microstructure of AMX602 and its effects on the deformation mechanisms, as well as the distinct fracture modes of the alloy at different loading rates will be discussed.

4.1.4.1 Strengthening Mechanism in AMX602

It has been well documented in the literature that grain refinement, known as Hall-Petch effect, is one of the most noteworthy methods to strengthen metals. Due to the nature of the limited ductility of pure Mg, the prevalent severe plastic deformation method, i.e., ECAP, has been shown to have limitations, because it can only refine the grains of Mg alloys down to about a few microns [13, 25, 99]. In the present work, the very high strength of this alloy partially comes from the fine and uniformly distributed grains, which resulted from the combination of two bottom-up processing steps. Firstly,

using a spinning water atomization process, extremely fine powders were produced due to a high rapid solidification rate; secondly, the formation of an intermetallic compound Al_2Ca assisted dynamic recrystallization by promoting the nucleation sites in one way, and by stopping the motion of grain boundaries in the other during hot extrusion. Therefore, fine and uniform grains were obtained by promotion of nuclei and suppression of grain growth as discussed in Ref.[78]. In addition, the grain growth by migrating of grain boundaries is a strongly temperature-dependent process [201], which is to say that the grain boundaries move faster and easier to overcome the barriers at higher temperatures. Hence, the grain size of the alloy from the highest extrusion temperature is the largest as shown in Figure 4.2, which in turn has the lowest strength due to Hall-Petch effect.

On the other hand, the ultrafine particles, in addition to assisting the dynamic recrystallization process, also act as barriers during deformation process of the alloy by stopping the motion of dislocations so that they pile up in front of the compound-matrix interface. This introduces a severe strain incompatibility at the interfaces that generates geometrically necessary dislocations (GNDs) according to strain gradient theory. As a result, both of them provide high strength and work hardening rate [105, 202]. In addition, since the intermetallic phase precipitates through a eutectoid reaction between Al and Ca during high temperature extrusion, the interface between the particle and matrix should have strong bonding. Thus, the bonding force between the matrix and second phase is much stronger than that for example between SiC and the matrix in SiC-reinforced MMCs where the contamination cannot be completely avoided. It then preserves the ductility in this alloy along with the strength improvement [203].

4.1.4.2 The anisotropy of strain hardening

The strain hardening rates, $\Theta = d\sigma / d\varepsilon$, of AMX602 along the two orthogonal orientations and at the different loading rates were evaluated. Figure 4.8(a) and (b) display the representative curves of the hardening rate vs. compressive true strain for the samples loaded along the flow and transverse directions, respectively.

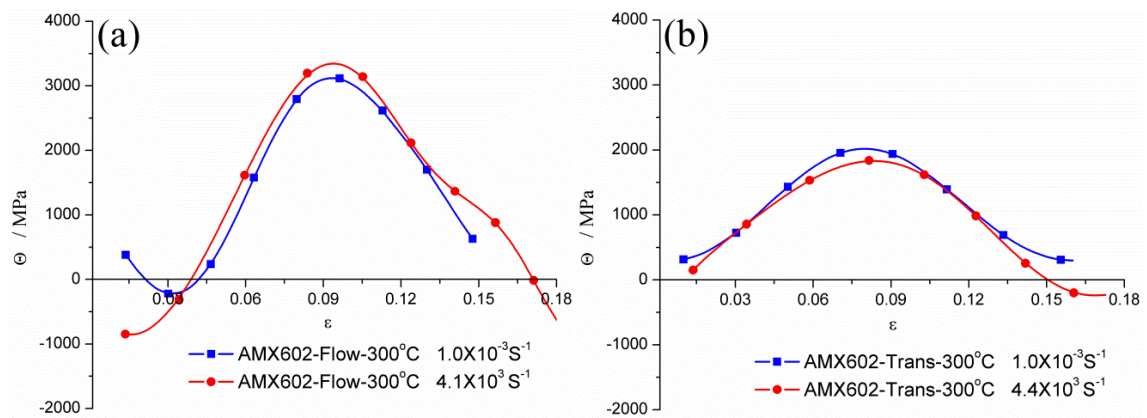


Figure 4.8: The strain hardening rate Θ vs. the strain ε of AMX602 with different loading rates: (a) along flow direction; (b) along transverse direction.

The curves indicate that not only the alloy exhibits different strain hardening rates in the two directions, but also it has different strain hardening rates as a function of strain rate. To be specific, in the plastic region beyond $\sim 3.5\%$, the strain hardening rate constantly displays higher values under dynamic loading than that under quasi-static loading along the flow direction, whereas, it reverses in the transverse loading direction. Since thermal softening effects are to be expected under impact loading that offsets the strain hardening effect [204], a smaller strain hardening rate under dynamic loading than that under quasi-static loading should be more reasonable. However, the strain hardening

rate for the flow direction sample shows a behavior similar to pure Mg as shown in the previous chapter. That is to say, there must be some strain-rate-dependent hardening mechanisms that took place as well in the flow direction specimen. According to the observations from pure Mg, it is reasonable to speculate that this strain-rate hardening was also achieved by excessive formation of twins at extra-high loading rates than that at low loading rates.

There are also several other reasons: (i) twinning has been frequently reported in Mg alloys with the grain size from micro- to nano-regimes [39, 82, 205]; (ii) twinning has a much higher critical resolved shear stress (CRSS) than dislocation slips [82]; (iii) unlike non-basal dislocation slips, twinning shows weak thermal-sensitivity, or even regarded as an athermal process [31, 206-208]; and (iv) experiments have confirmed the increase of the volume fraction of twins with the increase of either the plastic strain or the loading rate [40, 43, 209]. In addition, Li et al. [39] indirectly confirmed this speculation by using XRD measurements, and they also provided the explanation for the reason of minor possibility to detect twins in post-loaded Mg samples with the grain size less than microns directly. Thus, we attribute the anisotropy of strain-hardening rate in Fig. 4.8(a) to the initiation of twinning, although we have also failed in detecting twins in our TEM examinations.

4.1.4.3 Strain Rate Sensitivity

As well documented and discussed in Ref. [210] the steady-state creep rate is strongly temperature-dependent, because a lower external mechanical energy is required to let the dislocations surmount the obstacles at a high temperature. It only requires a lower applied stress to drive processes such as dislocation motion at a high temperature

than at a low temperature. Alternatively, the required applied stress is strongly dependent on the difficulty of dragging around a dislocation (or diffuse an atom) inside a crystal at a constant temperature. In this context, the strain rate sensitivity is then equivalent to the difficulty in increasing the dragging velocity. It is easy to understand that, the energy required to drag around the dislocation/atom in a large free space is less than that in a small free space; it is much less affected by the kinematic velocity of the dislocation/atom as well. This is because extra energy is required in a small free space in order to surmount excessive obstacles. It is the fundamental reason that the applied stress may change at different loading rates for most of metals in order to cause plastic flow. As deliberately derived by Wei et al. [192, 211], the free space or normally called activation volume can be related to the strain rate sensitivity, as illustrated in Eq.(3.4). By using that equation, the activation volume of AMX602 is obtained to be from $\sim 48b^3$ to $\sim 57b^3$ for extrusion temperatures from 250 °C to 350 °C. Those values are very close to our previous results of Mg-Y alloy with grain size of ~ 400 nm. Even though the database may not be large enough, the comparable activation volumes for similarly sized Mg alloys may probably indicate that the activation volume of Mg also has a strong dependence on its grain size as those of FCC and BCC metals [192]. Review of the limited available SRS values of ~ 0.31 and ~ 0.6 respectively for 100-nm and 45-nm grain size pure Mg [212, 213], as well as our results for pure Mg with grain size of ~ 4.5 - μm ($m = \sim 0.058$), it is reasonable to conclude that the SRS of pure Mg could decrease with increasing the grain size. It is also reasonable then to say that if one disregard the transformation of dislocation types, one dislocation was much easier to meet the grain boundaries at small grain sizes due to limited grain space, so that the deformation mechanism may change from dislocation-

dominated to GB-activities-dominated as the grain size reduces down to nano-scale.

4.1.5 Summary

In terms of the mechanical behavior examined in this work for AMX602, the materials processing of melting, quick solidification, compaction and hot extrusion is effective in obtaining equiaxed ultrafine grains in a Mg alloy resulting in significant strength and moderate ductility. The extrusion at high temperatures assists the formation of intermetallic compound (i.e., Al_2Ca) with size ranging from ~ 100 nm to ~ 1 μm , which strengthens the alloy through formation of ultrafine equiaxed grains with less than 1 μm and stopping the motion of dislocations and grain boundaries. As those reinforcements were produced in-situ during a hot extrusion process, the strong bonding force at the matrix-particle interface insured the retention of moderate ductility in the alloy. The strain rate sensitivities of this alloy, ranging from ~ 0.015 to ~ 0.018 , plus limited available SRS values of other pure and alloyed Mg are believed to render the conclusion that the deformation mechanism of Mg and its alloys may change from dislocation dominated to GB activities dominated as the grain size is decreased down to nanoscale. On the other hand, the shear fracture failure present in the alloy has been saved for later in-depth discussion with the failure manner of AZXE7111, since there are similarities between them.

4.2 AZXE7111

In the preceding section, Mg alloy AMX602 produced through SWA technique plus later compaction and hot extrusion has been studied in terms of its mechanical properties and deformation mechanism. In this section, another Mg alloy AZXE7111 produced in the same way containing different constituents will be studied in terms of its texture,

mechanical properties as well as deformation mechanisms at different loading rates. The primary difference between these two alloys is that AZXE7111 is doped with lanthanum. Its nominal chemical composition is Mg-7Al-1Zn-1Ca-1La, all in wt.%. As shear localized failure mode has also been observed in AZXE7111 at various loading rates, it will also be held for further discussion in the shear banding failure section.

4.2.1 Texture and Microstructure of AZXE7111

Figure 4.9(a), (b), (c) and (d) display the pole figures of $(10\bar{1}0)$, (0002) , $(11\bar{2}0)$ and $(10\bar{1}1)$ of AZXE7111 extruded at 250 °C obtained by XRD analysis. Compared with the texture analysis results of Elsayed et al. [29] by EBSD on a similar La-doped Mg alloy (Mg-7Al-1Zn-1Ca-1.5La, in wt%, balance Mg) processed under similar conditions, we can see that AZXE7111 exhibits similar texture. Compared to conventional mischmetal-free Mg-alloys, its texture is relatively weak. It should be noted that the work of Elsayed et al. only presents the pole-figures and inverse pole-figures of (0001) (basal plane) orientation.

Figure 4.10 shows the optical micrographs of AZXE7111 extruded at 250 °C (a) and 200 °C (b), respectively. We can see that due to the resolution limit of optical microscopy finer microstructural information cannot be accessed via this technique. Figure 4.10(c) presents the grain size histogram of the two samples, showing that the grain size is on the border of ultrafine scale ($\sim 1.0 \mu\text{m}$). It is also observed that extrusion temperature does not impart a strong effect on the microstructure (primarily the grain size) of this La-doped Mg-alloy. It is worth noting that such fine grain size in an Mg-alloy is considerable since severe plastic deformation (SPD) has only rendered the grain size of Mg-alloys a few micrometers because of the poor workability which requires SPD temperature above

250 °C. Similar to that of AMX602, we believe such fine microstructure is owing to the nanometer-scale intermetallic precipitates that form in the SWA Mg-alloy during the hot extrusion process. These intermetallic precipitates serve as GB pinning centers which slow down the grain growth kinetics during dynamic recrystallization. Further evidence will be provided in what follows.

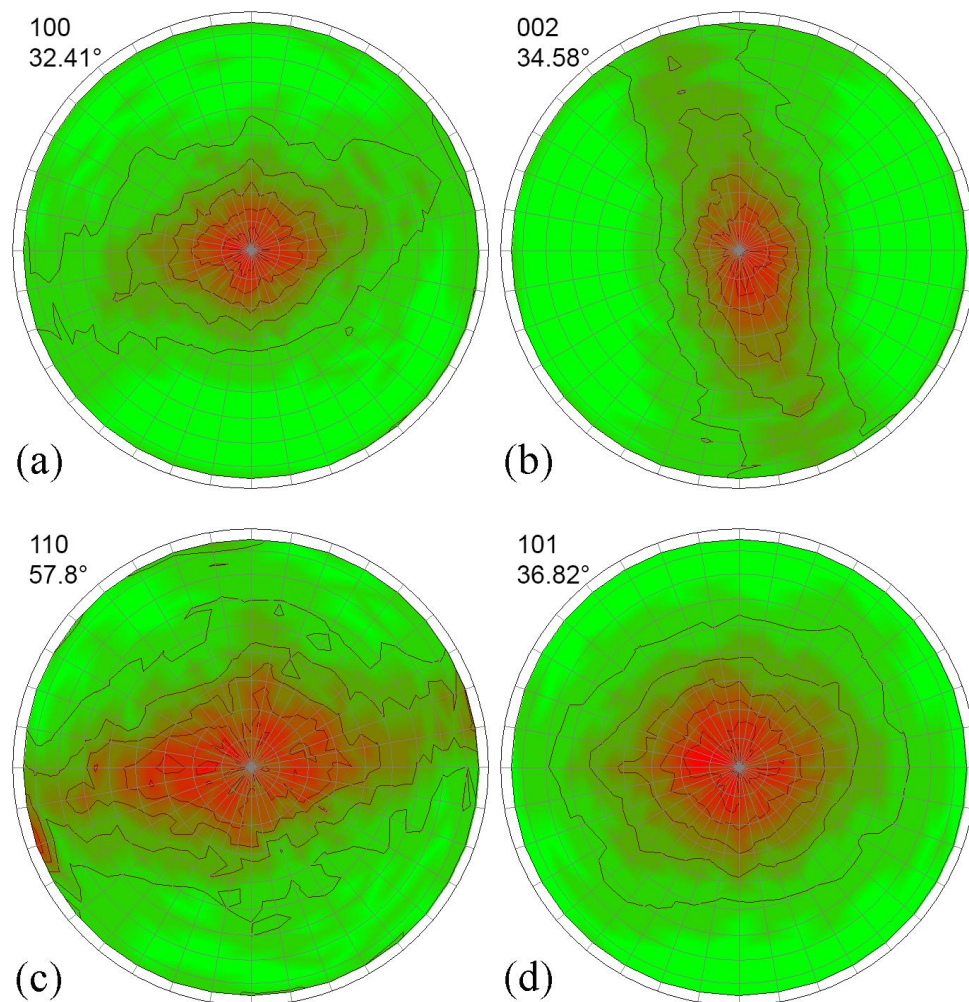


Figure 4.9: XRD texture measurement results of AZXE7111 (extruded at 250 °C). The results are very similar to those reported by El-Sayed and co-authors [27] on a similar alloy processed under similar conditions. The pole-figures shown here indicate that the La-doped Mg-alloy AZXE7111 still exhibits some texture upon extrusion, but the texture is not as strong as conventional Mg-alloys without addition of mischmetal.

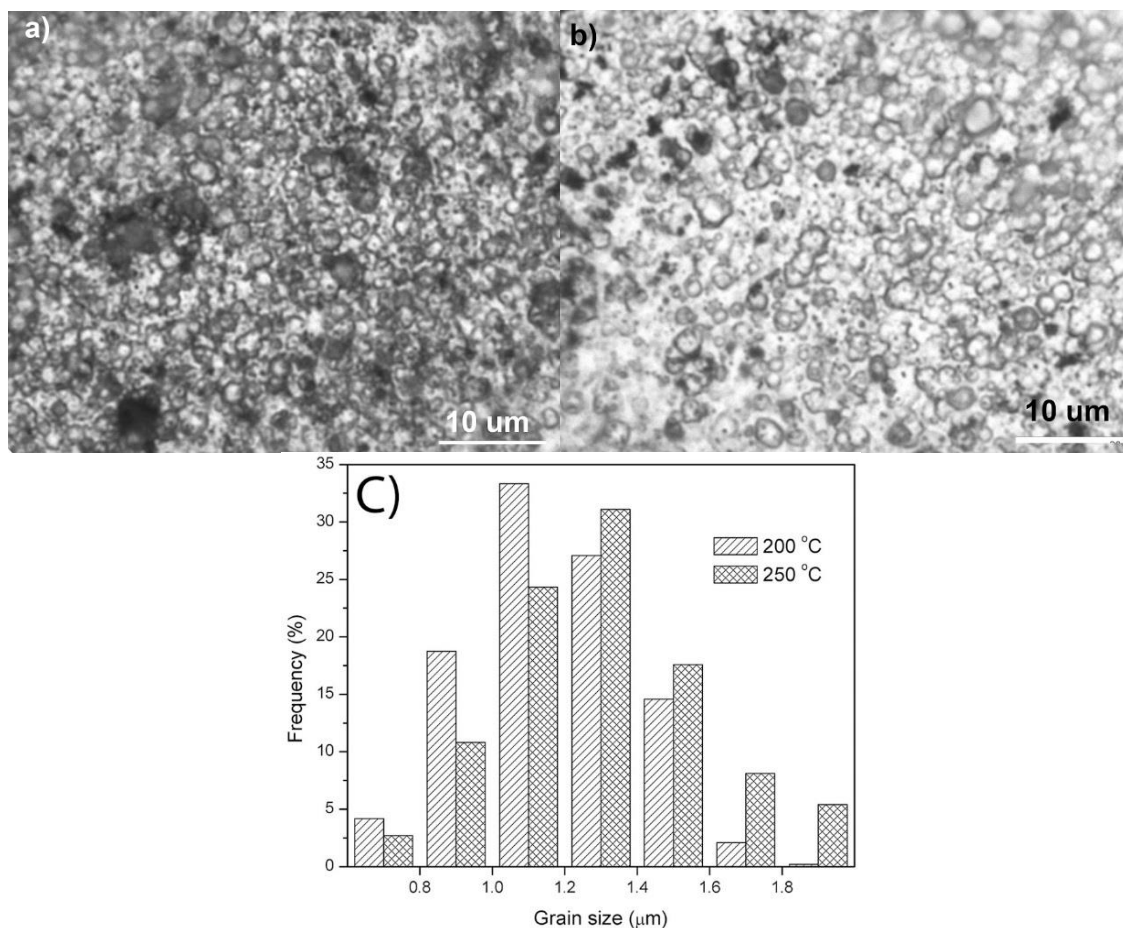


Figure 4.10: Optical micrographs of AZXE7111 extruded at 250 °C (a) and 200 °C, respectively, and the grain size distributions of the two samples based on measurement of the optical micrographs. We can see that the average grain size of both samples is around 1.0 μm. The extrusion temperature does not have a very strong effect on the grain size of this Mg-alloy.

Figures 4.11(a) and (b) show the representative bright- and dark-field TEM images of AZXE7111 extruded at 350 °C with the corresponding selected area diffraction pattern (SADP) shown as an inset in Figure 4.11(a). The image reveals a grain size of a few hundreds of nanometers. The bright-field TEM images of AZXE7111 extruded at 250 °C and 200 °C are shown in Figures 4.12(a) and (c) along with the SADP, again shown as an inset. The energy dispersive X-ray spectroscopy (EDX) examination (Figure 4.12(b)) of the small squared area of Figure 4.12(a) reveals that it is rich in aluminum, calcium and

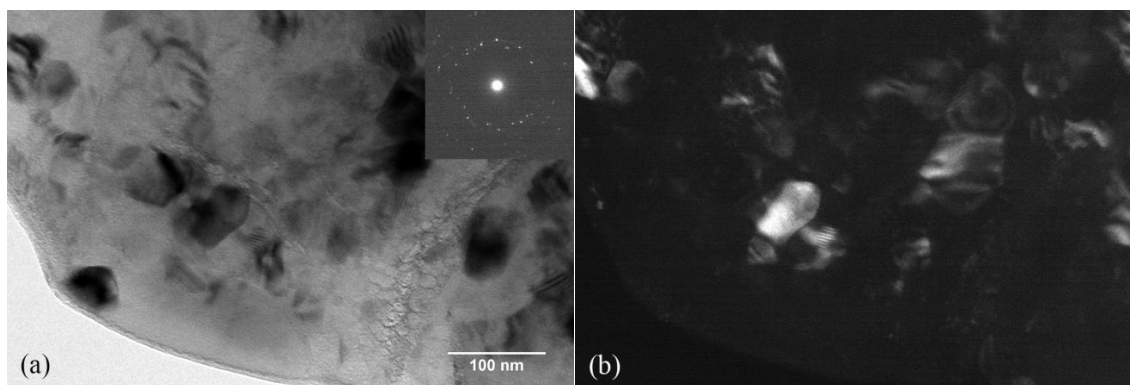


Figure 4.11: Bright- (a) and dark-field (b) TEM images of an AZXE7111 specimen, extruded at 350 °C, with an inset of the corresponding selected area diffraction pattern (SADP) in (a). Particles of size <100 nm can be observed. Note, particles are present both at the grain boundaries and inside the matrix grains.

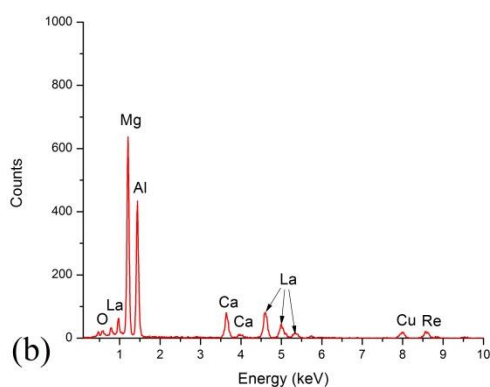
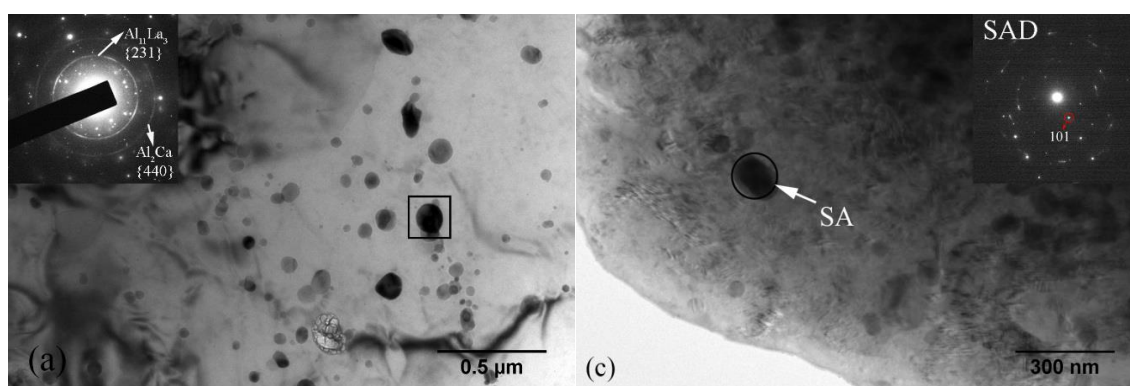


Figure 4.12: (a) A bright-field TEM image of an AZXE7111 specimen (extruded at 250 °C) with an inset of the corresponding SADP; (b) EDX analysis of the selected area of (a) (see boxed region); and, (c) Bright-field TEM image of an AZXE7111 specimen (extruded at 200 °C) with the SADP of the circled area shown as the inset.

lanthanum. More detailed analysis of particles from other areas in the alloy also yields similar results, namely, they are rich in Al-Ca-La. Indexing of the SADP in Figure 4.12(a) suggests that the innermost diffraction ring is from the intermetallic phase $\text{Al}_{11}\text{La}_3$, while the second ring might have a contribution from both $\text{Al}_{11}\text{La}_3$ and Al_2Ca (the d-spacing values of these two compounds are quite close and hard to distinguish from this diffraction ring). Al_2Ca has a cubic structure (space group $\text{Fd}\bar{3}\text{m}$) with a lattice constant $a = 0.802\text{-nm}$; while $\text{Al}_{11}\text{La}_3$ has two polymorphs: a high temperature phase of body centered tetragonal structure (space group I4/mmm) and an orthorhombic phase existing at relatively low temperatures [214]. Further, an SADP of the circled area in Figure 4.12(c) was taken and shown as an inset. The majority of the spots of this pattern can be indexed to be from $\text{Al}_{11}\text{La}_3$. The presence of this phase was identified by Fan et al. [74] as well through XRD in an AZ91 Mg-alloy doped with 1.0 wt% amount of La. Elsayed et al. [29, 77] also observed intermetallic particles of $\text{Al}_{11}\text{La}_3$ and Al_2Ca using X-ray diffraction (XRD) in the same Mg alloy. It is then reasonable to believe that the intermetallic particles found in our samples are also $\text{Al}_{11}\text{La}_3$ and Al_2Ca .

Our TEM observations also suggest that these intermetallic compound particles are uniformly distributed within the matrix. The size distribution of the intermetallic particles in the alloy with extrusion temperatures of 350° and 200°C were measured and the results are shown in Figures 4.13(a, b). A total number of ~ 110 particles for 350°C extrusion and a total number of ~ 50 particles for 200°C extrusion were measured. The particle size distributions suggest that, on the average, the intermetallic compound particles are smaller than 100 nm , with an average particle size $\sim 88\text{ nm}$ and $\sim 85\text{ nm}$ for extrusion temperatures of 350°C and 200°C , respectively, indicating that the extrusion temperature

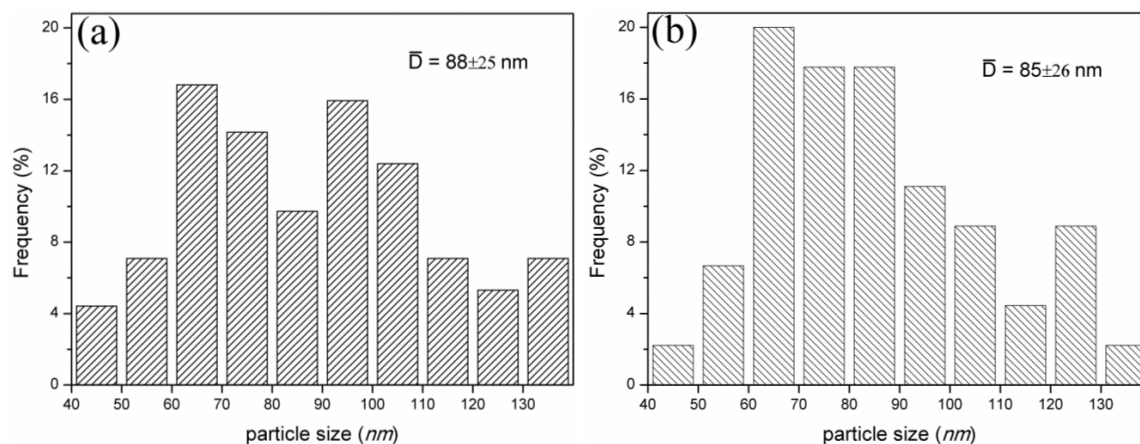


Figure 4.13: The particle size distribution of the AZXE7111 alloy, extrusion at temperatures of (a) 350 °C, and (b) 200 °C. The average particle size after extrusion at 350 °C is ~88 nm, while that after 200 °C extrusion is ~85 nm. Note, a lower temperature extrusion results in a relatively narrow particle size distribution. For each condition, the total number of particles measured is ~100.

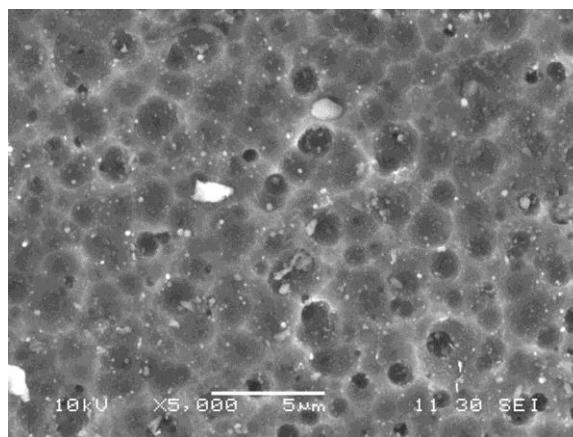


Figure 4.14: A representative SEM image of AZXE7111 sample (along transverse direction), extruded at 200 °C. The grain size revealed here is roughly the same as provided in Figure 4.10.

only has marginal effect on the intermetallic particle size of this La-doped Mg-alloy. However, as suggested by Figure 4.13, the extrusion temperature indeed affects the distribution of the particle size. A lower extrusion temperature leads to a narrower distribution, with more particles having a size below 100 nm. A higher extrusion

temperature produces more particles with larger sizes. A representative SEM image of the alloy extruded at 200 °C is shown in Figure 4.14, and again confirms the uniform distribution and the nano-scale of the intermetallic particles. It is also noticed that the grain size displayed by Figure 4.14 is in line with that of Figure 4.10. Our observations agree with the results of Ayman et al. [77] who found that the Al_2Ca and $\text{Al}_{11}\text{La}_3$ precipitates were formed in the Mg-Al-Zn-Ca-La alloy during the extrusion process; the presence of the hundred-nanometer intermetallic particles precipitated out during extrusion process promotes the formation of nuclei of strain free grains during dynamic recrystallization. Those particles also limit the grain growth kinetics during the dynamic recrystallization process, thus leading to the fine grain size of the extruded alloy.

In summary, the SWA produced AZXE7111 Mg-alloy exhibits a similar grain size (grain size $\sim 1.0 \mu\text{m}$) to that of AMX602 produced by the same method. Intermetallic compound phases of Al_2Ca and $\text{Al}_{11}\text{La}_3$ are found in the microstructure with an average particle size on the order of $\sim 85 \text{ nm}$. Extrusion temperature does not show strong effect on the average grain size of the matrix and average particle size of the intermetallic compound phases. However, a lower extrusion temperature indeed leads to a narrower particle size distribution.

4.2.2 Mechanical Properties of AZXE7111

We have tested the AZXE7111 alloy and found that it exhibits similar mechanical behavior in the axial and the transverse directions (relative to the flow or extrusion direction). In other words, the mechanical behavior of the extruded alloy is more or less isotropic, particularly when the extrusion temperature is relatively high. Figure 4.15 displays representative true stress-strain curves of the La-doped Mg-alloy AZXE7111 for

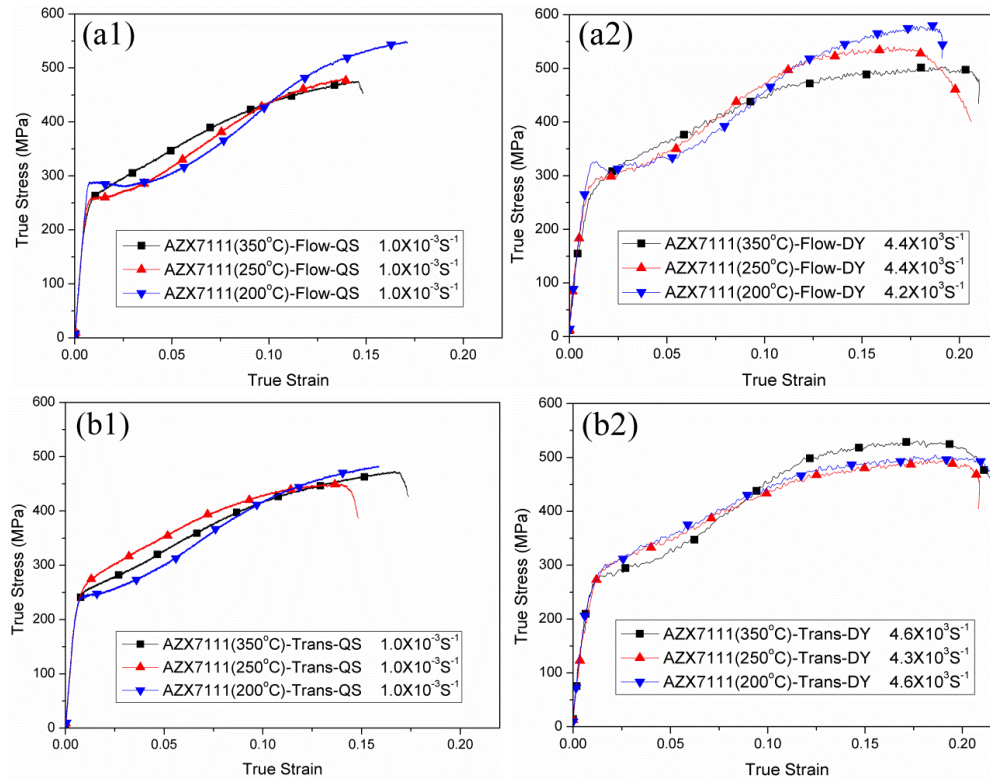


Figure 4.15: Compressive true stress vs. true strain curves of the AZXE7111 alloy; (a) in the flow direction and (b) in the transverse direction under at both quasi-static (a1 and b1) and dynamic (a2 and b2) loading conditions. The extrusion temperatures are also indicated in the captions. Note the strong strain hardening under both quasi-static and dynamic loading, and the relatively isotropic behavior of this Mg-alloy.

each processing condition, tested under quasi-static and dynamic loading, as well as in the flow and the transverse directions. More specifically, Figure 4.15(a1) shows the representative flow-direction quasi-static stress-strain curves of the alloy extruded at different temperatures; Figure 4.15(a2) displays the flow-direction dynamic stress-strain curves of the alloy extruded at different temperatures. Figure 4.15(b1, b2) presents the transverse-direction quasi-static and dynamic stress-strain curves of AZXE7111 extruded at different temperatures. These true stress-true strain curves are found to exhibit very similar trends under quasi-static and high strain rate loading though the dynamic stress

levels are slightly higher than the quasi-static stress levels for the same materials processing condition. As such, our results suggest that the fundamental deformation mechanisms of AZXE7111 at both loading rates may be similar. It is also observed that as the extrusion temperature increases, the first “easy-glide” stage disappears under both quasi-static and dynamic loading. Furthermore, under all processing and loading conditions, the stress-strain curves of this alloy exhibit very strong strain hardening. When the extrusion temperature is 200 °C, both quasi-static and high rate curves in the flow direction show two stages in their plastic part: a nearly flat region followed by gradually steeper strain hardening (Figure 4.15(a1, a2)). This effect is absent from the transverse direction specimens (Figure 4.15(b1, b2)). However, overall, the extrusion temperature seems only to have marginal effect on the flow behavior of the alloy. The specimens extruded at the lowest temperature (200 °C) exhibit the so-called “sigmoidal” shape in their stress-strain curves, which is commonly taken as the signature for the operation of extension twinning [39, 215], as discussed in a previous section. This suggests that the orientation of the grains favors mechanical twinning during compression. The sigmoidal shape is smeared for specimens extruded at higher temperature, indicating weaker texture due to more thorough dynamic recrystallization.

In order to further evaluate the strain hardening behavior, we use the Hollomon equation, $\sigma_T = K\varepsilon_T^n$, to fit the experimental data after the easy glide portion under quasi-static loading [79]. In this equation, σ_T is the true stress and ε_T is the true strain in the plastic region of the stress-strain curve after the easy glide part, K is a constant, and n is the strain hardening exponent. Analysis for the specimens extruded at 200 and 250 °C renders the following results: $K = 757.5$ MPa and $n = 0.263$. There is only a smaller than

2% difference between these two conditions. However, when the extrusion temperature is 350 °C, our analysis yields a value of the hardening exponent $n = 0.274$, significantly greater than that of the specimens extruded at relatively low temperatures. In other words, specimens from the alloy extruded at this temperature (350 °C) exhibit stronger strain hardening under quasi-static loading than those extruded at the relatively low temperatures. This difference might have originated from the relatively coarse microstructure of the alloy, extruded at 350 °C.

Table 4.2: Yield and maximum compressive strengths of the AZXE7111 alloy, under quasi-static and dynamic compressive loading conditions (data in units of MPa)

Extrusion Temperature [°C]	Flow Direction				Transverse Direction			
	Yield Strength		Maximum Strength		Yield Strength		Maximum Dtrength	
	Quasi-Static ($\sigma_{0.2\%}$)	Dynamic ($\sigma_{5\%}$)	Quasi-Static	Dynamic	Quasi-Static ($\sigma_{0.2\%}$)	Dynamic ($\sigma_{5\%}$)	Quasi-Static	Dynamic
350	249 ±0	383 ±0	468 ±5	498 ±0	245 ±0	352 ±3	469 ±3	527 ±0
250	251 ±0	370 ±5	469 ±8	516 ±22	247 ±0	371 ±0	443 ±10	486 ±0
200	279 ±6	349 ±0	530 ±20	570 ±7	245 ±9	380 ±3	482 ±15	498 ±0

To facilitate comparison, Table 4.2 lists the yield strengths (at an offset strain of 0.2% for quasi-static, and 5% for dynamic loading) and ultimate strengths (or the peak stress in the stress-strain curves) of AZXE7111, extruded at different temperatures and tested at different loading rates. The strength values shown in the table is the average of three samples, tested under the same conditions; the errors are also given in Table 4.2. Again, we can see that neither the yield strength nor the ultimate strength of AZXE7111 is very sensitive to the extrusion temperature. The yield and ultimate strengths are on the order

of ~250 and ~500 MPa, respectively, at quasi-static loading rate for all processing conditions, with no obvious indications of anisotropy. The dynamic strengths are about 10% higher than their quasi-static counterparts, and the increase reduces with an increase in the extrusion temperature. In addition, the failure strains of AZXE7111 are ~15% and 20% under quasi-static and dynamic loading, respectively, for all processing conditions.

In summary, both quasi-static and dynamic mechanical testing of the La-doped AZXE7111 alloy extruded at different temperatures show only minor anisotropy in their strength and flow behavior, which is consistent with the XRD texture measurement results. Extrusion temperatures only have marginal effect on the mechanical properties of the alloy under both quasi-static and dynamic loading conditions. All processing conditions yield strong strain hardening of the alloy under both quasi-static and dynamic loading conditions.

4.2.3 Post-mortem Examination of AZXE7111

Figure 4.16 shows representative macro-scale SEM images taken from post-loading

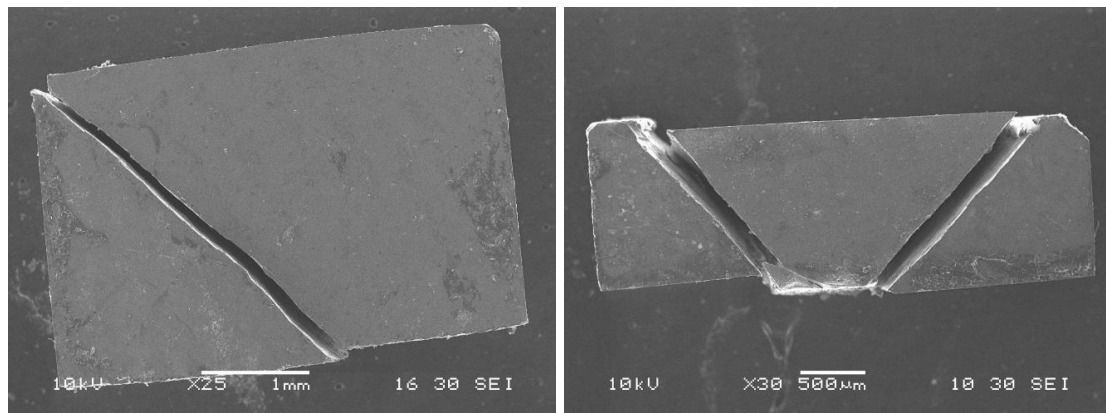


Figure 4.16: SEM images (low magnification) taken from the post-loaded AZXE7111 alloy (extruded at 200°C) under (a) quasi-static and (b) dynamic compression along transverse direction.

AZXE7111 specimens (extruded at 200 °C) under quasi-static and dynamic compression conditions along the transverse direction. Upon quasi-static compression, the specimen eventually failed into two parts (Figure 4.16(a)). The failure is along a major crack inclined at $\sim 45^\circ$ with respect to the loading direction. That is to say, the failure under quasi-static uniaxial compression is along the maximum shear stress plane. We should point out here that all of the quasi-static specimens failed in a way similar to the one shown in Figure 4.16(a). This is highly reminiscent of the failure mode of bulk metallic glasses under similar loading conditions [216]. However, unlike bulk metallic glasses, AZXE7111 exhibits a significant amount of plastic deformation prior to failure. In contrast, bulk metallic glasses usually show little or no global plasticity before failure along a major shear band [216, 217].

Figure 4.16(b) displays a typical post-mortem SEM image of a dynamic specimen of AZXE7111 extruded at 200 °C. The specimen has broken into three pieces, along two conjugate shear planes. Note that these two conjugate shear cracks are on planes which are nearly perpendicular to one another, with each inclined at an angle of about 45° with respect to the loading axis (roughly vertical in the figure). This failure mode is quite similar to that of AMX602, and is also reminiscent of that of many BCC UFG/NC metals, such as vanadium, iron, tungsten, or tantalum under similar uniaxial dynamic compression conditions [218-224], and titanium strengthened by interstitial impurities [225]. However, unlike those BCC UFG/NC metals that exhibit similar shear localization mode in the absence of strong strain hardening, in the case of AZXE7111, the conjugate shear cracks are preceded by large strain hardening. Another difference between this La-doped AZXE7111 alloy and the UFG/NC BCC metals in terms of their dynamic behavior

is that the latter usually do not show failure as a consequence of adiabatic shear localization. Also worth noting is that usually a stress collapse or precipitous stress drop accompanies the adiabatic shear localization as observed in the dynamic stress-strain curves of UFG/NC BCC metals exhibiting ASB [224]. As such, the duration of the shear localization process is considerably extended. In contrast, for the case of AZXE7111, this localization process is much shorter and more abrupt, leading to a faster failure of the specimen.

Figure 4.17 presents the side view at a high magnification of one of the dynamic specimens of the AZXE7111 alloy that did not fail yet. A macro-scale image of the specimen is shown in the inset. We can observe a primary crack and multiple secondary small cracks in the SEM image (indicated by black arrows in the figure). A more detailed discussion about the failure mechanism will be described in the following sub-section.

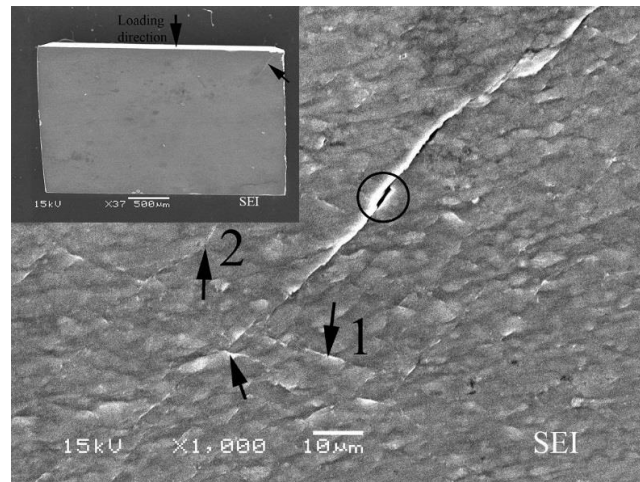


Figure 4.17: High magnification side view of an incomplete crack in an unfailed dynamic AZXE7111 specimen (extruded at 200°C) along transverse direction. The inset shows a macroscale side view of the entire specimen. The primary crack runs from the top right corner to the lower left corner of the specimen at an angle of $\sim 45^\circ$ with respect to the loading direction, i.e., in the maximum shear stress plane. Secondary cracks can also be identified in this image.

The fracture surfaces of the fragmented specimen recovered from both quasi-static and dynamic loading tests were also examined by SEM. All of the fracture surfaces of the alloy at the same loading rate have similar surface characteristics. Figures 4.18(a) and (b) show typical fracture surfaces of the AZXE7111 alloy extruded at 350 °C, loaded at two different strain rates.

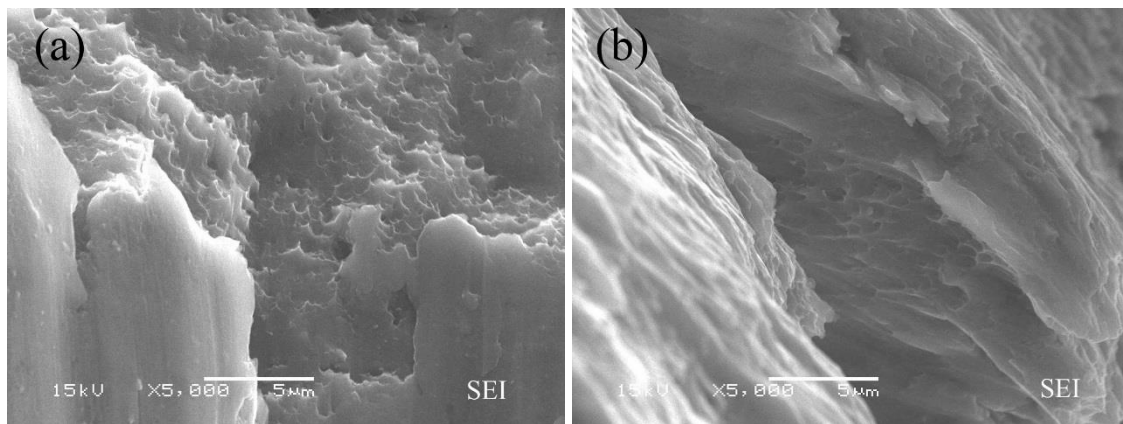


Figure 4.18: SEM images of the fracture surfaces of AZXE7111 (extruded at 350 °C): (a) after quasi-static loading; (b) after dynamic loading along transverse direction. Note that both images are taken at the same magnification level. In (a) for the quasi-static specimen more ductile features are present which are also smaller than those observed in the dynamic specimen (b).

The dimples on the fractured surfaces indicate that ductile fracture is the predominant failure mode at both quasi-static and dynamic loading rates, as shown in Figure 4.18(a) for quasi-static loading and (b) for dynamic loading. Such dimple patterns characterize the fracture behavior of all the post-mortem samples under the different extrusion conditions. No micro-cracks associated with the nanometer-scale intermetallic compounds were observed in post-mortem SEM examinations. This is consistent with the results from previous tensile testing reported by Ayman et al. [77], who ascribed the

remarkable mechanical behavior of this La-doped Mg-alloy partly to the existence of these fine and uniformly dispersed intermetallic compounds [29]. Although the fractographic observations do verify the overall ductile fracture of the alloy, the fracture behavior still exhibits a dependence on the loading rate, as shown by the fracture surfaces of Figures 4.18(a) and (b). Unlike the quasi-statically fractured sample, the dimples generated under dynamic loading exhibit a visco-plastic drag mode that seems to be in a state of viscous flow. Additional discussion about the prevailing fracture mechanism that takes place in this alloy at different loading rates will be provided in what follows.

Therefore, to summarize briefly, we observed shear failure along major shear cracks of this La-doped Mg-alloy under both quasi-static and dynamic loading conditions. It is particularly surprising to observe the failure of quasi-static specimens along a primary shear crack after a significant amount of uniform compressive plastic deformation. Under dynamic loading, the failure is clearly a consequence of adiabatic shear localization.

4.2.4 Discussion and Conclusion of AZXE7111

In this part, we will discuss the experimental results of this work. We will focus on the strengthening mechanisms responsible for the significant strength level of this La-doped Mg alloy and the plastic deformation and failure mechanisms. Particularly we will attempt to provide an explanation about the shear localization observed both under quasi-static and high strain rate uni-axial compressive loading as this is very important for the wide application of Mg-alloys.

First of all, we would like to briefly comment on the weakened texture as evidenced by the XRD texture analysis and the mechanical testing results. As we have pointed out many times previously, the basal-slip dominated plastic deformation of pure Mg and

many Mg-alloys renders these materials with undesirable poor tensile ductility and a strong anisotropy, especially in extruded and rolled conditions, due to the evolution of significant basal-plane texture. Obviously, this translates into poor workability and considerable limitations in potential applications. One way to mitigate this issue is to activate non-basal slip systems such as prismatic and/or pyramidal of $\langle \mathbf{a} \rangle$ dislocations, and even $\langle \mathbf{c}+\mathbf{a} \rangle$ slip systems. Prismatic slip systems include $\{10\bar{1}0\}/\langle 11\bar{2}0 \rangle$, and pyramidal slip systems include $\{10\bar{1}1\}/\langle 11\bar{2}0 \rangle$; the Burgers vector for $\langle \mathbf{c}+\mathbf{a} \rangle$ slip is $\mathbf{b} = 1/3 \langle \bar{2}11\bar{3} \rangle$ [38]. It has been found that some alloying elements can increase the relative strength of basal slip and decrease that of non-basal slip systems [16, 17, 226]. As such, these elements can weaken the basal texture in rolled or extruded Mg and Mg alloys [11]. Our XRD texture analysis and mechanical testing results are consistent with such hypotheses. It is particularly observed that high temperature extrusion weakens the basal textures, as suggested from the absence of sigmoidal shape in the compressive stress-strain curves of these samples.

Recently, micro-alloying of Mg-alloys with rare earth (RE) metals such as cerium or lanthanum has been proven to effectively weaken the basal texture and improve the tensile ductility of rolled and extruded Mg-alloys [58, 226-234]. Our results reveal that the spinning water atomization (SWA) technique, together with subsequent material processing, renders the AZXE7111 alloy to have outstanding properties compared to many other Mg alloys. It is believed that the very high ultimate strength of this alloy may have contributions from two main factors, which have already been pointed out in the previous section for AMX602: strengthening from the small and uniform grain size (on order of $\sim 0.5 \mu\text{m}$), and from the nano-meter scale intermetallic compound particles. Of

course, these two strengthening factors should be added to the solution strengthening of the alloy to achieve the extraordinarily high strength level of this alloy. We will discuss these two strengthening mechanisms in the context of the experimental results of this work.

In general, we can take into consideration the common strengthening mechanisms for metals and alloys which include GB strengthening (Hall-Petch effect), second-phase particle strengthening in the sense of Orowan, forest dislocation hardening (work hardening), and solute strengthening. Since we are looking at the yield strength of this La-doped Mg-alloy, here it should suffice to evaluate the Orowan mechanism and the Hall-Petch effect, assuming the solute strengthening is intrinsic for this complex alloy.

4.2.4.1 Precipitation strengthening

The presence of cerium was reported to assist in altering the texture of an extruded Mg alloy during recrystallization [28]. Therefore, it is reasonable to argue that the presence of lanthanum in AZXE7111 may also contribute in a similar manner to improving the isotropy of AZXE7111 by softening its texture since La resides next to cerium in the Periodic Table and has very close atomic properties to cerium. This is partly supported by the true stress-strain curves of AZXE7111 that show similar behavior when loaded in two orthogonal directions. Another sign of the homogeneous distribution of texture comes from the low strain hardening rate at the beginning of yielding, as shown in Figure 4.15. On one hand, according to Bhattacharya and Niewczas and Gharghour, et al. [18, 235], basal slip contributes significantly to ductility at the onset of plastic deformation of pure Mg and Mg alloys. On the other hand, Ayman et al. [77] realized that with increased La content much coarser precipitates could form, and they

concluded that a La content of 1.5 wt.% serves better for the Mg-Al-Zn-Ca-La alloy than 3.3 wt% La. The ~1.5 wt% La contained in AZXE7111 has led to the formation of nanoscale Al-La-Ca intermetallic compounds. The results from statistics shown in Figure 4.13 also confirm the presence of nanoscale particles, while the TEM and SEM images of Figures 4.12 and 4.14 suggest the presence of the particles at GBs and within the grains. Owing to the quick accumulation of dislocations at GBs and/or the compound-matrix interfaces, the initially easy dislocation slip stops quickly due to the exhaustion of basal slips. Thereafter, the stress needed to further deform the alloy by dislocation motion elevates dramatically. As the applied stress increases, it is reasonable to believe that the critical stress for twinning may be achieved, and once attained, twinning may take place in the alloy. Bhattacharya et al. [18, 82] pointed out that deformation twinning takes place after a finite amount of plastic deformation, or at the last stage of plastic deformation. Somekawa and Mukai [43] also observed an increasing density of twins with strain, whereas they thought the formation of twinning is the signature of macro-yielding in Mg alloys. To some extent, this is probably true because dislocations can move more easily inside a grain than twinning without large change of the grain shape. Thus, no macro-yielding might be observed before the exhaustion of easy-glide systems. In turn, twinning and/or intra-grain dislocation activities are the predominant deformation mechanisms and account for macro-yielding. With further plastic deformation, several strengthening mechanisms may be involved to contribute to the stress increment, such as interactions between dislocations and twin boundaries [18], and dislocation pile-ups against GBs [236] or intermetallic particles [237, 238]. Here, we hypothesize that the nanoscale particles contribute significantly by impeding the motion of dislocations. In

addition, similar to AMX602, AZXE7111 is also an in situ particle reinforced Mg-alloy vis-à-vis Mg/SiC metal-matrix composites [203], where the in-situ particles can render a much stronger bonding force between the particles and matrix than ex-situ particles. As a result, these particles are more efficient than those in Mg/SiC metal-matrix composites. Usually, the contribution from Orowan mechanism can be written as

$$\Delta\sigma_{Or} = \alpha \cdot \frac{\mu^m b}{\lambda} \quad (4.1)$$

where α is a geometrical factor that is usually taken to be unity, μ^m is the shear modulus of the matrix (17 GPa for Mg), b the Burgers vector of the matrix dislocations (0.321 nm for Mg), and λ the inter-particle spacing in the material. Based on the TEM observations, we have measured the inter-particle spacing in AZXE7111, and the results for 250 °C extrusion are shown in Figure 4.19.

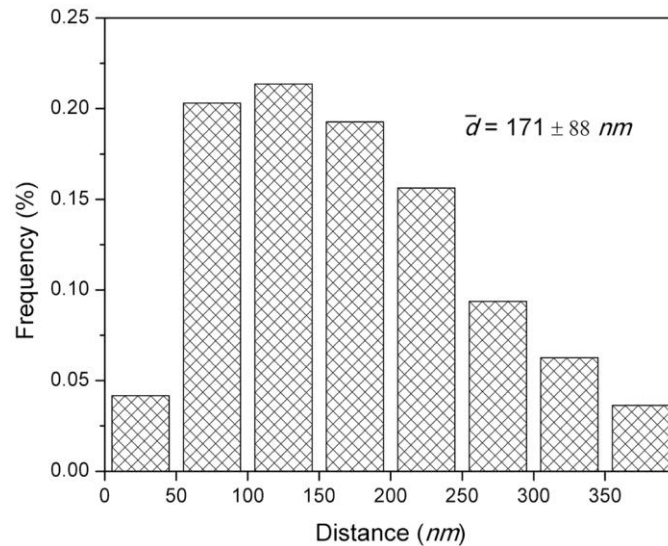


Figure 4.19: Inter-particle distance distribution of the intermetallic compound phases for AZXE7111 extruded at 250 °C. The vast majority of the particles have an inter-particle distance on the order of ~100 nm.

We may reasonably assume that the short inter-particle distance dictates, and taken a value of 100 nm. Based on Eq.(4.1), the contribution from the Orowan mechanism to the yield strength of AZXE7111 is ~55 MPa. This strengthening effect is thus quite significant.

4.2.4.2 Hall-Petch strengthening

It is a well-established notion that the strength of Mg and Mg-alloys is a strong function of grain size. As pointed out by Barnett et al. [82], the Hall-Petch slope (k) of Mg-alloys is not strongly affected by the alloying with Al and Zn, the primary alloy elements for Mg-alloys. Various efforts cited by Barnett et al. shows that the average k value for pure Mg is ~6.0 MPa.mm^{1/2}. Experimental results of Ayman et al. [77] on a La-doped Mg alloy with chemical composition similar to that of AZXE7111 which was extruded at different temperatures show a Hall-Petch coefficient very close to ~6.0 MPa.mm^{1/2}. The contribution to the overall strength from the Hall-Petch effect can be written as

$$\Delta\sigma_d = k_{H-P}d^{-1/2} \quad (4.2)$$

If the grain size of the AZXE7111 Mg-alloy is taken to be ~1.0 μm , then from Eq.(4.2), the contribution to strength from the Hall-Petch effect is ~190 MPa. The yield strength of pure Mg with very large grain size is ~15 MPa [101]. Therefore, the estimated yield strength based on second-phase strengthening and Hall-Petch effect will be ~260 MPa, which is a little bit larger but still very close to our experimental results.

We, therefore, believe that the primary strengthening mechanisms responsible for the high yield strength of this La-doped Mg-alloy are the second-phase particles and the fine grain size, which, when combined with the existing solute strengthening, render the high

strength level of this alloy.

4.2.4.3 Strain-rate hardening, adiabatic heating and strain hardening

The SRS value of AZXE7111 Mg alloy was derived by Eq.(3.5) using the data from nanoindentation rate jump test. The SRS values of AZXE7111 extruded at 350 °C and 200 °C are approximately ~0.026 and ~0.039, as shown in Figure 4.20.

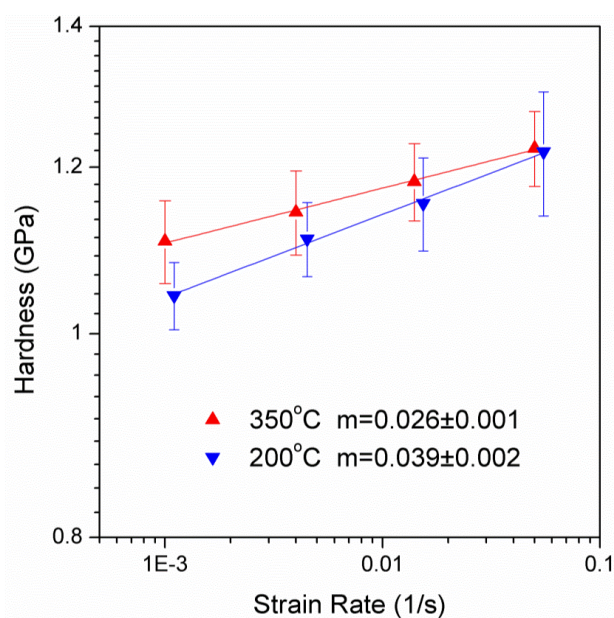


Figure 4.20: The strain rate sensitivity of AMXE7111 extruded at 350 °C and 200 °C as measured by instrumented nanoindentation. The material extruded at 200 °C exhibits higher SRS, presumably because of its finer microstructure.

These values are smaller than that reported by Trojanova et al. [212] and Hwang et al. [213] for a 100-nm grain size pure Mg (~0.3) and 45-nm grain size pure Mg (0.6), but comparable to our previous results of pure Mg (grain size: ~ 4.5- μ m), Mg-Y alloy (grain size: ~400-nm) and Mg alloy AMX602 (grain size: ~1.0- μ m). Only a limited number of publications are available in addressing the strain rate sensitivity of Mg-based materials,

therefore, the fundamental mechanism is yet waiting to be uncovered. This level of SRS cannot be explained by basal-slip as basal-slip is not so much thermally activated compared to other slip-systems, particularly prismatic and pyramidal slip systems [239]. Neither can it be attributed to deformation twinning as is well known that twinning is an athermal process and thus rate-independent [240].

Under high strain rate loading, heat transfer is limited or even prevented and the plastic deformation can be considered adiabatic. As such, taken the prescribed strain to be 0.2 (20%), the adiabatic temperature rise can be estimated to be ~ 47 K for the whole specimen under dynamic loading. Considering the relatively low melting point of Mg, this adiabatic temperature rise should lead to a reduction of the strain hardening rate. However, the strain hardening rate of AZXE7111 does not show a significant decrease as expected. Furthermore, the strain hardening rates beyond a strain of ~ 0.06 are even higher at high strain rates than those at low strain rates, as shown in Figure 4.21.

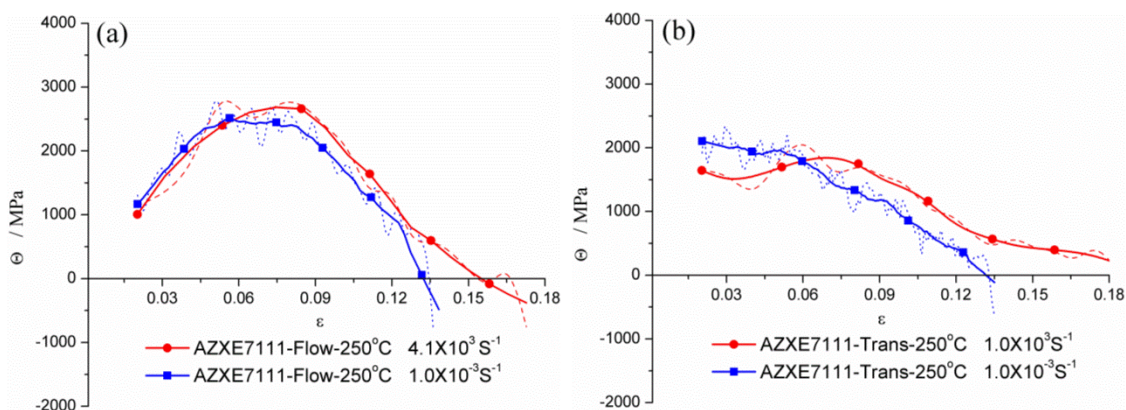


Figure 4.21: The strain hardening rates of AZXE7111 vs. strain in the (a) flow and (b) transverse directions. The solid lines are the smoothed results of the dash lines.

This abnormal phenomenon suggests that an increased strain hardening mechanism is invoked at high strain rates. We believe that deformation twinning can be the reason to reconcile this discrepancy, as the interaction between twin boundaries and dislocations can greatly enhance strain hardening of a metal. Firstly, twinning has been frequently reported in Mg alloys with grain sizes ranging from the micro- to nano-regimes [39, 82, 205, 206, 241]. Secondly, twinning has a much higher critical resolved shear stress (CRSS) and is less sensitive to temperature than dislocation slip [31]. Thirdly, the volume fraction of twins increases with either plastic strain or loading rate [40, 43]. The fact that our TEM analysis failed to reveal strong evidence of twinning can be explained by the observations of Li et al. [39] who ascribed this to the elimination of twins during TEM sample preparation. However, a more plausible explanation is the lack of sharp twin boundaries of Mg and its alloys.

In summary, we believe that the strong strain hardening and moderate strain rate sensitivity of AZXE7111 is due to the interaction between twin boundaries and dislocations, particularly at high loading rates where this strain hardening even prevails and outplay the thermal softening due to adiabatic temperature rise. This is primarily because deformation twinning process is an athermal process.

4.2.5 Summary

The La-doped Mg alloy AZXE7111 (Mg-7Al-1Zn-1Ca-1La, all in wt%) processed in the same way as AMX602 also exhibits impressive mechanical properties. Microstructure examination suggests that the improved properties are partially attributed to the uniform distribution of particles with dimensions of less than ~100nm. These particles located at grain boundaries or within grains impeding the grain boundary evolution and dislocation

motion, thus increasing the strength. In the meantime, in-situ formed particulates preserve the strong bonding force between the Mg matrix and particle, which as a result retains the moderate ductility of the alloy. On the other hand, the strong hardening emerging after a perfect plastic flow may be attributed to the occurrence of twinning and the interaction between twin boundaries and dislocations. The shear banding failure has been observed in the alloy with visco-plastic dragged dimples appearing in the fracture surface, which usually occur in viscous flow. Again, this will be discussed in the following section.

4.3 Adiabatic Shear Banding

In addition to the highly improved mechanical properties obtained in the Mg alloys, the post-mortem examination suggested that those alloys failed in a similar manner, i.e., via shear fracture mode. Obviously, these alloys experienced intense local temperature rise within the fractured banding area based on the fractographic investigation. Thus, the shear fracture may also be called adiabatic shear fracture or adiabatic shear banding. This is due to an intense strain localization or strain instability taking place around the fractured area during plastic deformation. A few factors are required for interpreting the phenomenon appearing in the fracture surface of the alloys: (i) strain localization must occur; (ii) the heat converted from the plastic deformation of the alloys has to be confined within the localized band, thus can increase the temperature in the range only. Therefore, in the next sub-section, the above two points will be testified for these two alloys; thereafter the failure mechanism of the alloys will be discussed; finally a summary will be provided.

4.3.1 Temperature Rise and Heat Diffusion in Shear Bands

It is well-known that when metals are deformed plastically, the mechanical energy is

split into two forms: one is stored in the form of the increased internal energy which is largely due to the dislocation multiplication, while the other is converted into heat and diffuses into the environment. Farren and Taylor [242] have measured that approximately 90% of the work done by the external force may convert into heat in metals during plastic deformation. Thus, there is no doubt that the specimen can be heated up if the heat does not have sufficient time to diffuse into the environment. In this case, it is then easy to bring up the question: for a strain localization process, may the heat be confined within the locally deformed region without noteworthy diffusion into the remaining part of the specimen during the compression? To answer this question, there are a couple of techniques that may be used, such as in-situ measurement or numerical modelling of the temperature evolution of the specimen. Here, a numerical code is developed to model the heat diffusion process.

4.3.1.1 The Estimation of Temperature Rise

In this sub-section, the temperature rise of the alloys within the localized region is presumed in advance based on the experimental observations and the value is estimated. The following equation is used to estimate the temperature rise in the local region:

$$\beta V_{spec} \int_{\varepsilon_{start}}^{\varepsilon_{end}} \sigma_{ij} d\varepsilon_{ij} = \rho V_{loc} \cdot C_{spec} \cdot \Delta T \quad , \quad (4.3)$$

where

β is the ratio of the thermal energy converted from the work done by the applied force, also called the Taylor-Quinney factor;

V_{spec} and V_{loc} are the volume of the specimen and the localized region;

ε_{start} and ε_{end} are the strain at the beginning and at failure of the localization;

σ_{ij} and ε_{ij} are the stress and strain tensors (uniaxial tensor components will be considered only in this work);

ρ , C_{spec} and ΔT are the material density, heat capacity and temperature rise.

It has already been reviewed previously that approximate 90% of the plastic work may be converted into the thermal energy. Thus, assuming complete adiabatic condition, a factor of 0.9 is applied for the Taylor-Quinney factor β . Values of other parameters are employed from the experimental results of AMX602 only for simplification. The width of the shear band of the dynamic specimen here is $\sim 6\text{-}\mu\text{m}$, as indicated by the inset in Fig. 4.6(b). As there is usually a gradient of the strain around the shear band, we apply a width of intensely localized deformation which is ten times the measured shear band width for the calculation. Thus, the volume of the locally deformed region is roughly $V_{loc} = 0.679\text{ mm}^3$. In addition, taking the values of $V_{spec} = 12.5\text{ mm}^3$, $\rho = 1.74\text{ g/cm}^3$, and $C_{spec} = 1.02\text{ J/g}\cdot\text{K}$, and then apply the integration from the point where strain hardening rate begins to decrease, i.e. ~ 0.09 , to the end of strain from Fig. 4.8, one obtains a temperature rise of $\sim 392\text{ K}$ by Eq. (4.3). Considering that the strain localization can be more intense within the center of the shear band, the temperature rise close to the fracture surface could have been underestimated. On the other hand, the melting temperature of Mg alloys is only around 923 K . Thus, there is a large possibility that the temperature at the fracture surface may meet or at least be close to the melting temperature. Nevertheless, the above estimation was based on the presumption that the heat was confined within the localized region during the compression. To confirm the estimation, we performed some numerical simulations on the thermal diffusion during the process.

4.3.1.2 Thermal Diffusion during Strain Localization

The best way to accurately simulate the thermal diffusion around the shear band is to establish the model close enough to the realistic situation. On the other hand, a simulation model cannot be too complicated in the consideration of analyzability. Thus, the model is simplified as shown in Figure 4.22.

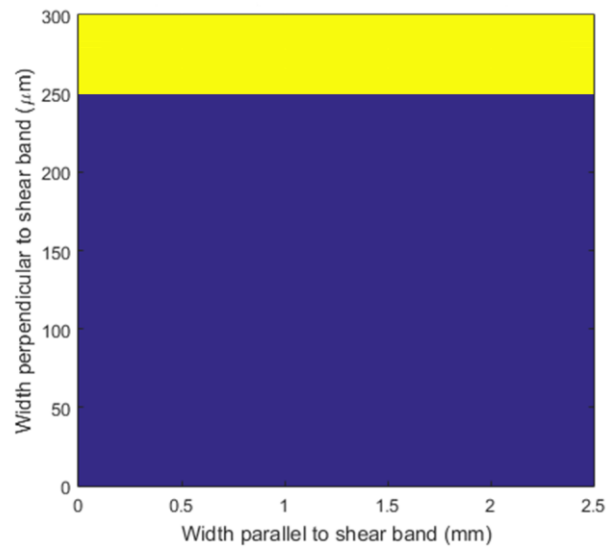


Figure 4.22: A simplified two dimensional illustration of the heated shear banding region (yellow) and unheated remaining region (blue).

The yellow part represents the shear banding where the temperature increases due to the higher plastic deformation than the remaining region (blue part) associated with strain localization. The plastic deformation in the blue area is assumed uniform and the temperature rise is negligible. To investigate the temperature evolution in this system, the two-dimensional heat-transfer equation (4.4) is employed.

$$\frac{\partial u}{\partial t} = \alpha^2 \left(\frac{\partial^2 u}{\partial x^2} + \frac{\partial^2 u}{\partial y^2} \right) \quad (4.4)$$

The numerical Crank-Nicolson method was applied to solve the above equation for this problem, while applying the following initial conditions: the estimated temperature rise is used as the initial temperature for the shear banding region and the initial temperature of the remaining part of the specimen is assumed the same as room temperature, as well as the infinite temperature of the whole specimen. The detailed information of the calculation process and computation code is shown in APPENDIX A.

Figure 4.23 shows the temperature of the localized band at the following time steps:

(a) $t = 25 \mu\text{s}$; (b) $t = 100 \mu\text{s}$; (c) $t = 0.5 \text{ ms}$; (d) $t = 1 \text{ ms}$; (e) $t = 5 \text{ ms}$ and (f) $t = 25 \text{ ms}$.

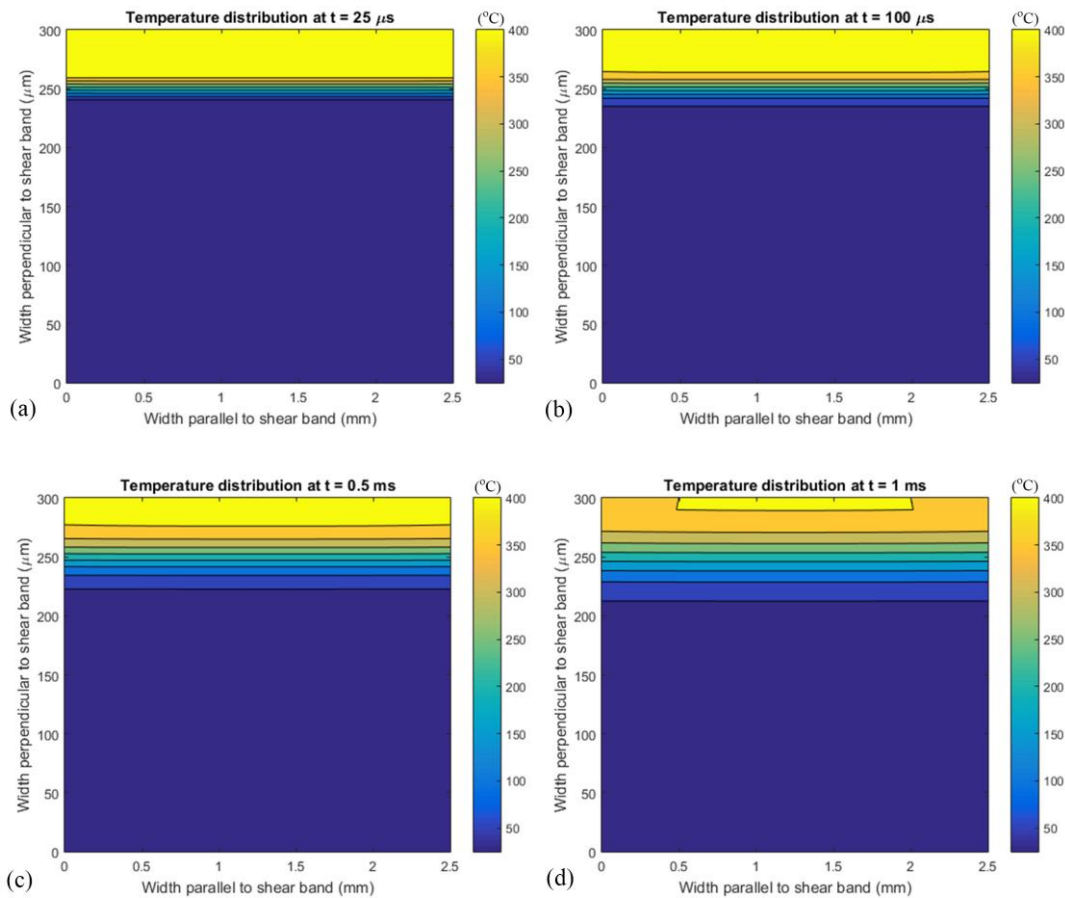
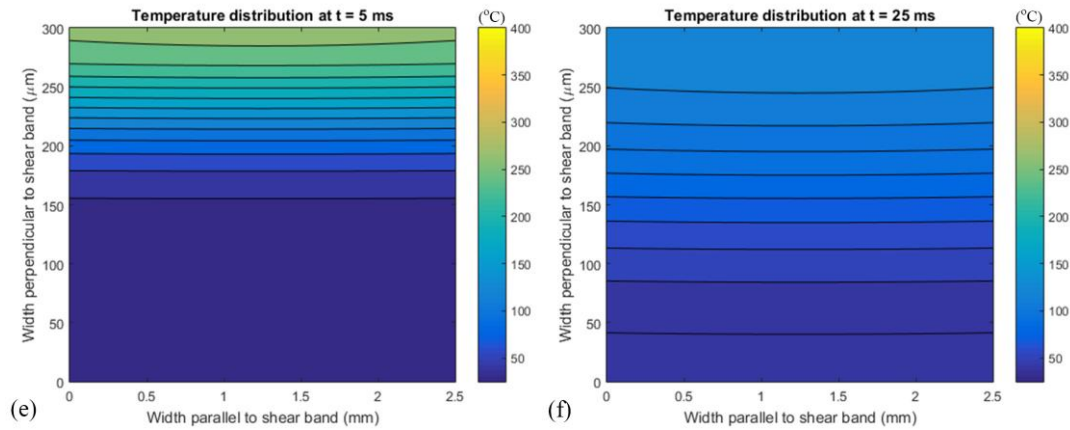


Figure 4.23: The temperature evolution around an adiabatic shear band: (a) $t = 25 \mu\text{s}$; (b) $t = 100 \mu\text{s}$; (c) $t = 0.5 \text{ ms}$; (d) $t = 1 \text{ ms}$; (e) $t = 5 \text{ ms}$ and (f) $t = 25 \text{ ms}$.

(Continued from previous page)



It is obvious that, even after 0.5 ms, the temperature of most region in this shear band does not show significant drop. On the other hand, one dynamic compression test for these alloys lasts no longer than 200 μs . It is noted that the numerical analysis may not truly represent the realistic situation, since the heat or high temperature is progressively accumulated in reality, while it is prescribed in the simulation. However, the computational results indeed suggest one thing: as the heat accumulates increasingly in the localized band due to the non-uniform deformation, it is confined within it, at least during the loading process. That means the dynamic test may be considered to be performed under adiabatic condition.

Based on the numerical analysis, a high temperature rise in the locally deformed area is very possible since most of the work converted into the thermal energy contributes only to the small region. In particular, when the gradient of the strain localization is steep, a sharply increased temperature gradient towards the center of the shear band is predicted. In the above estimation of the temperature rise, we assumed that the strain localization takes place within ten times the width that was measured in dynamically-loaded

AMX602. It gives an estimated value of 392 K. However, when narrowing down the width to about six times width instead of ten, it then gives a value of 616 K. Such a large temperature rise could make the absolute temperature almost near the melting temperature of Mg alloys in the localized zone. Although this approximation may not represent the actual situation, there is no doubt that a very high temperature can be reached within those shear bands. The smooth feature of the fracture surface in Figure 4.7(a) can serve as evidence for local melting during dynamic loading.

4.3.2 Strain Localization in Mg Alloys

The SEM image in Figure 4.24 obviously shows a gradual formation of the localized shear band.

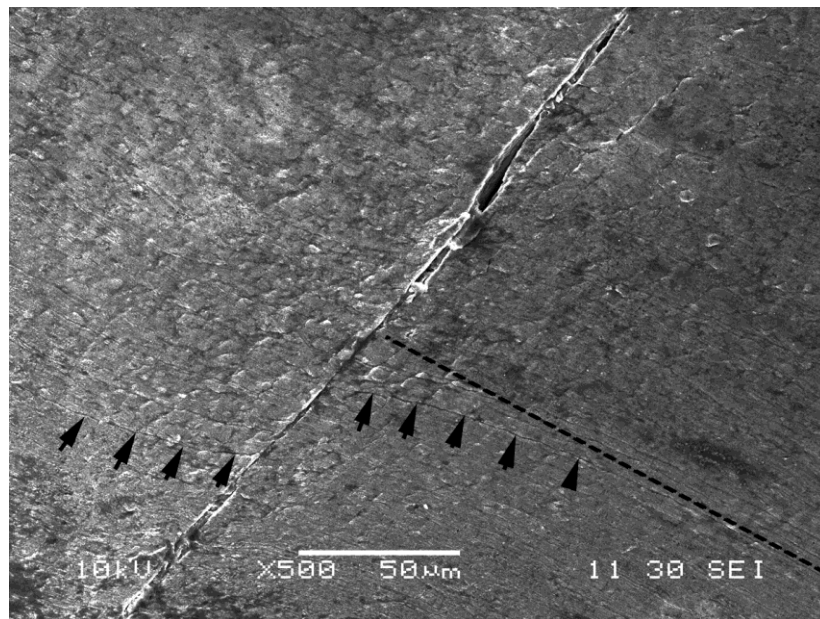


Figure 4.24: SEM image of an incomplete ASB in AZXE7111 (extruded at 250 °C) after high strain rate compression along transverse direction. The image shows evidence of shear flow on both sides of the shear band. That is, the shear band exhibits a “canonical structure” in the sense of Wright [115], where the flow lines curve into the ASB while they curve away from it the other side of the band.

In this image, we can identify the evidence of localized shearing around the ASB. More specifically, we can observe the canonical structure of the ASB in the sense of Wright [137] where the flow lines curve into the band on one side and curve away on the other side of the band. This feature suggests a strain gradient around the fracture line with the maximum in the center. In the previous sub-sections, it has been established that when strain localization takes place at high strain rate loading a higher temperature rise must occur in the localized zone than that in the remaining part of the specimen. It has also been specified many times previously that Mg alloys have a rather low melting temperature, and thus are very sensitive to the temperature in the consideration of their mechanical properties. In accordance to this, the central part of shear bands would be softened more severely than the other parts, which in turn may accelerate the strain concentration at the center. The distinct appearance of the fracture surface, shown in Figure 4.18, from both quasi-static and dynamic specimens strongly suggests that, due to the high temperature rise, extensive plastic flow has occurred at the fracture surface of the dynamically loaded specimen.

4.3.3 Discussion of the Failure Mechanism in the Alloys

Fracture lines, oriented at 45° to the loading direction, were found in both AMX602 and AZXE7111. Through the fracture surface observation and numerical analysis, it suggests that adiabatic shear banding occurred in both alloys under dynamic loading. Nevertheless, the observed physical phenomenon and simulated results may only suggest the occurrence of the adiabatic shear banding, but not clarify the fundamental mechanism that renders it. As reviewed in the introduction chapter, the pre-existing defects and the strain softening factors that outplay the strain hardening factor, i.e. that a negative strain

hardening rate appears, are considered as the primary cause of strain localization. On the other hand, the strain hardening exponent (n) and strain rate sensitivity (m) of the alloys are measured to be larger than 0.2 and 0.03, respectively. According to the models and theories of ASB occurrence available in the literature [137], such materials should be possess strong enough resistance to shear localization unless very strong thermal softening happens. In addition, the stress decrease with strain phenomenon is hardly observed for the alloys, particularly for the quasi-statically loaded specimens. Hence, there must be some other explanations for the observed phenomenon of strain localization in the alloys.

To explore the underlying reason, we employ the model from Molinari and Clifton's work [144], where in this model a pre-existing defect and pre-strain are assumed in the specimen before the distinct onset of shear localization. For example, we can take points A and B to be the defect and perfect (defect-free) locations, similar to the usage in Reference [144]. The area of point A is slightly smaller than that of point B, i.e., $A_A < A_B$. Then, the equilibrium condition (i.e., the balance of forces) at the onset renders

$$\tau_{A0} \cdot A_A = \tau_{B0} \cdot A_B. \quad (4.5)$$

From this equation, it follows that $\tau_{A0} > \tau_{B0}$ and $\varepsilon_{A0} > \varepsilon_{B0}$, as these two points have the same true stress-strain behavior with the strain hardening capacity. Then, if we let the deformation increase to the next point of balance (at time t), with the corresponding strain increments of $d\varepsilon_A$ for point A, and $d\varepsilon_B$ for point B, we have

$$\tau_{At} \cdot A_A = \tau_{Bt} \cdot A_B. \quad (4.6)$$

The corresponding stress increments at these points are then

$$d\tau_A = \Theta_A \cdot d\varepsilon_A, \quad (4.7)$$

and

$$d\tau_B = \Theta_B \cdot d\varepsilon_B, \quad (4.8)$$

where Θ_A and Θ_B are the strain hardening rate at points A and B. Then,

$$\Theta_A \cdot d\varepsilon_A \cdot A_A = \Theta_B \cdot d\varepsilon_B \cdot A_B, \quad (4.9)$$

$$\int_{\varepsilon_{A0}}^{\varepsilon_A} \Theta_A \cdot A_A \cdot d\varepsilon_A = \int_{\varepsilon_{B0}}^{\varepsilon_B} \Theta_B \cdot A_B \cdot d\varepsilon_B. \quad (4.10)$$

Equation (4.10) indicates that when the strain hardening rate is constant or is increasing with strain, the deformation is stable. However, when $\Theta(\varepsilon) > 0$ but is a monotonically decreasing function of strain, the equation may lead to an infinite ε_A corresponding to a finite ε_B , or at least an increasing ratio of the strains between points A and B. In other words, the following inequality may also serve as a critical condition for localized deformation:

$$0 < \frac{d\tau_A}{d\varepsilon_A} < \frac{d\tau_B}{d\varepsilon_B}. \quad (4.11)$$

As is observed in the strain hardening rate vs. strain curves for both alloys, the strain hardening rates of both alloys begin to decrease at a strain between 0.08 and 0.09. Thus, we may propose that the strain hardening rate is perhaps the main reason that leads to the shear localization failure of the alloys. This could also explain why the shear localization takes place even at low strain rates. For sure, under dynamic loading condition, the high temperature generated within the shear band due to strain localization can make the area to show viscous flow behavior. Again, this is supported by the appearance of the fracture surface of dynamically loaded AZXE7111, shown in Figure 4.18(b). On the other hand,

according to the simulated result, the heat can diffuse into the remaining regions of the specimen in less than a few hundreds of micro-seconds, thus causing a fast drop of the temperature in the narrow region. By considering that all of the heat converted from plastic work is used to heat up the whole specimen, the temperature rise would be about 42 K. It means that the temperature of the narrow region may drop to about 335 K (293 K+42 K) within dozens of microseconds. Such a temperature drop can definitely lead to a thermal shock, leading to a strain of at least 2.5% in the narrow region, which is accomplished at a very fast cooling rate. Hence, there must be no doubt to have a high internal stress in the cooled shear band that has been melted during the dynamic compression. This high internal stress is probably the cause of the micro-cracks observed in Figure 4.6. On the other hand, under quasi-static loading it has enough time to diffuse the heat so that the temperatures rise in the specimen was negligible. That is why there were no adiabatic molten features but only ductile dimples showing in the fracture surface under quasi-static loading.

4.3.4 Hypotheses on the Formation of ASB

In this sub-section, the formation of ASB will be viewed from two perspectives: the micro and the macro views. Through the micro-view of the ASB formation, the microstructural aspect will be mostly considered, while through the macro-view the stress state within the ASB will be discussed. After the discussion, we will then bring out some hypotheses on the formation of ASB.

It has been well reported that materials exhibiting propensity to strain instability also have some common properties, such as low or negative strain hardening rates, low strain rate sensitivities and probably low thermal diffusivity [137]. However, it is noticed that

one part of the research works has focused on the stabilizing factors to the strain instability by examining the macroscopic physical parameters through physical tests or numerical analysis, while the other part has focused on the evolution of the microstructure along the ASB. Thanks to those works, now we have a comprehensive understanding about what are the suppressers and what are accelerators to strain instability, as well as how the microstructure changes when the ASB occurs. One remaining question is where and how an ASB starts in terms of the microstructure. It has been reported that the defects causing non-uniform stress distribution can all be the initiators [144], while the strain hardening and high strain rate sensitivity are suggested to suppress the unstable deformation. However, if looking down into the microstructure level, the instability may be caused by different deformation mechanisms between the localized and the surrounding areas. For example, Cao et al. [243] found in metallic glass that structural softening may precede thermal softening as the primary reason for shear banding. In addition, a recent publication on modeling the formation of strain localization in HCP metals [244] found that twin clustering is the primary cause of strain localization, which eventually leads to crack initiation and failure. This result agrees with what Qu et al. [245] found by using molecular dynamics (MD) simulations. In this case, it is probably reasonable to argue that geometric softening, i.e. deformation mechanism induced softening, is an optional cause for the formation of shear banding in highly work-hardening metals like Mg alloys. For sure, this hypothesis still needs to be tested thoroughly through multiple experiments.

On the other hand, from the stress-state view around the adiabatic shear band, there is an important scenario that has not been examined seriously, i.e., the non-equilibrium

stress state. Commonly, researchers determine the initiation of shear localization by using the macro stress strain curve combined with in-situ imaging techniques. In the treatment, the stress is treated as uniform in the sample along the loading direction. Nevertheless, the stress distribution cannot be uniform around the shear localization zone. Particularly, in those experiments where irregular specimens are used, such as hat-shaped specimens [246]. It is clear that the non-uniform and concentrated stress triggers strain localization. Due to this, using macro stress strain curves to analyze strain instability problems may not be the correct way. An in-situ stress analysis around strain localization zone may be required to better understand the macro-behavior of shear banding.

4.4 Discussion and Conclusions

It has been shown that both Mg alloys of AMX602 and AZXE7111 have balanced mechanical properties between strength and ductility. Table 4.3 displays a collection of the strengths of two conventional Mg alloys (AZ91E and WE43) that have also been tested as controls along with AMX602 and AZXE7111 for the purpose of comparison.

Table 4.3: Yield and maximum compressive strengths of two conventional alloys, under quasi-static and dynamic compressive loading conditions (data in units of MPa)

Mg Alloy	Quasi-Static				Dynamic			
	Yield Strength ($\sigma_{0.2\%}$)		Maximum Strength		Yield Strength ($\sigma_{5\%}$)		Maximum Strength	
	Flow	Trans.	Flow	Trans.	Flow	Trans.	Flow	Trans.
AZ91E	178 \pm 0	164 \pm 0	396 \pm 1	423 \pm 0	314 \pm 3	340 \pm 5	454 \pm 5	403 \pm 0
WE43	168 \pm 6		302 \pm 2		254 \pm 0		360 \pm 0	

Comparing the results with that of Table 4.1 and Table 4.2, it is obvious that the SWA processed Mg alloys exhibit extraordinary strength levels. Although there are some

differences between the SWA alloys and the conventional alloys in terms of their ingredients, it is the unique microstructure that produced by the SWA technique and subsequent procedures that eventually renders the superior properties of AZXE7111 and AMX602. Our studies suggest that two primary reasons, i.e., ultrafine grained structure and formation of in-situ intermetallic compounds of size ≤ 100 nm, are responsible for the improved mechanical properties. The first one is attributed to the ultrafast cooling of the alloy melt that suppresses the grain growth, whereas the second may be due to the hot extrusion process which not only densifies the product but also promotes the formation of nano-sized precipitates, which contribute to microstructure from the dynamic recrystallization. Microstructural examination has indeed revealed uniformly distributed equiaxed grains in these alloys, which are generally found in fully recrystallized metals upon annealing. On the other hand, owing to the formation of nanoscale particles, the grain growth was impeded during the hot extrusion process, and the recrystallized grains were thus kept under sub-micron. It is worth noting that only because of the powders produced during SWA process and consolidation at room temperature that eventually lead to a high volume of distorted and unstable GB interfaces in the green compact, which subsequently promote dynamic recrystallization at elevated temperatures in the hot extrusion process. Thus, the production of the Mg alloys with decent mechanical properties is a consequence of the combination of the SWA technique, consolidation at cold or room temperature and the hot extrusion. However, all these factors are rooted in the chemical composition of the alloys. Pure Mg examined in the previous section was completely recrystallized as well and has a grain size in the order of ~ 4.5 - μm . Applying Eq.(4.2), the difference of strength increment between the pure Mg and SWA Mg alloys

from grain refinement can be estimated as follows:

$$\Delta\sigma_{GF} = (6.0MPa \cdot mm^{1/2}) \cdot \left(\frac{1}{\sqrt{1.0\mu m}} - \frac{1}{\sqrt{4.5\mu m}} \right) \approx 100MPa. \quad (4.12)$$

This value is smaller than the difference of the yield strength between the pure Mg and SWA Mg alloys, which is more than 140 MPa. That is to say, the strength improvement in SWA Mg alloys is not uniquely from grain refinement, but the addition of alloying elements as well. It is reasonable because the addition of alloying elements increases the CRSS of the slip systems [16, 247], which as a result increases the intrinsic strength, σ_0 , in Eq.(1.1). The microstructural examinations through TEM and EDS techniques both revealed intermetallic compounds in AMX602 and AZXE7111 alloys. The similarity of the dimension of both grains and precipitates in those alloys consequently produced somewhat similar mechanical properties: comparable yield and ultimate strengths, transition from easy-glide to rapid hardening and equivalent compressive strains.

Nevertheless, there are still some differences between those Mg alloys. For example, regardless of the same materials processing, the AMX602 Mg alloy exhibits roughly 17% higher strengths along flow direction than those along transverse direction, whereas the AZXE7111 shows minor strength anisotropy. Figure 4.9 has displayed the pole figures of the AZXE7111 alloy, indicating a very soft texture. Even though the XRD measurement was not performed for the AMX602 and the texture property of the alloy was not entirely understood, the elongated spots or arcs shown in the SADP of the alloy (see Figure 4.1(b)) indeed indicates the textured microstructure; whereas only scattered spots show up for the matrix of AZXE7111 in the SADP shown as an inset in Figure 4.12(a). The addition of the rare earth element, La, is held responsible for the improvement of texture based on two reasons: first, rare earths have been extensively proved effective in the property

improvement of Mg alloys by softening the texture [27, 74, 248, 249]; second, while the underlying mechanism of rare earths on modifying the microstructure is still an open question, the role of rare earths on improving ductility has been partially uncovered. Sandlöbes et al. [52] studied the relation between ductility and stacking fault energies in Mg the Mg-Y alloy, whereas a reduction of I_1 intrinsic stacking fault energy was discovered with the addition of element Y that promotes the ductility of Mg-Y alloy. Then, they further accomplished an investigation about the development of stacking fault energies in Mg with an addition of different elements [185], where they concluded that all studied rare earth and RE-like elements reduce the I_1 stacking fault energies and render similar HCP phases while the other elements increase the I_1 stacking fault energies. With the addition of RE-elements, the room temperature ductility of Mg was improved by up to 4 ~ 5 times compared to pure Mg.

In addition, the adiabatic shear failure in the alloys has been studied in terms of the temperature rise, the occurrence of strain localization and the associated mechanism. It is found that, under dynamic compression, the shear localization process can be viewed as adiabatic in these alloys, and the temperature rise in the region can be remarkable. On the other hand, the primary reason leading to localized straining in such strain hardening materials can probably be the deformation mechanism induced non-uniform plasticity. Yet, more investigations are required to confirm the hypothesis.

CHAPTER 5: MG-BASED METAL-MATRIX COMPOSITES

To enhance the creep resistance of Mg alloys due to their relatively low melting points, attentions have been given to Mg-based composites using nanocrystalline ceramic particles as reinforcements. The pioneer work of Ferkel and Mordike [250], for example, shows increased creep resistance by adding SiC nano-particles into Mg matrix to form a Mg-matrix composite, or metal matrix nano-composites (MMNCs). The composite is processed by milling Mg powders and SiC nano-powders together followed by warm consolidation. Microstructural analysis shows that the nano-particles of SiC reside in the vicinity of the grain boundaries of the Mg matrix, which leads to two orders of magnitude increase in creep resistance vis-à-vis that of pure Mg. The work of Ferkel and Mordike has been followed by a slight flood of publications using the concept of metal-matrix composite (MMC) to improve the mechanical properties of Mg alloys. Other reinforcement media have been explored, including Al₂O₃, yttria (Y₂O₃), titanium (to improve ductility) and so forth [251-255]. Fabrication techniques used to this end include ball co-milling of Mg and the ceramic nano-particles followed by consolidation, stir casting, ultrasonic assisted casting and injection molding and so forth [256-259]. More recently, Dieringa has provided a comprehensive review on the brief history as well as the state-of-the-art of Mg-based nano-composites [260]. Mg-based MMCs have also been investigated by other groups in order to evaluate the effect of different reinforcements, of their size, shape and volume fractions, on the mechanical properties of the composites

[257-259, 261-265]. As one of the most outstanding merits of Mg-based MMC/MMNC is its light weight, potential applications in body and vehicle armors have been expected. For such applications, as well as applications in aircraft industries, impact-loading conditions are frequently encountered. However, only limited efforts could be identified in the literature on the dynamic mechanical properties of Mg-based alloys in general, and of Mg-based MMNCs in particular [241, 266]. In light of this, we examined the high-strain rate (dynamic) mechanical properties of the processed Mg-MMCs/MMNCs by the SHPB (or Kolsky bar) system. In this chapter, the microstructure, mechanical properties, and fracture manners of Mg-based MMCs/ MMNCs will be presented and summarized.

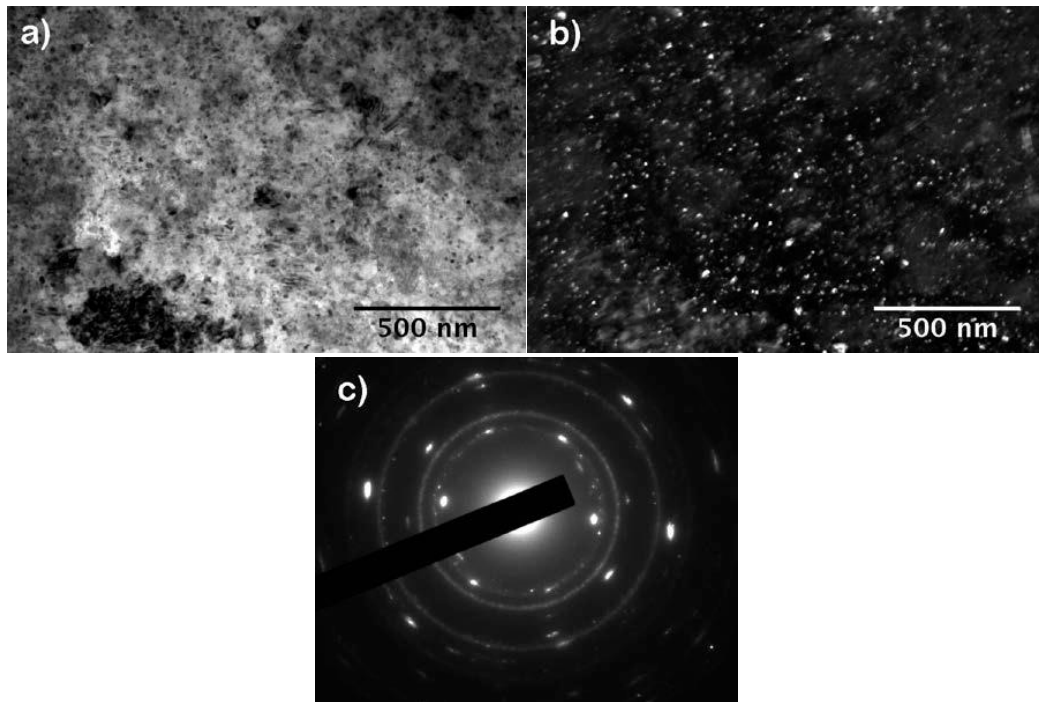


Figure 5.1: (a) Bright field TEM image of 5 vol. % SiC MMNC. The nano-particles appear to be uniformly distributed within the matrix. Some large agglomerates of the Mg-matrix are present. (b) Dark field TEM image corresponding to (a). The dark bright particles are the nano-particles of the β -SiC phase. (c) Selected area diffraction pattern of the sample. This pattern can be indexed according to the cubic β -SiC phase and the hcp Mg matrix.

5.1 Materials Characterization

Figure 5.1(a) displays the bright field TEM image of Mg-based MMNC with 5 vol.% SiC nano-particles. The inset is the selected area diffraction pattern (SADP). It shows that the SiC particles are very fine as suggested by the continuous rings in the SADP as well as the bright and dark field TEM micrographs. It also shows that the grain size of the Mg-matrix is very fine. Figure 5.1(b) is the corresponding dark field TEM image taken using diffracted electrons from the SiC phase. Again it shows the nanometer size SiC particles. Indexing of the SADP suggests that the SiC phase is of the cubic lattice structure. Both the bright field and dark field TEM micrographs suggest that the nano-particles of SiC are uniformly distributed in the MMNC. Some large particles of Mg with a high density of defects (presumably dislocations) are present in this sample, indicating some agglomerations of the matrix phase during the co-milling process even in the presence of the process control agent. Growth might have occurred during the warm consolidation process that led to the current observed particle size. No significant agglomeration of the SiC particles can be identified in this sample.

Figure 5.2(a) presents the SiC particle size distribution of the Mg-5 vol.% SiC MMNC sample based on statistics of the TEM images. As we have mentioned in Sec. II, the starting SiC particles have an average particle size of ~20 nm. It follows from Figure 5.2(a), then, that the SiC particles have been further refined during ball-milling, as the majority of the particles in the MMNC have size smaller than 20 nm. Figure 5.2(b) shows the inter-particle spacing distribution of the Mg-5 vol. % SiC MMNC sample based on statistics of the TEM images. It suggests that the majority of the particles have inter-particle distance smaller than 100 nm. This observation should be translated into an

effective grain size of the Mg-based MMNC smaller than 100 nm. This is broadly in line with our x-ray diffraction line-broadening analysis results, which provide an average grain size for Mg matrix of the order of 57 nm.

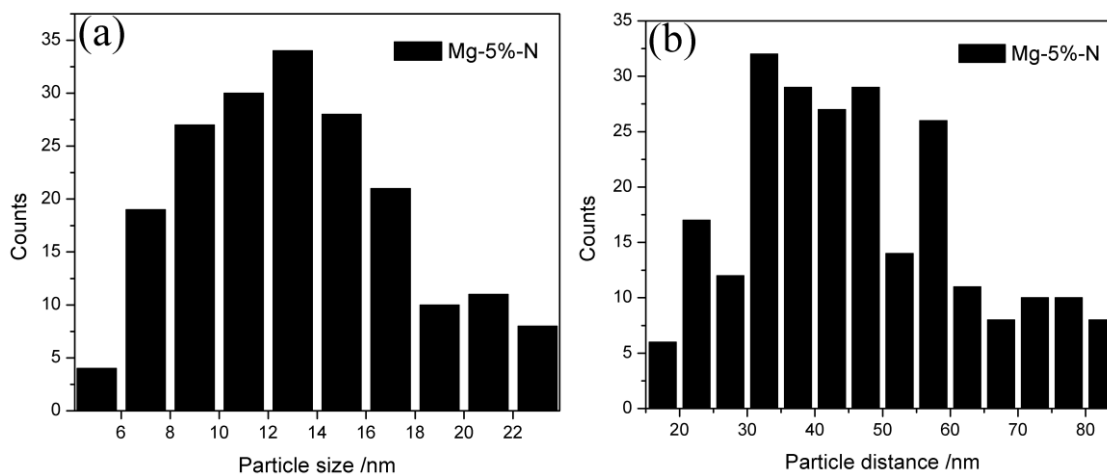


Figure 5.2: (a) Particle size distribution in the Mg-5 vol% SiC MMNC. Most of the particles have been refined during the comilling process as the start SiC powder has an average particle size of ~ 20 nm. (b) The distribution of the interparticle distance in the Mg-5 vol% SiC MMNC. It shows that the interparticle distance is mostly below 60 nm.

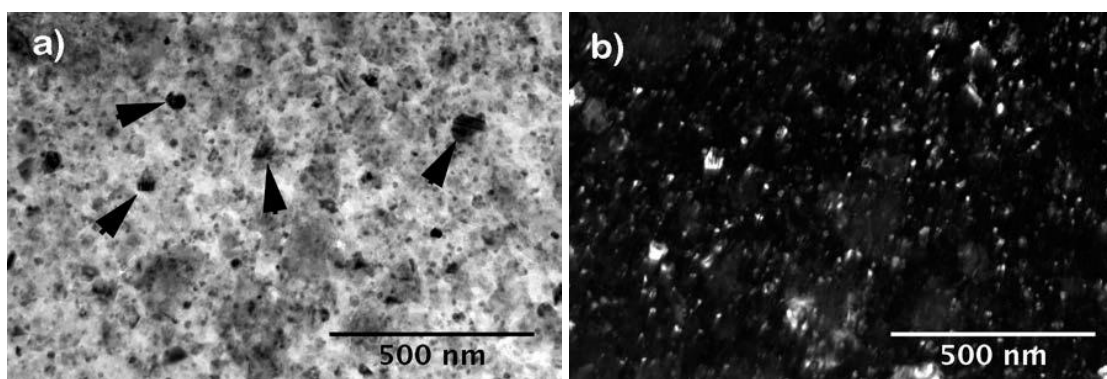


Figure 5.3: (a) Bright-field TEM image of the Mg-10 vol% SiC MMNC. Again the nanoparticles of the β -SiC phase appear to be uniformly distributed. However, large particles are seen in this material, with some of the large particles marked by black arrows. (b) Dark-field TEM image corresponding to (a). The bright particles in the dark-field TEM image is the β -SiC phase.

Figures 5.3(a) and 3(b) are the bright field and the corresponding dark field TEM micrographs of the Mg-10 vol% SiC MMNC sample. The SADP (not shown here) shows again continuous rings for the SiC phase with a cubic structure. The particle size distribution of this sample is quite similar to that of the Mg-5 vol% SiC MMNC sample, and is thus not included here. This is not surprising as the particle size of the SiC phase should primarily depend on the milling time with other conditions kept the same. Comparing Figure 5.1(a) and Figure 5.3(a), we can see the latter have some ~100 nm or smaller particles with irregular, faceted shapes (some of them are marked by arrows). That is to say, with increased volume fraction of the ceramic phase, agglomeration of the nanoparticles of SiC has occurred during the co-milling process. It might also be possible that such particles were the pre-existing particles in the starting ceramic powder which somehow survive the co-milling process without breaking-up. As a matter of fact, this surmise is more reasonable as we will show later that such particles are single crystal particles, thus unlikely to be formed by agglomeration during the co-milling process. A detailed TEM analysis will be presented on such large SiC particles when we describe the microstructures of the Mg-15 vol% SiC MMNCs sample. Less agglomeration of the Mg matrix phase has been observed in this sample. This is understandable as increased volume fraction of the SiC nanoparticles can both prevent agglomeration of the Mg phase and retard its further growth during subsequent growth, as the SiC nanoparticles can work as grain boundary pinning centers (Zener pinning effect). The interparticle distance of this sample is smaller compared with the previous sample, with the distance in majority of the cases being smaller than 60 nm. Again this is consistent with our XRD line profile analysis results, which suggest that the volume average grain size of the Mg-matrix is

about 43 nm.

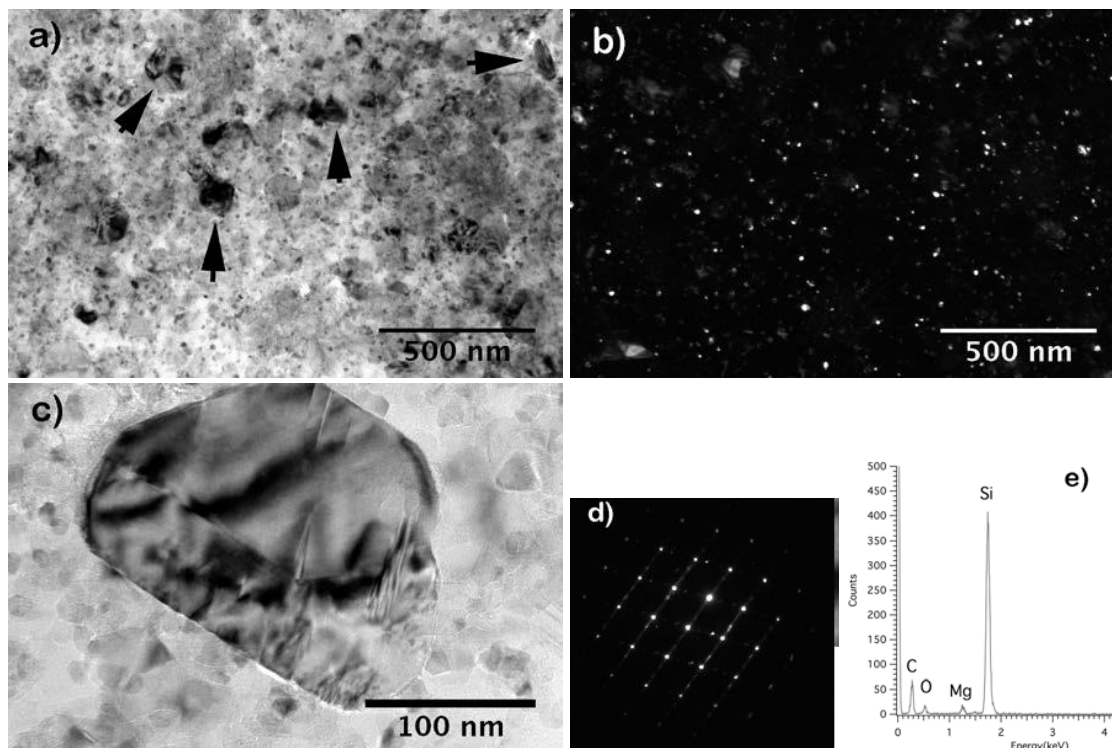


Figure 5.4: (a) Bright-field TEM image of the Mg-15 vol% MMNC sample. Again large particles with size around ~ 100 nm are seen. Some of these large particles are marked by arrows. (b) Dark-field TEM image of (a), the bright particles being the b-SiC phase. (c) An enlarged view of one of the large particles in this material. It is faceted, with stacking faults or twinning in the particle. (d) SADP from the faceted particle of (c), which is from the [011] zone of the b-SiC cubic phase. This SAD pattern can be indexed to be from two twinned crystals. (e) Energy-dispersive spectroscopic result from the particle of (c). It shows clearly that the particle is the b-SiC cubic phase.

Figure 5.4(a) is the bright field TEM image of the Mg-15 vol.% SiC MMNC, with Figure 5.4(b) being the corresponding dark field image. Similar to the previous sample, some ~ 100 -nm SiC particles are observed in this sample. To confirm that such large, faceted particles are indeed the SiC phase, we have performed some detailed analytical TEM examinations on one such particle. Figure 5.4(c) is a bright field TEM micrograph

of such a particle. The particle is clearly faceted. Figure 5.4(d) is the diffraction pattern of this particle. This diffraction pattern is indexed to be from the [011] zone of the cubic SiC phase (zinc blende structure). It should be noted that this particle, as well as many other such particles of similar size, has single crystal structure. It is thus unlikely that they were formed by agglomeration during the co-milling process. Further, Figure 5.4(e) is the energy dispersive X-ray spectroscopy (EDS) result of this particle. It clearly shows that it is the SiC phase. Therefore, we believe that such relatively large SiC particles come from the starting ceramic powder and have survived the co-milling process. The primary particle size distribution (not included here) is similar to that of the previous two samples, which can be explained in a similar manner. The inter-particle spacing of the majority of the nanoparticles is smaller than 45 nm. This interparticle spacing result is consistent with the XRD peak broadening analysis result for this sample, which gives an average grain size of the Mg matrix of the order of 26 nm. It should be kept in mind that XRD analysis tends to underestimate the grain size of severely deformed samples as compared with TEM examination [267].

Finally, Figure 5.5 presents the SEM micrographs of pure Mg consolidated from 20-hour ball milled Mg powders (a), and Mg-based MMNC samples with 5 (b), 10 (c) and 15 (d) vol% SiC nanoparticles, respectively. Figure 5.5(a) just suggests single phase Mg metal. The rest of the images included in this figure indicate that with increased volume fraction of the SiC nanoparticles, Mg-agglomerates decreased, and the size of large Mg particles is also decreased. This is qualitatively consistent with the TEM analysis. However, the nanoparticles of the SiC phase are beyond the resolving power of the SEM.

It should be pointed out that neither TEM nor SEM reveals significant evidence for

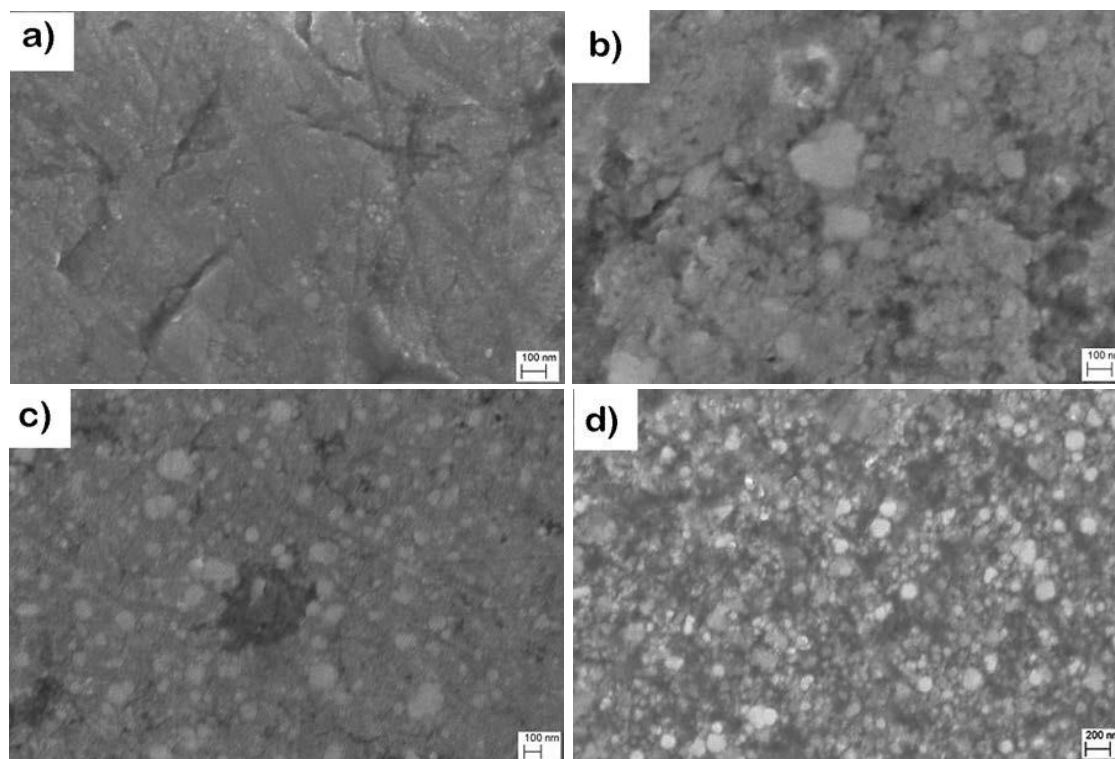


Figure 5.5: Scanning electron micrographs (back scattered images) of consolidated pure Mg (a), Mg-5 vol% SiC MMNC (b), Mg-10 vol% SiC MMNC (c) and Mg-15 vol% SiC MMNC, respectively. In (b–d), the lighter particles are the SiC particles due to charging effect (SiC is an insulator). Thus we can see that the as-processed MMNC samples have some large reinforcement particles. Notice the scale bar of (d) is different from other images.

porosity in the processed MMNCs.

In summary, our TEM and SEM examinations show that the size of the SiC reinforcements has been further reduced by co-milling with the matrix phase. The final particle size seems not changed with the volume fraction of the SiC phase. The inter-particle distance of the 5-vol% SiC MMNC is smaller than 100 nm, and the inter-particle distance of the Mg-based MMNC decreases with increase in the volume fraction of the SiC nanoparticles. Agglomeration of the matrix phase has been observed primarily in the 5-vol% SiC MMNC, where TEM reveals Mg-particles of ~ 100 nm or larger diameter. It

appears that some large SiC particles, with average size greater than 100 nm, have survived the co-milling process. This has been confirmed both by diffraction analysis and EDS results. The high processing temperature might have led to recrystallization of the Mg matrix [78], but dislocations might have been generated during cooling because of the mismatch of the coefficients of thermal expansion between Mg and the SiC particles [268].

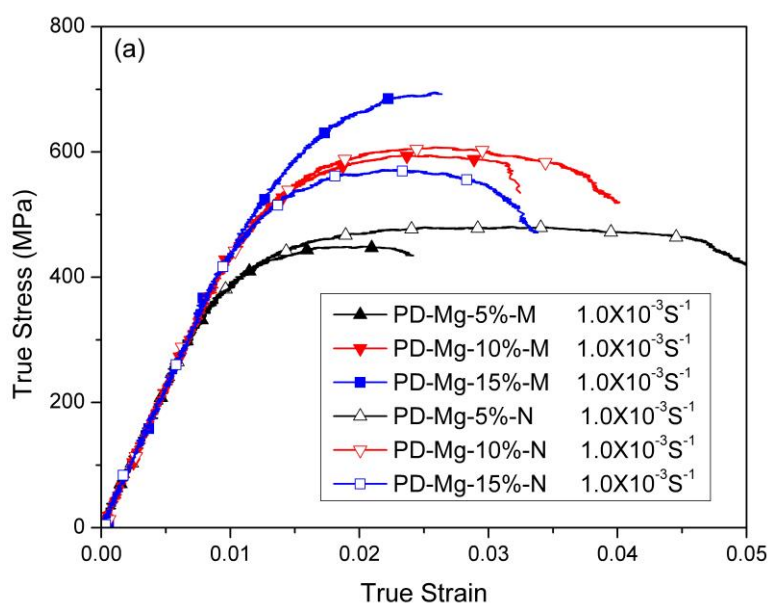


Figure 5.6: Quasistatic true stress-strain curves of the micro- and nanoparticle-reinforced Mg-based composites. The curves with solid symbols are for the conventional MMCs, whereas those with hollow symbols are for the nanoparticle-reinforced MMNCs. PD means the loading is in the hot pressing direction.

5.2 Mechanical Properties

Figure 5.6 displays the representative quasi-static true stress-strain curves of the Mg-based MMNC, along with the MMC control samples. In this plot, the last capital letter of the legend of each sample, M or N, means the sample is either the MMC (M) or MMNC

(N). PD stands for “pressing direction”, indicating that the loading direction during mechanical testing is along the hot-pressing direction during materials processing. It can be observed that for the nano-composites, the compressive plasticity, or malleability, of the samples decreases with increased volume fraction of the SiC nanoparticles. The MMNC sample with the lowest volume fraction of SiC (5%) exhibits the lowest strength. The 10 vol% SiC MMNC sample shows much higher strength than the 5 vol% SiC sample. However, further increasing the SiC volume fraction renders saturation of the strength of the MMNCs, as the strength of the Mg-15 vol% SiC MMNC sample is even lower than that of the Mg-10 vol% SiC MMNC sample. Similar results have been reported in an Al-based MMNC. Possible reasons for this will be provided in a later section. This is in sharp contrast with the conventional MMC as suggested by the stress strain curves in Figure 5.6. With the increase of the volume fraction of the SiC particles, the strength of the conventional MMC keeps increasing, showing no sign of saturation. Overall, the malleability of the MMNC samples is improved in comparison with their conventional MMC counterparts of the same volume fraction of the reinforcement phase. Whereas the strength of the nanocomposites containing 5 and 10 vol% ceramic phase is slightly higher than that of the microcomposites with the same amount of microsized ceramic particles, the strength of the nanocomposites containing 15 vol% of ceramic nanoparticles is much lower than that of the microcomposite containing the same amount of ceramic microsized particles. However, all the samples exhibit quite poor malleability.

It should be noted that all the tested samples failed during quasi-static compressive loading.

Figure 5.7 gives the representative high strain rate true stress-true strain curves of

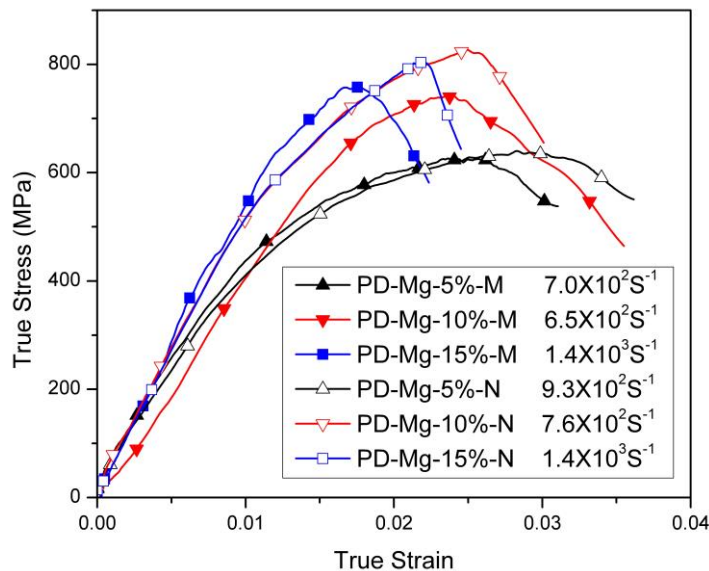


Figure 5.7: High-strain-rate true stress-strain curves of the Mg-based composites. The solid symbols are for the conventional MMCs reinforced with microsized SiC particles (M in the legend), and the hollow symbols are for the nanoparticle-reinforced MMNCs (N). As the materials are very brittle, all samples pulverized upon high-strain rate loading. In these samples, only the peak stresses are used to indicate the dynamic strength of the samples.

Mg-based MMNC samples along with those of the MMC controls. Again, the loading direction is in the hot-pressing direction. It shows that under dynamic loading, all the samples are quite brittle and show little or no observable plastic deformation. In the MMNC samples, the dependence of the peak stress on the volume fraction of the nanoparticle SiC exhibits trend similar to that of the quasi-static strength. That is to say, with increased volume fraction of SiC nanoparticles, the dynamic peak stress of the MMNC increases, but it saturates at high volume fraction, as the dynamic peak stress of the Mg-15 vol% SiC MMNC sample is slightly lower than that of the Mg-10 vol% SiC MMNC sample. Again, such behavior is in contrast with the conventional MMC samples. All dynamically loaded MMC and MMNC samples were pulverized.

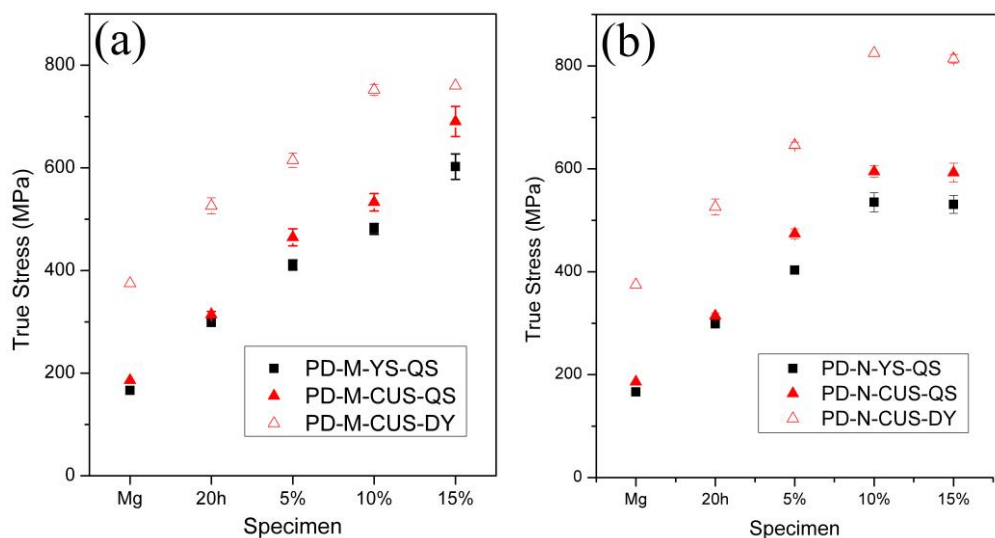


Figure 5.8: (a) Yield strength (YS) and Compressive ultimate stress (CUS) of the conventional Mg-based MMC reinforced with microsized particles samples; and (b) those Mg-based MMNC samples reinforced with nanoparticles of SiC. Mg means pure, as received Mg. 20 h means pure Mg milled for 20 h followed by warm consolidation. DY means dynamic loading. All samples were loaded in the hot-pressing direction (PD). 5, 10 and 15% are the volume fraction of the reinforcement phase.

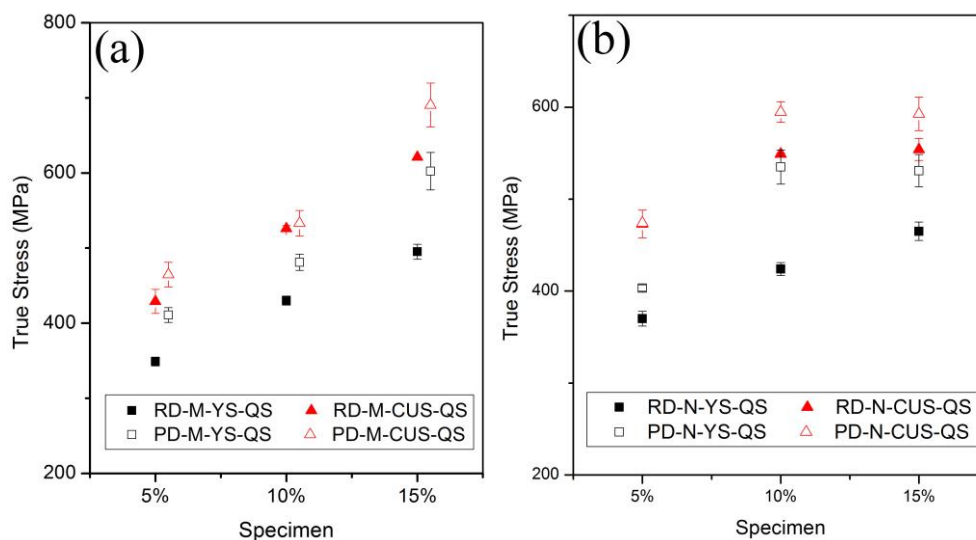


Figure 5.9: Comparison of the strength of the conventional Mg-based MMC samples (a) and the nano-particle reinforced Mg-MMNC samples (b) between the pressing direction and radial direction. In either case, the PD samples are consistently stronger than their RD counterparts, indicating some anisotropy in the mechanical properties of the hot pressed materials.

To facilitate comparison among the samples, we have collated the quasi-static yield strength (YS) and compressive ultimate strength (CUS), as well as the dynamic (DY) compressive ultimate strength (or peak stress). Figures 5.8(a) and (b) show the compressive quasi-static (QS) yield strength and CUS and the dynamic CUS as a function of the volume fraction of the β -SiC particles for the Mg-based MMC controls and the MMNC samples, respectively. All samples were loaded in the pressing direction. In these two plots, below the abscissa, Mg stands for the as received pure Mg; 20h designates the 20-h ball-milled pure Mg followed by consolidation; 5, 10 and 15% are the volume fractions of the SiC reinforcements. Figure 5.8(a) suggests that ball-milling of the pure Mg-powder increases the quasi-static yield strength and maximum stress, as well as the dynamic peak stress. It also shows that the strength of the conventional Mg-based MMCs increases almost linearly with the volume fraction of the micro-sized SiC particles. The leveling off of the dynamic peak stress of the conventional MMC at higher SiC volume fraction might be due to early failure of the specimen under dynamic loading. On the other hand, for the nanoparticle-reinforced MMNCs, all strength values saturate at high SiC volume fractions. Figure 5.8(b) shows that the QS yield strength; the QS and dynamic CUS of the 15 vol% SiC MMNC samples are all lower than those of the 10 vol% SiC MMNC samples. It then means that strengthening effect of the SiC nanoparticles saturates beyond ~10 vol%.

Due to the asymmetric stress distribution of the material during the hot-pressing consolidation process, density and microstructure of the product may be anisotropic, leading to anisotropic mechanical behavior. In view of this, we have also tested samples in the radial direction. Figure 5.9 displays the collection of quasi-static strength data in

the pressing direction (PD) and radial direction (RD). Figure 5.9(a) indicates that for all the compositions, the conventional Mg-based MMC samples are stronger in the pressing direction than in the radial direction. The MMNC samples exhibit a similar trend.

It is interesting to notice from a comparison between Figure 5.8(a) and Figure 5.8(b) that, under uniaxial quasi-static compressive loading, the strengths of the MMNC samples with 5 vol% β -SiC nanoparticles are almost the same as those of MMCs with the same volume fraction of microparticle of SiC. However, at 10 vol% SiC, the strengths of the MMNCs surpass those of the MMCs (see Figure 5.8). However, as the volume fraction of β -SiC phase is increased to 15 vol%, the strengths of the MMNC samples become lower than those of the MMCs. In other words, this indicates that the strengthening effect of the nanoparticle SiC reinforcement has reached its limit somewhere between 10 and 15 vol%, as we have mentioned previously. On the other hand, the high-rate strength or peak stress values of MMNC samples are higher than those of the MMC samples for all the volume fractions of the SiC phase. This observation suggests that the nanoparticles of SiC are more effective in strengthening the Mg matrix at dynamic loading rates. In other words, the MMNC samples show stronger rate dependence than the MMC samples.

5.3 Post-loading Examination

For investigating the fracture process of the MMNC samples, we have performed detailed SEM analysis of the fracture surfaces of the MMNC samples with different volume fractions of the nanoparticle SiC phase. As the dynamic samples were all pulverized upon high-strain rate compression, in what follows, we will focus on the quasi-static samples.

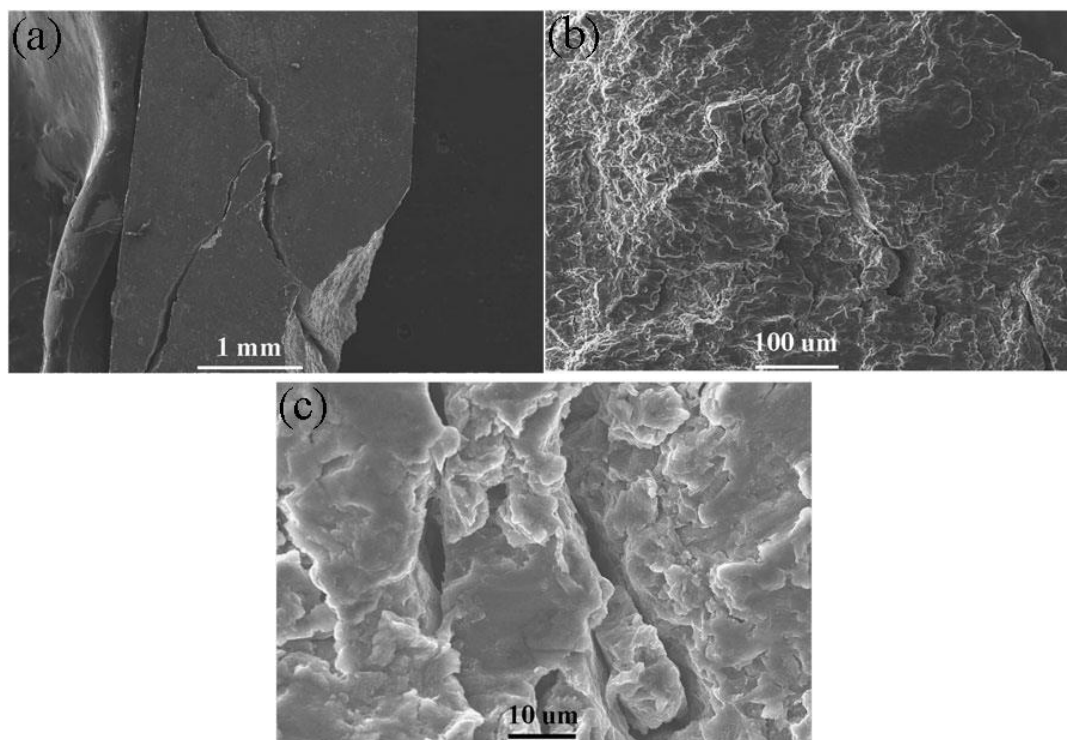


Figure 5.10: (a) Low-magnification SEM micrograph of the fractured specimen of Mg-5 vol% SiC MMNC partially recovered after quasi-static loading. The sample was broken into several pieces. Loading was roughly in the vertical direction. This low-magnification SEM image reveals off-axis cracks, presumably initiated from the specimen corners. (b) Medium-magnification SEM micrograph of the same sample, showing microcracks on the fracture surface. (c) High-magnification SEM micrograph of multiple microcracks. All images show minor evidence for ductile fracture.

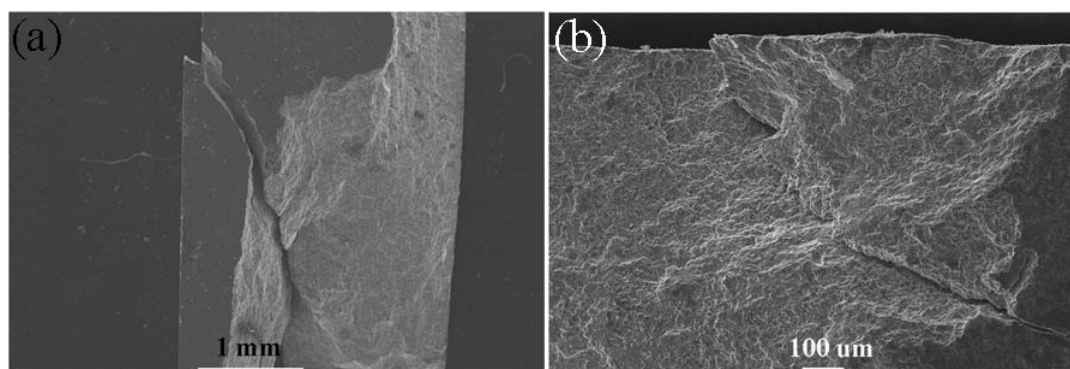


Figure 5.11: (a) Low-magnification SEM of a fractured sample of Mg-10 vol% SiC MMNC partially recovered after quasi-static loading. Loading is roughly in the vertical direction. (b) An enlarged view of fracture surface to show the macrocrack. Loading was in the horizontal direction in (b). No strong evidence for ductile fracture can be found in this sample.

Figure 5.10 displays SEM images of the fracture surface of a representative Mg-5 vol% SiC MMNC. The sample was broken into two pieces. The low-magnification SEM image (Fig. 5.10(a)) shows some degree of roughness of the fracture surface of this sample. No macro-cracks are visible from the low-magnification SEM micrograph. An enlarged view (Fig. 5.10(b)) shows a few micro-cracks on the fracture surface. Figure 5.10(c) displays multiple micro-cracks.

Figure 5.11(a) is an overview of one half of the whole fractured sample of Mg-10 vol% SiC MMNC. Loading was in the horizontal direction. The fracture surface is quite flat. It appears that the sample was fractured along a major plane, as a primary crack can be observed at the top right corner of the specimen. Figure 5.11(b) presents an enlarged view of the primary crack.

Figure 5.12(a) is the SEM image of one of the broken pieces of a sample of the Mg-15 vol% SiC MMNC. The sample was broken into several pieces upon quasi-static compression. The fracture surface appears flat. At relatively high magnification, numerous cracks can be seen (Fig. 5.12(b)). Figure 5.12(c) shows cracks and crack branching in this sample. No evidence of ductile fracture can be found in this sample. Figure 5.12(d) is a high magnification of a local region. The bright particle marked by the black arrow seems to be the SiC phase. This is because, first, considerable charging was observed during SEM analysis, indicating this particle insulating, and secondly, EDS (not shown here) suggests that it is indeed the SiC phase. This SiC particle is about $\sim 1.0 \mu\text{m}$ in size. Therefore, we can reasonably believe that such particles can play as stress concentrators, leading to crack initiation during mechanical loading.

In summary, SEM fractography indicates that large cracks exist on the fracture

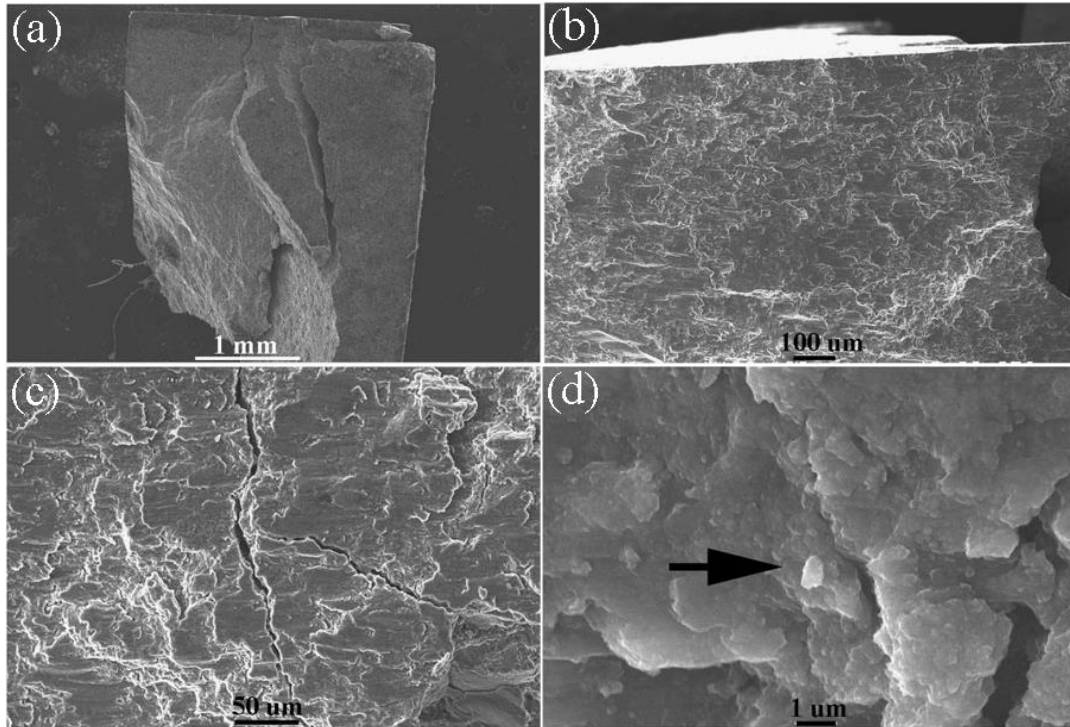


Figure 5.12: (a) Low-magnification SEM image of specimen of Mg-15 vol% SiC MMNC partially recovered after quasi-static loading. Loading is roughly vertical. The sample was broken into a few pieces upon quasi-static compression. The fracture surface is quite flat, and typical of brittle fracture. (b) An enlarged view of the fracture surface, showing cracks on the surface. (c) Cracks and crack branching in this sample. (d) A high magnification SEM micrograph. The arrow points to a particle of size close to 1.0 μm . The light (bright) contrast of this particle comes from charging of the insulating SiC phase. EDS analysis (not shown here) also indicates that the particle is SiC.

surface of the Mg-MMNC sample with the highest volume fraction of reinforcement. Whereas the samples with relatively low SiC content exhibit limited evidence of ductile failure, with off-axis cracks presumably initiated from the specimen corners, the 15 vol% SiC sample were broken into several pieces whose partially recovered sample shows axial cracks. The fractography observations are thus consistent with the quasi-static stress-strain curves which show that the malleability of the Mg-based MMNC decreases with increasing volume fraction of the reinforcement. Detailed analysis indicates that

certain large size SiC particles remain in the MMNC, which may be responsible for the low malleability of the MMNC samples. Such particles can be the stress raisers.

5.4 Discussion

5.4.1 Microstructure Features

It is well known that the mechanical properties of structural materials are determined by their microstructure. Particularly, for discontinuously reinforced MMCs, mechanical properties are dependent on the type, size, volume fraction and geometrical shape of the reinforcing particles [269-274]. The microstructure of a discontinuously reinforced MMC can be characterized by the following parameters: the average particle size (d), volume fraction of the particles (f_v), and the average interparticle spacing (λ), which is also the thickness of the metallic ligament between the two neighboring particles. These parameters can be related to one another as follows [87]:

$$\lambda = d \left(\frac{1}{f_v^{1/3}} - 1 \right). \quad (5.1)$$

According to Equation (5.1) and the average particle size (~ 14 nm) as shown in Figure 5.2 for the 5 vol% MMNC, the calculated interparticle spacing is ~ 24 nm, which is about half the measured interparticle spacing (~ 45 nm) as shown in Figure 5.2(b). Han et al. [90] used the Hellman-Hillert approach to calculate the interparticle spacing as follows:

$$\lambda = 1.8 \cdot \frac{d}{f_v^{1/3}}. \quad (5.2)$$

This equation results a calculated interparticle spacing of ~ 68 nm, which over-estimates the interparticle spacing as compared with the measured result. Yet from the Humphrey estimation,

$$\lambda = d \left(\frac{1-f_v}{f_v} \right)^{1/3}, \quad (5.3)$$

the calculated inter-particle spacing is ~37 nm, still slightly underestimating the interparticle spacing between the SiC nanoparticles. Finally, based on a simple geometrical model, Han et al. derived the following equation [90],

$$\lambda = 1.12 \times \frac{d}{f_v^{1/3}}. \quad (5.4)$$

Using Equation (5.4) for our experimental results, the calculated interparticle spacing is then ~43 nm. This result is the one in closest agreement with the experimentally measured interparticle spacing. However, this nice agreement appears fortuitous. We believe that the calculated results should be taken as significant in a statistical sense as distribution of either the particle size or the interparticle spacing, which is unavoidable. Each equation has its own assumptions and the geometrical models that simplify the analytic derivation, therefore only approximate the experimental scenario. Another point of importance is that clustering of the nanoparticles prohibits accurate theoretical calculations of the interparticle spacing, as each of the above formulas assumes a single value particle size, and does not factor the clustering effect into consideration.

Application of the above equations to the Mg-based MMNCs reinforced with 10 and 15 vol% SiC nanoparticles should result in further reduced interparticle spacing values. For example, the Han-equation ((Eq.(5.4)) gives ~33.8 nm and ~30 nm interparticle spacings for the 10 and 15 vol% SiC nanoparticle reinforced MMNCs, respectively (assuming ~14 nm for the average nanoparticle size), close to the experimental results based on TEM measurements. However, we see that an exact agreement is missing among the calculated TEM and XRD grain size analyses. This is not surprising as in such

MMNC materials, a clear definition of grain size is lacking.

Both experimental results and calculations indicate that the interparticle spacing of the SiC nanoparticle reinforced Mg-based MMNCs of this work is below 50 nm, which is in the true nanometer regime. Apparently, such interparticle spacing will lead to similar effective grain size of the Mg-matrix phase, and will impart strong effect on the mechanical behavior of these MMNCs in terms of the strengthening mechanisms.

5.4.2 Strengthening Effects

A few strengthening mechanisms have been proposed for discontinuously reinforced MMCs with micrometer-sized particles [90, 105, 269]. As pointed out by Nan and Clarke [94], there are generally two approaches in the literature regarding theoretical treatment of the strengthening effect in MMCs. The first one is based on dislocation plasticity, including various dislocation blocking mechanisms that may contribute to the strengthening effect due to the presence of the “rigid” reinforcing particles. The second is based on micromechanics in the context of the Eshelby inclusion theory [275]. In the former, particle size effect can be dealt with in a natural manner as in the effective medium approach proposed by Nan and Clarke [94].

It should be noted that there are two types of size effect [276]. The first is the grain size effect, or Hall-Petch effect, which is based on the notion that grain boundaries are barriers to dislocation motion, and thus dislocations tend to pile-up in front of a GB, and because of this reason, refined grain size translates to increased yield or flow strength of the material [85, 277]. Other equivalently valid theories have also been proposed to explain the empirical Hall-Petch relation, such as GBs as sources or sinks of dislocations [84], geometrically necessary dislocations (GNDs) to account for the compatibility of

polycrystalline plasticity [278], and dislocation avalanche as collective behavior in the presence of GBs [279]. For pure Mg, the Hall-Petch relation in the literature is based on powder-metallurgy-processed samples [280], and consists of three regimes. In the first regime, a steep Hall-Petch relation is observed with a large Hall-Petch coefficient of the order of $\sim 13 \text{ GPa}\cdot\text{nm}^{1/2}$. However, this behavior levels off when the grain size is smaller than 1000 nm, and in this second regime, the Hall-Petch coefficient is only of the order of $1.16 \text{ GPa}\cdot\text{nm}^{1/2}$, which is one order of magnitude smaller than that of the first regime. When the grain size is below 100 nm, the grain size effect enters into the third regime where an inverse Hall-Petch relation is observed in the powder-metallurgy-processed monolithic magnesium. Whereas it is possible that artifacts may exist in such experimental results from porosity, poor interparticle bonding, and so on, it is also highly possible that such behavior represents the intrinsic properties of monolithic magnesium based on the following reasons. First, as the authors have observed, the strain rate sensitivity (SRS, defined as $m = \frac{\partial \ln \sigma}{\partial \ln \dot{\epsilon}}$, where σ is the yield or flow stress and $\dot{\epsilon}$ is the imposed strain rate) of monolithic Mg increases almost in a manner of the Hall-Petch relation, viz. m is nearly proportional to the inverse square root of the grain size. When the grain size is $\sim 50 \text{ nm}$, the SRS is about 0.1, suggesting that plasticity other than dislocation mechanisms-related is operating, including GB sliding [192], GB shuffling [281] and grain rotation [282], and so on. This can be understood based on the fact that the melting point of monolithic magnesium is only 923 K, and room temperature (300 K) translates to 1/3 of the melting point of Mg. Therefore, GB activities can prevail in nanocrystalline Mg to accommodate plastic deformation, which brings about the inverse Hall-Petch effect in the nanocrystalline regime. Based on this reasoning, we believe that grain

size refinement in the nanoparticle reinforced MMNCs will not be of much benefit in terms of strengthening in these materials, as the interparticle spacing is smaller than 50 nm, which happens to be in the third regime of the grain size effect of the monolithic Mg. We can also argue alternatively that dislocation pile-up within such small space is practically impossible, as pointed by Groh et al. [276]. Our TEM observations did not find evidence for dislocation pile-up in the matrix between the SiC nanoparticles.

The second size effect stems from the dislocation line tension and confinement, which gives rise to a dependence of the critical stress on the inverse of a characteristic length, such as the distance between unsharable obstacles. Operations of the Frank-Read source and the Orowan mechanism serve as typical examples for the second size effect. Traditionally, as has been pointed out previously, Orowan strengthening in the presence of second phase particles or reinforcing ceramic particulates is regarded as one of the primary contribution to the elevated strength of MMCs with micrometer-sized ceramic particles [105, 202, 269, 283]. When dealing with particle size effect, Nan and Clarke considered four contributions [94] to the strength increase due to the presence of the reinforcing particles. The first is the Orowan stress as

$$\Delta\sigma_{Or}^m = \alpha \cdot \frac{\mu^m b}{\lambda}, \quad (5.5)$$

where λ is the average interparticle spacing, given in Ref.[94] as

$$\lambda = \left(\frac{\pi d^2}{4f_v} \right)^{1/2}. \quad (5.6)$$

In Eq.(5.5), μ^m is the shear modulus of the matrix, b the Burgers vector of the dislocations of the matrix material and α a geometric factor of the order of unity. Using

the parameters of Mg (shear modulus 16.6 GPa, Burgers vector strength 0.321 nm), and the measured interparticle spacing for 5 vol% MMNC, the Orowan stress contribution is ~120 MPa. However, from Eq.(5.6), we can see that for a given volume fraction, the interparticle spacing should decrease with decreasing particle size in a linear fashion. Or for a given particle size, the interparticle spacing will decrease with increased particle volume fraction. This will in turn increase the Orowan stress. That means, according to this contribution, for the Mg-based MMNC considered here, increased vol% of the SiC nanoparticles should lead to increased strength, which is not the case as the strengthening effect levels off when vol% of the SiC nanoparticles exceeds 10%.

The second contribution comes from the isotropic form of the strain gradient effect in the sense of Brown's theory, and the stress increase is

$$\Delta\sigma_{ISO}^m = \beta \cdot \mu^m \sqrt{\frac{f_v \varepsilon_p b}{d}} \quad (5.7)$$

In Eq.(5.7), β is a geometric factor of ~0.4, and ε_p is the plastic strain in the matrix. Taking the plastic strain of the matrix to be 0.002 (0.2%), and using the parameters of Mg and experimental results of the 5 vol% SiC Mg-based MMNC of this work, we obtain a value of only ~10 MPa for the Brown stress. It is observed from Eq.(5.7) that with a given particle size d , the Brown stress should increase with the volume fraction of the reinforcing particles, which is not the case for the Mg-based MMNCs considered here when the volume fraction is greater than ~10 vol%. In other words, even if the Brown model is valid for small vol% of the nanoparticles, it fails at higher vol%.

The third contribution is also from the strain gradient but is due to the so called kinematic gradient contribution, which has the form

$$\Delta\sigma_{KIN}^m = \gamma \cdot \mu^m \cdot f_v \sqrt{\frac{\varepsilon_p b}{d}}. \quad (5.8)$$

In Eq.(5.8), the numerical value of γ is ~ 2.0 . This equation produces a stress increment in the amount of ~ 10 MPa. Therefore, the total contribution due to strain gradient effect adds up to ~ 20 MPa. Similarly to the Brown stress, for a given particle size, the kinematic gradient strengthening should increase linearly with the particle volume fraction, which is found to be inconsistent with our experimental results at relatively high vol% of the nanoparticles.

Finally, the fourth contribution to the strengthening is the statistically stored dislocations (SSD) due to, e.g., the thermal mismatch between the particle and the metal matrix, which has the following form (in the spirit of the Taylor formula)

$$\Delta\sigma_{CTE}^m = \eta \cdot \mu^m \cdot b \sqrt{\rho}, \quad (5.9)$$

where η is a factor of unity, and ρ the dislocation density depending on the temperature drop, and difference of coefficients of thermal expansion (CTE) between the matrix and the ceramic phase, as well as the particle size and volume fraction, such that

$$\rho = \frac{6\Delta T \cdot \Delta\alpha \cdot f_v}{b \cdot d \cdot (1 - f_v)}. \quad (5.10)$$

Based on Eq.(5.10), the density of SSD in the Mg-matrix due to thermal mismatch is $14.3 \times 10^{13} \text{ m}^{-2}$, which when put into Eq.(5.9) yields a stress increase in the amount of ~ 167 MPa (temperature drop $\sim 550\text{K}$; CTE of Mg $\sim 29.9 \times 10^{-6}/\text{K}$ [54]; CTE of SiC $\sim 4.5 \times 10^{-6}/\text{K}$). Again, Eq.(5.10) shows that the SSD density increases with increasing particle volume density for a given particle size, which translates to increased strength from the Taylor Eq.(5.9). This again is inconsistent with our experimental results at relatively high vol% of the nanoparticles.

One commonly used approach to calculate the total contribution to the strength from the various strengthening mechanisms is the one adopted by Han et al. [90], whereas the total strengthening effect is simply a sum of all the terms.

$$\Delta\sigma_{Total}^m = \Delta\sigma_{Or}^m + \Delta\sigma_{ISO}^m + \Delta\sigma_{KIN}^m + \Delta\sigma_{CTE}^m \cdot \quad (5.11)$$

Based on this equation, the total strengthening effect can then be calculated to be of the order of ~206 MPa. If this is combined with the base strength of the pure Mg, the total yield strength is calculated to be ~386 MPa for the 5 vol% MMNC, which is in good agreement with the experimental results (Fig. 5.8(b)).

One more strengthening mechanism in MMCs has often been underrated and ignored by the research community, which is the load sharing or load transfer from the soft matrix to the more rigid ceramic particles during mechanical loading. In what follows, we will apply the modified shear-lag model proposed by Nardone [284]. Based on the load transfer from the matrix to the hard reinforcing phase during mechanical loading, Nardone and Prewo derived the following equation for the yield strength of the composite:

$$\sigma_{cy} = \sigma_{my} \left[\frac{1}{2} f_v (s + 2) + f_m \right]. \quad (5.12)$$

In Eq.(5.12), σ_{cy} is the yield strength of the composite, σ_{my} is the yield strength of the matrix, s is the aspect ratio (length to diameter ratio) for fiber reinforcements, and f_m is the volume fraction of the matrix. Apparently, for the two phase structure such as in this work, $f_m + f_v = 1$.

Nardone et al. have shown that this shear-lag model could predict the yield strength of certain discontinuously reinforced aluminum (DRA) reasonably well, keeping in line with experimental results. However, a clear guidance as to how to choose the yield

strength of the matrix material is yet to be established. Basically, we are left with two choices. The first option is to use the yield strength of the un-reinforced matrix material in its annealed state. With this choice, the calculated yield strength of the composite with 5 vol% SiC nanoparticles, according to the result of Figure 5.8 of this work, is only ~185 MPa, which is only merely half of the measured yield strength of the MMNC in question. The second option is to use the yield strength of the reinforced matrix, thus taking into account the in-situ strengthening of the matrix phase [274]. We believe it is more reasonable to use the yield strength of the matrix in the presence of the reinforcing particles, as that is the actual yield stress during loading. We can use an indirect method to derive yield strength of the reinforced matrix. This is achieved by adding the strengthening effects from Orowan mechanism, Brown mechanism, and so on, as we have discussed previously using Eq.(5.11), to the yield strength of the un-reinforced Mg (~180 MPa from Fig. 5.8). This will lead to a yield strength value of ~386 MPa for the matrix in the MMNC with 5 vol% SiC nanoparticles. Then the Nardone formula of (5.12) gives yield strength for the composite in the amount of 393.6 MPa. This value is in close agreement to the experimentally measured yield strength of the 5 vol% reinforced MMNC (Fig. 5.8).

If the above methods are used to all the volume fractions studied in this work, we have the results as shown in Table 5.1. It shows that Nardone's modified shear-lag model provides the closest prediction of the yield strength of the SiC nanoparticle- reinforced Mg-based MMNC at 5 vol% of SiC. However, neither the Nardone model nor the dislocation plasticity theory can give good prediction at higher volume fractions of the SiC phase. What is more, both models fail to account for the inverse volume fraction

Table 5.1: Strengthening effect estimations (all stress terms in MPa).

Vol%	λ nm	ρ (m^{-2}) $\times 10^{13}$	$\Delta\sigma_{Or}^m$	$\Delta\sigma_{ISO}^m$	$\Delta\sigma_{KIN}^m$	$\Delta\sigma_{CTE}^m$	$\Delta\sigma_{Tot}^m$	σ_y^{Cal}	Nardone Eqn.	Exp. σ_y
5	43	14.3	120	10.0	10.0	64	204	384	394	400
10	34	30.0	157	14.2	22.5	92	285.7	465.7	489.0	539
15	29	48.0	184	17.4	33.7	116	351.8	531.8	572.0	530

effect when the vol% of SiC is greater than 10%.

We should point out that in the above discussion we have not considered the grain size refinement effect on the yield strength of the Mg-matrix. According to Choi et al. [280], and Hwang et al. [213], we can establish an inverse Hall-Petch relation for pure Mg for grain size smaller than 100 nm, as follows:

$$\sigma_y = 437.0 - 1760 \cdot d^{-1/2}. \quad (5.13)$$

In Eq.(5.13), the yield strength is in MPa, and the grain size (d) is in nm. For the Mg-based MMNC of this work, it is difficult to obtain an accurate evaluation of the grain size of the Mg matrix. As a reasonable approximation, we use the interparticle spacing (Table 5.1) for the matrix grain size d . Then according to Eq.(5.13), as the inter-particle spacing is reduced from 34 nm (10 vol% SiC) to 29 nm (15 vol% SiC), there is a drop of the order of ~20 MPa in the yield strength, which may partially explain the strength decrease in the MMNCs with higher volume fraction of SiC nanoparticles. However, the exact underlying mechanism that causes this strength drop calls for further effort.

The next issue of interest is the rate dependence of the Mg-based MMCs. Even though a more detailed investigation is needed to provide a more accurate examination of the strain rate sensitivity (SRS) of the MMNCs of this work, via experiments such as strain rate jump test, stress relaxation or instrumented nanoindentation [192, 285], we can

still obtain approximate values of the SRS based on our quasi-static and dynamic mechanical testing results. Toward this, we use the popular definition of SRS as follows

$$m = \frac{\partial \ln \sigma}{\partial \ln \dot{\epsilon}} = \frac{\Delta \ln \sigma}{\Delta \ln \dot{\epsilon}} = \frac{\ln \sigma_2 - \ln \sigma_1}{\ln \dot{\epsilon}_2 - \ln \dot{\epsilon}_1}. \quad (5.14)$$

From Eq.(5.14) and the experimental results (Figure 5.8), the SRS values for all three MMNCs of this work are very close to 0.03. This is much smaller than the SRS values obtained for 100 nm grain size pure Mg (~0.3) by Trojanova et al. [212] and the 45 nm grain size pure Mg (0.6) by Hwang et al. [213]. Nevertheless, it is very close to our preceding results for 400 nm grain size Mg-Y alloy (~0.06). The large SRS values of nanocrystalline pure Mg obtained by Trojanova et al. [212] and Hwang et al. [213] strongly suggest that grain boundary activities are prevalent in accommodating the plastic deformation in nanocrystalline Mg at room temperature. On the other hand, the small SRS obtained for our MMNCs indicates that the deformation behavior of MMNCs is quite different from pure nanocrystalline Mg, and some other mechanisms that play a key role in the deformation behavior of MMNCs are yet to be uncovered. The presence of the SiC nanoparticles may play an important role that leads to this difference.

We believe the poor malleability of the MMNCs is primarily due to the clustering of the nanoparticles as well as the large particles in the MMNCs that have survived the processing.

In summary, further investigation is needed to clarify the unusual behavior of the MMNCs with large volume fraction of reinforcing hard particles as described in this work. Considering the very small interparticle spacing, and thus the very small effective grain size of the matrix, atomistic simulation may be invoked for this purpose. We envision that this will become an interesting area of research, and many potential

opportunities are yet to be explored.

5.5 Summary

The effect of micro- and nano- reinforcements on the mechanical properties of Mg-based MMCs/MMNCs was investigated under quasi-static and dynamic loading rates and the underlying mechanisms were discussed in this work. The following conclusions can be drawn based on the experimental results and the discussion of this study.

a). Mechanical attrition of Mg and nanocrystalline SiC powders followed by sub-solidus consolidation is an effective way to produce Mg-based MMNCs. The reinforcing ceramic nanoparticles (average particle size ~14 nm) appear to be homogeneously dispersed within the matrix. Some large SiC particles have survived the synthesis processes. The average values of the interparticle spacing of all the MMNCs are smaller than 50 nm. Neither TEM nor SEM reveals significant porosity in the as-processed MMNCs.

b). All the MMNCs exhibit considerably increased strength compared with the monolithic magnesium, indicating strong strengthening effect from the SiC nanoparticles. However, when the volume fraction of the SiC nanoparticles is greater than 10%, the strengthening effect levels off, and an inverse volume fraction effect emerges. No significant plastic deformation is observed in the MMNCs under either quasi-static or high-strain rate uniaxial compression.

c). A combination of dislocation plasticity models and modified shear-lag model based on Nardone and Prewo provides quite close prediction of the yield strength of the MMNC with small SiC volume fraction. However, neither the dislocation-based models nor the modified shear-lag model can give close estimation of the yield strength of

MMNC with larger SiC volume fractions. In particular, the existing models fail in predicting the inverse volume fraction effect at higher vol% levels. Further efforts are needed to uncover the underlying mechanisms responsible for such effect.

d). The estimated strain rate sensitivity of all the MMNCs of this work is around 0.03, which is much smaller than that of nanocrystalline Mg with 100 nm and 45 nm grain sizes. This observation points to strong effect of the SiC nanoparticles on the plastic deformation of the MMNCs. However, the detailed mechanisms of the effect are yet to be uncovered.

CHAPTER 6: SUMMARY AND CONCLUDING REMARKS

In the last three chapters (Chapters 3, 4 and 5), pure Mg, binary-alloy Mg-Y, recently designed and fabricated Mg alloys AZXE7111 and AMX602 and Mg-based metal matrix composites reinforced with micro-/nano-SiC were investigated in terms of various important aspects: mechanical behavior at quasi-static and dynamic loading rates, deformation mechanisms, fracture modes and the effects of microstructure features such as the size, distribution and volume fraction of second phase particles on the properties of Mg-based materials and so on and so forth. The pure Mg and Mg-Y alloy were chosen to study the effects of yttrium, one of the elements that were widely reported to be effective in ductility improvement for Mg alloys, on the evolution of microstructure and deformation mechanisms in ECAPed Mg. The Mg alloys, AZXE7111 and AMX602, were studied at various loading rates for the purpose of (i) understanding the mechanical behavior of those alloys in terms of their potential ballistic applications and (ii) the common or different modes of deformation compared with other Mg samples produced by different methods. The Mg-based metal matrix composites, reinforced with either micro- or nano-sized SiC particles in different volume fractions, were examined to study (i) the effect of the volume fraction and dimension of particles on the mechanical properties of Mg-based composites and (ii) the effect of ex-situ formed reinforcements on the mechanical behavior of Mg composites. Over all, the dissertation work shall contribute to the understanding of some interesting and critical issues associated with Mg

based materials: the mechanism of strength or ductility improvement via different production techniques, the fracture behavior as well as deformation mechanisms, as they vary with the microstructure or composition of the material and so on.

According to the Hall-Petch relation, grain refinement can improve the strength of metals effectively down to hundreds of nanometers. The top-down (ECAP) and bottom-up (powder consolidation) approaches were used to produce ultrafine grained Mg-based samples. Both of them verified the effectiveness of grain refinement in the strength improvement of Mg-based materials. Besides, our researches on MMCs/MMNCs proved that adding ex-situ particles can improve the strength of Mg considerably as well through two mechanisms: (i) promoting grain refinement and (ii) acting as dislocation barriers. Whereas, the moderate ductility of Mg-alloys was found to be maintained only when at least two conditions are satisfied: (a) complete dynamic recovery or recrystallization and (b) strong bonding between the matrix and reinforcement. The former can be concluded based on the work on ECAPed Mg-Y alloy, where the residual internal strain significantly diminishes its ductility compared with the well-annealed counterparts. The latter can be concluded from the comparison between Mg alloys (AZXE7111 and AMX602) and Mg-based MMCs/MMNCs. Neither the micro-SiC reinforced Mg-MMCs nor the nano-SiC reinforced Mg-MMNCs exhibited comparable ductility to those Mg alloys reinforced by in-situ particles. In addition to the strain incompatibility that leads to high stress concentration, the weak bonding between the matrix and reinforcement is also detrimental to the ductility of Mg. The careful examination of the fracture surface of Mg-based composites indicates the occurrence of cracks around the large single or agglomerated particles due to the possible contamination of reinforcement that leads to

the weak bonding at the matrix-particle interface.

The inverse volume fraction effect of nano-particle reinforced MMCs was explored against the continuous increase of the strength of Mg-composites with increasing vol% of micro-particles. While its underlying mechanism is still unclear, we proposed several possibilities: (i) the inverse Hall-Petch relation, which is owing to the estimated grain size within the range of 10-nm ~ 100-nm and a decreased particle-particle spacing with increasing the particle volume fraction; (ii) the increased particle aggregates at the large volume fraction of particles, which as a result increases the potential nuclei of cracks; (iii) the increased area of matrix-particle interface, which is usually weakly-bonded compared to in-situ formed particles, partially due to contamination.

Another important observation from the work is the sigmoidal stress-strain curves of pure Mg and the various Mg alloys. This behavior, in fact, has been broadly observed in Mg and its alloys [39, 42, 46, 82, 241]. A general understanding is the occurrence of twinning that dramatically increases the strain hardening rate. Experimentally, we did not observe any twins in our post-loading samples using TEM. However, the application of Barnett et al.'s theory [82], which was used to determine the critical grain size at which twinning-slip transition takes place, verifies the possibility of twinning in pure Mg, AMX602 and AZXE7111, but not in Mg-based metal matrix composites.

The localized shear failure, currently known as adiabatic shear banding failure, was recognized in pure Mg and Mg-alloys, while a completely brittle failure was discovered in Mg-based metal matrix composites. For the former, a reduced strain hardening rate with strain was regarded responsible for the occurrence of the localized plastic deformation. The reduced strain hardening rate, for seeking further mechanism, was a

result of the exhaustion of twinning and/or dislocation multiplication as well as the occurrence of dynamic recovery.

CHAPTER 7: FUTURE WORK

Through this dissertation work, the mechanical behavior of Mg and Mg-based alloys and composited produced via different techniques and/or containing different types of second-phases has been compared. Some possible mechanisms have been proposed to associate the microstructure with its macro-performance. Nevertheless, there are still some remaining questions that need to be answered concerning the deformation process of Mg and Mg-based alloys and composites. Here are a few aspects:

a. Twinning in ultrafine grained Mg

The occurrence of deformation twinning in ultrafine grained Mg has been proposed many times by different research efforts, including our work, mainly based on the rapid increase of strain hardening and/or the critical estimation of the grain size for twinning-slip transition. Nevertheless, neither experimental nor computational efforts have deformation twinning been successfully observed in Mg having a grain size equivalent to or less than 1- μm . Thus, even though we also employed twinning to explain the mechanical behavior of p-Mg and Mg alloys, whether twinning can operate in ultrafine grained Mg is still uncertain and waiting to be validated.

b. Adiabatic shear localization

This is a failure mode that is commonly known in strain-softening materials and bulk metallic glasses. Although the reduced strain hardening rate, due to the

dynamic recovery as well as the exhaustion of twinning and/or dislocation multiplication, may also contribute to the strain localization, the adiabatic shear banding in Mg and Mg-alloys is still far from being well understood. A potential method is proposed to study the gradual process of strain localization, as shown in Figure 7.1. The resolved shear component of loading force should be considered in association with the strain gradient along y -direction. A preliminary idea is that, the shear component of the load at point A shall be a function of the spacing w , shear strain γ and the shear strain rate $\dot{\gamma}$ of this point, i.e.

$$\tau = \tau(w, \gamma, \dot{\gamma}). \quad (6.1)$$

Direct observation implies that, for localized plastic deformation to take place, a rapidly decreased strain gradient with y shall be expected. But, the mathematic form of such a strain gradient is still an untouched problem. The solution of the expression may throw some light on the understanding of shear localization in ductile metals.

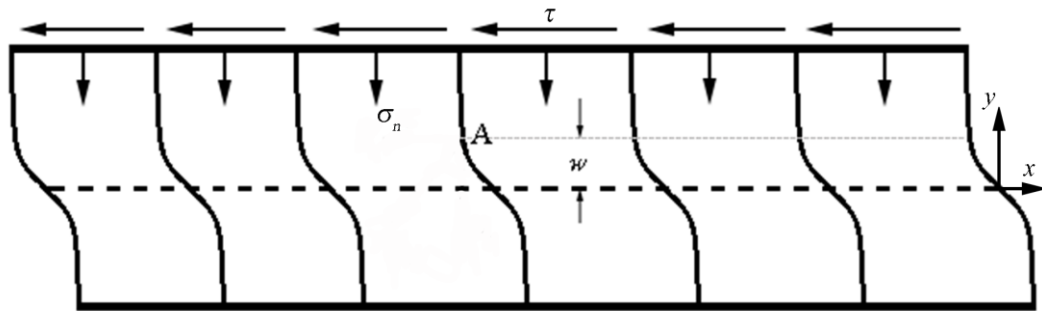


Figure 7.1: A schematic illustration of shear localization formation, where point A is a random location. w is the distance between the shear plane and point A; while τ is the shear component of applied compressive loading stress parallel to the shear plane, σ_n the normal component.

REFERENCES

- [1] M. Gupta and N. M. L. Sharon, *Magnesium, Magnesium Alloys, and Magnesium Composites*: John Wiley & Sons, 2011.
- [2] Y. Nishizawa, H. Morii, and J. Durlach, *New Perspectives in Magnesium Research: Nutrition and Health*: Springer-Verlag London Limited, 2007.
- [3] H. E. Friedrich and B. L. Mordike, *Magnesium Technology: Metallurgy, Design Data, Automotive Applications*: Springer Berlin Heidelberg, 2006.
- [4] A. Luque, M. Ghazisaeidi, and W. A. Curtin, "Deformation modes in magnesium (0001) and (01-11) single crystals: simulations versus experiments," *Modelling and Simulation in Materials Science and Engineering*, vol. 21, p. 045010, 2013.
- [5] R. E. Reed-Hill and W. D. Robertson, "Additional modes of deformation twinning in magnesium," *Acta Metallurgica*, vol. 5, pp. 717-727, 1957.
- [6] R. E. Reed-Hill and W. D. Robertson, "Pyramidal slip in magnesium," *Trans. Met. Soc. AIME.*, vol. 212, pp. 256-9, 1958.
- [7] H. Yoshinaga and R. Horiuchi, "On the Nonbasal Slip in Magnesium Crystals," *Transactions of the Japan Institute of Metals*, vol. 5, pp. 14-21, 1963.
- [8] H. Yoshinaga and R. Horiuchi, "Deformation Mechanisms in Magnesium Single Crystals Compressed in the Direction Parallel to Hexagonal Axis," *Transactions of the Japan Institute of Metals*, vol. 4, pp. 1-8, 1963.
- [9] P. G. Partridge, "The crystallography and deformation modes of hexagonal close-packed metals," *Metall. Rev.*, vol. 12, p. 169, 1967.
- [10] D. S. Li, S. Ahzi, S. M'Guil, W. Wen, C. Lavender, and M. A. Khaleel, "Modeling of deformation behavior and texture evolution in magnesium alloy using the intermediate ϕ -model," *International Journal of Plasticity*, vol. 52, pp. 77-94, 2014.
- [11] J. H. Shen, Y. L. Li, and Q. Wei, "Statistic derivation of Taylor factors for polycrystalline metals with application to pure magnesium," *Materials Science and Engineering: A*, vol. 582, pp. 270-275, 2013.
- [12] S. Agnew, "Enhanced ductility in strongly textured magnesium produced by equal channel angular processing," *Scripta Materialia*, vol. 50, pp. 377-381, 2004.

- [13] W. Kim, S. I. Hong, Y. S. Kim, S. H. Min, H. T. Jeong, and J. D. Lee, "Texture development and its effect on mechanical properties of an AZ61 Mg alloy fabricated by equal channel angular pressing," *Acta Materialia*, vol. 51, pp. 3293-3307, 2003.
- [14] P. W. Bakarian and C. H. Mathewson, *Trans. AIME*, vol. 152, p. 226, 1943.
- [15] H. Conrad and W. D. Robertson, *Trans. AIME*, vol. 209, p. 503, 1957.
- [16] A. Akhtar and E. Teghtsoonian, "Solid solution strengthening of magnesium single crystals—I alloying behaviour in basal slip," *Acta Metallurgica*, vol. 17, pp. 1339-1349, 1969.
- [17] A. Akhtar and E. Teghtsoonian, "Solid solution strengthening of magnesium single crystals—ii the effect of solute on the ease of prismatic slip," *Acta Metallurgica*, vol. 17, pp. 1351-1356, 1969.
- [18] B. Bhattacharya and M. Niewczas, "Work-hardening behaviour of Mg single crystals oriented for basal slip," *Philosophical Magazine*, vol. 91, pp. 2227-2247, 2011.
- [19] P. W. Flynn and J. E. D. J. Mote, *Trans. AIME*, vol. 221, p. 1148, 1961.
- [20] E. Lilleodden, "Microcompression study of Mg (0001) single crystal," *Scripta Materialia*, vol. 62, pp. 532-535, 2010.
- [21] C. M. Byer, B. Li, B. Cao, and K. T. Ramesh, "Microcompression of single-crystal magnesium," *Scripta Materialia*, vol. 62, pp. 536-539, 2010.
- [22] H. Lin, J. Huang, and T. Langdon, "Relationship between texture and low temperature superplasticity in an extruded AZ31 Mg alloy processed by ECAP," *Materials Science and Engineering: A*, vol. 402, pp. 250-257, 2005.
- [23] M. R. Barnett, M. D. Nave, and C. J. Bettles, "Deformation microstructures and textures of some cold rolled Mg alloys," *Materials Science and Engineering: A*, vol. 386, pp. 205-211, 2004.
- [24] M. D. Nave and M. R. Barnett, "Microstructures and textures of pure magnesium deformed in plane-strain compression," *Scripta Materialia*, vol. 51, pp. 881-885, 2004.
- [25] S. Agnew, P. Mehrotra, T. Lillo, G. Stoica, and P. Liaw, "Texture evolution of five wrought magnesium alloys during route A equal channel angular extrusion: Experiments and simulations," *Acta Materialia*, vol. 53, pp. 3135-3146, 2005.

- [26] Y. N. Wang and J. C. Huang, "The role of twinning and untwinning in yielding behavior in hot-extruded Mg–Al–Zn alloy," *Acta Materialia*, vol. 55, pp. 897-905, 2007.
- [27] J. Bohlen, M. R. Nürnberg, J. W. Senn, D. Letzig, and S. R. Agnew, "The texture and anisotropy of magnesium–zinc–rare earth alloy sheets," *Acta Materialia*, vol. 55, pp. 2101-2112, 2007.
- [28] R. K. Mishra, A. K. Gupta, P. R. Rao, A. K. Sachdev, A. M. Kumar, and A. A. Luo, "Influence of cerium on the texture and ductility of magnesium extrusions," *Scripta Materialia*, vol. 59, pp. 562-565, 2008.
- [29] A. Elsayed, J. Umeda, and K. Kondoh, "The texture and anisotropy of hot extruded magnesium alloys fabricated via rapid solidification powder metallurgy," *Materials & Design*, vol. 32, pp. 4590-4597, Sep 2011.
- [30] X. Feng and T. Ai, "Microstructure evolution and mechanical behavior of AZ31 Mg alloy processed by equal-channel angular pressing," *Transactions of Nonferrous Metals Society of China*, vol. 19, pp. 293-298, 2009.
- [31] A. Chapuis and J. H. Driver, "Temperature dependency of slip and twinning in plane strain compressed magnesium single crystals," *Acta Materialia*, vol. 59, pp. 1986-1994, 2011.
- [32] Q. Huo, X. Yang, H. Sun, B. Li, J. Qin, J. Wang, *et al.*, "Enhancement of tensile ductility and stretch formability of AZ31 magnesium alloy sheet processed by cross-wavy bending," *Journal of Alloys and Compounds*, vol. 581, pp. 230-235, 2013.
- [33] D. Ji, C. Liu, L. Tang, Y. Wan, and C. Huang, "Microstructures and mechanical properties of a hot extruded Mg–4.45Zn–0.46Y–0.76Zr alloy plate," *Materials & Design*, vol. 53, pp. 602-610, 2014.
- [34] W.J. Kim, C.W. An, Y.S. Kim, and S. I. Hong, "Mechanical properties and microstructures of an AZ61 Mg Alloy produced by equal channel angular pressing," *Scripta Materialia*, vol. 47, pp. 39–44, 2002.
- [35] G. W. Groves and A. Kelly, "Independent slip systems in crystals," *Philosophical Magazine*, vol. 8, pp. 877-887, 1963/05/01 1963.
- [36] R. E. Reed-Hill and W. D. Robertson, "Deformation of magnesium single crystals by nonbasal slip," *Trans AIME*, vol. 209, pp. 496-502, 1957.
- [37] K. Ishikawa, H. Watanabe, and T. Mukai, "High strain rate deformation behavior of an AZ91 magnesium alloy at elevated temperatures," *Materials Letters*, vol. 59, pp. 1511-1515, 2005.

- [38] S. R. Agnew and Ö. Duygulu, "Plastic anisotropy and the role of non-basal slip in magnesium alloy AZ31B," *International Journal of Plasticity*, vol. 21, pp. 1161-1193, 2005.
- [39] B. Li, S. P. Joshi, O. Almagri, Q. Ma, K. T. Ramesh, and T. Mukai, "Rate-dependent hardening due to twinning in an ultrafine-grained magnesium alloy," *Acta Materialia*, vol. 60, pp. 1818-1826, 2012.
- [40] A. Khosravani, J. Scott, M. P. Miles, D. Fullwood, B. L. Adams, and R. K. Mishra, "Twinning in magnesium alloy AZ31B under different strain paths at moderately elevated temperatures," *International Journal of Plasticity*, vol. 45, pp. 160-173, 2013.
- [41] A. Levinson, R. K. Mishra, R. D. Doherty, and S. R. Kalidindi, "Influence of deformation twinning on static annealing of AZ31 Mg alloy," *Acta Materialia*, 2013.
- [42] M. R. Barnett, M. D. Nave, and A. Ghaderi, "Yield point elongation due to twinning in a magnesium alloy," *Acta Materialia*, vol. 60, pp. 1433-1443, 2012.
- [43] H. Somekawa and T. Mukai, "Hall–Petch relation for deformation twinning in solid solution magnesium alloys," *Materials Science and Engineering: A*, vol. 561, pp. 378-385, 2013.
- [44] S. Graff, W. Brocks, and D. Steglich, "Yielding of magnesium: From single crystal to polycrystalline aggregates," *International Journal of Plasticity*, vol. 23, pp. 1957-1978, 2007.
- [45] X. Y. Lou, M. Li, R. K. Boger, S. R. Agnew, and R. H. Wagoner, "Hardening evolution of AZ31B Mg sheet," *International Journal of Plasticity*, vol. 23, pp. 44-86, 2007.
- [46] S. R. Agnew, M. H. Yoo, and C. N. Tomé "Application of texture simulation to understanding mechanical behavior of Mg and solid solution alloys containing Li or Y," *Acta Materialia*, vol. 49, pp. 4277-4289, 2001.
- [47] X. Li, T. Al-Samman, S. Mu, and G. Gottstein, "Texture and microstructure development during hot deformation of ME20 magnesium alloy: Experiments and simulations," *Materials Science and Engineering: A*, vol. 528, pp. 7915-7925, 2011.
- [48] D. Miracle, "Metal matrix composites – From science to technological significance," *Composites Science and Technology*, vol. 65, pp. 2526-2540, 2005.

- [49] T. Frolov, K. A. Darling, L. J. Kecskes, and Y. Mishin, "Stabilization and strengthening of nanocrystalline copper by alloying with tantalum," *Acta Materialia*, vol. 60, pp. 2158-2168, 2012.
- [50] N. Tahreen, D. F. Zhang, F. S. Pan, X. Q. Jiang, C. Li, D. Y. Li, *et al.*, "Influence of yttrium content on phase formation and strain hardening behavior of Mg-Zn-Mn magnesium alloy," *Journal of Alloys and Compounds*, vol. 615, pp. 424-432, Dec 2014.
- [51] G. H. Wu, Y. Fan, H. T. Gao, C. Q. Zhai, and Y. P. Zhu, "The effect of Ca and rare earth elements on the microstructure, mechanical properties and corrosion behavior of AZ91D," *Materials Science and Engineering a-Structural Materials Properties Microstructure and Processing*, vol. 408, pp. 255-263, Nov 2005.
- [52] S. Sandlöbes, M. Friák, S. Zaeferrer, A. Dick, S. Yi, D. Letzig, *et al.*, "The relation between ductility and stacking fault energies in Mg and Mg-Y alloys," *Acta Materialia*, vol. 60, pp. 3011-3021, 2012.
- [53] Y. Z. Lu, Q. D. Wang, X. Q. Zeng, W. J. Ding, C. Q. Zhai, and Y. P. Zhu, "Effects of rare earths on the microstructure, properties and fracture behavior of Mg-Ag alloys," *Materials Science and Engineering a-Structural Materials Properties Microstructure and Processing*, vol. 278, pp. 66-76, Feb 15 2000.
- [54] M. Gupta and N. M. L. Sharon, *Magnesium, Magnesium Alloys, and Magnesium Composites*: Wiley, 2011.
- [55] M. S. Dargusch, K. Pettersen, K. Nogita, M. D. Nave, and G. L. Dunlop, "The Effect of Aluminium Content on the Mechanical Properties and Microstructure of Die Cast Binary Magnesium-Aluminium Alloys," *MATERIALS TRANSACTIONS*, vol. 47, pp. 977-982, 2006.
- [56] A. S. El-Amoush, "Effect of aluminum content on mechanical properties of hydrogenated Mg-Al magnesium alloys," *Journal of Alloys and Compounds*, vol. 463, pp. 475-479, 9/8/ 2008.
- [57] A. Luo and M. O. Pekguleryuz, "Cast magnesium alloys for elevated temperature applications," *Journal of Materials Science*, vol. 29, pp. 5259-5271, 1994/10/01 1994.
- [58] T. Laser, C. Hartig, M. R. Nuernberg, D. Letzig, and R. Bormann, "The influence of calcium and cerium mischmetal on the microstructural evolution of Mg-3Al-1Zn during extrusion and resulting mechanical properties," *Acta Materialia*, vol. 56, pp. 2791-2798, Jul 2008.

- [59] L. Han, H. Hu, D. O. Northwood, and N. Li, "Microstructure and nano-scale mechanical behavior of Mg–Al and Mg–Al–Ca alloys," *Materials Science and Engineering: A*, vol. 473, pp. 16-27, 1/25/ 2008.
- [60] C. D. Yim, B. S. You, R. S. Jang, and S. G. Lim, "Effects of melt temperature and mold preheating temperature on the fluidity of Ca containing AZ31 alloys," *Journal of Materials Science*, vol. 41, pp. 2347-2350, 2006/04/01 2006.
- [61] T. Wang, L. Jiang, R. K. Mishra, and J. J. Jonas, "Effect of Ca Addition on the Intensity of the Rare Earth Texture Component in Extruded Magnesium Alloys," *Metallurgical and Materials Transactions a-Physical Metallurgy and Materials Science*, vol. 45A, pp. 4698-4709, Sep 2014.
- [62] D. B. Lee, L. S. Hong, and Y. J. Kim, "Effect of Ca and CaO on the high temperature oxidation of AZ91D Mg alloys," *Materials Transactions*, vol. 49, pp. 1084-1088, May 2008.
- [63] B. H. Choi, I. M. Park, B. S. You, and W. W. Park, "Effects of Ca and Be additions on high temperature oxidation behavior of AZ91 alloys," in *Magnesium Alloys 2003, Pts 1 and 2*. vol. 419-4, Y. Kojima, T. Aizawa, K. Higashi, and S. Kamado, Eds., ed Zurich-Uetikon: Trans Tech Publications Ltd, 2003, pp. 639-644.
- [64] C. G. Interrante and L. Raymond, "Corrosion: Fundamentals, Testing and Protection," in *ASM Handbook*. vol. 13A, ed: ASM International.
- [65] M. Celikin, A. A. Kaya, and M. Pekguleryuz, "Effect of manganese on the creep behavior of magnesium and the role of alpha-Mn precipitation during creep," *Materials Science and Engineering a-Structural Materials Properties Microstructure and Processing*, vol. 534, pp. 129-141, Feb 2012.
- [66] Y. Tamura, Y. Kida, H. Tamehiro, N. Kono, H. Soda, and A. McLean, "The effect of manganese on the precipitation of Mg(17)Al(12) phase in magnesium alloy AZ91," *Journal of Materials Science*, vol. 43, pp. 1249-1258, Feb 2008.
- [67] P. Cao, M. Qian, and D. H. StJohn, "Effect of manganese on grain refinement of Mg–Al based alloys," *Scripta Materialia*, vol. 54, pp. 1853-1858, 6// 2006.
- [68] T. Laser, M. R. Nürnberg, A. Janz, C. Hartig, D. Letzig, R. Schmid-Fetzer, *et al.*, "The influence of manganese on the microstructure and mechanical properties of AZ31 gravity die cast alloys," *Acta Materialia*, vol. 54, pp. 3033-3041, 6// 2006.
- [69] A. A. Luo and A. K. Sachdev, "Development of a New Wrought Magnesium-Aluminum-Manganese Alloy AM30," *Metallurgical and Materials Transactions A*, vol. 38, pp. 1184-1192, 2007/06/01 2007.

- [70] Y. Wang, Q. Wang, C. Ma, W. Ding, and Y. Zhu, "Effects of Zn and RE additions on the solidification behavior of Mg–9Al magnesium alloy," *Materials Science and Engineering: A*, vol. 342, pp. 178-182, 2/15/ 2003.
- [71] J. F. Nie, X. Gao, and S. M. Zhu, "Enhanced age hardening response and creep resistance of Mg–Gd alloys containing Zn," *Scripta Materialia*, vol. 53, pp. 1049-1053, 2005.
- [72] K. Maruyama, M. Suzuki, and H. Sato, "Creep strength of magnesium-based alloys," *Metallurgical and Materials Transactions a-Physical Metallurgy and Materials Science*, vol. 33, pp. 875-882, Mar 2002.
- [73] Y. Wang, S. Guan, X. Zeng, and W. Ding, "Effects of RE on the microstructure and mechanical properties of Mg–8Zn–4Al magnesium alloy," *Materials Science and Engineering: A*, vol. 416, pp. 109-118, 1/25/ 2006.
- [74] Y. Fan, G. Wu, H. Gao, G. Li, and C. Zhai, "Influence of lanthanum on the microstructure, mechanical property and corrosion resistance of magnesium alloy," *Journal of Materials Science*, vol. 41, pp. 5409-5416, 2006/09/01 2006.
- [75] S. Sandlöbes, S. Zaeferrer, I. Schestakow, S. Yi, and R. Gonzalez-Martinez, "On the role of non-basal deformation mechanisms for the ductility of Mg and Mg–Y alloys," *Acta Materialia*, vol. 59, pp. 429-439, 2011.
- [76] K. Kondoh, E. L. S. A. Hamada, H. Imai, J. Umeda, and T. Jones, "Microstructures and mechanical responses of powder metallurgy non-combustive magnesium extruded alloy by rapid solidification process in mass production," *Materials & Design*, vol. 31, pp. 1540-1546, 2010.
- [77] E. Ayman, U. Junko, and K. Katsuyoshi, "Application of rapid solidification powder metallurgy to the fabrication of high-strength, high-ductility Mg–Al–Zn–Ca–La alloy through hot extrusion," *Acta Materialia*, vol. 59, pp. 273-282, Jan 2011.
- [78] R. D. Doherty, D. A. Hughes, F. J. Humphreys, J. J. Jonas, D. J. Jensen, M. E. Kassner, *et al.*, "Current issues in recrystallization: a review," *Materials Science and Engineering: A*, vol. 238, pp. 219-274, 1997.
- [79] J. H. Hollomon, *Trans. Metall. Soc. AZME*, vol. 162, pp. 268-90, 1945.
- [80] A. Zhilyaev, "Experimental parameters influencing grain refinement and microstructural evolution during high-pressure torsion," *Acta Materialia*, vol. 51, pp. 753-765, 2003.
- [81] H. Conrad, "Grain size dependence of the plastic deformation kinetics in Cu," *Materials Science and Engineering: A*, vol. 341, pp. 216-228, 2003.

- [82] M. R. Barnett, Z. Keshavarz, A. G. Beer, and D. Atwell, "Influence of grain size on the compressive deformation of wrought Mg–3Al–1Zn," *Acta Materialia*, vol. 52, pp. 5093-5103, 2004.
- [83] A. H. Cottrell, "Theory of Brittle Fracture in Steel and Similar Metals," *Trans. TMS-AIME*, vol. 212, p. 192, 1958.
- [84] J. C. M. Li, "Petch relation and grain boundary sources," *Transactions of the Metallurgical Society of AIME*, vol. 227, pp. 239-247, 1963.
- [85] N. J. Petch, "The cleavage strength of polycrystals," *Journal of Iron and Steel Institute*, vol. 174, pp. 25-28, 1953.
- [86] S. C. Tjong and Z. Y. Ma, "Microstructural and mechanical characteristics of in situ metal matrix composites," *Materials Science and Engineering: R: Reports*, vol. 29, pp. 49-113, 2000.
- [87] K. S. Ravichandran, "A simple model of deformation behavior of two phase composites," *Acta Metallurgica Et Materialia*, vol. 42, pp. 1113-1123, 1994.
- [88] P. Hellman and M. Hillert, "ON THE EFFECT OF SECOND-PHASE PARTICLES ON GRAIN GROWTH," *Scandinavian Journal of Metallurgy*, vol. 4, pp. 211-219, 1975.
- [89] M. Hillert, "Inhibition of grain growth by second-phase particles," *Acta Metallurgica*, vol. 36, pp. 3177-3181, 1988.
- [90] B. Q. Han and D. C. Dunand, "Microstructure and mechanical properties of magnesium containing high volume fractions of yttria dispersoids," *Materials Science and Engineering: A*, vol. 277, pp. 297-304, 2000.
- [91] F. J. Humphreys, W. S. Miller, and M. R. Djazeb, "Microstructural development during thermomechanical processing of particulate metal-matrix composites," *Materials Science and Technology*, vol. 6, pp. 1157-1166, Nov 1990.
- [92] G. Garcés, P. Pérez, and P. Adeva, "Effect of the extrusion texture on the mechanical behaviour of Mg–SiCp composites," *Scripta Materialia*, vol. 52, pp. 615-619, 2005.
- [93] L. Li, M. O. Lai, M. Gupta, B. W. Chua, and A. Osman, "Improvement of microstructure and mechanical properties of AZ91/SiC composite by mechanical alloying," *Journal of Materials Science*, vol. 35, pp. 5553-5561, Nov 2000.
- [94] C. W. Nan and D. R. Clarke, "The influence of particle size and particle fracture on the elastic/plastic deformation of metal matrix composites," *Acta Materialia*, vol. 44, pp. 3801-3811, 1996.

- [95] G. Garces, M. Rodriguez, P. Perez, and P. Adeva, "Effect of volume fraction and particle size on the microstructure and plastic deformation of Mg–Y₂O₃ composites," *Materials Science and Engineering: A*, vol. 419, pp. 357-364, 2006.
- [96] S.-J. Hong, H.-M. Kim, D. Huh, C. Suryanarayana, and B. S. Chun, "Effect of clustering on the mechanical properties of SiC particulate-reinforced aluminum alloy 2024 metal matrix composites," *Materials Science and Engineering: A*, vol. 347, pp. 198-204, 2003.
- [97] J. Koike, T. Kobayashi, T. Mukai, H. Watanabe, M. Suzuki, K. Maruyama, *et al.*, "The activity of non-basal slip systems and dynamic recovery at room temperature in fine-grained AZ31B magnesium alloys," *Acta Materialia*, vol. 51, pp. 2055-2065, 2003.
- [98] R. Z. Valiev and T. G. Langdon, "Principles of equal-channel angular pressing as a processing tool for grain refinement," *Progress in Materials Science*, vol. 51, pp. 881-981, 2006.
- [99] K. Xia, J. Wang, X. Wu, G. Chen, and M. Gurvan, "Equal channel angular pressing of magnesium alloy AZ31," *Materials Science and Engineering: A*, vol. 410-411, pp. 324-327, 2005.
- [100] K. Matsubara, Y. Miyahara, Z. Horita, and T. G. Langdon, "Developing superplasticity in a magnesium alloy through a combination of extrusion and ECAP," *Acta Materialia*, vol. 51, pp. 3073-3084, 2003.
- [101] J. Li, W. Xu, X. Wu, H. Ding, and K. Xia, "Effects of grain size on compressive behaviour in ultrafine grained pure Mg processed by equal channel angular pressing at room temperature," *Materials Science and Engineering: A*, vol. 528, pp. 5993-5998, 2011.
- [102] D. Yamaguchi, Z. Horita, M. Nemoto, and T. G. Langdon, "Significance of adiabatic heating in equal-channel angular pressing," *Scripta Materialia*, vol. 41, pp. 791-796, 9/10/ 1999.
- [103] F. Penghuai, P. Liming, J. Haiyan, C. Jianwei, and Z. Chunquan, "Effects of heat treatments on the microstructures and mechanical properties of Mg–3Nd–0.2Zn–0.4Zr (wt.%) alloy," *Materials Science and Engineering: A*, vol. 486, pp. 183-192, 2008.
- [104] D. K. Xu, L. Liu, Y. B. Xu, and E. H. Han, "The effect of precipitates on the mechanical properties of ZK60-Y alloy," *Materials Science and Engineering: A*, vol. 420, pp. 322-332, 2006.

- [105] I. A. Ibrahim, F. A. Mohamed, and E. J. Lavernia, "Particulate reinforced metal matrix composites — a review," *Journal of Materials Science*, vol. 26, pp. 1137-1156, 1991.
- [106] B. S. Murty and S. Ranganathan, "Novel materials synthesis by mechanical alloying/milling," *International Materials Reviews*, vol. 43, pp. 101-141, 1998.
- [107] Z. Fan, "Semisolid metal processing," *International Materials Reviews*, vol. 47, pp. 49-85, Apr 2002.
- [108] M. A. Gonzaleznunez, C. A. Nunezlopez, P. Skeldon, G. E. Thompson, H. Karimzadeh, P. Lyon, *et al.*, "A non-chromate conversion coating for magnesium alloys and magnesium-based metal-matrix composites," *Corrosion Science*, vol. 37, pp. 1763-1772, Nov 1995.
- [109] T. P. D. Rajan, R. M. Pillai, and B. C. Pai, "Reinforcement coatings and interfaces in aluminium metal matrix composites," *Journal of Materials Science*, vol. 33, pp. 3491-3503, 1998/07/01 1998.
- [110] L. Ci, Z. Ryu, N. Y. Jin-Phillipp, and M. Rühle, "Investigation of the interfacial reaction between multi-walled carbon nanotubes and aluminum," *Acta Materialia*, vol. 54, pp. 5367-5375, 12// 2006.
- [111] J. Corrochano, M. Lieblich, and J. Ibáñez, "The effect of ball milling on the microstructure of powder metallurgy aluminium matrix composites reinforced with MoSi₂ intermetallic particles," *Composites Part A: Applied Science and Manufacturing*, vol. 42, pp. 1093-1099, 2011.
- [112] M. Krasnowski and J. R. Dąbrowski, "Ti-Y₂O₃ Composites with Nanocrystalline and Microcrystalline Matrix," *Metallurgical and Materials Transactions A*, vol. 43, pp. 1376-1381, 2011.
- [113] M. Paramsothy, J. Chan, R. Kwok, and M. Gupta, "Enhanced mechanical response of hybrid alloy AZ31/AZ91 based on the addition of Si₃N₄ nanoparticles," *Materials Science and Engineering: A*, vol. 528, pp. 6545-6551, 2011.
- [114] R. Jamaati, M. R. Toroghinejad, and H. Edris, "Effect of SiC nanoparticles on the mechanical properties of steel-based nanocomposite produced by accumulative roll bonding process," *Materials & Design*, vol. 54, pp. 168-173, 2014.
- [115] H. Ye and X. Liu, "Review of recent studies in magnesium matrix composites," *Journal of Materials Science*, vol. 39, pp. 6153-6171, 2004.
- [116] V. Sklenička, M. Svoboda, M. Pahutová, K. Kuchařová, and T. G. Langdon, "Microstructural processes in creep of an AZ 91 magnesium-based composite and

- its matrix alloy," *Materials Science and Engineering: A*, vol. 319–321, pp. 741-745, 2001.
- [117] Y. Li and T. Langdon, "Creep behavior of an AZ91 magnesium alloy reinforced with alumina fibers," *Metallurgical and Materials Transactions A*, vol. 30, pp. 2059-2066, 1999/08/01 1999.
- [118] Z. Huang, S. Yu, J. Liu, and X. Zhu, "Microstructure and mechanical properties of in situ Mg₂Si/AZ91D composites through incorporating fly ash cenospheres," *Materials & Design*, vol. 32, pp. 4714-4719, 2011.
- [119] C. Zener and J. H. Hollomon, "Effect of Strain Rate Upon Plastic Flow of Steel," *J. Appl. Phys*, vol. 15, p. 22, 1944.
- [120] Z. Xiaoqing, L. Shukui, L. Jinxu, W. Yingchun, and W. Xing, "Self-sharpening behavior during ballistic impact of the tungsten heavy alloy rod penetrators processed by hot-hydrostatic extrusion and hot torsion," *Materials Science and Engineering: A*, vol. 527, pp. 4881-4886, 2010.
- [121] G. J. Irwin, C. d. r. p. l. d. e. n. s. e, C. D. R. Board, C. D. o. N. Defence, C. d. r. p. l. d. Valcartier, and D. R. E. Valcartier, *Metallographic Interpretation of Impacted Ogive Penetrators*. Canada: Defence Research Board, 1972.
- [122] T. J. Burns and M. A. Davies, "Nonlinear dynamics model for chip segmentation in machining," *Physical Review Letters*, vol. 79, pp. 447-450, Jul 21 1997.
- [123] M. A. Davies and T. J. Burns, "Thermomechanical oscillations in material flow during high-speed machining," *Philosophical Transactions of the Royal Society of London Series a-Mathematical Physical and Engineering Sciences*, vol. 359, pp. 821-846, Apr 15 2001.
- [124] T. J. Burns and M. A. Davies, "On repeated adiabatic shear band formation during high-speed machining," *International Journal of Plasticity*, vol. 18, pp. 487-506, 2002 2002.
- [125] R. F. Recht, "Catastrophic thermoplastic shear," *J. Appl. Mech.*, vol. 86, p. 189, 1964.
- [126] H. C. Rogers, "Adiabatic plastic-deformation," *Annual Review of Materials Science*, vol. 9, pp. 283-311, 1979 1979.
- [127] A. Molinari, C. Musquar, and G. Sutter, "Adiabatic shear banding in high speed machining of Ti-6Al-4V: experiments and modeling," *International Journal of Plasticity*, vol. 18, pp. 443-459, 2002.

- [128] K. M. Cho, S. Lee, S. R. Nutt, and J. Duffy, "Adiabatic shear band formation during dynamic torsional deformation of an hy-100 steel," *Acta Metallurgica Et Materialia*, vol. 41, pp. 923-932, Mar 1993.
- [129] T. J. Burns, "Does a shear-band result from a thermal-explosion," *Mechanics of Materials*, vol. 17, pp. 261-271, Mar 1994.
- [130] A. K. Zurek, "The study of adiabatic shear-band instability in a pearlitic 4340-steel using a dynamic punch test," *Metallurgical and Materials Transactions a-Physical Metallurgy and Materials Science*, vol. 25, pp. 2483-2489, Nov 1994.
- [131] W.-S. Lee and C.-F. Lin, "Plastic deformation and fracture behaviour of Ti-6Al-4V alloy loaded with high strain rate under various temperatures," *Materials Science and Engineering: A*, vol. 241, pp. 48-59, 1998.
- [132] T. C. Hufnagel, T. Jiao, Y. Li, L. Q. Xing, and K. T. Ramesh, "Deformation and failure of Zr₅₇Ti₅CU₂₀Ni₈Al₁₀ bulk metallic glass under quasi-static and dynamic compression," *Journal of Materials Research*, vol. 17, pp. 1441-1445, Jun 2002.
- [133] S. L. Semiatin and G. D. Lahoti, "Deformation and unstable flow in hot forging of Ti-6Al-2Sn-4Zr-2Mo-0.1Si," *Metallurgical Transactions A*, vol. 12, pp. 1705-1717, 1981/10/01 1981.
- [134] D. L. Zou, L. Zhen, C. Y. Xu, and W. Z. Shao, "Characterization of adiabatic shear bands in AM60B magnesium alloy under ballistic impact," *Materials Characterization*, vol. 62, pp. 496-502, 2011.
- [135] Q. Wei, D. Jia, K. T. Ramesh, and E. Ma, "Evolution and microstructure of shear bands in nanostructured Fe," *Applied Physics Letters*, vol. 81, pp. 1240-1242, Aug 2002.
- [136] Y. B. Xu, W. L. Zhong, Y. J. Chen, L. T. Shen, Q. Liu, Y. L. Bai, *et al.*, "Shear localization and recrystallization in dynamic deformation of 8090 Al-Li alloy," *Materials Science and Engineering: A*, vol. 299, pp. 287-295, 2001.
- [137] T. W. Wright, *The Physics and Mathematics of Adiabatic Shear Bands*: Cambridge University Press, 2002.
- [138] L. S. Magness Jr, "High strain rate deformation behaviors of kinetic energy penetrator materials during ballistic impact," *Mechanics of Materials*, vol. 17, pp. 147-154, 1994.
- [139] L. W. Meyer and F. Pursche, "Experimental Methods," in *Adiabatic Shear Localization (Second Edition)*, B. Dodd and Y. Bai, Eds., ed Oxford: Elsevier, 2012, pp. 21-109.

- [140] B. Dodd and Y. Bai, *Adiabatic Shear Localization: Frontiers and Advances*: Elsevier Science, 2012.
- [141] L. E. Murr, A. C. Ramirez, S. M. Gaytan, M. I. Lopez, E. Y. Martinez, D. H. Hernandez, *et al.*, "Microstructure evolution associated with adiabatic shear bands and shear band failure in ballistic plug formation in Ti-6Al-4V targets," *Materials Science and Engineering: A*, vol. 516, pp. 205-216, 2009.
- [142] A. G. Odeshi, M. N. Bassim, and S. Al-Ameeri, "Effect of heat treatment on adiabatic shear bands in a high-strength low alloy steel," *Materials Science and Engineering: A*, vol. 419, pp. 69-75, 2006.
- [143] C. K. Syn, D. R. Lesuer, and O. D. Sherby, "Microstructure in adiabatic shear bands in a pearlitic ultrahigh carbon steel," *Materials Science and Technology*, vol. 21, pp. 317-324, Mar 2005.
- [144] A. Molinari and R. J. Clifton, "Analytical Characterization of Shear Localization in Thermoviscoplastic Materials," *Journal of Applied Mechanics*, vol. 54, pp. 806-812, 1987.
- [145] M. R. Staker, "The relation between adiabatic shear instability strain and material properties," *Acta Metallurgica*, vol. 29, pp. 683-689, 1981.
- [146] R. J. Clifton, J. Duffy, K. A. Hartley, and T. G. Shawki, "On critical conditions for shear band formation at high strain rates," *Scripta Metallurgica*, vol. 18, pp. 443-448, 1984.
- [147] Y. L. Bai, "Thermo-plastic instability in simple shear," *Journal of the Mechanics and Physics of Solids*, vol. 30, pp. 195-207, 1982.
- [148] D. E. Grady, "Properties of an adiabatic shear-band process zone," *Journal of the Mechanics and Physics of Solids*, vol. 40, pp. 1197-1215, Aug 1992.
- [149] D. E. Grady, "Dissipation in adiabatic shear bands," *Mechanics of Materials*, vol. 17, pp. 289-293, 1994.
- [150] T. J. Burns, "Similarity and bifurcation in unstable visco-plastic shear," *Siam Journal on Applied Mathematics*, vol. 49, pp. 314-329, Feb 1989.
- [151] A. M. Merzer, "Modeling of adiabatic shear band development from small imperfections " *Journal of the Mechanics and Physics of Solids*, vol. 30, pp. 323-, 1982.
- [152] T. W. Wright, "Steady shearing in a viscoplastic solid," *Journal of the Mechanics and Physics of Solids*, vol. 35, pp. 269-282, 1987.

- [153] T. W. Wright and J. W. Walter, "On stress collapse in adiabatic shear bands," *Journal of the Mechanics and Physics of Solids*, vol. 35, pp. 701-720, 1987.
- [154] T. W. Wright, "Approximate analysis for the formation of adiabatic shear bands," *Journal of the Mechanics and Physics of Solids*, vol. 38, pp. 515-530, 1990.
- [155] T. W. Wright, "Shear band susceptibility: Work hardening materials," *International Journal of Plasticity*, vol. 8, pp. 583-602, 1992.
- [156] T. G. Shawki, "The Phenomenon of Shear Strain Localization in Dynamic Viscoplasticity," *Applied Mechanics Reviews*, vol. 45, pp. S46-S61, 1992.
- [157] H. P. Cherukuri and T. G. Shawki, "An energy-based localization theory: I. Basic framework," *International Journal of Plasticity*, vol. 11, pp. 15-40, 1995.
- [158] H. P. Cherukuri and T. G. Shawki, "An energy-based localization theory: II. Effects of the diffusion, inertia, and dissipation numbers," *International Journal of Plasticity*, vol. 11, pp. 41-64, 1995.
- [159] K. A. Hartley, J. Duffy, and R. H. Hawley, "Measurement of the temperature profile during shear band formation in steels deforming at high strain rates," *Journal of the Mechanics and Physics of Solids*, vol. 35, pp. 283-301, 1987.
- [160] Q. Wei, L. J. Keeskes, and K. T. Ramesh, "Effect of low-temperature rolling on the propensity to adiabatic shear banding of commercial purity tungsten," *Materials Science and Engineering: A*, vol. 578, pp. 394-401, 2013.
- [161] Y. L. Bai, Q. Xue, Y. B. Xu, and L. T. Shen, "Characteristics and microstructure in the evolution of shear localization in Ti-6Al-4V alloy," *Mechanics of Materials*, vol. 17, pp. 155-164, Mar 1994.
- [162] Y. B. Xu, Y. L. Bai, Q. Xue, and L. T. Shen, "Formation, microstructure and development of the localized shear deformation in low-carbon steels," *Acta Materialia*, vol. 44, pp. 1917-1926, May 1996.
- [163] A. Marchand and J. Duffy, "An experimental study of the formation process of adiabatic shear bands in a structural steel," *Journal of the Mechanics and Physics of Solids*, vol. 36, pp. 251-&, 1988.
- [164] H. J. Kestenbach and M. Meyers, "The effect of grain size on the shock-loading response of 304-type stainless steel," *Metallurgical Transactions A*, vol. 7, pp. 1943-1950, 1976.
- [165] M. A. Meyers, Y. B. Xu, Q. Xue, M. T. Perez-Prado, and T. R. McNelley, "Microstructural evolution in adiabatic shear localization in stainless steel," *Acta Materialia*, vol. 51, pp. 1307-1325, Mar 2003.

- [166] B. F. Wang and Y. Yang, "Microstructure evolution in adiabatic shear band in fine-grain-sized Ti–3Al–5Mo–4.5V alloy," *Materials Science and Engineering: A*, vol. 473, pp. 306-311, 2008.
- [167] Y. Xu and M. A. Meyers, "Nanostructural and Microstructural Aspects of Shear Localization at High-Strain Rates for Materials," in *Adiabatic Shear Localization (Second Edition)*, B. Dodd and Y. Bai, Eds., ed Oxford: Elsevier, 2012, pp. 111-171.
- [168] D. Jia, K. T. Ramesh, and E. Ma, "Effects of nanocrystalline and ultrafine grain sizes on constitutive behavior and shear bands in iron," *Acta Materialia*, vol. 51, pp. 3495-3509, Jul 2003.
- [169] M. A. Meyers, G. Subhash, B. K. Kad, and L. Prasad, "Evolution of microstructure and shear-band formation in α -hcp titanium," *Mechanics of Materials*, vol. 17, pp. 175-193, 1994.
- [170] M. T. Pérez-Prado, J. A. Hines, and K. S. Vecchio, "Microstructural evolution in adiabatic shear bands in Ta and Ta–W alloys," *Acta Materialia*, vol. 49, pp. 2905-2917, 2001.
- [171] V. F. Nesterenko, M. A. Meyers, J. C. LaSalvia, M. P. Bondar, Y. J. Chen, and Y. L. Lukyanov, "Shear localization and recrystallization in high-strain, high-strain-rate deformation of tantalum," *Materials Science and Engineering: A*, vol. 229, pp. 23-41, 1997.
- [172] D. Rittel, Z. G. Wang, and M. Merzer, "Adiabatic Shear Failure and Dynamic Stored Energy of Cold Work," *Physical Review Letters*, vol. 96, pp. 075501 - 075504, 2006.
- [173] L. Zhen, D. L. Zou, C. Y. Xu, and W. Z. Shao, "Microstructure evolution of adiabatic shear bands in AM60B magnesium alloy under ballistic impact," *Materials Science and Engineering: A*, vol. 527, pp. 5728-5733, 2010.
- [174] J. Liu, "High volume fraction Mg-based Nanocomposites: Processing, Microstructure and Mechanical Behavior," Doctor of Philosophy, Materials Science and Engineering, University of Central Florida, 2013.
- [175] H. Zhao and G. Gary, "On the use of SHPB techniques to determine the dynamic behavior of materials in the range of small strains," *International Journal of Solids and Structures*, vol. 33, pp. 3363-3375, 1996.
- [176] A. M. Lennon and K. T. Ramesh, "A technique for measuring the dynamic behavior of materials at high temperatures," *International Journal of Plasticity*, vol. 14, pp. 1279-1292, 1998.

- [177] M. A. Meyers, *Dynamic Behavior of Materials*: Wiley, 1994.
- [178] L. Yang, F. Zhou, and L. Wang, *Foundations of Stress Waves*: Elsevier Ltd., 2007.
- [179] R. Haberman, *Applied Partial Differential Equations with Fourier Series and Boundary Value Problems: International Edition*, 5th ed.: Pearson, 2012.
- [180] F. Zhou, L. Wang, and S. Hu, "On the Effect of Stress Nonuniformness in Polymer Specimen of SHPB Tests," *Journal of Experimental Mechanics*, vol. 01, 1992.
- [181] G. Ravichandran and G. Subhash, "CRITICAL-APPRAISAL OF LIMITING STRAIN RATES FOR COMPRESSION TESTING OF CERAMICS IN A SPLIT HOPKINSON PRESSURE BAR," *Journal of the American Ceramic Society*, vol. 77, pp. 263-267, Jan 1994.
- [182] L. M. Yang and V. P. W. Shim, "An analysis of stress uniformity in split Hopkinson bar test specimens," *International Journal of Impact Engineering*, vol. 31, pp. 129-150, 2005.
- [183] W. W. Chen and B. Song, *Split Hopkinson (Kolsky) Bar: Design, Testing and Applications*: Springer, 2010.
- [184] L. Brewer, D. Field, and C. Merriman, "Mapping and Assessing Plastic Deformation Using EBSD," in *Electron Backscatter Diffraction in Materials Science*, A. J. Schwartz, M. Kumar, B. L. Adams, and D. P. Field, Eds., ed: Springer US, 2009, pp. 251-262.
- [185] S. Sandlöbes, Z. Pei, M. Friák, L. F. Zhu, F. Wang, S. Zaefferer, *et al.*, "Ductility improvement of Mg alloys by solid solution: Ab initio modeling, synthesis and mechanical properties," *Acta Materialia*, vol. 70, pp. 92-104, 2014.
- [186] G. D. Fan, M. Y. Zheng, X. S. Hu, K. Wu, W. M. Gan, and H. G. Brokmeier, "Internal friction and microplastic deformation behavior of pure magnesium processed by equal channel angular pressing," *Materials Science and Engineering: A*, vol. 561, pp. 100-108, 2013.
- [187] Akihiro Yamashita, Zenji Horita, and T. G. Langdonb., "Improving the mechanical properties of magnesium and a magnesium alloy through severe plastic deformation," *Mat. Sci. & Eng. A*, vol. 300, pp. 142-147, 2001.
- [188] E. Fitzpatrick and A. Lodini, *Analysis of Residual Stress by Diffraction using Neutron and Synchrotron Radiation*: Taylor & Francis, 2003.

- [189] A. Jäger and V. Gärtnerová "Equal channel angular pressing of magnesium at room temperature: the effect of processing route on microstructure and texture," *Philosophical Magazine Letters*, vol. 92, pp. 384-390, 2012/08/01 2012.
- [190] J. Shen, W. Yin, K. Kondoh, T. L. Jones, L. J. Kecskes, S. N. Yarmolenko, *et al.*, "Mechanical Behavior of a Lanthanum-Doped Magnesium Alloy at Different Strain Rates," 2014 submitted.
- [191] D. Caillard and J. L. Martin, *Thermally Activated Mechanisms in Crystal Plasticity*: Elsevier Science, 2003.
- [192] Q. Wei, "Strain rate effects in the ultrafine grain and nanocrystalline regimes— its influence on some constitutive responses," *Journal of Materials Science*, vol. 42, pp. 1709-1727, 2007.
- [193] Y. Z. Guo, N. A. Behm, J. P. Ligda, Y. L. Li, Z. Pan, Z. Horita, *et al.*, "Critical issues related to instrumented indentation on non-uniform materials: Application to niobium subjected to high pressure torsion," *Materials Science and Engineering a-Structural Materials Properties Microstructure and Processing*, vol. 586, pp. 149-159, Dec 2013.
- [194] D. Hull and D. J. Bacon, *Introduction to Dislocations*: Elsevier Science, 2001.
- [195] N. A. Fleck, G. M. Muller, M. F. Ashby, and J. W. Hutchinson, "Strain gradient plasticity: Theory and experiment," *Acta Metallurgica Et Materialia*, vol. 42, pp. 475-487, 1994.
- [196] K. A. Darling, M. A. Tschopp, R. K. Guduru, W. H. Yin, Q. Wei, and L. J. Kecskes, "Microstructure and mechanical properties of bulk nanostructured Cu–Ta alloys consolidated by equal channel angular extrusion," *Acta Materialia*, vol. 76, pp. 168-185, 2014.
- [197] Y. Li, T. Suo, and M. Liu, "Influence of the strain rate on the mechanical behavior of the 3D needle-punched C/SiC composite," *Materials Science and Engineering: A*, vol. 507, pp. 6-12, 2009.
- [198] T. Suo, Y.-l. Li, K. Xie, F. Zhao, K.-s. Zhang, and Y.-y. Liu, "The effect of temperature on mechanical behavior of ultrafine-grained copper by equal channel angular pressing," *Materials Science and Engineering: A*, vol. 527, pp. 5766-5772, 2010.
- [199] T. Suo, Y. Li, F. Zhao, X. Fan, and W. Guo, "Compressive behavior and rate-controlling mechanisms of ultrafine grained copper over wide temperature and strain rate ranges," *Mechanics of Materials*, vol. 61, pp. 1-10, 2013.

- [200] R. Kapoor and J. K. Chakravartty, "Deformation behavior of an ultrafine-grained Al–Mg alloy produced by equal-channel angular pressing," *Acta Materialia*, vol. 55, pp. 5408-5418, 2007.
- [201] K. Lucke and K. Detert, "A quantitative theory of grain-boundary motion and recrystallization in metals in the presence of impurities," *Acta Metallurgica*, vol. 5, pp. 628-637, 1957.
- [202] D. J. Lloyd, "Particle reinforced aluminium and magnesium matrix composites," *International Materials Reviews*, vol. 39, pp. 1-23, 1994.
- [203] J. Shen, W. Yin, Q. Wei, Y. Li, J. Liu, and L. An, "Effect of ceramic nanoparticle reinforcements on the quasistatic and dynamic mechanical properties of magnesium-based metal matrix composites," *Journal of Materials Research*, vol. 28, pp. 1835-1852, 2013.
- [204] N. Ono, R. Nowak, and S. Miura, "Effect of deformation temperature on Hall–Petch relationship registered for polycrystalline magnesium," *Materials Letters*, vol. 58, pp. 39-43, 2003.
- [205] X. L. Wu, K. M. Youssef, C. C. Koch, S. N. Mathaudhu, L. J. Kecskés, and Y. T. Zhu, "Deformation twinning in a nanocrystalline hcp Mg alloy," *Scripta Materialia*, vol. 64, pp. 213-216, 2011.
- [206] P. Klimanek and A. Potzsch, "Microstructure evolution under compressive plastic deformation of magnesium at different temperatures and strain rates," *Materials Science and Engineering a-Structural Materials Properties Microstructure and Processing*, vol. 324, pp. 145-150, Feb 2002.
- [207] N. Stanford, U. Carlson, and M. R. Barnett, "Deformation Twinning and the Hall–Petch Relation in Commercial Purity Ti," *Metallurgical and Materials Transactions A*, vol. 39, pp. 934-944, 2008/04/01 2008.
- [208] S. V. Zherebtsov, G. S. Dyakonov, A. A. Salem, V. I. Sokolenko, G. A. Salishchev, and S. L. Semiatin, "Formation of nanostructures in commercial-purity titanium via cryorolling," *Acta Materialia*, vol. 61, pp. 1167-1178, 2013.
- [209] X. Wu and Y. Zhu, "Inverse Grain-Size Effect on Twinning in Nanocrystalline Ni," *Physical Review Letters*, vol. 101, 2008.
- [210] T. H. Courtney, *Mechanical behavior of materials*: Waveland Press, 2005.
- [211] G. Taylor, "Thermally-activated deformation of bcc metals and alloys," *Progress in Materials Science*, vol. 36, pp. 29-61., 1992.

- [212] Z. Trojanová, P. Lukáč, and Z. Szárz, "Deformation Behaviour of Nanocrystalline Mg Studied at Elevated Temperatures," *Reviews on Advanced Materials Science*, vol. 10, p. 437, 2005.
- [213] S. Hwang, C. Nishimura, and P. G. McCormick, "Deformation mechanism of nanocrystalline magnesium in compression," *Scripta Materialia*, vol. 44, pp. 1507-1511, 2001.
- [214] H. Baker, *Alloy Phase Diagrams* vol. 3. Materials Park, OH: ASM International, 2006.
- [215] B. Li, S. Joshi, K. Azevedo, E. Ma, K. T. Ramesh, R. B. Figueiredo, *et al.*, "Dynamic testing at high strain rates of an ultrafine-grained magnesium alloy processed by ECAP," *Materials Science and Engineering a-Structural Materials Properties Microstructure and Processing*, vol. 517, pp. 24-29, Aug 20 2009.
- [216] C. A. Schuh, T. C. Hufnagel, and U. Ramamurty, "Mechanical Behavior of amorphous alloys," *Acta Materialia*, vol. 55, pp. 4067-4109, 2007.
- [217] X. L. Wu, Y. Z. Guo, Q. Wei, and W. H. Wang, "Prevalence of shear banding in compression of Zr₄₁Ti₁₄Cu_{12.5}Ni₁₀Be_{22.5} pillars as small as 150 nm in diameter " *Acta Materialia*, vol. 57, pp. 3562-3571, 2009.
- [218] Q. Wei, T. Jiao, K. T. Ramesh, and E. Ma, "Nano-structured vanadium: processing and mechanical properties under quasi-static and dynamic compression," *Scripta materialia*, vol. 50, pp. 359-364, 2004.
- [219] Q. Wei, T. Jiao, K. T. Ramesh, E. Ma, L. J. Kecskes, L. Magness, *et al.*, "Mechanical behavior and dynamic failure of high-strength ultrafine grained tungsten under uniaxial compression," *Acta Materialia*, vol. 54, pp. 77-87, 2006.
- [220] Q. Wei, L. J. Kecskes, T. Jiao, K. T. Hartwig, K. T. Ramesh, and E. Ma, "Adiabatic shear banding in ultrafine grained Fe processed by severe plastic deformation," *Acta materialia*, vol. 52, pp. 1859-1869, 2004.
- [221] Q. Wei, L. J. Kecskes, and K. T. Ramesh, "Effect of Low-Temperature Rolling on the Propensity to Adiabatic Shear Banding of Commercial Purity Tungsten," *Materials Science and Engineering A*, vol. 578, pp. 394-401, 2013.
- [222] Q. Wei, Z. L. Pan, X. L. Wu, B. E. Schuster, L. J. Kecskes, and R. Z. Valiev, "Microstructure and mechanical properties at different length scales and strain rates of nanocrystalline tantalum produced by high pressure torsion," *Acta Materialia*, vol. 59, pp. 2423-2436, 2011.
- [223] Q. Wei, H. Zhang, B. E. Schuster, K. T. Ramesh, R. Z. Valiev, L. J. Kecskes, *et al.*, "Microstructure and mechanical properties of super-strong nanocrystalline

- tungsten processed by high-pressure torsion," *Acta Materialia*, vol. 54, pp. 4079-4089, 2006.
- [224] Q. M. Wei and L. J. Kecskes, "Dynamic mechanical behavior of ultrafine and nanocrystalline refractory metals," in *Mechanical Properties of Nanocrystalline Materials*, J. C. M. Li, Ed., ed Singapore: Pan Stanford Publishing, 2011, pp. 213-243.
- [225] W. H. Yin, F. Xu, O. Ertorer, Z. Pan, X. Y. Zhang, L. J. Kecskes, *et al.*, "Mechanical behavior of microstructure engineered multi-length-scale titanium over a wide range of strain rates," *Acta Materialia*, vol. 61, pp. 3781-3798, 2013.
- [226] J. P. Hadorn, K. Hantzsche, S. B. Yi, J. Bohlen, D. Letzig, J. A. Wollmershauser, *et al.*, "Role of Solute in the Texture Modification During Hot Deformation of Mg-Rare Earth Alloys," *Metallurgical and Materials Transactions a-Physical Metallurgy and Materials Science*, vol. 43A, pp. 1347-1362, Apr 2012.
- [227] J. Bohlen, S. B. Yi, D. Letzig, and K. U. Kainer, "Effect of rare earth elements on the microstructure and texture development in magnesium-manganese alloys during extrusion," *Materials Science and Engineering a-Structural Materials Properties Microstructure and Processing*, vol. 527, pp. 7092-7098, Oct 2010.
- [228] K. Hantzsche, J. Bohlen, J. Wendt, K. U. Kainer, S. B. Yi, and D. Letzig, "Effect of rare earth additions on microstructure and texture development of magnesium alloy sheets," *Scripta Materialia*, vol. 63, pp. 725-730, Oct 2010.
- [229] C. J. Ma, M. P. Liu, G. H. Wu, W. J. Ding, and Y. P. Zhu, "Tensile properties of extruded ZK60-RE alloys," *Materials Science and Engineering a-Structural Materials Properties Microstructure and Processing*, vol. 349, pp. 207-212, May 2003.
- [230] L. W. F. Mackenzie and M. O. Pekguleryuz, "The recrystallization and texture of magnesium-zinc-cerium alloys," *Scripta Materialia*, vol. 59, pp. 665-668, Sep 2008.
- [231] N. Stanford, "Micro-alloying Mg with Y, Ce, Gd and La for texture modification-A comparative study," *Materials Science and Engineering a-Structural Materials Properties Microstructure and Processing*, vol. 527, pp. 2669-2677, Apr 2010.
- [232] N. Stanford, D. Atwell, A. Beer, C. Davies, and M. R. Barnett, "Effect of microalloying with rare-earth elements on the texture of extruded magnesium-based alloys," *Scripta Materialia*, vol. 59, pp. 772-775, Oct 2008.
- [233] N. Stanford and M. R. Barnett, "The origin of "rare earth" texture development in extruded Mg-based alloys and its effect on tensile ductility," *Materials Science*

and Engineering a-Structural Materials Properties Microstructure and Processing, vol. 496, pp. 399-408, Nov 2008.

- [234] T. Al-Samman and X. Li, "Sheet texture modification in magnesium-based alloys by selective rare earth alloying," *Materials Science and Engineering a-Structural Materials Properties Microstructure and Processing*, vol. 528, pp. 3809-3822, Apr 2011.
- [235] M. A. Gharghouri, G. C. Weatherly, J. D. Embury, and J. Root, "Study of the mechanical properties of Mg-7.7at.% Al by in-situ neutron diffraction," *Philosophical Magazine a-Physics of Condensed Matter Structure Defects and Mechanical Properties*, vol. 79, pp. 1671-1695, Jul 1999.
- [236] M. Meyers, A. Mishra, and D. Benson, "Mechanical properties of nanocrystalline materials," *Progress in Materials Science*, vol. 51, pp. 427-556, 2006.
- [237] X. L. Zhong, W. L. E. Wong, and M. Gupta, "Enhancing strength and ductility of magnesium by integrating it with aluminum nanoparticles," *Acta Materialia*, vol. 55, pp. 6338-6344, 2007.
- [238] M. Paramsothy, S. F. Hassan, N. Srikanth, and M. Gupta, "Enhancing tensile/compressive response of magnesium alloy AZ31 by integrating with Al₂O₃ nanoparticles," *Materials Science and Engineering: A*, vol. 527, pp. 162-168, 2009.
- [239] S. Agnew, W. Whittington, A. Oppedal, H. Kadiri, M. Shaeffer, K. T. Ramesh, *et al.*, "Dynamic Behavior of a Rare-Earth-Containing Mg Alloy, WE43B-T5, Plate with Comparison to Conventional Alloy, AM30-F," *JOM*, vol. 66, pp. 277-290, 2014.
- [240] K. S. Prasad, B. Li, N. Dixit, M. Shaffer, S. N. Mathaudhu, and K. T. Ramesh, "The Dynamic Flow and Failure Behavior of Magnesium and Magnesium Alloys," *JOM*, vol. 66, pp. 291-304, 2014.
- [241] I. Ulacia, N. V. Dudamell, F. Gálvez, S. Yi, M. T. Pérez-Prado, and I. Hurtado, "Mechanical behavior and microstructural evolution of a Mg AZ31 sheet at dynamic strain rates," *Acta Materialia*, vol. 58, pp. 2988-2998, 2010.
- [242] W. S. Farren and G. I. Taylor, "The Heat Developed during Plastic Extension of Metals," *Proceedings of the Royal Society of London. Series A, Containing Papers of a Mathematical and Physical Character*, vol. 107, pp. 422-451, 1925.
- [243] A. J. Cao, Y. Q. Cheng, and E. Ma, "Structural processes that initiate shear localization in metallic glass," *Acta Materialia*, vol. 57, pp. 5146-5155, 2009.

- [244] G. Timár and J. da Fonseca, "Modeling Twin Clustering and Strain Localization in Hexagonal Close-Packed Metals," *Metallurgical and Materials Transactions A*, vol. 45, pp. 5883-5890, 2014/12/01 2014.
- [245] S. Qu, H. Zhou, and Z. Huang, "Shear band initiation induced by slip-twin boundary interactions," *Scripta Materialia*, vol. 65, pp. 715-718, 10// 2011.
- [246] A. Mishra, M. Martin, N. N. Thadhani, B. K. Kad, E. A. Kenik, and M. A. Meyers, "High-strain-rate response of ultra-fine-grained copper," *Acta Materialia*, vol. 56, pp. 2770-2783, 2008.
- [247] W. B. Hutchinson and M. R. Barnett, "Effective values of critical resolved shear stress for slip in polycrystalline magnesium and other hcp metals," *Scripta Materialia*, vol. 63, pp. 737-740, 2010.
- [248] M. Suzuki, H. Sato, K. Maruyama, and H. Oikawa, "Creep behavior and deformation microstructures of Mg–Y alloys at 550 K," *Materials Science and Engineering: A*, vol. 252, pp. 248-255, 1998.
- [249] M. Suzuki, H. Sato, K. Maruyama, and H. Oikawa, "Creep deformation behavior and dislocation substructures of Mg–Y binary alloys," *Materials Science and Engineering: A*, vol. 319–321, pp. 751-755, 2001.
- [250] H. Ferkel and B. L. Mordike, "Magnesium strengthened by SiC nanoparticles," *Materials Science and Engineering A*, vol. 298, pp. 193-199, 2001.
- [251] M. K. Habibi, S. P. Joshi, and M. Gupta, "Hierarchical magnesium nanocomposites for enhanced mechanical response," *Acta Materialia*, vol. 58, pp. 6104-6114, 2010.
- [252] S. F. Hassan, "Effect of primary processing techniques on the microstructure and mechanical properties of nano-Y₂O₃ reinforced magnesium nanocomposites," *Materials Science and Engineering: A*, vol. 528, pp. 5484-5490, 2011.
- [253] S. F. Hassan and M. Gupta, "Development of high performance magnesium nanocomposites using nano-Al₂O₃ as reinforcement," *Materials Science and Engineering: A*, vol. 392, pp. 163-168, 2005.
- [254] P. Jayaramanavar, M. Paramsothy, A. Balaji, and M. Gupta, "Tailoring the tensile/compressive response of magnesium alloy ZK60A using Al₂O₃ nanoparticles," *Journal of Materials Science*, vol. 45, pp. 1170-1178, 2010.
- [255] M. K. Habibi, M. Paramsothy, A. M. S. Hamouda, and M. Gupta, "Using integrated hybrid (Al+CNT) reinforcement to simultaneously enhance strength and ductility of magnesium," *Composites Science and Technology*, vol. 71, pp. 734-741, 2011.

- [256] S. Liu, F. Gao, Q. Zhang, X. Zhu, and W. Li, "Fabrication of carbon nanotubes reinforced AZ91D composites by ultrasonic processing," *Transactions of Nonferrous Metals Society of China*, vol. 20, pp. 1222-1227, 2010.
- [257] X. Y. Jia, S. Y. Liu, F. P. Gao, Q. Y. Zhang, and W. Z. Li, "Magnesium matrix nanocomposites fabricated by ultrasonic assisted casting," *International Journal of Cast Metals Research*, vol. 22, pp. 196-199, 2009.
- [258] Z. Wang, X. Wang, Y. Zhao, and W. Du, "SiC nanoparticles reinforced magnesium matrix composites fabricated by ultrasonic method," *Transactions of Nonferrous Metals Society of China*, vol. 20, Supplement 3, pp. s1029-s1032, 2010.
- [259] C. Rauber, A. Lohmueller, S. Opel, and R. F. Singer, "Microstructure and mechanical properties of SiC particle reinforced magnesium composites processed by injection molding," *Materials Science and Engineering a-Structural Materials Properties Microstructure and Processing*, vol. 528, pp. 6313-6323, Jul 25 2011.
- [260] H. Dieringa, "Properties of magnesium alloys reinforced with nanoparticles and carbon nanotubes: a review," *Journal of materials science*, vol. 46, pp. 289-306, Jan 2011.
- [261] A. Luo, "Processing, microstructure, and mechanical-behavior of cast magnesium metal-matrix composites," *Metallurgical and Materials Transactions a-Physical Metallurgy and Materials Science*, vol. 26, pp. 2445-2455, Sep 1995.
- [262] M. R. Krishnadev, R. Angers, C. G. K. Nair, and G. Huard, "THE STRUCTURE AND PROPERTIES OF MAGNESIUM-MATRIX COMPOSITES," *Jom-Journal of the Minerals Metals & Materials Society*, vol. 45, pp. 52-54, Aug 1993.
- [263] K. B. Nie, X. J. Wang, X. S. Hu, L. Xu, K. Wu, and M. Y. Zheng, "Microstructure and mechanical properties of SiC nanoparticles reinforced magnesium matrix composites fabricated by ultrasonic vibration," *Materials Science and Engineering a-Structural Materials Properties Microstructure and Processing*, vol. 528, pp. 5278-5282, Jun 15 2011.
- [264] P. Poddar, V. C. Srivastava, P. K. De, and K. L. Sahoo, "Processing and mechanical properties of SiC reinforced cast magnesium matrix composites by stir casting process," *Materials Science and Engineering a-Structural Materials Properties Microstructure and Processing*, vol. 460, pp. 357-364, Jul 15 2007.
- [265] G. Huard, R. Angers, M. R. Krishnadev, R. Tremblay, and D. Dube, "SiCp/Mg composites made by low-energy mechanical processing," *Canadian Metallurgical Quarterly*, vol. 38, pp. 193-200, Jul 1999.

- [266] Y. B. Guo, V. P. W. Shim, and B. W. F. Tan, "Response of Magnesium Nanocomposites to Quasi Static and Dynamic Loading," in *IMPLAST 2010*, Rhode Island.
- [267] K. Zhang, I. V. Alexandrov, R. Z. Valiev, and K. Lu, "Structural characterization of nanocrystalline copper by means of x - ray diffraction," *Journal of Applied Physics*, vol. 80, pp. 5617-5624, 1996.
- [268] G. Garcés, E. Oñorbe, P. Pérez, M. Klaus, C. Genzel, and P. Adeva, "Influence of SiC particles on compressive deformation of magnesium matrix composites," *Materials Science and Engineering: A*, vol. 533, pp. 119-123, 2012.
- [269] T. W. Clyne and P. J. Withers, *An Introduction to Metal Matrix Composites*: Cambridge University Press, 1995.
- [270] Y. Li and K. T. Ramesh, "Influence of particle volume fraction, shape, and aspect ratio on the behavior of particle-reinforced metal-matrix composites at high rates of strain," *Acta Materialia*, vol. 46, pp. 5633-5646, Oct 9 1998.
- [271] Y. Li, K. T. Ramesh, and E. S. C. Chin, "Viscoplastic deformations and compressive damage in an A359/SiCp metal-matrix composite," *Acta Materialia*, vol. 48, pp. 1563-1573, Apr 19 2000.
- [272] G. Bao and Z. Lin, "High strain rate deformation in particle reinforced metal matrix composites," *Acta Materialia*, vol. 44, pp. 1011-1019, Mar 1996.
- [273] S. Yadav, D. R. Chichili, and K. T. Ramesh, "THE MECHANICAL RESPONSE OF A 6061-T6 AL/AL₂O₃ METAL-MATRIX COMPOSITE AT HIGH-RATES OF DEFORMATION," *Acta Metallurgica et Materialia*, vol. 43, pp. 4453-4464, Dec 1995.
- [274] T. Christman, A. Needleman, and S. Suresh, "An experimental and numerical study of deformation in metal-ceramic composites," *Acta Metallurgica*, vol. 37, pp. 3029-3050, 1989.
- [275] J. D. Eshelby, "The determination of the elastic field of an ellipsoidal inclusion, and related problems," *Proceedings of the Royal Society A*, vol. 241, pp. 376-396, 1957.
- [276] S. Groh, B. Devincre, L. P. Kubin, A. Roos, F. Feyel, and J. L. Chaboche, "Size effects in metal matrix composites," *Materials Science and Engineering a-Structural Materials Properties Microstructure and Processing*, vol. 400, pp. 279-282, Jul 2005.
- [277] E. O. Hall, "The deformation and ageing of mild steel: III. Discussion of results," *Proceedings of the Physical Society B*, vol. 64, pp. 747-753, 1951.

- [278] M. F. Ashby, "The deformation of plastically non-homogeneous materials," *Philosophical Magazine*, vol. 21, pp. 399-424, 1970/02/01 1970.
- [279] F. Louchet, J. Weiss, and T. Richeton, "Hall-Petch law revisited in terms of collective dislocation dynamics," *Physical Review Letters*, vol. 97, p. 075504, 2006.
- [280] H. J. Choi, Y. Kim, J. H. Shin, and D. H. Bae, "Deformation behavior of magnesium in the grain size spectrum from nano- to micrometer," *Materials Science and Engineering: A*, vol. 527, pp. 1565-1570, 2010.
- [281] M. Dao, L. Lu, R. J. Asaro, J. T. M. de Hosson, and E. Ma, "Toward a quantitative understanding of mechanical behavior of nanocrystalline metals," *Acta Materialia*, vol. 55, pp. 4041-4065, 2007.
- [282] Z. W. Shan, E. A. Stach, J. M. K. Wiezorek, J. A. Knapp, D. M. Follstaedt, and S. X. Mao, "Grain boundary mediated plasticity in nanocrystalline nickel," *Science*, vol. 305, pp. 654-657., 2004.
- [283] A. Mortensen and J. Llorca, "Metal Matrix Composites," in *Annual Review of Materials Research, Vol 40*. vol. 40, D. R. Clarke, M. Ruhle, and F. Zok, Eds., ed Palo Alto: Annual Reviews, 2010, pp. 243-270.
- [284] V. C. Nardone and K. M. Prewo, "ON THE STRENGTH OF DISCONTINUOUS SILICON-CARBIDE REINFORCED ALUMINUM COMPOSITES," *Scripta Metallurgica*, vol. 20, pp. 43-48, Jan 1986.
- [285] Q. Wei and L. J. Kecskes, "Effect of low-temperature rolling on the tensile behavior of commercially pure tungsten," *Materials Science and Engineering: A*, vol. 491, pp. 62-69, 2008.

APPENDIX A: HEAT DIFFUSION

1. Convert the continuous problem into 2-D finite element problem

Equation (2) is the heat-transfer equation used for our computation, and the sketch represents the corresponding finite elements:

$$\frac{\partial u}{\partial t} = \alpha^2 \left(\frac{\partial^2 u}{\partial x^2} + \frac{\partial^2 u}{\partial y^2} \right), \text{ where } \alpha^2 = \frac{k}{\rho c_p} \text{ is the thermal diffusivity.} \quad (2)$$

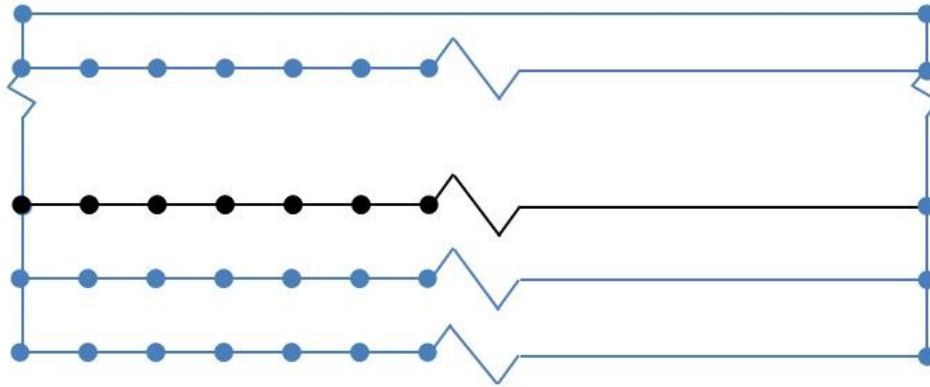


Figure 1. A sketch of the finite element of the system.

The boundary conditions are:

Un-heated region:

$$\text{Left face: } k_c \frac{u_{1,j}^n - u_{0,j}^n}{\Delta x} = h(u_{0,j}^n - u_\infty) \text{ or } (1 + \alpha_1)u_{0,j}^n - u_{1,j}^n = \alpha_1 u_\infty, \left(\alpha_1 = \frac{h \cdot \Delta x}{k_c} \right);$$

$$\text{Right face: } k_c \frac{u_{I-1,j}^n - u_{I,j}^n}{\Delta x} = h(u_{I,j}^n - u_\infty) \text{ or } u_{I-1,j}^n - (1 + \alpha_1)u_{I,j}^n = -\alpha_1 u_\infty;$$

$$\text{Bottom face: } k_c \frac{u_{i,1}^n - u_{i,0}^n}{\Delta y} = 0 \text{ or } u_{i,0}^n - u_{i,1}^n = 0;$$

Heated region:

$$\text{Left face: } k_s \frac{u_{1,j}^n - u_{0,j}^n}{\Delta x} = h(u_{0,j}^n - u_\infty) \text{ or } (1 + \alpha_2)u_{0,j}^n - u_{1,j}^n = \alpha_2 u_\infty, (\alpha_2 = \frac{h \cdot \Delta x}{k_s});$$

$$\text{Right face: } k_s \frac{u_{1-1,j}^n - u_{1,j}^n}{\Delta x} = h(u_{1,j}^n - u_\infty) \text{ or } u_{1-1,j}^n - (1 + \alpha_2)u_{1,j}^n = -\alpha_2 u_\infty;$$

$$\text{Top face: } k_s \frac{u_{i,J-1}^n - u_{i,J}^n}{\Delta y} = h(u_{i,J}^n - u_\infty) \text{ or } u_{i,J-1}^n - (1 + \gamma_2)u_{i,J}^n = -\gamma_2 u_\infty, (\gamma_2 = \frac{h \cdot \Delta y}{k_s});$$

Interface:

$$k_s \frac{u_{i,k+1}^n - u_{i,k}^n}{\Delta y} = k_c \frac{u_{i,k}^n - u_{i,k-1}^n}{\Delta y} \text{ or } -\frac{k_c}{\Delta y} u_{i,k-1}^n + (\frac{k_s}{\Delta y} + \frac{k_c}{\Delta y})u_{i,k}^n - \frac{k_s}{\Delta y} u_{i,k+1}^n = 0;$$

The initial conditions are:

$$\text{Un-heated part: } u_c^0 = 298K \text{ and } u_c^\infty = 298K;$$

$$\text{Heated part: } u_s^0 = 1123K \text{ and } u_s^\infty = 298K;$$

$$\text{Interface: } u_{i,k}^0 = \frac{\alpha_s \cdot 1123K + \alpha_c \cdot 298K}{\alpha_s + \alpha_c} \text{ and } u_{i_n}^\infty = 298K.$$

2. The Crank-Nicolson method

The 2-D heat-transfer equation is discretized using the Crank-Nicolson method:

$$\begin{aligned} \frac{u_{i,j}^{n+1} - u_{i,j}^n}{\Delta t} = & \frac{\alpha^2}{2} \left(\frac{u_{i-1,j}^{n+1} - 2u_{i,j}^{n+1} + u_{i+1,j}^{n+1}}{\Delta x^2} + \frac{u_{i-1,j}^n - 2u_{i,j}^n + u_{i+1,j}^n}{\Delta x^2} \right) \\ & + \frac{\alpha^2}{2} \left(\frac{u_{i,j-1}^{n+1} - 2u_{i,j}^{n+1} + u_{i,j+1}^{n+1}}{\Delta y^2} + \frac{u_{i,j-1}^n - 2u_{i,j}^n + u_{i,j+1}^n}{\Delta y^2} \right). \end{aligned} \quad (3)$$

where $u_{i,j}^n$ indicates the temperature locates at $x = i \cdot \Delta x$, $y = j \cdot \Delta y$ and at time $t = n \cdot \Delta t$.

In this problem, we set $\Delta x = \Delta y = l$ and let $\beta = \frac{\alpha^2 \Delta t}{\Delta x^2} = \frac{\alpha^2 \Delta t}{\Delta y^2} = \frac{\alpha^2 \Delta t}{l^2}$, then

$$u_{i-1,j}^{n+1} - \frac{4\beta+1}{\beta} u_{i,j}^{n+1} + u_{i+1,j}^{n+1} + u_{i,j-1}^{n+1} + u_{i,j+1}^{n+1} = -u_{i-1,j}^n + \frac{4\beta-1}{\beta} u_{i,j}^n - u_{i+1,j}^n - u_{i,j-1}^n - u_{i,j+1}^n. \quad (4)$$

Set $\vec{b}^n = -u_{i-1,j}^n + (\frac{4\beta-1}{\beta})u_{i,j}^n - u_{i+1,j}^n - u_{i,j-1}^n - u_{i,j+1}^n$, then we can rewrite the equation into

$$A\vec{u}^{n+1} = \vec{b}^n, \text{ where } A = [A_{pq}]_{[(I+1)\cdot(J+1)] \times [(I+1)\cdot(J+1)]} \quad (5)$$

For the bottom face, where $j = 0$, we have the condition

$$u_{i,0}^n - u_{i,1}^n = 0 \quad (6)$$

Then, $A_{ii} = 1$ and $A_{i(i+1)} = -1$; where $i = 0, 1, \dots, I$.

For the part below interface (un-heated), where $1 \leq j < k$

The front part of Eq.(4) can be rewritten as

$$\begin{aligned} (1 + \alpha_1)u_{0,j}^n - u_{1,j}^n &= \alpha_1 u_\infty \\ A_{j,j-1}\vec{u}_{j-1}^{n+1} + A_{j,j}\vec{u}_j^{n+1} + A_{j,j+1}\vec{u}_{j+1}^{n+1} &= \vec{b}_j^n \\ -u_{I-1,j}^n + (1 + \alpha_1)u_{I,j}^n &= \alpha_1 u_\infty \end{aligned} \quad (7)$$

Then, $A_{[j(I+1)+1][j(I+1)+1]} = A_{[(j+1)(I+1)][(j+1)(I+1)]} = 1 + \alpha_1$;

$$A_{[j(I+1)+1][j(I+1)+2]} = A_{[(j+1)(I+1)][(j+1)(I+1)-1]} = -1;$$

$$A_{[j(I+1)+i][j(I+1)+i]} = -4 - \frac{1}{\beta_c};$$

$$A_{[j(I+1)+i][j(I+1)+i-1]} = A_{[j(I+1)+i][j(I+1)+i+1]} = 1;$$

$$A_{[j(I+1)+i][(j-1)(I+1)+i]} = A_{[j(I+1)+i][(j+1)(I+1)+i]} = 1.$$

where $i = 1, 2, \dots, I$, and $\vec{u}_j^{n+1} = \{\vec{u}_{0,j}^{n+1}, \vec{u}_{1,j}^{n+1}, \dots, \vec{u}_{I,j}^{n+1}\}^T$.

For the part of interface, where $j = k$

By the condition $-\frac{k_c}{\Delta y}u_{i,k-1}^n + (\frac{k_s}{\Delta y} + \frac{k_c}{\Delta y})u_{i,k}^n - \frac{k_s}{\Delta y}u_{i,k+1}^n = 0$, ($a = \frac{k_s}{k_c}$), we have

$$A_{k,k-1}\vec{u}_{k-1}^{n+1} + A_{k,k}\vec{u}_k^{n+1} + A_{k,k+1}\vec{u}_{k+1}^{n+1} = \vec{b}_k^n \quad (8)$$

where $A_{k,k} = (a+1)I_{(I-1)\times(I-1)}$; $A_{k,k-1} = -I_{(I-1)\times(I-1)}$; $A_{k,k+1} = -aI_{(I-1)\times(I-1)}$ and

$$\vec{b}_k^n = \{0, 0, \dots, 0\}_{(I-1)\times 1}.$$

For the part above interface (heated), where $J-1 \geq j > k$, set $\beta_s = \frac{k_s \cdot \Delta t}{\rho_s c_{ps} \Delta x^2} = \frac{k_s \cdot \Delta t}{\rho_s c_{ps} \Delta y^2}$,

The front part of Eq.(4) can be rewritten as

$$\begin{aligned} (1 + \alpha_2)u_{0,j}^n - u_{1,j}^n &= \alpha_2 u_\infty \\ A_{j,j-1}\vec{u}_{j-1}^{n+1} + A_{j,j}\vec{u}_j^{n+1} + A_{j,j+1}\vec{u}_{j+1}^{n+1} &= \vec{b}_j^n \\ -u_{I-1,j}^n + (1 + \alpha_2)u_{I,j}^n &= \alpha_2 u_\infty \end{aligned} \quad (9)$$

Then, $A_{[j(I+1)+1][j(I+1)+1]} = A_{[(j+1)(I+1)][(j+1)(I+1)]} = 1 + \alpha_2$;

$$A_{[j(I+1)+1][j(I+1)+2]} = A_{[(j+1)(I+1)][(j+1)(I+1)-1]} = -1;$$

$$A_{[j(I+1)+i][j(I+1)+i]} = -4 - \frac{1}{\beta_s};$$

$$A_{[j(I+1)+i][j(I+1)+i-1]} = A_{[j(I+1)+i][j(I+1)+i+1]} = 1;$$

$$A_{[j(I+1)+i][(j-1)(I+1)+i]} = A_{[j(I+1)+i][(j+1)(I+1)+i]} = 1.$$

where $i = 1, 2, \dots, I$, and $\vec{u}_j^{n+1} = \{\vec{u}_{0,j}^{n+1}, \vec{u}_{1,j}^{n+1}, \dots, \vec{u}_{I,j}^{n+1}\}^T$.

For the top face (heated), where $j = J$

we have condition

$$-u_{i,J-1}^n + (1 + \gamma_2)u_{i,J}^n = \gamma_2 u_\infty \quad (10)$$

Then, $A_{(J(I+1)+i)(J(I+1)+i)} = 1 + \gamma_2$ and $A_{[J(I+1)+i][(J-1)(I+1)+i]} = -1$; where $i = 0, 1, \dots, I$.

From Eq.(6) ~ (10), the matrix A and the vector \vec{u}^{n+1} are obtained, as well as the vector \vec{b}^n that relies on the vector \vec{u}^n . Then, by inputting the initial and boundary conditions, a repetitive process of evaluating the successive temperature evolution in the system starts according to time steps. This will keep working until a stop condition is arrived, which is set to be that the difference is less than 1°C between the temperature in the system and environment. In this problem, the computation work was carried out by Matlab, and the LU decomposition of the matrix A was applied during the computation. The code for Matlab can be found in APPENDIX B.

APPENDIX B: CODE FOR MATLAB

```

%% values of parameters %%

h=3000; % heat-transfer coefficient W/m^2/K%

dc=0.00025; % unheated parts, y-direction, unit m %

ds=0.00005; % width of the shear band, y-direction, unit m %

W=0.0025; % length at x direction, unit m %

dx=0.00025; % mesh size at x direction, unit m %

dy=0.00001; % mesh size at y direction, unit m %

T=100; % total time, unit s %

dt=0.000005; % time step size, unit s %

%% at the time points used to plot the temperature field %%

TP1=ceil(0.000025/dt); % at time t = 25 us %

TP2=ceil(0.0001/dt); % at time t = 100 us %

TP3=ceil(0.0005/dt); % at time t = 0.5 ms %

TP4=ceil(0.001/dt); % at time t = 1 ms %

TP5=ceil(0.005/dt); % at time t = 5 ms %

TP6=ceil(0.025/dt); % at time t = 25 ms %

%% number of mesh grids %%

k=ceil(dc/dy); % place of the interface of heated and unheated region %

I=ceil(W/dx); % total mesh size number at x-direction %

Mid=ceil(I/2)+1; % place of points A and B along x-direction %

J=ceil((dc+ds)/dy); % total mesh size number at y-direction %

```

$N = \text{ceil}(T/dt)$; % total mesh size number of time %

%% properties of Mg at heated area %%

$k_s = 156$; % W/m/K %

$\rho_{\text{Mg}} = 1740$; % kg/m³ %

$c_p = 1020$; % J/kg/K %

%% properties of Mg at unheated area %%

$k_c = 156$; % W/m/K %

$\rho_{\text{Mg}} = 1740$; % kg/m³ %

$c_p = 1020$; % J/kg/K %

%% the effusivity %%

$\alpha_c = (k_c \cdot \rho_{\text{Mg}} \cdot c_p)^{0.5}$;

$\alpha_s = (k_s \cdot \rho_{\text{Mg}} \cdot c_p)^{0.5}$;

%% initial boundary conditions %%

$u_{\text{inf}} = 298$; % temperature at infinite time, unit K %

$u_{c0} = 298$; % initial temperature of ceramic, unit K %

$u_{s0} = 680$; % initial temperature of steel, unit K %

$u_{k0} = 489$; % initial temperature of the interface, unit K %

%% New temporary parameters, assume $dx = dy$ %%

$\beta_c = k_c \cdot dt / (\rho_{\text{Mg}} \cdot c_p \cdot dx^2)$;

$\beta_s = k_s \cdot dt / (\rho_{\text{Mg}} \cdot c_p \cdot dx^2)$;

```

a=ks/kc;
alpha1=h*dx/kc;
alpha2=h*dx/ks;
gamma2=h*dy/ks;

%% new parameters for calculation %%

beta1=1/betac;
beta2=1/betas;

%% assign the temperature field vectors %%
un=zeros(I+1,J+1); % temperatures at t=ndt %
un1=zeros(I+1,J+1); % temperatures at t=(n+1)dt %
u1=zeros(I+1,J+1); % temperatures at t=1min %
u2=zeros(I+1,J+1); % temperatures at t=5mins %
u3=zeros(I+1,J+1); % temperatures at t=15mins %
u4=zeros(I+1,J+1); % temperatures at t=1hour %
u5=zeros(I+1,J+1); % temperatures at t=2hours %

%% initially set the final temperatures of points A and B %%
uA(1)=680;
uB(1)=(alphac*uc0+alphas*us0)/(alphac+alphas);

%% assign the initial conditions to the temperature matrix %%
% initial temperature of the un-heated zone %
for j=1:k
    un(:,j)=298;

```

```

end
% initial temperature of the heated zone %
for j=(k+2):(J+1)
    un(:,j)=680;
end
% initial temperature of the interface %
un(:,k+1)=(alphac*uc0+alphas*us0)/(alphac+alphas);

%% put in the A matrices %%
A=zeros((I+1)*(J+1),(I+1)*(J+1));

% start of the bottom face at j = 1 %
for i=1:(I+1)
    A(i,i)=1;
    A(i,i+I+1)=-1;
end
% end of the bottom face %

% start of un-heated part at 1 < j < k+1 %
for j=2:k
    p=(j-2)*(I+1);
    m=(j-1)*(I+1);
    q=j*(I+1);
    A(m+1,m+1)=1+alpha1;

```

```

A(m+1,m+2)=-1;
for i=2:I
    A(m+i,m+i)=-beta1-4;
    A(m+i,m+i-1)=1;
    A(m+i,m+i+1)=1;
    A(m+i,p+i)=1;
    A(m+i,q+i)=1;
end
A(m+I+1,m+I+1)=1+alpha1;
A(m+I+1,m+I)=-1;
end
% end of un-heated part %

% start of interface at j = k+1 %
p=(k-1)*(I+1);
m=k*(I+1);
q=(k+1)*(I+1);
for i=1:(I+1)
    A(m+i,m+i)=a+1;
    A(m+i,p+i)=-1;
    A(m+i,q+i)=-a;
end
% end of interface %

% start of heated part at k+1 < j < J+1 %

```

```

for j=(k+2):J
    p=(j-2)*(I+1);
    m=(j-1)*(I+1);
    q=j*(I+1);
    A(m+1,m+1)=1+alpha2;
    A(m+1,m+2)=-1;
    for i=2:I
        A(m+i,m+i)=-beta2-4;
        A(m+i,m+i-1)=1;
        A(m+i,m+i+1)=1;
        A(m+i,p+i)=1;
        A(m+i,q+i)=1;
    end
    A(m+I+1,m+I+1)=1+alpha2;
    A(m+I+1,m+I)=-1;
end

% end of heated part %

% start of the top face at j = J+1 %
p=(J-1)*(I+1);
m=J*(I+1);
for i=1:(I+1)
    A(m+i,m+i)=1+gamma2;
    A(m+i,p+i)=-1;
end

```

```

% end of the top face %

%% End of A-matrix input %%

%% LU decomposition of A matrix %%
[L,U]=lu(A);

%% input the b vector %%
b=zeros((I+1)*(J+1),1);
y=zeros((I+1)*(J+1),1);

%% calculate u at step n %%
VecU=zeros((I+1)*(J+1),1);
VecU=298;

%% solve the equation Au=b step by step %%
for n=1:N
% bottom face b(i) = 0, i = 1,2,...,I+1%
% start of un-heated part %
for j=2:k
    m=(j-1)*(I+1);
    b(m+1)=alpha1*uinf;
    for i=2:I
        b(m+i)=-un(i,j-1)-un(i-1,j)+(4-beta1)*un(i,j)-un(i+1,j)-un(i,j+1);
    end
    b(m+I+1)=alpha1*uinf;

```

```

end

% end of unheated part %

% at the interface  $b(i) = 0$ ,  $i=k*(I+1)+1$ ,  $k*(I+1)+2$ , ... ,  $k*(I+1)+I+1$  %

% start of heated part %

for j=(k+2):J
    m=(j-1)*(I+1);
    b(m+1)=alpha2*uinf;
    for i=2:I
        b(m+i)=-un(i,j-1)-un(i-1,j)+(4-beta2)*un(i,j)-un(i+1,j)-un(i,j+1);
    end
    b(m+I+1)=alpha2*uinf;
end

% end of heated part %

% start of the top face %

m=J*(I+1);
for i=1:(I+1)
    b(m+i)=gamma2*uinf;
end

% end of the top face %

% start of calculation %

y=L\b;
un1=U\y;

```

```

% record the temperature field and flux components at desired time %
if (n == TP1)
    u1=reshape(un1,I+1,[]); % temperature field at 25  $\mu$ s %
elseif (n == TP2)
    u2=reshape(un1,I+1,[]); % temperature field at 100  $\mu$ s %
elseif (n == TP3)
    u3=reshape(un1,I+1,[]); % temperature field at 0.5 ms %
elseif (n == TP4)
    u4=reshape(un1,I+1,[]); % temperature field at 1 ms %
elseif (n == TP5)
    u5=reshape(un1,I+1,[]); % temperature field at 5 ms %
elseif (n == TP6)
    u6=reshape(un1,I+1,[]); % temperature field at 25 ms%%
end

%% refresh un and record the temperature at points A and B %%
un=reshape(un1,I+1,[]); % refresh the temperature field matrix un %
uA(n+1)=un(Mid,J+1); % record the temperature at point A %
uB(n+1)=un(Mid,k+1); % record the temperature at point B %

% set stop point %
if ( max(abs(un1-VecU)) <= 5)
    StepT=n; % record the total step %
    break;
end

```

```
end

u1=u1.';
uf1=uf1.';
u2=u2.';
uf2=uf2.';
u3=u3.';
uf3=uf3.';
u4=u4.';
uf4=uf4.';
u5=u5.';
uf5=uf5.';
u6=u6.';
uf6=uf6.';
un=un.';

StepT % output the eventual total steps %

%% x, y axis, time t-axis %%
Xaxis=zeros(I+1,1);
for i=1:(I+1)
    Xaxis(i)=(i-1)*dx*1000;
end
Yaxis=zeros(J+1,1);
for j=1:(J+1)
```

```

    Yaxis(j)=(j-1)*dy*1000000;
end
Taxis=zeros(StepT+1,1);
for n=1:(StepT+1)
    Taxis(n)=(n-1)*dt;
end

uc1=u1-273;
uc2=u2-273;
uc3=u3-273;
uc4=u4-273;
uc5=u5-273;
uc6=u6-273;
ucn=un-273;
uA=uA-273;
uB=uB-273;

%% codes for plot temperature fields %%
contourf(Xaxis,Yaxis,uc1)
caxis([25,400])
colorbar
xlabel('Width parallel to shear band (mm)')
ylabel('Width perpendicular to shear band (\mum)')
title('Temperature distribution at t = 25 \mus')

```

LIST OF PUBLICATIONS

1. **J. Shen**, V. Gärtnerová, A. Jäger, L. J. Kecskes and Q. Wei, "Effect of yttrium on the mechanical behavior of magnesium subjected to equal channel angular pressing". *In preparation*.
2. **J. Shen**, W. Yin, K. Kondoh, T. L. Jones, S. N. Mathaudhu, L. J. Kecskes and Q. Wei, "Mechanical properties and deformation mechanism of magnesium alloy AMX602". *In preparation*.
3. **J. Shen**, W. Yin, K. Kondoh, T. L. Jones, L. J. Kecskes, S. N. Yarmolenko and Q. Wei, "Mechanical Behavior of a Lanthanum-Doped Magnesium Alloy at Different Strain Rates". *Materials Science and Engineering A*, vol. 626, pp. 108-121, 2015.
4. Vincent H Hammond, Tomoko Sano, Joseph P Labukas, Teresa A Dillon, Brady G Butler, **Jianghua Shen** and Qiuming Wei, "Evaluation of an Al, La Modified MgZn2Y2 Alloy". ARL-TR-6807, US Army Research Laboratory, Aberdeen Proving Ground, MD, February 2014.
5. **J.H. Shen**, Y.L. Li and Q. Wei, "Statistic derivation of Taylor factors for polycrystalline metals with application to pure magnesium". *Materials Science and Engineering: A*, vol. 582, pp. 270-275, 2013.
6. **Jianghua Shen**, Weihua Yin, Qiuming Wei, Yulong Li, Jinling Liu and Linan An, "Effect of ceramic nanoparticle reinforcements on the quasi-static and dynamic mechanical properties of magnesium-based metal matrix composites". *Journal of Materials Research*, vol. 28, pp. 1835-1852, 2013.
7. **J. Shen**, K. Kondoh, T.L. Jones, S.N. Mathaudhu, L.J. Kecskes and Q. Wei, "Mechanical Properties of Newly Developed Mg-Alloys AMX602 AND AZXE7111 under Quasi-Static and Dynamic Loading" in *Magnesium Technology 2012*, John Wiley & Sons, Inc., pp. 371-375, 2012.

VITA

Jianghua (Jon-Hwa) Shen was born in Fuyang, a small city of Zhejiang Province of P. R. China, on December 10, 1985. After he received his bachelor's degree in Mechanical Engineering from Zhejiang University in 2008, he joined the School of Aeronautics in Northwestern Polytechnical University to study Solid Mechanics. In 2010, he received a scholarship from China Scholarship Council to study at University of North Carolina in Charlotte (UNC Charlotte), as an exchange doctoral student. After two years, he joined the PhD program in the Department of Mechanical Engineering and Engineering Science of the same university. He is married to Hongju Yin in May 10th 2012, and has a son, Ruopu Shen.